Technische Universität München
TUM School of Natural Sciences

Neutron Star Formation in Accretion-Induced Collapse of White Dwarfs

Eirini Batziou

Vollständiger Abdruck der von der TUM School of Natural Sciences der Technischen Universität München zur Erlangung des akademischen Grades einer

Doktorin der Naturwissenschaften (Dr. rer. nat.)

genehmigten Dissertation.

Vorsitz:		Prof. Dr. Bruno Leibundgut
Prüfer*innen der Dissertation:	1.	Prof. Dr. Hans-Thomas Janka
	2.	Prof. Dr. Sherry Suyu

Die Dissertation wurde am 13.06.2023 bei der Technischen Universität München eingereicht und durch die TUM School of Natural Sciences am 10.07.2023 angenommen.

Contents

1 Introduction **1**

1.1 Neutron Stars 2

1.1.1 Neutron stars from core-collapse supernovae 2

1.1.2 Neutron stars from double neutron star mergers 4

1.1.3 Neutron stars from the accretion-induced collapse of white dwarfs . 5

1.2 Significance and Observations of AICs 7

1.3 Physics of the AIC of White Dwarfs to Neutron Stars 10

1.4 Modeling of AICs 12

1.5 Goals and Structure of this Thesis 13

2 Numerical Simulations with the ALCAR code **15**

2.1 Hydrodynamics 15

2.1.1 Equation of State 16

2.2 Radiation Transport 17

2.3 Numerical Methods 22

3 Initial Models **23**

3.1 Pre-collapse Models 23

3.2 Properties of the Progenitor Models 26

3.3 Circum-stellar Medium 29

3.4 Grids and Resolution 30

4 Collapse and Evolution of AIC models **33**

4.1 Collapse of AIC Models 33

4.1.1 Collapse and bounce of the non-rotating model 35

4.1.2 Collapse and pressure bounce of the rotating models 36

4.1.3 Collapse and centrifugal bounce of the rotating models 39

4.2 Development of the Neutrino-Driven Outflow from AICs 40

4.2.1 Overview of explosion dynamics 41

4.2.2 Non-rotating spherical symmetric model 42

4.2.3 Rotating models 43
4.3 Angular Momentum Evolution and Disk Formation 45
4.4 Explosion Energy 54
4.5 Neutron Star Properties 56

5 Neutrino Signal **61**
5.1 Neutrino Signatures 61
5.2 Effect of Rotation on the Neutrino Signal 66

6 Ejecta Properties **75**
6.1 Ejecta Mass 75
6.2 Composition of the Ejecta 76
6.3 Effect of Rotation on the Ejecta Composition 80
6.4 Nucleosynthesis Implications from the AIC Ejecta 84

7 Summary and Conclusions **87**

A Appendix **91**

Additional Information **119**

Bibliography **135**

Acknowledgements **149**

Chapter 1

Introduction

> "On 28 November 1967, it came
> again, a string of pulses
> one-and-a-third seconds apart."
>
> – Jocelyn Bell

In England's cold and windy countryside, Jocelyn Bell, a graduate student at the University of Cambridge, discovered a new type of astronomical object on 28 November 1967. With her astounding observability, Jocelyn Bell noticed the odd signal among the vast amount of data collected daily and could distinguish its pulsating nature. Jocelyn Bell and her supervisor Antony Hewish jokingly called the signal LGM-1 for "little green men". Little did they know, this signal did not come from an alien civilization or any other human-made source but was the first discovery of an unknown object; a pulsating radio source or pulsar (Hewish et al., 1968). This was the first discovery of a pulsar, which is a highly-magnetized and rotating neutron star, and the first observation of a neutron star.

Neutron stars, predicted by Baade & Zwicky (1934), are tightly connected to core-collapse supernovae which are luminous explosions of massive stars that can outshine a whole galaxy and leave behind a remnant that can either be a neutron star or a black hole. Even though the first observed supernova in recorded history might be in 4500±1000 BC, as the rock carvings found in the Burzahama region in Kashmir, India, indicate (Joglekar et al., 2011), the earliest widely observed supernova explosion was in 1054 by Chinese astronomers (Clark & Stephenson, 1977). This is associated with the supernova remnant named the Crab Nebula and hosts a neutron star that has been widely studied (e.g., Comella et al., 1969).

In this thesis, I aim to explore a different kind of "explosion" that has yet to be observed, but it is considered to also give birth to neutron stars, namely the accretion-induced collapse (AIC) of white dwarfs to neutron stars.

1.1 Neutron Stars

Neutron stars, together with black holes, are one of the most dense objects in the observable Universe. Being the compact remnants of violent explosions, they present much interest across different fields of physics and astrophysics. Neutron stars have masses of $\sim 1.4 - 2.3\,\mathrm{M}_\odot$ (e.g., Hartle, 1978; Romani et al., 2022), and mean radii of a few tens of kilometers, implying an extreme density of the matter. They mainly consist of free neutrons, and the degeneracy pressure of neutrons prevents them from collapsing under their gravity. Neutron stars are characterized by rapid rotation with spin periods ranging from 1.4 ms to 30 s and strong magnetic fields of the order of $\sim 10^8 - 10^{15}$ G (e.g., Manchester et al., 2005).

Neutron stars are probes of extreme physics, formed under very strong gravity, and are perfect laboratories to study the equation of state of nuclear matter. Matter under these conditions cannot be found on Earth. Thus neutron stars are an excellent environment to study and test theories of nuclear physics and condensed matter. For example, neutron star observations that infer their radii and masses can constrain the equation of state of nuclear matter (e.g., Burgio et al., 2021; Lattimer, 2012; Lattimer & Swesty, 1991). Gravitational wave emission was observed when two neutron stars collided. In fact, the first observation of such a collision came with the direct gravitational wave signal in the event named GW170817 (Abbott et al., 2017), for which Kip Thorne, Rainer Weiss and Barry C. Barish were awarded the Nobel Prize in Physics of the same year for their contributions to said observation with the LIGO[1] detector.

Understanding neutron stars is an essential part of astrophysics. Neutron stars are the endpoints of stellar evolution for massive stars, are involved in nucleosynthesis, and are responsible for various high-energy phenomena, such as gamma-ray bursts or X-ray binaries. The study of neutron stars can lead us to gain insight into stellar evolution or heavy element production and, therefore, continue building the puzzle of how the Universe works. To comprehend better the nature of these extreme objects, it is crucial to understand and investigate the different systems in which neutron stars are born and evolve. Neutron stars are formed during the core collapse of massive stars, via the accretion-induced collapse of white dwarfs, and also via existing neutron stars that merge. A schematic overview of the different formation channels of neutron stars is shown in figure 1.1.

1.1.1 Neutron stars from core-collapse supernovae

Neutron stars are the end products of stellar evolution for most massive stars with initial mass $\gtrsim 8\,\mathrm{M}_\odot$. Massive stars evolve by burning hydrogen (H) in their cores to form helium (He) and heavier elements. The low end of massive stars, i.e., ZAMS[2] mass of $8 - 10\,\mathrm{M}_\odot$, develop an oxygen-neon-magnesium (ONeMg) core via carbon (C) burning before they start to burn neon (Ne). Massive stars above $\sim 10\,\mathrm{M}_\odot$ continue to burn heavier elements to

---

[1] LIGO; Laser Interferometer Gravitational-Wave Observatory

[2] Zero Age Main Sequence; where the stars start burning H in their cores

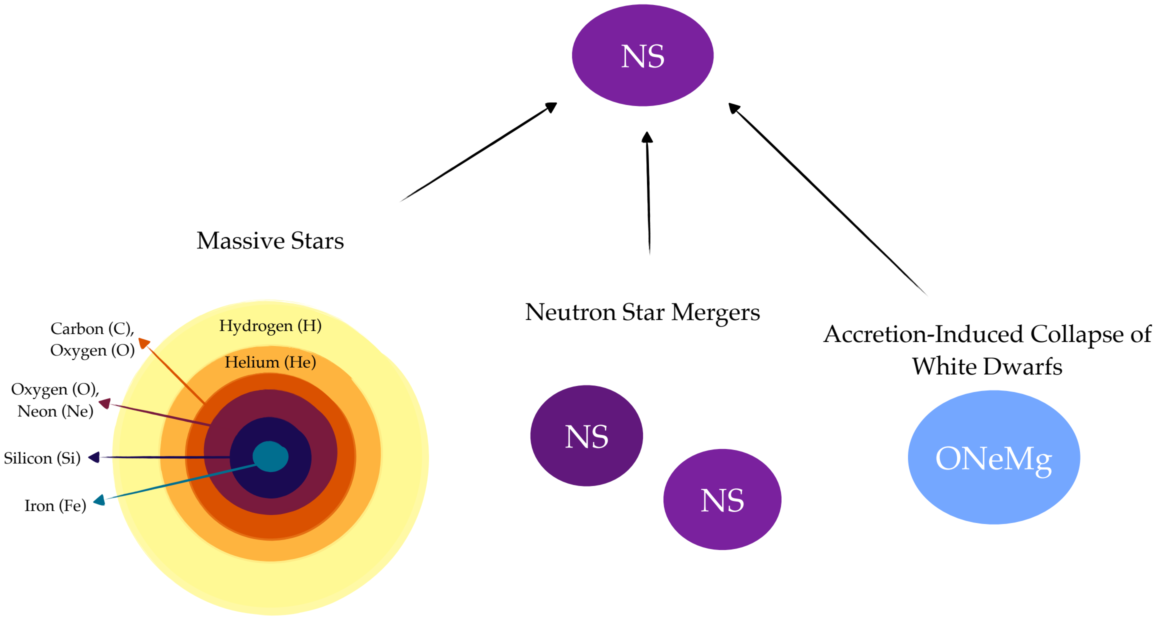

Figure 1.1: Schematic representation of neutron star (NS) formation channels. Neutron stars are mainly formed in the core collapse of massive stars with masses $\geq 8\,\mathrm{M}_\odot$ that have evolved through the advanced nuclear-burning stages to create an onion-shell structure. Apart from the massive stellar collapse, they are also formed in the accretion-induced collapse of ONeMg white dwarfs. However, existing ones in a binary neutron star system can merge and also give birth to a new neutron star. Sizes are not shown in scale.

form an onion-shell structure with lighter-element mass shells surrounding layers of heavier elements and cores consisting of Fe and Fe-group chemical elements. In ONeMg or Fe cores of evolved stars, the gravitational instability, which initiates the core collapse, is triggered by electron captures on nuclei and free protons and by the photodissociation of Fe and Fe-group elements into α particles and free nucleons (e.g., Janka et al., 2007; Langanke & Schatz, 2013). The collapsing core is suddenly reversed when the density of the core reaches nuclear saturation densities ($\rho \geq 2.7 \cdot 10^{14}\,\mathrm{g/cm^3}$) (see, e.g., Janka, 2012), the equation of state (EoS) stiffens, the adiabatic index rises, and the matter reaches a new equilibrium state, that of nuclear matter. In the center, a proto-neutron star (PNS) is formed, and a shock wave is launched, propagating outwards. Initially, the launched shock wave was thought to be the driver of the supernova explosion (Colgate & Johnson, 1960). However, the shock wave is not energetic enough to propagate through the infalling material of the star and stalls. It was only in 1966 when Colgate & White (1966) investigated the role of neutrinos in the re-launching of the shock wave. They proposed that some of the emitted neutrinos are reabsorbed and deposit energy in the post-shock region. The heating of the reabsorbed neutrinos can launch the stalled shock that eventually powers the explosion. This is the so-called delayed-neutrino mechanism of core-collapse supernovae (CCSNe) and can explain the majority of the observed explosions, see Burrows (2013); Foglizzo et al. (2015); Janka (2012, 2017a); Kotake et al. (2006) for reviews.

1.1.2 Neutron stars from double neutron star mergers

One possible way to form a binary neutron star system is by tidal capture of a neutron star by another companion. Should the companion meet the conditions to end up as a neutron star, the system will create a double neutron star binary that will merge. The tidal capture of a neutron star is possible to occur in a dense stellar environment such as globular clusters (Clark, 1975). For a detailed discussion of the possible outcomes of such a scenario, we refer to the review by Canal et al. (1990).

Another way to form neutron star binaries is by neutron stars belonging to a binary system that survive the supernova explosions and remain bound to the system. The gravitational wave emission makes them lose energy that will shrink their orbit, and therefore, they can merge to form a new neutron star or a black hole. After the famous observation of the gravitational wave signal GW170817 (Abbott et al., 2017), which was emitted during the coalescence of a binary neutron star system, neutron star mergers became a topic of intense research. They are progenitors of kilonovae[3] and are considered to be a significant site for heavy-element nucleosynthesis (see, e.g., Metzger, 2019, for a review).

Given the binary neutron star population of our Galaxy, Margalit & Metzger (2019) estimated that the vast majority of neutron star mergers would form a hypermassive neutron star (HMNS) or a supramassive neutron star (SMNS). HMSNs have masses $\mathrm{M_{tot}} \gtrsim 1.2\,\mathrm{M_{TOV}}$[4] and are supported by differential rotation. They are unlikely to survive for more than a few hundred milliseconds after the merger and before collapsing into a black hole because of the gravitational wave emission and internal hydro-magnetic torques, which lead to the loss of the differential rotation (Duez et al., 2006; Shibata & Taniguchi, 2006; Siegel et al., 2013). SMSNs have masses $\sim 1 - 1.2\,\mathrm{M_{TOV}}$, and they are supported by solid body rotation. Therefore, they need a longer time to lose their rotation via spin-down mechanisms, such as magnetic dipole radiation, and they survive for $\gg 300\,\mathrm{ms}$ before they collapse into a black hole. HMSNs account for $\sim 0 - 79\%$ of mergers while SMNSs for $\sim 18 - 65\%$ (Margalit & Metzger, 2019; Metzger, 2019). For neutron star mergers with total mass $\mathrm{M_{tot}} \gtrsim 1.3 - 1.6\,\mathrm{M_{TOV}}$ the remnant neutron star undergoes prompt collapse to a black hole on the dynamical time of milliseconds (e.g., Bauswein et al., 2013a; Shibata & Uryū, 2000). This scenario is estimated to be up to 30% of the neutron star merger outcome(s). Finally, on the lower mass end, with a total binary mass of $\mathrm{M_{tot}} < \mathrm{M_{TOV}}$, a stable neutron star will be formed that will not collapse to a black hole (Giacomazzo & Perna, 2013; Metzger et al., 2008b). The probability for a stable neutron star formation from binary neutron star mergers represents only a $\sim 3\%$ of the neutron star mergers in our Galaxy (Metzger, 2019).

---

[3] Kilonovae are transients that mainly come from neutron star mergers, and they are powered by the radioactive decay of isotopes synthesized during the merger.

[4] $\mathrm{M_{TOV}}$ or the Tolman–Oppenheimer–Volkoff limit is an upper bound to the mass of cold, non-rotating neutron stars.

1.1.3 Neutron stars from the accretion-induced collapse of white dwarfs

An alternative scenario for direct neutron star formation, apart from the massive stellar collapse, is the collapse of white dwarfs to neutron stars, which is the topic of this Thesis.

White dwarfs are the end stages of stellar evolution for low-mass stars ($\lesssim 8\,\mathrm{M}_\odot$) that evolved to develop a degenerate core mainly consisting of CO or ONeMg. White dwarfs represent the end phases for 97% of the stars in our Galaxy (e.g., Fontaine et al., 2001). They are often found in binaries, and in a fraction of these systems, mass transfer from a companion star onto the white dwarf can occur. If the mass of the white dwarf grows to exceed the Chandrasekhar mass limit (Chandrasekhar, 1931, 1935), then the white dwarf collapses to form a neutron star. This is widely called the *Accretion-Induced Collapse* of white dwarfs to neutron stars or *AIC* in short. AICs can also occur after the merger of two white dwarfs in a binary system. The latter case is often called "merger-induced collapse", but we will use the widely accepted term "accretion-induced collapse" to describe both scenarios.

The formation of neutron stars via the AIC channel in close binaries is an idea first proposed by Bailyn & Grindlay (1990) to explain the discrepancy in the birthrates of low-mass binary pulsars, which is profoundly lower than their progenitor systems, i.e., the low-mass X-ray binaries. Additionally, AICs have been suggested to explain young neutron stars in older globular clusters (e.g., Boyles et al., 2011), the large population of neutron stars in globular clusters (e.g., Bailyn & Grindlay, 1990; Dessart et al., 2006; Kitaura et al., 2006), as an alternative scenario for millisecond pulsars (e.g., Bhattacharya & van den Heuvel, 1991; Hurley et al., 2010; Ivanova et al., 2008), or to explain mass-accreting neutron stars with strong magnetic fields in low-mass X-ray binaries and some pulsars with He white dwarf companion (e.g., Li & Wang, 1998; Taam & van den Heuvel, 1986).

An extensive set of conditions is needed to make an AIC occur. The appropriate composition of the white dwarf, the accreted material, and the accretion rate must transpire so that explosive nuclear burning of the white dwarf material does not occur. The explosive ignition would lead to a thermonuclear explosion called a SN type Ia. Both AICs and SN type Ia could occur during accretion onto the white dwarf from a companion star and from double white dwarf mergers. The conditions to distinguish between the two scenarios were first explored by Nomoto & Kondo (1991) but are still under debate (e.g., Schwab et al., 2016). Traditionally, two classes of progenitors can form neutron stars via the AIC channel or lead to the complete disruption of the white dwarf together with a SN type Ia explosion. The single-degenerate scenario includes a white dwarf (i.e., degenerate star) and a companion star, and the double-degenerate scenario describes the merging of two white dwarfs in a binary system. In the following, we summarize the two scenarios for AICs and SN type Ia, highlighting the differences that distinguish the fate of the progenitor systems.

Single-degenerate scenario for SN type Ia Mass accretion from a companion star to a CO white dwarf has long been theorized to be the progenitor of SN type Ia (Hillebrandt & Niemeyer, 2000; Whelan & Iben, 1973). The companion star could be a main sequence

(MS) star, a red giant (RG), or a He star (e.g., Hachisu et al., 1996; Han & Podsiadlowski, 2004; Langer et al., 2000; Li & van den Heuvel, 1997). In this case, mass accretion onto the white dwarf occurs if the companion star fills its Roche Lobe, or in the case of a RG companion, the mass accretion could occur from the stellar wind. In the single-degenerate model, the white dwarf grows in mass via accretion of H/He-rich material by the companion star, which burns into C and O on the surface of the white dwarf while it grows in mass. Should central carbon burning be initiated via this process, the white dwarf will explode as type Ia, leaving no compact remnant behind.

Double-degenerate scenario for SN type Ia Another path to form SN type Ia is the double degenerate scenario which involves the merger of two CO white dwarfs (Iben & Tutukov, 1984; Webbink, 1984). Gravitational-wave radiation drives the orbital inspiral of the two white dwarfs that eventually merge. The merger of the two white dwarfs whose total mass exceeds the Chandrasekhar mass leads to the central ignition of C burning and, thus, to a thermonuclear SN type Ia. In the double degenerate scenario, the lower-mass white dwarf fills its Roche Lobe, and dynamically unstable mass transfer occurs to the heavier white dwarf while the mass donor (i.e., the low-mass white dwarf) is tidally disrupted. This process initiates central carbon burning, which could result in carbon detonation that subsequently explodes the white dwarf as a SN type Ia (Hillebrandt & Niemeyer, 2000; Webbink, 1984). However, the off-center ignition of C in CO white dwarfs converts it to a ONeMg white dwarf and does not explode as Type Ia (e.g., Schwab et al., 2015). The exact outcome of a double CO white dwarf merger depends on various conditions, such as the mass of the He-layer on the surface of the two white dwarfs, and is still under consideration (e.g., Han & Webbink, 1999; Kromer et al., 2013; Pakmor et al., 2022; Schwab et al., 2016; Taubenberger et al., 2013; Wu et al., 2019; Yoon et al., 2007). Another path to form SN type Ia from double CO white dwarf binaries is the violent merger scenario, which assumes the dynamical driven of a detonation that could lead to the thermonuclear explosion (e.g., Pakmor et al., 2010, 2012; Raskin et al., 2014; Ruiter et al., 2013).

Single-degenerate scenario for white dwarf collapse In the single-degenerate scenario, the ONeMg white dwarf grows in mass when accretion occurs from the companion star. The crucial difference for white dwarf collapse compared to type Ia is that the white dwarf consists of ONeMg instead of CO. The companion star can be a main-sequence star or red giant (e.g., Bailyn & Grindlay, 1990; Nomoto & Kondo, 1991; Wang, 2018; Wang & Liu, 2020). However, off-center C ignition of an accreting CO white dwarf could also lead to the formation of an ONeMg white dwarf that will collapse to form a neutron star according to the AIC scenario (e.g., Brooks et al., 2016; Nomoto & Iben, 1985; Saio & Nomoto, 1985; Wang et al., 2017). Recent studies (e.g., Tauris et al., 2013; Wang et al., 2017) show that mass accretion from a He-star onto an ONeMg white dwarf or a CO white dwarf could also lead to an AIC. ONeMg white dwarfs with high central densities ($\sim 4 \cdot 10^9$ g/cm^3, Nomoto & Kondo, 1991) undergo electron captures which reduces the effective Chandrasekhar mass and thermonuclear O burning occurs which forms a deflagration. The final outcome of the white dwarf (explosion or collapse) is determined by the competition of nuclear burning and electron captures which heavily depends on the exact central density that the nuclear burning is initiated. The current understanding is that the ONeMg white dwarfs will lead to collapse and form a neutron star (e.g., Isern et al., 1991; Jones et al., 2014; Nomoto, 1984; Nomoto & Kondo, 1991; Schwab et al., 2015).

In the case of rapidly rotating white dwarfs, the Chandrasekhar mass limit increases substantially (e.g., Ostriker & Bodenheimer, 1968; Wang et al., 2014; Yoon & Langer, 2005), allowing for more massive progenitor models. The single degenerate scenario that leads to the white dwarf collapse to form a neutron star could present a channel for double neutron star binaries.

Double-degenerate scenario for white dwarf collapse In the case of a double white dwarf system, the orbital period shrinks after the orbital energy losses due to gravitational waves emission, as was already discussed in the progenitors of SN type Ia. This evolutionary scenario for neutron star formation via the AIC mechanism mainly includes double ONeMg white dwarfs, the merger of an ONeMg with a CO white dwarf but also the merger of double CO white dwarfs (see, e.g., Wang & Liu, 2020, for a review). If the white dwarf mergers include an ONeMg white dwarf, the collapse occurs due to the high central temperatures and densities that lead to electron capture by Ne and Mg (Minerbo, 1978; Nomoto & Kondo, 1991; Nomoto et al., 1979). In the case of double CO white dwarfs, it is thought to produce SN type Ia, as discussed above. However, this kind of merger could trigger the quiescent conversion to an ONeMg white dwarf via inward propagating carbon flame (e.g., Nomoto & Iben, 1985; Saio & Nomoto, 1985; Schwab et al., 2016). To summarize, the current understanding supports that double CO white dwarf mergers could lead to neutron star formation or SN type Ia depending on the mass ratio of the white dwarfs, the exact composition (i.e., the mass of He-layer), and accretion rates, while the violent CO white dwarf mergers will most likely lead to a SN type Ia.

The mass accretion rate, the mass and composition of the white dwarf are the fundamental parameters that distinguish between the SN type Ia and the AIC (Nomoto & Kondo, 1991; Schwab et al., 2016). For a summary we refer to figure 1.2 that displays the different evolutionary scenarios for accretion onto ONeMg and CO white dwarfs, as presented in Nomoto & Kondo (1991). In the double-degenerate scenario of the white dwarf collapse, single neutron stars can be born.

1.2 Significance and Observations of AICs

AICs occur from different progenitor systems and can form double neutron star binaries or isolated neutron stars. Apart from explaining various astrophysical systems, AICs play a remarkable role in the multi-messenger and transient astronomy era. The AIC scenario has been thought to contribute to various topics, from the chemo-dynamic evolution of galaxies to gravitational wave sources. The main contributions from AICs can be summarized as

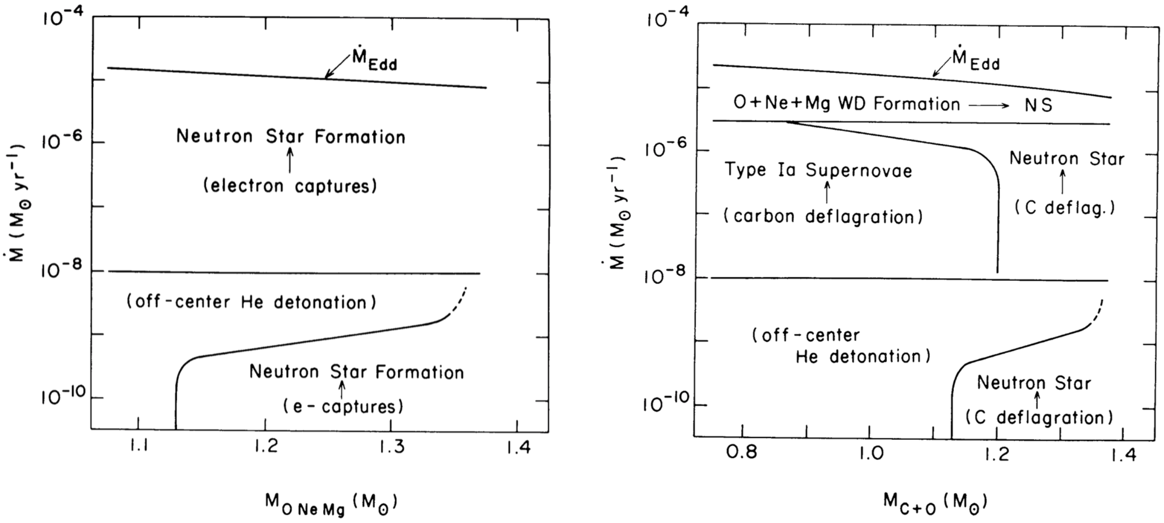

Figure 1.2: Mass accretion rate as a function of the mass of an ONeMg white dwarf (left panel) and a CO white dwarf (right panel). Nomoto & Kondo (1991) present the regions where white dwarf collapse is possible by electron captures. In the case of a massive and cold CO white dwarf, C deflagration could still lead to the collapse because of the high central densities. Figure taken from Nomoto & Kondo (1991).

follows:

- AICs are sites of heavy-element nucleosynthesis. Heavy elements produced by the rapid neutron capture, i.e., r-process, are considered to take place in AICs, although the exact amount of r-process material produced and the extension of the relative importance of AICs compared to other r-process astrophysical sites is still under debate (e.g., Dessart et al., 2006; Ehring et al., 2023; Fryer & Heger, 2000; Qian & Wasserburg, 2007; Wheeler et al., 1998).
- Collapsing white dwarfs and particularly rotating white dwarfs are predicted to be gravitational wave sources (e.g., Abdikamalov et al., 2010). Close white dwarf binaries are predicted to emit gravitational waves with a frequency of the order of $10^{-4} - 10^{-1}$ Hz before their collapse, which should populate the gravitational-wave galactic background (Evans et al., 1987; Nelemans et al., 2001). It is expected that this signal will be observed by future space-based gravitational wave detectors such as the Laser Interferometer Space Antenna (LISA, e.g., Cooray et al., 2004; Nelemans et al., 2004; Ruiter et al., 2010). An additional gravitational wave signal is expected at the white dwarf collapse (Abdikamalov et al., 2010; Dessart et al., 2006).
- Cao et al. (2018); Margalit et al. (2019); Moriya (2019) argue that some fast radio bursts (FRBs) could be explained by AICs.
- Belczynski et al. (2018) suggest that double neutron stars could be formed in globular clusters. In that scenario, double neutron star binaries could form when a neutron star - ONeMg white dwarf binary interacts with a CO white dwarf. The interacting white dwarfs will form a neutron star via the AIC scenario.

The corresponding rate of these events can constrain the importance of AICs. However, there is no confirmed observation of AICs. The absence of an observation cannot give definite answers to the AIC rates, and we can only obtain limits from the theoretical modeling. The estimated rates for AICs in our Galaxy are in the order of $\sim 0.3{-}0.9{\cdot}10^{-3}$/yr for the single-degenerate scenario and $\sim 1.4{-}8.9{\cdot}10^{-3}$/yr for the double-degenerate scenario (Liu & Wang, 2020; Wang, 2018). Fryer et al. (1999) estimated the rate for AICs to be much lower in the range from $10^{-7} - 10^{-5}$/yr in both scenarios. They estimated the AIC rate by modeling the r-process nucleosynthetic yields from the neutron-rich ejecta from AICs. However, r-process element production in AICs is a matter of discussion (Dessart et al., 2006; Ehring et al., 2023; Fryer et al., 1999; Qian & Wasserburg, 2007).

Until now, there has been no confirmed observation of an AIC event even though an increasing number of observed transients speculate this possibility (e.g., Gillanders et al., 2020; McBrien et al., 2019). Apart from the faint nature of AIC-associated mass ejection, the lack of detailed models with predictions of observables makes the detection of such events even more challenging. It is predicted that AICs result in relatively faint optical transients compared to a typical SN with a canonical explosion energy of 10^{51} erg (e.g., Dessart et al., 2006). Additionally, there are only limited predictions about the electromagnetic signals of these events (Darbha et al., 2010). Therefore, identified transients could be misinterpreted as other faint transients (e.g., Gillanders et al., 2020, see discussion later on).

There is an increase in observations of transients that do not convincingly fit the conventional scenarios of stellar deaths. A recent discovery of a fast radio transient (Anderson et al., 2019) opened the discussion of AIC observations in radio frequencies (Margalit et al., 2019). Moriya (2019) suggests that the radio emission could potentially result from the interaction by the shock wave from the AIC and the circum-stellar medium. In addition, they showed that the observed signal could give us a glimpse of whether the AIC comes from a single or double degenerate system. Scholz et al. (2016) discovered a radio source connected to the fast radio burst FRB 121102. The persistent radio source is considered a "weak stellar explosion" with low energy and mass ejection that might be consistent with the AIC scenario (Margalit et al., 2019; Sharon & Kushnir, 2020; Waxman, 2017). Margalit et al. (2019) propose that AICs could be progenitors of some FRBs considering that magnetars could be born via the AIC channel (Dessart et al., 2007). Thus, due to the low-energetic, low-ejecta mass and thus faint nature of AICs, they could be first detected as radio transients. Even though these radio observations have been associated with the possibility of an AIC event, the speculations are far from a confirmed case.

A relatively recent observation of a rapidly declining transient, namely the AT2018kzr, has also been connected to a plausible AIC event. McBrien et al. (2019) performed spectroscopic and lightcurve analysis of the transient and discussed different explosion scenarios that could explain the observed signal. They consider that this observation could be explained by an AIC event or the merger of a white dwarf and a neutron star. Their conclusion favors the white dwarf-neutron star merger scenario based on the composition found in their spectroscopic analysis. Their skepticism on the AIC scenario is driven by the current predictions that AICs are sources of heavier nuclei via the r-process (Darbha et al., 2010; Dessart et al., 2006; Metzger et al., 2009a). Their modeling proposes that the ejecta composition mainly consists of intermediate-mass elements, including O, Mg, Si, and Ca, in addition to a small amount of Fe. However, detailed nucleosynthesis calculations for the AIC ejecta from self-consistent models are missing from the literature, and thus there is still considerable uncertainty on the heavy-element production in AICs.

A similar analysis was performed by Gillanders et al. (2020) for the same fast-evolving transient. Gillanders et al. (2020) obtained models to explain the early epoch of the observed photospheric spectra, and thus, they extracted properties of the ejecta such as the ejecta velocity and composition. They disfavor the AIC scenario via ONeMg white dwarf collapse or double-white dwarf mergers based on the discrepancy of their derived composition and the composition predicted from theoretical calculations of AICs (Darbha et al., 2010; Dessart et al., 2006; Metzger et al., 2009a) and double white dwarf mergers (Brooks et al., 2017), in agreement with the conclusions of McBrien et al. (2019). It is worth noticing that the existing attempts for nucleosynthesis predictions from AICs are based on a very limited set of simulations and with approximation in the physics involved (see discussion in section 1.4).

Apart from the observations that could plausibly be an AIC event, only a few observations point to potential progenitor models. Recently, a super-Chandrasekhar object, named IRAS 00500+6713, was identified, and it is expected to end its life as an AIC (Gvaramadze et al., 2019; Oskinova et al., 2020). The observed object consists of a central star which is identified as a super-Chandrasekhar white dwarf that it is embedded in a circular nebula which probably comes from a SN type Iax[5]. Gvaramadze et al. report that the discovered object matches a rapidly rotating stellar object with strong magnetic fields. Additionally, they suggest that the observations are in accordance with the post-merger evolution of a double-white dwarf merger (Schwab et al., 2016). Oskinova et al. conclude that the object IRAS 00500+6713 resulted from the coalescence of an ONeMg and a CO white dwarf. This scenario has also been recently studied by Wu et al. (2023). Both Gvaramadze et al. (2019) and Oskinova et al. (2020) conclude that the white dwarf remnant will stay above the Chandrasekhar mass limit and will probably undergo core collapse to form a neutron star in an AIC event. Caiazzo et al. (2021) report on discovering a highly magnetized and rapidly rotating white dwarf identified as ZTF J190132.9+145808.7. Their analysis cannot confidently conclude the fate of this object, but they suggest that it will end its life as an AIC event or a SN type Ia.

1.3 Physics of the AIC of White Dwarfs to Neutron Stars

The evolutionary paths to form a neutron star or a double-neutron star binary via the AIC mechanism depend on various conditions as it was already discussed, which are poorly constrained due to the absence of a verified AIC observation. However, white dwarfs that evolve at the stage to end up as an AIC will undergo electron captures on Ne, Mg, and free nuclei (Miyaji et al., 1980) and collapse to form a neutron star.

---

[5] SN Type Iax is a sub-category of SN type Ia that has lower luminosity and ejecta mass.

The road to collapse When a white dwarf exceeds the Chandrasekhar mass limit, the degeneracy pressure support from the matter is insufficient to balance the self-gravity. While the mass increases, the core of the white dwarf will contract to result in higher core densities. When the central density exceeds $\sim 10^9\,\mathrm{g/cm^3}$ (Nomoto & Kondo, 1991; Schwab et al., 2015), electron captures on Ne and Mg are favorable, via the inverse β-decay:

$$e^- + p \rightarrow n + \nu_e, \tag{1.1}$$

$$e^- + (A, Z) \rightarrow (A, Z-1) + \nu_e$$

and produce neutrons, n, and electron neutrinos, ν_e. The electron captures reduce the Chandrasekhar mass limit and decrease the pressure in the core. This process triggers gravitational instability, leading to the core collapsing and forming a hot proto-neutron star (PNS). The PNS is a preceding object that will eventually become a neutron star. As the gravitational collapse occurs, the matter will reach higher and higher densities until nuclear matter density ($\rho \geq 2.7 \cdot 10^{14}\,\mathrm{g/cm^3}$) is reached, as in CCSNe. Initially, the electron neutrinos ν_e from the electron captures can escape, but as the density increases, the neutrinos get trapped in the high-density core. Since the neutrinos cannot escape, the infall continues adiabatically, and the inner core collapses homologously, i.e., the radial velocity is proportional to the radius ($u_\mathrm{r} \sim r$, where r is the radius). For a comprehensive discussion on collapse physics, we refer the reader to Shapiro & Teukolsky (1983, Chapter 18). The infall stops when nuclear matter densities are reached because the repulsive nuclear forces between nucleons become significant and prevent the further contraction of the matter. Then, the matter undergoes a phase transition to nuclear matter resulting in the rise of the adiabatic index and the stiffening of the equation of state (EoS) of the matter. Since further compression cannot occur, the matter is bouncing back, and the core emits pressure waves that eventually stiffen to create a shock wave propagating outwards. In the center, a neutron star forms, and the shock wave, assisted by neutrino heating, drives the outflow.

Neutrino-driven outflow Electron neutrinos are produced in large numbers by electron captures and carry away most of the binding energy of the core; however, they remain trapped in the high densities of the core. As the shock moves to lower densities, the neutrinos start to diffuse. As the shock wave propagates in even lower densities, the neutrinos propagate in neutrino-transparent regions.

There is a general consensus that a small fraction of the emitted neutrinos will be reabsorbed in the post-shock region, thus heating that region (Colgate & White, 1966). This raises the post-shock pressure; therefore, the shock accelerates outwards and breaks out of the surface of the contracting white dwarf. For a thorough discussion of the physics involved in the neutrino-driven mechanism, which is similar in AICs and CCSNe, we refer to the review of Bethe (1990).

The neutrino emission that accelerates the shock wave can last several seconds, and with this mechanism, the ejecta is launched from the white dwarf. As the ejecta, we account for the material that propagates outwards and is unbound. Furthermore, after the ejecta driven by the shock wave, the ongoing neutrino heating on the surface of the new-born neutron star will create a “secondary” outflow of baryonic matter of high entropy that originates from the neutron star’s surface. This is referred to as the neutrino-driven wind and adds on the total mass ejecta in an AIC (e.g., Dessart et al., 2006; Woosley & Baron, 1992).

1.4 Modeling of AICs

Even though the underlying mechanism that drives the explosion is theoretically established, the parameter space of the different properties of the pre-collapse AIC systems and how this affects the AIC dynamics and observed signals is widely unexplored. The complexity and uncertainty of the AIC progenitor systems create a gap in the connection to observables. However, numerical modeling of physically motivated pre-collapse systems can significantly improve the understanding of AICs and connect them with potential observations.

The first attempts for modeling the AICs were made by Woosley & Baron (1992), who laid the foundations for the neutrino-driven outflow in one-dimensional AIC models, and Fryer et al. (1999), who explored the AIC scenario in one and two dimensions and set preliminary constraints on the nucleosynthetic output of the AIC events.

Following the advances in the CCSN modeling (see, e.g., Burrows, 2013; Janka, 2017a, for reviews), the neutrino-radiation hydrodynamics modeling has significantly advanced, allowing for the modeling of sophisticated multi-dimensional simulations of CCSNe (e.g., Bollig et al., 2021; Glas et al., 2019b; Nagakura et al., 2021; Powell et al., 2023; Vartanyan et al., 2022). However, multi-dimensional simulations addressing the AIC scenario, including the current advancements in neutrino-hydrodynamics modeling, are rare in the literature. Some existing ones were constrained to the phase around core bounce without neutrino transport to determine the characteristic gravitational-wave signal associated with the collapse and bounce of rotating white dwarfs (Abdikamalov et al., 2010). Some recent studies (Chan et al., 2022, 2023; Leung et al., 2019; Zha et al., 2019) performed numerical simulations of dark matter-admixed white dwarfs, suggesting that a potential AIC observation could also set constraints in the dark matter on small scales. Other simulations were constrained to the very early phases of the shock evolution until a few 100 milliseconds (Dessart et al., 2006), covering only the onset of the mass ejection for a small fraction of the total mass loss of the collapsing white dwarfs. Moreover, these modeling efforts considered only a few progenitor conditions and suffered from simplified approximations in the neutrino treatment (via flux-limited diffusion and with a small subset of the relevant neutrino interactions).

Besides overcoming such limitations, it is of paramount importance to follow the evolution of the ejected material and the newly formed neutron star until much later stages when the neutrino emission declines and the ejecta approaches a self-similar expansion. Such long-time simulations are indispensable for reliable and meaningful predictions of the observables as an attempt to bridge the theoretical knowledge to the current and increasing observational signals of transients that do not fit the traditional picture of stellar deaths.

1.5 Goals and Structure of this Thesis

The goal of our project is to conduct, for the first time, self-consistent two-dimensional (2D) neutrino-hydrodynamical simulations of AICs from the onset of white dwarf collapse through core bounce and all the way to the homologous expansion of the ejecta several seconds later for a set of six models of non-rotating and rotating white dwarfs with different initial masses, different spin rates, and angular momentum profiles. These simulations will be the first ones of their kind to cover the significant fraction of the neutrino-cooling evolution of the PNSs formed in the collapse of white dwarfs when gravitational instability is triggered by mass accretion from a companion star or in the secular evolution of the product of a binary white dwarf merger.

Given the absence of stellar-evolution models of white dwarf mergers or accreting white dwarfs on the verge of collapse, we employ physically motivated progenitor models that represent the final evolutionary state of a system that ends as an AIC. We use pre-collapse models that are computed configurations of degenerate matter in rotational equilibrium. The initial pre-collapse AIC models are based on the calculations of Abdikamalov et al. (2010) with improvements in the stability of the rotational equilibrium (Ehring, 2019). The selected models cover a representative set of conditions that could incorporate both the single-degenerate and the double-degenerate scenario for AICs (see section 1.1.3). This gives us the advantage of simulating, for the first time, a representative set of AIC progenitors with a neutrino-hydrodynamics code that includes all the relevant physical processes crucial for AICs.

Our modeling employs fully multi-dimensional, multi-energy-group neutrino transport (by a two-moment treatment) (Just et al., 2018, 2015b; Obergaulinger, 2008) with a state-of-the-art description of the neutrino interactions (Just et al., 2018) (based on Bruenn (1985); Hannestad & Raffelt (1998); Horowitz (2002); O'Connor (2015); Pons et al. (1998)) and a modern nuclear equation of state (Steiner et al., 2013) that satisfies all current experimental and astrophysical constraints, including the radius bounds deduced from the recent gravitational-wave detection for the neutron star-merger event of GW170817. The ALCAR code is widely used and tested in multi-dimensional simulations of CCSNe (e.g., Bugli et al., 2023, 2021; Glas et al., 2020, 2019a,b; Just et al., 2018; Obergaulinger & Aloy, 2021; Obergaulinger et al., 2014) and neutron star mergers (e.g., Just et al., 2022, 2023; Sneppen et al., 2023).

Our simulations will determine characteristic properties of the AIC events such as ejecta masses, ejecta geometry, and the composition, entropy, and expansion time scale of the ejecta, which are needed to compute their chemical composition by detailed nucleosynthetic post-processing. Employing the frontiers of neutrino-hydrodynamics modeling and a large set of progenitors, we improve the understanding of AICs, the dependence of different initial conditions such as white dwarf masses or rotational profiles, and calculate the properties of the ejecta and the newly-born neutron stars. Our self-consistent dynamical simulations can be used for further predictions of the nucleosynthetic output of AICs and electro-magnetic properties of an observed signal and therefore bridge the gap between the theoretical understanding of AICs and observations. Thus, our work serves to predict the observational signatures of AIC events and their contribution to the production of heavy elements in the Universe.

Organisation of this Thesis Having given a summary of the underlying theoretical understanding of AICs, the importance of the event, potential observations, and current modeling of AICs in this Chapter, we move to Chapter 2, where we describe the numerical code ALCAR that we use to conduct the simulations. In Chapter 3 we summarize the progenitor models that we use in the numerical simulations. In Chapter 4, we focus on the hydrodynamical evolution of the collapse and the onset of the neutrino-driven outflow and how the different properties of each progenitor alter the dynamical evolution of each model. In Chapter 5, we focus on analyzing the neutrino signal for each model which is significant for the neutrino-driven outflow of AICs and the ejecta composition. In Chapter 6 we focus on the ejecta properties of each model. Finally, we conclude this work in Chapter 7.

Chapter 2

Numerical Simulations with the ALCAR code

In this Thesis, we explore the accretion-induced collapse of white dwarfs to neutron stars by performing six long-time axisymmetric simulations of non-rotating and rotating white dwarfs using the code ALCAR (Just et al., 2018, 2015b; Obergaulinger, 2008). The code combines non-relativistic hydrodynamics, a Newtonian gravitational potential with general relativistic corrections, and an energy-dependent three-flavor treatment of the neutrino transport based on a two-moment scheme with an analytical closure relation for the Eddington tensor. In this chapter, we describe the technical part of this Thesis, focusing on the numerical methods used to simulate the long-time evolution of AICs. We present the basic framework of the ALCAR code developed to model the neutrino transport and hydrodynamics in CCSNe simulations and the modifications we used to adjust the code for our long-time AIC simulations. The description of the code properties is based on Just et al. (2018, 2015b) and in the detailed explanations of Glas (2019); Just (2012).

2.1 Hydrodynamics

The equations of hydrodynamics describe the fluid motions as a function of time in the stellar plasma. In this formulation, we do not include numerical viscosity or magnetic fields. Therefore, the Euler equations, which consist of the conservation law for density ρ, momentum density ρu, electron fraction Y_e, and total energy e_t, are given below:

$$\partial_t \rho + \nabla_j(\rho u^j) = 0, \tag{2.1a}$$

$$\partial_t(\rho Y_e) + \nabla_j(\rho Y_e u^j) = Q_{\mathrm{N}}, \tag{2.1b}$$

$$\partial_t(\rho u^i) + \nabla_j(\rho u^i u^j + P_g) = -\rho \nabla^i \phi + Q^i_{\mathrm{M}}, \tag{2.1c}$$

$$\partial_t e_t \nabla_j(u^j(e_t + P_g)) = -\rho u_j \nabla^j \phi + Q_{\mathrm{E}} + u_j Q^i_{\mathrm{M}} \tag{2.1d}$$

In the above equations, the right-hand side includes the gravitational terms ($\nabla\phi$) and the neutrino-matter interactions, with Q_{N} to be the source term for the electron number,

Q^i_{M} the momentum, and Q_{E} for the energy. The source terms are calculated through the neutrino-matter interaction rates and are explained in section 2.2. Additionally ϕ is the gravitational potential for a density field ρ, such as $\nabla^2\phi = 4\pi G\rho(\mathbf{r})$. Here G is the gravitational constant.

The self-gravity of the stellar fluid is described by a Newtonian gravitational potential (ϕ) obtained as the solution of Poisson's Equation in 2D. General relativistic corrections are applied by replacing the monopole of the potential with an effective relativistic formulation that reproduces the solution of hydrostatic equilibrium according to the Tolman–Oppenheimer–Volkoff (TOV) equation, following case A of Marek et al. (2006). The Poisson's equation in two spatial dimensions is based on the algorithm developed in Müller & Steinmetz (1995), which uses spherical coordinates and an expansion into spherical harmonics.

In the Euler equations for a stellar fluid, the conservation of the chemical composition of matter is included. For a chemical species i we can define the number fraction Y_i as $Y_i = n_i/n_{\mathrm{B}}$, where n_i is the number density of the species i and n_{B} is the total baryon number density. For the physics problem at hand, we define the electron fraction, a fundamental conserved quantity that is included in equation (2.1) as

$$Y_e = \frac{n_e^- - n_e^+}{n_{\mathbf{B}}}, \tag{2.2}$$

where n_e^- is the electron fraction and n_e^+ is the positron fraction.

The equations of hydrodynamics are closed by a microphysical equation of state (EoS) that describes the gas pressure P_g as a function of the gas density ρ, the electron fraction Y_e, and the internal energy. A brief summary of the EoS is given in section 2.1.1.

2.1.1 Equation of State

Since we treat a problem that covers a large spectrum of densities and temperatures, we employ a tabulated high-density EoS extended to low temperatures and a semi-tabulated one for low densities. In this section, we briefly describe the ingredients of both regimes.

High-density Equation of State We employ the microphysical SFHo EoS by Steiner et al. (2013, SFH; Steiner Fischer Hempel), which is based on a covariant Langrangian using the Walecka model for nucleon interactions via the exchange of σ, ω, and ρ mesons in a mean-field approximation. This is a high-density nuclear equation of state with a lower density limit of 1660 g/cm^3 and a lower temperature limit down to 0.1 MeV or $8.6 \cdot 10^8$ K We use an extended version with a lower temperature of 10^{-3} MeV. The equation of state closes the hydrodynamical equations of the stellar fluid. The EoS comes in a tabulated form, and we can choose the density threshold in which the high-density EoS is used, which is 2000 g/cm^3 in our case. In the high-density EoS, nuclear statistical equilibrium is assumed. This approximation assumes that above temperatures of $5 \cdot 10^9$ K, there is enough energy to balance forward and reverse nuclear reactions. In this state, the mass fractions of any element can be calculated from Maxwell-Boltzmann statistics as

$$X_i(A_i, Z_i, T, \rho) = \frac{A}{N_A \cdot \rho} \cdot \omega(T) \left(\frac{2\pi k_\mathrm{B} T m(A_i, Z_i)}{h^2} \right)^{3/2} \cdot \exp\left(\frac{\mu(A_i, Z_i) + B(A_i, Z_i)}{k_\mathrm{B} T} \right) \tag{2.3}$$

with A the atomic number of the nucleus, T is the temperature, k_B is the Boltzmann constant, N_A is the Avogadro's number, $\omega(T)$ the temperature dependent partition function, $m(A_i, Z_i)$ the mass of the nucleus, μ the chemical potential and $B(A_i, Z_i)$ the binding energy of the nucleus.

Low-density Equation of State For lower densities, we employ a partially tabulated and analytical EoS. That includes an electron/positron gas, a photon gas, and baryons. Additional corrections include Coulomb lattice corrections for pressure, energy density, entropy, and adiabatic index using a Wigner-Seitz approximation for a body-centered cubic Coulomb lattice of nuclei embedded by uniformly distributed ionization electrons. We use a two-dimensional table available in $\rho \cdot Y_e$, and T for the leptonic part, while the rest is in analytic form. Nuclear statistical equilibrium is assumed for temperatures higher than $T > 5 \cdot 10^9$ K, and the NSE table gives the composition. For temperatures lower than $T < 5 \cdot 10^9$ K, the composition has to be given as an input in the EoS in addition to ρ, Y_e, and T. The electrons are non-relativistic and non-degenerate; the full EoS (ρ, Y_e, T, and composition) can be calculated analytically. In ALCAR, when the conditions for NSE are not met, we keep the composition constant, i.e., the fraction of electrons, protons, alpha particles, and heavy nuclei remain the same. In that case, we use a representative nucleus for the heavy nuclei, which is ^{54}Mn.

2.2 Radiation Transport

Apart from the stellar gas, neutrinos will be emitted, absorbed, and transported during the collapse of the white dwarf and the birth of the neutron star. In high densities inside the proto-neutron star, neutrinos are trapped and can only escape through slow diffusive processes. In the less dense matter, neutrinos are decoupled from the matter and are in the free-streaming regime. The modeling of these processes is accomplished with the theory of radiation transport. The description of this section follows Just et al. (2018, 2015b); Munier & Weaver (1986a,b).

Neutrinos are described by the Boltzmann equation, which describes the temporal evolution for a particle distribution given by the function f in the six-dimensional phase space. The intensity of radiation I that is often used in neutrino transport is correlated to the distribution function f as:

$$I(\mathbf{x}, t, \mathbf{n}, \epsilon) = \frac{h}{c^3} \epsilon^3 f(\mathbf{x}, t, \mathbf{n}, \epsilon), \tag{2.4}$$

where $\mathbf{x}$ is the position, $\mathbf{n}$ the unit vector in the momentum direction, ϵ the neutrino energy, h the Planck constant and c the speed of light. The temporal evolution of the specific intensity I is given by the Boltzmann equation:

$$\frac{1}{c}\partial_t I + n^i \nabla_i I = [I]_{\text{coll}} \tag{2.5}$$

assuming a neutrino distribution with velocity c. The source term in the right-hand side $[I_{\text{coll}}]$ represents the neutrino-matter interactions that will be described in section 2.2.

We measure the specific intensity I in the comoving frame (i.e., fluid frame). The momentum space coordinates are measured using fixed Eulerian coordinates in the laboratory frame (lab frame). This mixed-frame approach optimizes the efficiency of the computation. Therefore, the radiation transport equation in the mixed-frame using Lorentz transformations up to order $\mathcal{O}(c/u)$ becomes:

$$\begin{aligned}
&\frac{1}{c}\partial_t I + \frac{u_i n^i}{c^2}\partial_t I + n^j \nabla_j I + \frac{u^j}{c}\nabla_j I \qquad (2.6)\\
&- \partial_\epsilon \left[I\epsilon \left(\frac{a_i n^i}{c^2} + \frac{1}{c} n^j n^k \nabla_j u_k \right) \right] \\
&+ \nabla_{n,i} \left[I \left(\frac{a_j n^j}{c^2} n^i - \frac{a^i}{c^2} + \frac{1}{c} n^i n^j n^k \nabla_j u_k - \frac{1}{c} n^j \nabla_j u^i - \Gamma^i_{jl} n^j n^l - \frac{1}{c}\Gamma^i_{jl} n^l u^j \right) \right] \\
&+ I \left[2\frac{a_i n^i}{c^2} + \frac{1}{c}\nabla_i u^i + \Gamma^i_{il} n^l + \frac{1}{c} n^j n^k \nabla_j u_k \right] = [I]_{\text{coll}}.
\end{aligned}$$

In the last equation, u is the fluid velocity, $\mathbf{a} = \partial_t \mathbf{u}$ is the fluid acceleration, Γ are the Christoffel symbols, and the ∇ refers to the derivative in the momentum space. The indices follow Einstein's sum notation.

To reduce the dimensionality of the problem, we make use of the fact that the specific intensity is related to the specific energy density E, the energy flux density F^i, and the pressure tensor P^{ij}. Consequently, instead of directly solving equation (2.6), we construct the moments of the specific intensity as follows:

$$E = \frac{1}{c}\int d\Omega_n I, \tag{2.7}$$

$$F^i = \int d\Omega_n I n^i, \tag{2.8}$$

$$P^{ij} = \frac{1}{c}\int d\Omega_n I n^i n^j, \tag{2.9}$$

$$Q^{ijk} = \int d\Omega_n I n^i n^j n^k. \tag{2.10}$$

Here, Q^{ijk} is the analog 3rd-moment quantity, and $d\Omega_n$ refers to the solid angle in momentum space.

The system of equations for the first two moments of equation (2.6) is given by taking the angular integrals of equation (2.6) and ignoring terms higher than $\mathcal{O}(u^2/c^2)$. To include general-relativistic redshift and time dilation effects, we correct the source terms and write them as a function of the lapse function α (Just et al., 2018). Therefore, the two-moment equations system according to Just et al. (2018) reads

$$\begin{aligned} \partial_t E + \nabla_j(\alpha F^j + u^j E) + P^{ij}\nabla_i u_j + F^i \nabla_i \alpha \\ - \partial_\epsilon[\epsilon(P^{ij}\nabla_i u_j + F^i \nabla_i \alpha)] = \alpha C_{\mathrm{E}}, \end{aligned} \tag{2.11a}$$

$$\begin{aligned} \partial_t F^i + \nabla_j(\alpha c^2 P^{ij} + u^j F^i) + F^j \nabla_j u_i + c^2 E \nabla^i \alpha \\ - \partial_\epsilon[\epsilon(Q^{ijk}\nabla_j u_k + c^2 P^{ij}\nabla_j \alpha)] = \alpha C^i_{\mathrm{F}}. \end{aligned} \tag{2.11b}$$

The lapse function α is calculated by integrating the relativistic Euler equation and is given by

$$\frac{\partial \alpha}{\partial r} = -\frac{1}{\rho c^2 + \epsilon_{\mathrm{int}} + p}\left(\frac{\partial p}{\partial r} - \frac{Q_{\mathrm{M}}}{\Gamma}\right). \tag{2.12}$$

The integration starts from the surface to the center, and the boundary condition at the surface is $\alpha = \Gamma$, where Γ is the metric function (van Riper, 1979). For more details, we refer the reader to Rampp & Janka (2002).

The equation (2.11) represents the system of two-moment radiation transport used in the code ALCAR. This system is solved for all three neutrino species. Since the source terms are energy dependent, the above equations have to be solved for all the neutrino energies. In ALCAR, this is done by evolving the equations in a range of energies split in a specific energy range called ”energy group”. We also notice that each moment depends on another moment of a higher level. Thus, instead of calculating infinitely higher moments, we use an analytic closure relation to close the two-moment system.

Analytical Closure Relation

As discussed above, we use an analytical closure relation to close the equations of radiation transport. The Boltzmann equation can be written in an infinite series of conservation equations for the angular moments. Instead of solving the infinite series of equations, the series can be truncated at a level of $(m+1)$th moment, provided that this moment can close the set of m equations. This implies that we impose additional conditions or symmetries in the local radiation field. In ALCAR, the closure relation is an analytical equation that expresses the higher moments, i.e., P^{ij} and Q^{ijk} as a function of the first two moments E and F^i. This is equivalent to $P^{ij} = P^{ij}(E, F^i)$ and $Q^{ijk} = Q^{ijk}(E, F^i)$. According to Just et al. (2015b), the neutrino-pressure tensor is written as

$$P^{ij} = E\left(\frac{1-\chi}{2}\delta^{ij} + \frac{3\chi - 1}{2} n^i_{\mathrm{F}} n^j_{\mathrm{F}}\right), \tag{2.13}$$

where δ^{ij} is the Kronecker δ, $n^i_{\rm F} = F^i/|\mathbf{F}|$ the normalized flux direction, and χ is the generalised Eddington factor. Similarly, the third moment is written as

$$Q^{ijk} = cE \left[\frac{f-q}{2} \left(n^i_{\rm F}\delta^{jk} + n^j_{\rm F}\delta^{ik} + n^k_{\rm F}\delta^{ij} \right) + \frac{5q-3f}{2} n^i_{\rm F} n^j_{\rm F} n^k_{\rm F} \right], \tag{2.14}$$

where q is a parameter and $f = |\mathbf{F}|/cE$ is the flux factor.

The exact definitions for the χ and q depend on the closure relation that we are using. There are different closures in this form in the literature, but in our study, we use the one proposed in Minerbo (1978), and therefore the quantities above are given by

$$\chi(f) = \frac{1}{3} + \frac{1}{15}(6f^2 - 2f^3 + 6f^4) \tag{2.15}$$

$$q(f) = \frac{f}{15}(45 + 10f - 12f^2 - 12f^3 + 38f^4 - 12f^5 + 18f^6) \tag{2.16}$$

For more details on the derivation, see Just et al. (2015b).

Neutrino-Matter Interactions

The neutrino-matter interactions are introduced in the radiation-transport equations via the source terms (i.e., $C_{E,\nu}$ and $C^i_{F,\nu}$), including the necessary microphysics to describe the physical problem. These quantities are used to calculate the source terms for the hydrodynamics equations as follows

$$Q_{\rm N} = -\alpha m_{\rm B} \int (C_{E,\nu_e} - C_{E,\bar{\nu}_e})\epsilon^{-1} d\epsilon, \tag{2.17a}$$

$$Q^i_{\rm M} = -\alpha \frac{1}{c^2} \sum_\nu \int C^i_{F,\nu} d\epsilon, \tag{2.17b}$$

$$Q_{\rm E} = -\alpha \sum_\nu \int C_{E,\nu} d\epsilon. \tag{2.17c}$$

Here, α is the lapse function, $Q_{\rm N}$ is the source term for the electron number, $Q^i_{\rm M}$ is the source term for the momentum, and $Q_{\rm E}$ is the source term for the total energy. These source terms express the change in the fluid electron number, momentum, and energy due to the neutrino-matter interactions, and they are coupled to the hydrodynamics equations via equation (2.1). Each source term is a sum for all the neutrino species, and $m_{\rm B}$ is the atomic mass unit. The neutrino-matter interactions are described in terms of the energy density $C_{E,\nu}$ and the energy flux density $C^i_{F,\nu}$. We include absorption, emission, iso-energetic scattering processes, and inelastic scattering. Therefore, the source terms for the neutrino interactions can be written as

$$C_E = C_{E,\rm esc} + C_{E,\rm isc}, \tag{2.18a}$$

$$C^i_F = C^i_{F,\rm esc} + C^i_{F,\rm isc}. \tag{2.18b}$$

Here $C_{E,\mathrm{esc}}, C_{F,\mathrm{esc}}$ are the contributions from the absorption and emission while $C_{E,\mathrm{isc}}, C_{F,\mathrm{isc}}$ are the contributions from the iso-energetic scattering processes.

We express the source terms for radiation as a function of the opacities for the interactions considered. Below, we list all neutrino-matter interactions implemented in the ALCAR code together with the reference on which the implementation is based.

- Absorption and emission of ν_e and $\bar{\nu}_e$:
  $\nu_e + n \rightleftharpoons p + e^-$, Bruenn (1985); Mezzacappa & Bruenn (1993)
  $\bar{\nu}_e + p \rightleftharpoons n + e^+$, Bruenn (1985); Mezzacappa & Bruenn (1993)
  ν_e + (A,Z) $\rightleftharpoons$ (A,Z+1) + e^-, Bruenn (1985)
  $\bar{\nu}_e$ + (A,Z) $\rightleftharpoons$ (A,Z-1) + e^+, Bruenn (1985)

- Scattering:
  $n + \nu_i \rightleftharpoons n + \nu_i$, Bruenn (1985); Mezzacappa & Bruenn (1993)
  $p + \nu_i \rightleftharpoons p + \nu_i$, Bruenn (1985); Mezzacappa & Bruenn (1993)
  (A,Z) $+\nu_i$ $\rightleftharpoons$ (A,Z) + ν_i, Bruenn (1985); Horowitz (2002); Mezzacappa & Bruenn (1993)
  $e^\pm + \nu_i \rightleftharpoons e^\pm + \nu_i$, O'Connor (2015); Yueh & Buchler (1977)[1]

- Pair production annihilation of heavy-lepton neutrinos ν_x:
  $e^- + e^+ \rightleftharpoons \nu_x + \nu_x$, Bruenn (1985); Pons et al. (1998)[2].
- Bremsstrahlung - heavy-lepton neutrinos ν_x:
  $N_1 + N_2 \rightleftharpoons N_1 + N_2 + \nu_x + \nu_x$, Hannestad & Raffelt (1998)[2]

In the above we use the generic term ν_x to describe all the heavy-lepton neutrinos, i.e., ν_τ,$\bar{\nu}_\tau$,ν_μ, and $\bar{\nu}_\mu$. We neglect the absorption and emission of heavy-lepton neutrinos because their rates are suppressed due to the high muon mass. Moreover, we do not consider bremsstrahlung and pair production processes for ν_e and $\bar{\nu}_e$ since they are dominated by their absorption, emission, and scattering processes. According to the above and following Bruenn (1985); Rampp & Janka (2002), the radiation source terms are written as a function of the absorption opacity κ_a and the scattering opacity κ_s

$$C_{E,\mathrm{esc}} = c\kappa_a(E^{\mathrm{eq}} - E), \tag{2.19a}$$

$$C^i_{F,\mathrm{esc}} = -c(\kappa_a + \kappa_s)F^i, \tag{2.19b}$$

where E^{eq} is the equilibrium energy density associated with the Fermi-Dirac distribution and calculated as

$$E^{\mathrm{eq}}(\epsilon, \mu_\nu, T) = 4\pi \left(\frac{\epsilon}{hc}\right)^3 \left[\exp\left(\frac{\epsilon - \mu_\nu}{k_{\mathrm{B}}T} + 1\right)\right]^{-1}. \tag{2.20}$$

The above formula corresponds to neutrinos with a chemical potential μ_ν, energy ϵ, and a fluid temperature of T, while k_{B} is the Boltzmann constant. The opacities are calculated with methods described in the Appendix of Rampp & Janka (2002) with the addition that in ALCAR, we include corrections in the interaction with nucleons due to weak magnetism and nucleon recoil according to Horowitz (1997). Additionally, the bremsstrahlung and e^-e^+ pair processes are calculated in a simplified manner following O'Connor (2015), which treats them as absorption and emission terms.

---

[1] Damping the source terms for densities $\rho > 5 \cdot 10^{12}$ [g/cm^3]

[2] simplified as in O'Connor (2015)

2.3 Numerical Methods

Both the hydrodynamics equations and the system of the two-moment equations for the neutrino radiation transport are of hyperbolic mathematical nature; therefore, it is common to use Godunov-type finite-volume methods (Godunov, 1959) to discretize the equations. The evolved quantities are discretized as cell-volume averages. We employ approximate Riemann solvers to obtain the cell-interface fluxes between cells. We use the "HLLC" solver (Toro, 2013) and the "HLLE" solver for specific circumstances (Einfeldt, 1988; Einfeldt et al., 1991). The cell interfaces of an evolved quantity are reconstructed from the cell averages using the piecewise-parabolic method (Colella & Woodward, 1984; Mignone, 2014).

The integration is done in a mixed implicit-explicit way, where the left-hand-side of the two-moment equations (equation (2.11)) are treated explicitly in time while the source terms in the right-hand side are treated implicitly. The time integration is performed using a second-order Runge-Kutta scheme. We use the same timestep for both the hydrodynamics and the radiation transport equations, constrained by the Courant-Friedrichs-Lewy condition (Courant et al., 1928, CFL). The global timestep is computed as

$$\Delta t = f_{\mathrm{CFL}} \cdot \min\left[\Delta t_{\mathrm{hydro}}, \Delta t_{\mathrm{radiation}}\right], \tag{2.21}$$

where f_{CFL} is the CFL parameter set to 0.5, $\Delta t_{\mathrm{hydro}}$ is the integration timestep for hydrodynamics, and $\Delta t_{\mathrm{radiation}}$ for radiation. For a thorough explanation of the details of the numerical scheme of ALCAR, we refer the reader to Just et al. (2015b).

Chapter 3

Initial Models

This chapter describes the methods used to develop the progenitor models for the AIC simulations. We discuss and motivate the construction of the models, the improvements from previous work, and the technical details for the initial conditions used in ALCAR to perform the long-time evolution of AICs. The models constructed for this work are provided by Ehring (2019), and they are based on but significantly improved from the models presented in Abdikamalov et al. (2010).

3.1 Pre-collapse Models

The AIC scenario is either the outcome of a white dwarf binary merger or a white dwarf that accretes mass and angular momentum from a companion star. Non-rotating ONeMg white dwarfs undergo accretion-induced (i.e., electron-capture) collapse when their mass exceeds the Chandrasekhar mass limit, while rotating white dwarfs need more mass to undergo a collapse. Stellar evolution models can approximate the evolution of white dwarfs and the accretion process. However, due to the complexity of stellar evolution and the vast parameter space, there is a lack of self-consistent multi-dimensional pre-collapse AIC models that result from stellar evolution numerical simulations.

Therefore, we construct our initial models as differentially rotating equilibrium configurations with Newtonian gravity, applying the self-consistent field method (SCF; Ostriker & Bodenheimer, 1968) in a similar manner as in Abdikamalov et al. (2010) and Yoon & Langer (2005). The pressure of the self-gravitating fluid is assumed to be provided by degenerate electrons and formulated in terms of a barotropic relation (i.e., the pressure depends only on the density).

The constructed models we use in the Thesis are presented in Ehring (2019), and here we give a brief overview of the methods used to produce those models. They are a selection of representative cases calculated in Abdikamalov et al. (2010) with increased numerical accuracy of the rotation equilibrium and higher radial grid resolution. Our models span across various masses, spins, and total angular momentum to cover a representative sample of possible realistic progenitors (see table 3.1).

We employ the SCF method in Newtonian gravity for given rotational profiles. General relativistic effects are minor in the pre-collapse phase and thus neglected. The progenitors are set to have an equal number of protons and neutrons at initialization. Therefore, the electron fraction Y_e is set to 0.5.

In the white dwarfs, the stellar matter is supported against gravity due to the electron degenerate pressure. The following equation describes the equilibrium for a rotating white dwarf:

$$\int \rho^{-1} dP + \Phi - \int \Omega^2 \varpi d\varpi = C, \tag{3.1}$$

where ρ is the density, P the pressure, Φ is the gravitational potential, Ω is the rotational profile, ϖ is the radial cylindrical coordinate, and C is determined from the boundary conditions. In complete degenerate conditions, the pressure is given by

$$P = A[x(2x^2 - 3)(x^2 + 1)^{1/2} + 3\sinh^{-1} x] \tag{3.2}$$

$$x = (\rho/B)^{1/3},$$

where A is a constant, i.e., $A = 6.01 \cdot 10^{22}$ dyn cm^{-3} and B is inversely proportional to Y_e such as $B = 9.82 \cdot 10^5\ Y_\mathrm{e}^{-1}$ g cm^{-3}, in our case $B = 1.96 \times 10^6$g cm^{-3} for $Y_e = 0.5$.
The first integral in equation (3.1) is the enthalpy H which is given by

$$H = \frac{8A}{B} \left[1 + \left(\frac{\rho}{B} \right)^{2/3} \right]. \tag{3.3}$$

Therefore equation (3.1) is written as

$$H = C - \Phi + \int \Omega^2 \varpi d\varpi. \tag{3.4}$$

The rotational profile follows the rotational law for accreting white dwarfs by Yoon & Langer (2005). They show that the angular momentum transport via the dynamical-shear instability (DSI) affects the rotational profile in the inner region of the accreting white dwarf. In contrast, the secular-shear instability (SSI) shapes the outer layers. The rotation law results in a maximum angular velocity at the location that splits the DSI unstable core with the rest of the white dwarf. We identify this position at a distance ϖ_p from the rotational axis. The density at this position corresponds to a certain percentage of the white dwarf central density $\rho_\mathrm{c,i}$, in a manner such as $\rho_\mathrm{i}(\varpi_p, 0) = f_p \rho_\mathrm{c,i}(0, 0)$, with the second spatial variable is the polar angle $\theta = 0$. The parameter f_p shows the fraction of the central density at the outer location of the shear-unstable core. In our models, according to Abdikamalov et al. (2010), we choose $f_p = 0.05$ or $f_p = 0.1$. The rotational profile for the inner core (i.e., below the shear unstable layer) is given by

$$\Omega(\varpi) = \Omega_\mathrm{c,i} + \int_0^{\varpi} \frac{f_\mathrm{sh} \sigma_\mathrm{DSI,crit}}{\varpi'} d\varpi', \tag{3.5}$$

where $\Omega_{\mathrm{c,i}}$ is the initial central angular velocity, $\sigma_{\mathrm{DSI,crit}}$ describes the critical shear rate for the onset of the DSI in the inner core, f_{sh} is a dimensionless parameter that shows the deviation of the shear rate from its critical value $\sigma_{\mathrm{DSI,crit}}$.
According to Yoon & Langer (2005) the $\sigma_{\mathrm{DSI,crit}}$ is calculated as

$$\sigma^2_{\mathrm{DSI,crit}} \simeq \left(\frac{g}{10^9\ \mathrm{cm\ s^{-2}}}\right)\left(\frac{\delta}{0.01}\right)\left(\frac{H_{\mathrm{p}}}{8\cdot 10^7\ \mathrm{cm}}\right)^{-1}\left(\frac{\nabla_{\mathrm{ad}}}{0.4}\right), \tag{3.6}$$

where g is the free-fall acceleration, H_{p} is the pressure scale height, ∇_{ad} is the adiabatic temperature gradient and $\delta = (\partial \ln \rho / \partial \ln T)_P$.
At the equatorial surface, the white dwarf is assumed to rotate at a certain fraction f_{K} of the Keplerian angular velocity Ω_{K} at the equator, such as

$$\Omega(R_e) = f_{\mathrm{K}}\Omega_{\mathrm{K}}(R_e) \tag{3.7}$$

where R_e is the equatorial radius of the white dwarf. Accretion onto the white dwarf will carry angular momentum onto its surface, and it is expected to rotate near the critical velocity, therefore, $f_{\mathrm{K}} = 0.95$ is chosen. The angular velocity for matter above the shear-unstable layer is given by

$$\Omega(\varpi)/\Omega_{\mathrm{K}}(\varpi) = \Omega(\varpi_p)/\Omega_{\mathrm{K}}(\varpi_p) + \mathcal{C}(\varpi - \varpi_p)^{\alpha} \tag{3.8}$$

where ϖ_p is the location of the maximum angular velocity just above the shear-unstable core and $a = 1.2$ as chosen in Abdikamalov et al. (2010); Yoon & Langer (2005). The constant $\mathcal{C}$ is determined by

$$\mathcal{C} = \frac{f_{\mathrm{K}} - \Omega(\varpi_p)/\Omega_{\mathrm{K}}(\varpi)}{(R_e - \varpi_p)^{\alpha}} \tag{3.9}$$

In summary, the rotational law for the pre-collapse models is given by

$$\begin{aligned} \Omega(\varpi) &= \Omega_{\mathrm{c,i}} + \int_0^{\varpi} \frac{f_{\mathrm{sh}}\sigma_{\mathrm{DSI,crit}}}{\varpi'} d\varpi' && \text{for } 0 \leq \varpi \leq \varpi_p \\ \Omega(\varpi)/\Omega_{\mathrm{K}}(\varpi) &= \Omega(\varpi_p)/\Omega_{\mathrm{K}}(\varpi_p) + \mathcal{C}(\varpi - \varpi_p)^{\alpha} && \text{for } \varpi_p \leq \varpi \leq R_e \end{aligned}$$

Using the rotational profile above, we can employ the SCF method. Given a trial density distribution $\rho(r,\theta)$ and following the rotational profile defined above, we can calculate the value C (see equation (3.4)) from the boundary conditions and therefore update the enthalpy from equation (3.4). With the new value for the enthalpy H, we use equation (3.3) to estimate the new density distribution. We repeat the process until convergence, i.e., until the maximum absolute values for the differences of the iterative quantities become less than 10^{-5}. The convergence of the method is chosen with increased stability compared to the models constructed in Abdikamalov et al. (2010), where the accuracy was 10^{-3}.

Additionally, to estimate how accurate is the rotational equilibrium of the generated models, we calculate the relative acceleration (Ehring, 2019) as

$$\alpha_{\mathrm{rel}} = \left|\frac{\alpha_g + \alpha_c + \alpha_p}{\alpha_g}\right|, \tag{3.10}$$

Table 3.1: AIC progenitor properties. The columns list different physical parameters, where M is the mass of the white dwarf, Ω_c the central angular velocity, Ω_max the maximum value of the angular velocity at the equator, R_eq the equatorial radius, T_c the central temperature, J the initial total angular momentum, E_rot the total rotational energy, and β_init the ratio of the rotational to the gravitational energy in the initial white dwarf model.

Model	M $[\mathrm{M}_\odot]$	Ω_c [rad/s]	Ω_max [rad/s]	R_eq [km]	ρ_c [g/cm^3]	T_c [K]	J [10^{50}erg · s]	E_rot [10^{50}erg]	β_init
M1.42-J0	1.422	0	0	816	$5 \cdot 10^{10}$	$1.00 \cdot 10^{10}$	0.000	0.000	0.000
M1.42-J0.23-Dl	1.422	0	3.80	2250	$4 \cdot 10^{9}$	$4.13 \cdot 10^{9}$	0.231	0.299	0.007
M1.61-J0.47	1.609	12.0	19.64	1498	$5 \cdot 10^{10}$	$1.00 \cdot 10^{10}$	0.471	3.941	0.038
M1.61-J0.78-Dl	1.611	5.55	6.13	2897	$4 \cdot 10^{9}$	$4.13 \cdot 10^{9}$	0.782	2.094	0.046
M1.91-J1.09	1.919	18.0	25.66	2377	$5 \cdot 10^{10}$	$1.00 \cdot 10^{10}$	1.085	10.471	0.082
M1.91-J1.63-Dl	1.906	5.33	8.22	3982	$4 \cdot 10^{9}$	$4.13 \cdot 10^{9}$	1.630	5.033	0.091

where α_g is the gravitational acceleration, α_c is the acceleration from the centrifugal force, and α_p from the pressure gradient. We calculate the mass, m_5, included in the cells so that $\alpha_\mathrm{rel} > 0.05$. The non-rotating progenitor yields $m_5 = 7 \cdot 10^{-7}\,\mathrm{M}_\odot$, and the rotating models $m_5 \sim 0.003 - 5 \cdot 10^{-3}\,\mathrm{M}_\odot$ (Ehring, 2019). To consider a model in good rotational equilibrium, the value of the m_5 should be as small as possible. The improvements of Ehring (2019) provide us with a more accurate set of models with higher spatial resolution and better rotational stability, compared to Abdikamalov et al. (2010). For more details on the method, we refer the reader to Abdikamalov et al. (2010); Ehring (2019); Ehring et al. (2023); Yoon & Langer (2005).

According to the discussed method, the initial models are constructed in rotational equilibrium with a barotropic EoS, i.e., the pressure depends only on the density. Thus, the initial models are independent of the temperature. We impose a temperature profile, following Abdikamalov et al. (2010); Dessart et al. (2006) depending on the density and given by

$$T(r,\theta) = T_0 \cdot (\rho_\mathrm{c,i}/\rho(r,\theta))^{-0.35} \tag{3.11}$$

with T_0, $\rho_\mathrm{c,i}$ being the initial temperature and density, respectively. The initial central temperature T_0 is assumed to be 10^{10} K for all models. Note that due to the scaling with the initial central density, the initial central temperature in the center will be changed accordingly. A summary of the model properties is discussed in the next section and given in table 3.1.

3.2 Properties of the Progenitor Models

Six two-dimensional models have been created for this Thesis as described above and presented in Ehring (2019); Ehring et al. (2023). The exact structure and thermodynamics of the AIC progenitor are crucial for the subsequent core collapse and outcome of the explosion. Since the parameter range for the central density, temperature, and rotation are not tightly constrained, we will explore a representative and physically motivated range of

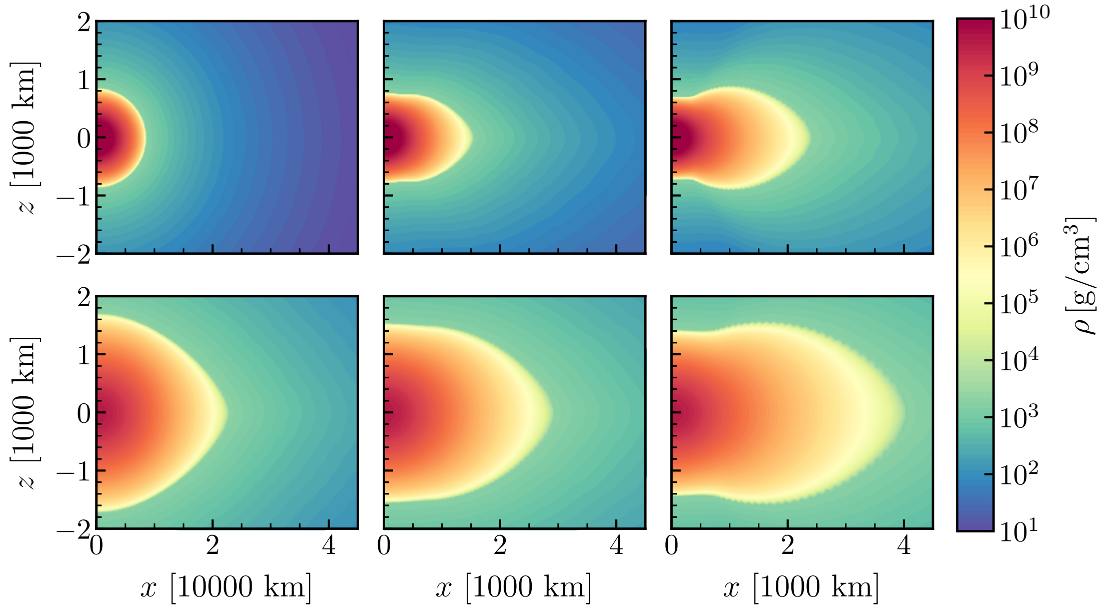

Figure 3.1: Color-coded density of each progenitor in the xz plane. From left to right, the upper left model has a mass of $1.42\,\mathrm{M}_\odot$, high central density, and no rotation, i.e. the model M1.42-J0, the bottom left one is the M1.42-J0.23-Dl with the same mass and slow rotation on the surface. The middle panels show the rotating progenitors with $1.61\,\mathrm{M}_\odot$, i.e., M1.61-J0.47 (middle top) and M1.61-J0.78-Dl (middle bottom). The right panels show the rotating progenitors with $1.91\,\mathrm{M}_\odot$, i.e., M1.91-J1.09 (right top) and M1.91-J1.63-Dl (right bottom). Mass and rotation increase towards the right panels. The models are embedded in a CSM with radially decreasing density and temperature profiles.

initial conditions and their outcome.

In order to study the effect of the initial central density on the AIC, we choose two different values, i.e. $5 \cdot 10^{10}\,\mathrm{g/cm^3}$ for three of the models and $4 \cdot 10^9\,\mathrm{g/cm^3}$ for the rest of the models (low-density models include a suffix, "-Dl", in their naming convention, see table 3.1). The models are constructed to have certain total masses of approximately 1.42, 1.61, and $1.91\,\mathrm{M}_\odot$. Each of those progenitors is initiated with a high central density of $5 \cdot 10^{10}\,\mathrm{g/cm^3}$ and a low central density of $4 \cdot 10^9\,\mathrm{g/cm^3}$, i.e., we have three pairs of equal mass progenitors. The models initiated with high central density are chosen with $f_p = 0.05$. This implies that the density above the shear-unstable core is 5% of the initial central density. For the low-central density progenitors, the parameter is $f_p = 0.1$. The shear parameter (see equation (3.5)) is chosen to be 1.0 for three models.

In total, we have one non-rotating and five differentially rotating white dwarfs. The naming convention of the models is as follows: every model starts with M followed by a number that indicates the mass of the model, then J refers to the total angular momentum of the white dwarf at the start of the simulation, and three of the models have a suffix "-Dl" that indicates that are initiated low central density at their cores.

The first pair of models have a mass of $1.42\,\mathrm{M}_\odot$. The model with the high central density ($5 \cdot 10^{10}\,\mathrm{g/cm^3}$), i.e., M1.42-J0 is non-rotating, and the model with low central

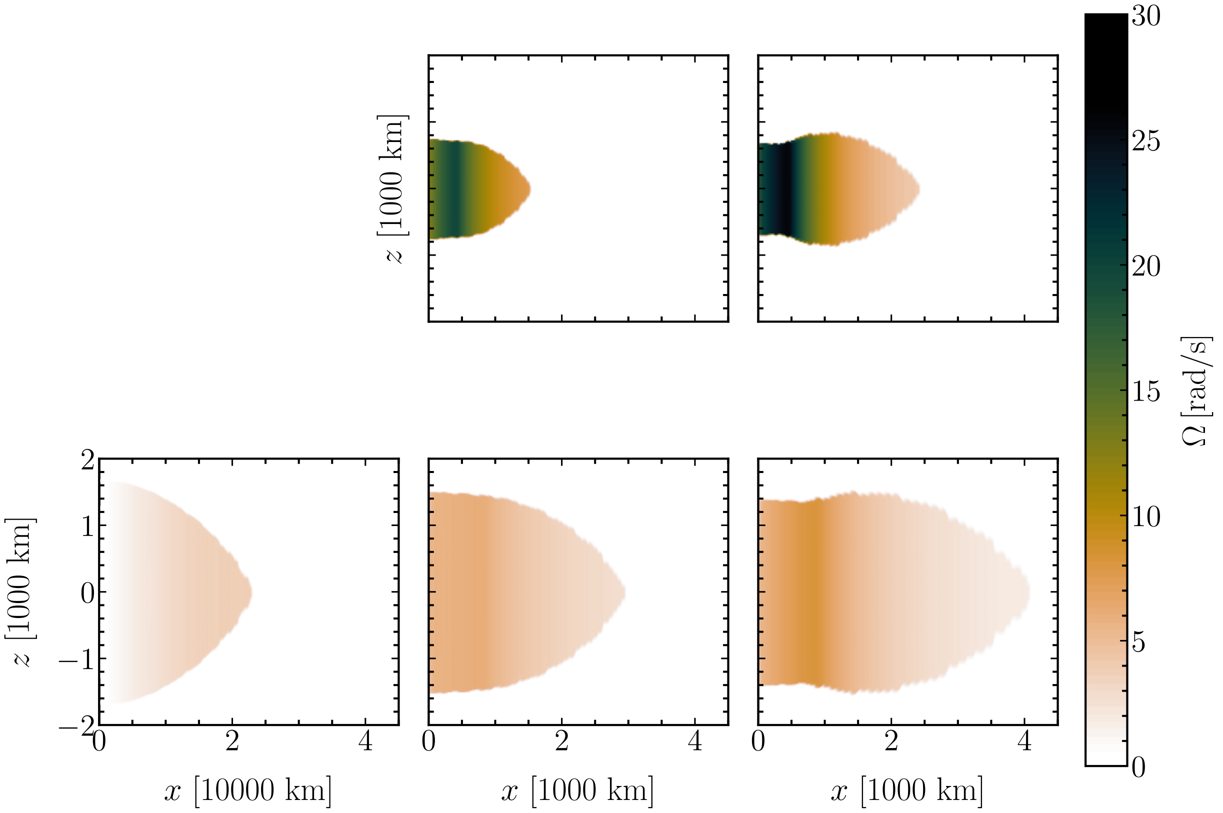

Figure 3.2: Color-coded angular velocity of each progenitor in the xz plane. From left to right, the bottom left is the model M1.42-J0.23-Dl, with a mass of 1.42 $M_\odot$. The middle panels show the rotating progenitors with 1.61 $M_\odot$, i.e., M1.61-J0.47 (middle top) and M1.61-J0.78-Dl (middle bottom). The right panels show the rotating progenitors with 1.91 $M_\odot$, i.e., M1.91-J1.09 (right top) and M1.91-J1.63-Dl (right bottom). The angular velocity in our progenitors depends on the distance x to the rotational axis. The circum-stellar medium is non-rotating.

density ($4 \cdot 10^9$ g/cm^3), i.e., M1.42-J0.23-Dl is non-rotating in the center but rotating in the outer layers with a surface rotation of 3.80 rad/s at the equator. The second pair of models have a mass of approximately 1.6 $M_\odot$, which is above the Chandrasekhar limit, but due to rotational support, the mass can exceed this limit. The high central density model, i.e., M1.61-J0.47, has a central rotation of 12.0 rad/s to match the desired mass and a shearing parameter $f_{\rm sh}$ of 1.0. The low central density model with the same mass, i.e., M1.61-J0.78-Dl, has a central rotation rate of 5.55 rad/s and the shear parameter is $f_{\rm sh} = 0.2$. The last two models are the heaviest and the ones with the largest total angular momentum. The high central density model, i.e., M1.91-J1.09, has a central rotation of 18.0 rad/s, while the low central density model, i.e., M1.91-J1.63-Dl, is rotating more slowly with a central rotation of 5.33 rad/s. Both models have the same shear parameter of $f_{\rm sh} = 1.0$.

Figure 3.2 displays the two-dimensional angular velocity profile for the rotating progenitors. The models M1.61-J0.47 and M1.91-J1.09 have high central density, are more compact and have high angular velocity in their centers. In contrast, the low-central density models rotate more slowly, even though they have higher angular momentum than their exact mass counterparts. All rotating models show a peak in their angular velocity above the shear-unstable core by contraction. This holds for the rotating models apart from the model M1.42-J0.23-Dl, where the angular velocity monotonically increases with the distance to the rotational axis. In figure 3.3, we plot the z-component of the specific angular momentum, which depends on the distance to the rotational axis, similarly to the angular velocity.

Figure 3.1 shows the two-dimensional projection of the progenitors, color-coded by the density. The low central density progenitors (i.e. M1.42-J0.23-Dl, M1.61-J0.78-Dl, M1.91-J1.63-Dl) are generally larger and hence less compact than their equal mass counterparts. The rotating high central density models (i.e., M1.61-J0.47, M1.91-J1.09) are more compact and have higher central angular velocity. The low central density models have a smaller f_p parameter, which indicates the percentage of the central density where angular velocity is the maximum and the peak of the angular velocity is located further out. This is also seen in figure 3.4, where the equatorial angular velocity is shown as a function of radius.

3.3 Circum-stellar Medium

The progenitor models are embedded in an artificial circum-stellar medium (CSM) due to the eulerian nature of our simulation code ALCAR. Since we don't have any observational constraints about the environment around the AIC, we set up the surroundings to be the least affecting conditions for the propagation of the AIC ejecta. The CSM is set up in a non-rotating hydrostatic equilibrium.

We assume a declining density profile, scaled to the white dwarf properties, as follows,

$$\rho(r,\theta) = \rho_{\mathrm{WD,min}} \left(\frac{R_{\mathrm{WD}}(\theta)}{r} \right)^{3+\epsilon} \tag{3.12}$$

where $\rho_{\mathrm{WD,min}}$ is the minimum density of the white dwarf, $R_{\mathrm{WD}}(\theta)$ is the angle-dependent radius of the white dwarf, and ϵ is a parameter set to $\epsilon = 0.1$ Apart from the non-rotating model spherical symmetric model, the rest have an angle-dependent CSM around them. Assuming a radiation-dominated ideal gas in the CSM, the temperature should be scaled as $T \sim \rho^{-4}$. Therefore, to approximate this dependence, we adopt a radially declining temperature profile, which is given by

$$T(r,\theta) = T_{\mathrm{WD,min}} \left(\frac{R_{\mathrm{WD}}(\theta)}{r} \right) \tag{3.13}$$

where $T_{\mathrm{WD,min}}$ is the minimum temperature of the white dwarf. For the composition, we assume 60% protons, 40% neutrons, and no other elements; thus, the Y_e is set to 0.6 in the CSM. The above configuration makes the CSM in approximate hydrostatic equilibrium because the assumed temperature is not identical to the one given in the numerical code ALCAR.

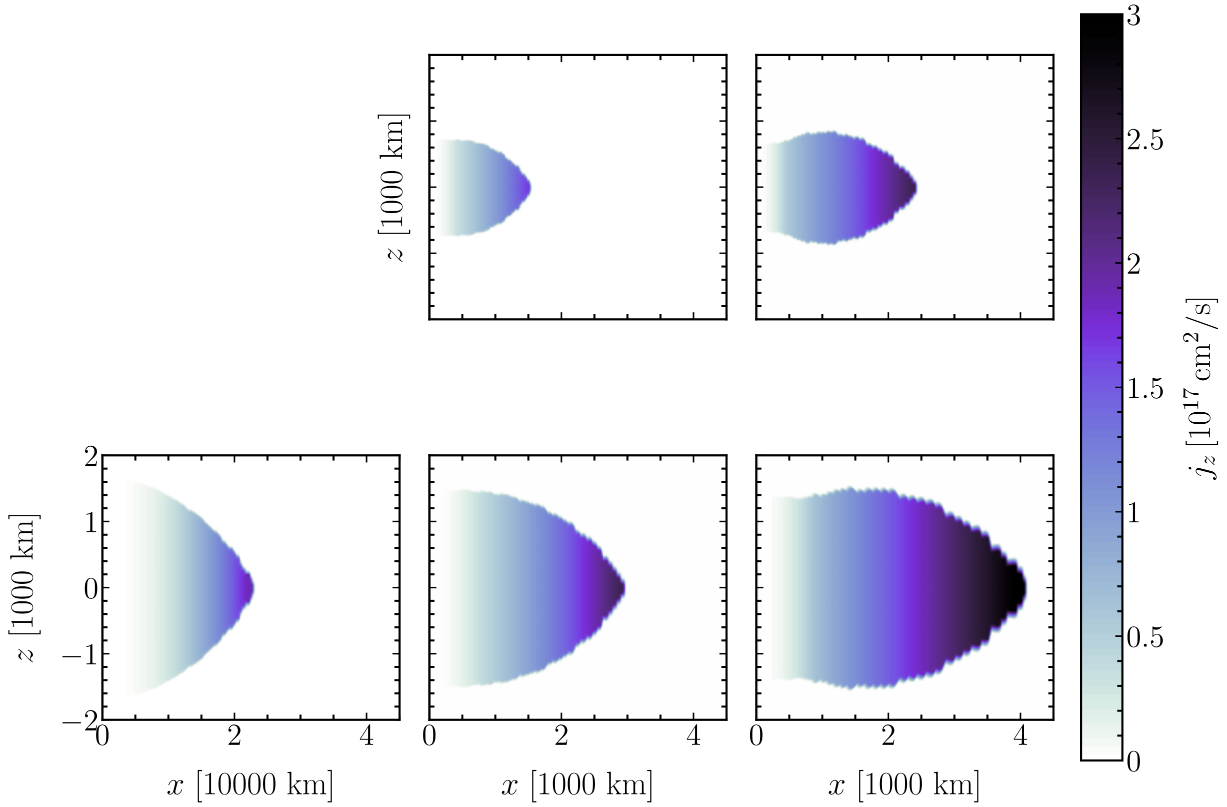

Figure 3.3: Color-coded z-component of the specific angular momentum of each progenitor in the xz plane. From left to right, the bottom left one is the model M1.42-J0.23-Dl. The middle panels show the rotating progenitors with M1.61-J0.47 in the middle top and M1.61-J0.78-Dl in the middle bottom panel. The right panels show the rotating progenitors M1.91-J1.09 in the right top and M1.91-J1.63-Dl in the right bottom panel. The z-component of the specific angular momentum depends on the distance x to the rotational axis, as does the angular velocity.

3.4 Grids and Resolution

Neutrino Energy Grid As discussed previously, for the neutrino radiation transport we evolve the two-moment equations (see equation (2.11)). In the code ALCAR, these are solved for three different neutrino species, i.e., the electron neutrinos ν_e, the electron anti-neutrinos $\bar{\nu}_e$, and the heavy-lepton neutrinos described by ν_x that represent the muon ν_μ and tau ν_τ neutrinos and their corresponding anti-neutrinos. For the energy grid, i.e., the discretization of the neutrino energy, we employ 15 logarithmically spaced bins in the interval $0 \leq \epsilon \leq 400$ MeV.

Spatial Grid The progenitors are mapped in a spherical grid of 1440 radial and 96 polar zones, which is identical for all the models. The inner 30 km are mapped in a radial grid with equal-width zones of 100 m each, while the rest of the radial zones have a logarithmically increasing width. The total radial grid reaches ∼600,000 km. The radial part of the grid is constructed so that there is enough resolution on the neutron star surface

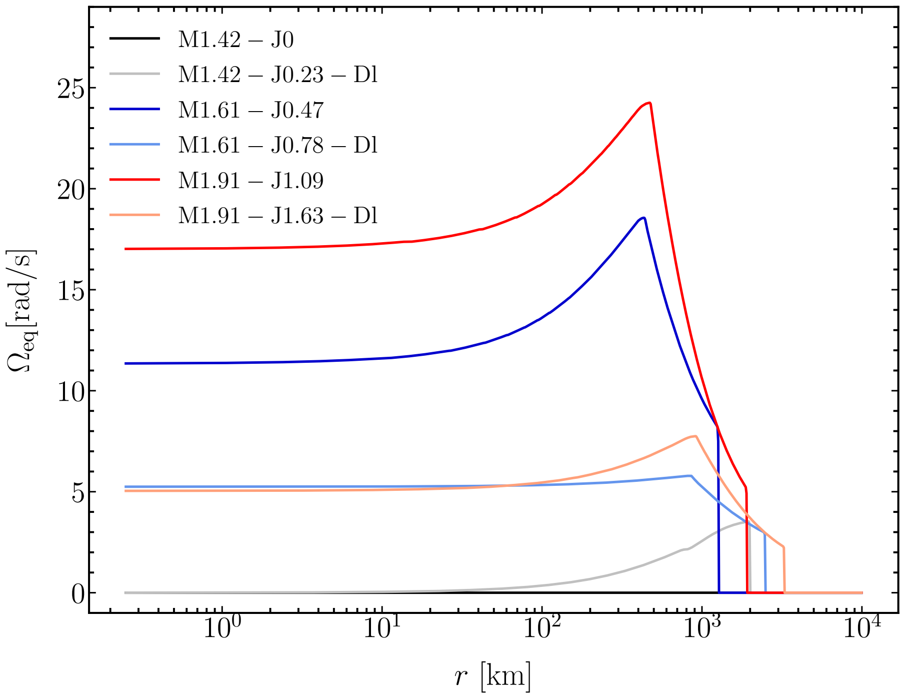

Figure 3.4: Rotational profiles of the angular velocity at the equator as a function of radius for all models. All models reach an angular velocity maximum at a certain radius except the non-rotating one (M.142-J0) and its low-density counterpart M1.42-J0.23, which shows increasing rotation on its surface.

which is required for the simulations we present here and allows following the ejecta for a long enough time until they reach homologous expansion. Specifically, as the neutron star contracts, there is a steep density gradient on the surface of the neutron star and the circum-stellar medium. Thus, high spatial resolution is required to capture all the relevant physical processes to describe neutrino physics and hydrodynamical phenomena accurately. In the polar direction, the 96 zones are equally distributed in the $\theta \in [0°, 180°]$, giving an angular resolution of 1.875°.

1D core To facilitate the long-time evolution of the models with a reasonable amount of computing time, we use a spherical symmetric core (1D core) in the center that allows for a larger timestep in our calculations. Since the timestep is constrained by the size of the inner cell of the spatial grid, using the 1D core, we take the spherical averages of the central quantities. The size of the 1D core varies from model to model because of the different degrees of rotation. For faster-rotating models, we use a smaller 1D core because the high spin of the core deforms the central region. For our non-rotating model, we use a 1D core with a radius of 1 km, for the slow rotating model (M1.42-J0.23-Dl), the 1D core has a radius of 600 km, and for the rest of the models 400 km.

For the rotating models, we allow the 1D core to rotate. The ϕ component of the momentum is advected in the 1D core, and thus, we can get non-zero ϕ velocities. The ϕ component of the momentum is redistributed in each radial shell of the 1D core and follows a sinusoidal function of the polar angle θ as $p_\phi \sim \sin\theta$. This treatment conserves the total ϕ momentum and is an acceptable approximation for the rotating models.

Chapter 4

Collapse and Evolution of AIC models

In this Thesis we investigate the white dwarf collapse and the long-time evolution of six non-rotating and rotating models of AIC progenitors. Our modeling employs the fully multi-dimensional, multi-energy-group neutrino transport and hydrodynamics code ALCAR with a state-of-the-art description of the neutrino interactions and a modern nuclear equation of state, as described in chapter 2. Our simulations follow the collapse and long-time evolution of the AIC models that were presented in chapter 3. In this chapter, we focus on the dynamical development of the models, the onset of the neutrino-driven outflow, the properties of the neutron stars born in the white dwarf collapse, and the overall properties of the simulations.

4.1 Collapse of AIC Models

In this section, we discuss the collapse dynamics of the non-rotating and rotating AIC models. All models are initialized with electron fraction $Y_e = 0.5$, which means that no electron captures have occurred so far. The AIC begins when the thermodynamical conditions are such (high enough central temperature and density) to initiate electron capture in the white dwarf core. In our simulations, all models become gravitationally unstable and begin to collapse. The collapse timescale (i.e., bounce time) differs from model to model, with a significant increase in the collapse time for the models with low central density. This is intuitively clear since the initial collapse is to first order happening on the gravitational free fall timescale, which scales inversely proportional to the square root of density. Thus, a priori one would expect that lower density models need longer to undergo gravitational collapse. The models with high central density (i.e., models M1.24-J0, M1.61-J0.47, and M1.91-J1.09) collapse on a timescale of $\sim$40 ms, and any differences in the bounce dynamics are attributed to the initial angular momentum distribution (figure 3.3). The rest of the models, i.e., those with low-central density (models M1.42-J0.23-Dl, M1.61-J0.78-Dl, and M1.91-J1.63-Dl) exhibit a significantly longer time to collapse, due to the low density and temperature at their cores and to their corresponding rotational profiles. These models need between 300 ms and 800 ms to collapse since the beginning of our simulations. The initial angular momentum profile for each model is crucial for the development of the collapse and subsequent outflow.

Similar to CCSNe (e.g., Moenchmeyer et al., 1991; Tohline, 1984; Zwerger & Mueller, 1997), the collapse of an AIC (e.g. Abdikamalov et al., 2010; Dessart et al., 2006) can be subdivided in three different phases (stages): infall, plunge and bounce, and ringdown. In the following, we will discuss these phases with respect to AICs and post the interested reader to Burrows (2013); Foglizzo et al. (2015); Janka (2017a); Kotake et al. (2006) for a comprehensive overview of the state of CCSN explosion theory. During the infall, the inner core, which is defined as the regions that are in sonic contact at the time of the bounce, contracts in a homologous way (i.e., $u_r \sim r$, where r is the radius) (Goldreich & Weber, 1980), while the outer layers of the progenitor follow at supersonic speeds. The core bounce occurs when the central density reaches nuclear saturation density ($\rho \geq 2.7 \cdot 10^{14}\,\mathrm{g/cm^3}$). At that point, the matter cannot be compressed any further because the repulsive nuclear forces between nucleons dominate and stabilize the further contraction of the matter. At that point of maximum compression, there is a phase transition to nuclear matter which leads to the sudden stiffening of the EoS and the rise of the adiabatic index. Because of the huge amount of kinetic energy enclosed in the collapsing core, the central density overshoots to a maximum value and then oscillates with small changes in the ρ_{central}. The infalling matter bounces back to form pressure waves that will steepen to form a shock wave that propagates outwards. This is referred to as *pressure bounce* or just *bounce* since is the usual way a CCSN undergoes core-bounce.

Figure 4.1 shows the maximum density in the core for each model as a function of post-bounce time. From figure 4.1 we can distinguish the infall phase in the slow rise of the central maximum density (i.e., during 20-40 ms before bounce), the plunge and bounce in the steep and sudden rise of the central density at around 0 ms[1] which corresponds to the time of the bounce, and finally the ringdown during the first millisecond post-bounce as the central density slightly drops again after the overshoot to a maximum value at the core bounce. There is a clear distinction of the time evolution of the central density for the models M.161-J0.78-Dl (light blue line) and M1.91-J1.63-Dl (orange line) and the other four simulated models. Due to the interplay of the low-central density and the high degree of rotation in the models M.161-J0.78-Dl and M1.91-J1.63-Dl those do not undergo a pressure bounce like the other models but evolve towards a centrifugal bounce before they can reach nuclear saturation density. The centrifugal bounce occurs because of the large angular velocities in the central region of the white dwarf (or other rotating collapsing stars) that centrifugally stabilize the matter. Therefore, the matter cannot collapse any further because is rotationally supported. In the following, we examine the collapse and bounce for each AIC model in more depth.

---

[1] The time axis is normalized to 0 ms for each model and 0 ms is equivalent to the core bounce for all the models. Thus negative times describe the time before the bounce.

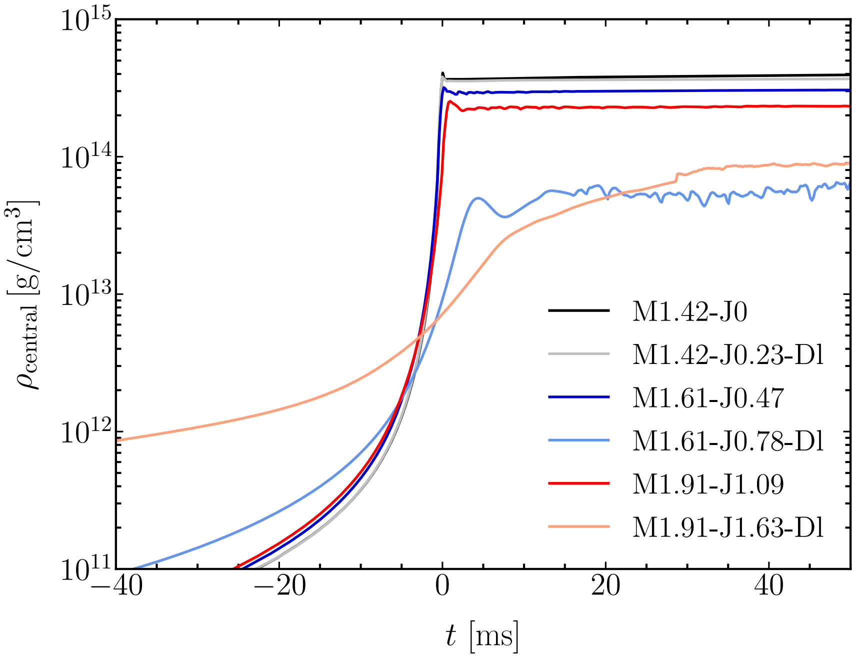

Figure 4.1: Maximum central density as a function of post-bounce time. We follow the evolution of the maximum density of the central region of the progenitor. The black line shows the central density of the non-rotating model M1.42-J0, the grey line shows its low-density counterpart M1.42-J0.23-Dl, the blue line corresponds to the rotating model M1.61-J0.47, the light blue line to the low-density model M1.61-J0.78-Dl, the red line displays the central density of the model M1.91-J1.09, and the light orange of the model M1.91-J1.63-Dl. We follow this color-scheme throughout this Thesis. For later times, we refer the reader to the corresponding figure A.1 in the Appendix.

4.1.1 Collapse and bounce of the non-rotating model

The spherical-symmetric non-rotating model, M1.42-J0, needs 37.7 ms to reach nuclear saturation densities and to undergo core bounce. The maximum density in the core of the white dwarf at core bounce is $4.07 \cdot 10^{14}\,{\rm g/cm^3}$. The evolution of the collapse and bounce agrees well with the spherical symmetric models of Abdikamalov et al. (2010). However, our model reaches a higher central density in its core in comparison to the models of Abdikamalov et al. (2010) that only reach $\rho_{\rm central} \sim 2.8 \cdot 10^{14}\,{\rm g/cm^3}$. The difference is attributed to the elaborated nuclear EoS that we are using in the simulations together with the neutrino radiation-transport scheme in contrast to Abdikamalov et al. (2010) who omit neutrino radiation and use a parameterized relation between the electron fraction Y_e and density. Additionally, for our non-rotating model, the inner core has a mass of $M_{\rm ic,b} = 0.58\,{\rm M}_\odot$. Our findings are in accordance with the results from previous simulations of CCSNe (e.g., Buras et al., 2006a,b; Liebendörfer et al., 2005). Abdikamalov et al. (2010) found $M_{\rm ic,b} \sim 0.27\,{\rm M}_\odot$ which is smaller than our values. The discrepancy is again due to the chosen EoS which leads to a different peak in the central density and therefore different sizes of the inner core. It has been shown (Dimmelmeier et al., 2008; Sumiyoshi et al., 2005;

Yasin et al., 2020) that the EoS choice can affect the exact value of the central density at core bounce, i.e., a softer EoS yields higher central densities at core bounce. In our simulations we chose the modern nuclear equation of state (version SFHo from Steiner et al. (2013), see chapter 2) that satisfies all current experimental and astrophysical constraints, including the radius bounds deduced from the recent gravitational-wave detection for the NS-merger event of GW170817 (Abbott et al., 2017).

Figure 4.2 and figure 4.3 show the time evolution of the radial velocity as a function of radius, from $\sim 10\,\mathrm{ms}$ before the core bounce until $\sim 100\,\mathrm{ms}$ after that. The different color lines present the time evolution with the lighter colors corresponding to early times and darker colors to later times. The left panels (purple lines) show the radial velocity at the poles and the right panels (orange lines) show the radial velocity at the equator. The first row corresponds to the non-rotating model M1.42-J0 and presents the radial velocity from the start of the simulation (i.e., $\sim 37\,\mathrm{ms}$ before bounce) until 100 ms after the bounce. Comparing the polar and equatorial radial velocity evolution, we notice the spherical symmetric way of collapse and subsequent launch of the shock.

4.1.2 Collapse and pressure bounce of the rotating models

Most of the rotating models follow comparable collapse dynamics as in the non-rotating case, but in a semi-homologous way of the infalling inner core. The infalling radial velocity strongly depends on the polar radius θ; thus, the inner core properties are angular dependent. This is seen in figure 4.2 and figure 4.3 for the rotating models that experience pressure bounce, i.e., models M1.42-J0.23-Dl, M1.61-J0.47, and M1.91-J1.09. Figure 4.1 shows the maximum central density of all models as a function of radius. We observe that the non-rotating M1.42-J0 model as well as the rotating M1.42-J0.23-Dl, M1.61-J0.47, M1.91-J1.09 models, exhibit a comparable increase of the central density towards the core bounce. Figure 4.1 shows clearly that the larger the (initial) core rotation, the lower the maximum central density. This is in alignment with rotational CCSN simulations (e.g., Ott et al., 2004; Shibata & Sekiguchi, 2004; Summa et al., 2018; Zwerger & Mueller, 1997) and previous AIC models (Abdikamalov et al., 2010; Dessart et al., 2006; Fryer et al., 1999). All of the aforementioned models experience oscillations of the inner core, seen as small density fluctuations in figure 4.1 until $\sim 10\,\mathrm{ms}$ when the PNS reaches a new equilibrium state.

Figure 4.4 shows the central angular velocity for each of the rotating models as a function of the post-bounce time. We calculate the angular velocity as the volume average of the first five kilometers in order to include a representative region of the inner core and not rely solely on the first cells (inner 400 m) that use an 1D core modeling (see section 3.4). The high-density high-rotation models, i.e. M1.61-J0.47 (dark blue line in figure 4.4) and M1.91-J1.09 (red line in the same figure) show an instant increase of the rotation of their inner core at bounce. The progenitors that are initially more compact (i.e., the ones with high central density, see chapter 3), collapse fast, and experience a spin-up of their cores due to the conservation of angular momentum. Furthermore, the low-central-density

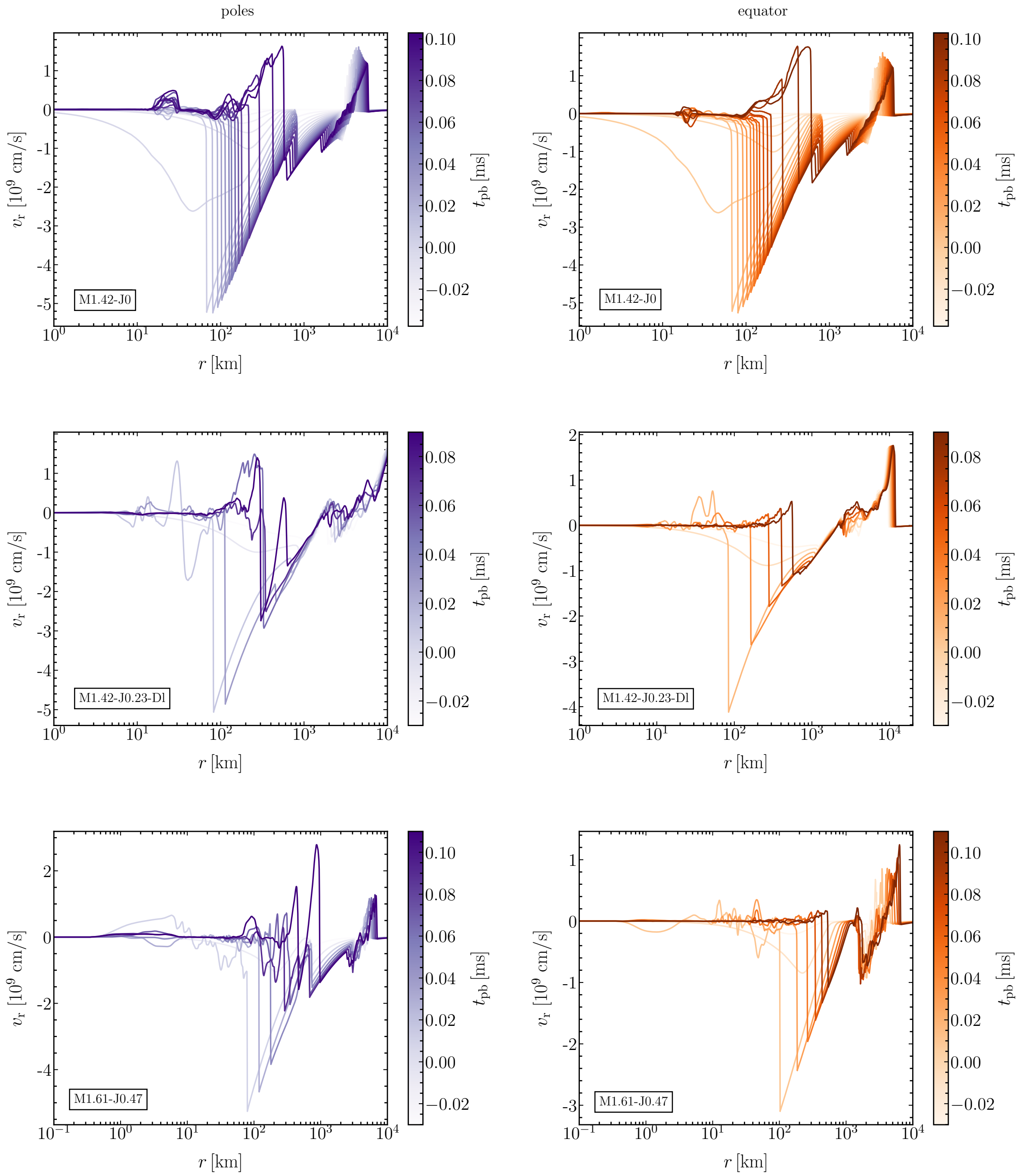

Figure 4.2: Radial profiles of the radial velocity at the poles (left panels, purple lines) and at the equator (right panels, orange lines) for each model. The different color lines show the time evolution from approximately 20 ms before the bounce until ∼100 ms after the bounce, with lighter purple/orange lines to represent early times and darker lines to correspond to later times. The first row corresponds to the model M1.42-J0, the middle row to the model M1.42-J0.23-Dl, and the bottom row to the model M1.61-J0.47.

.

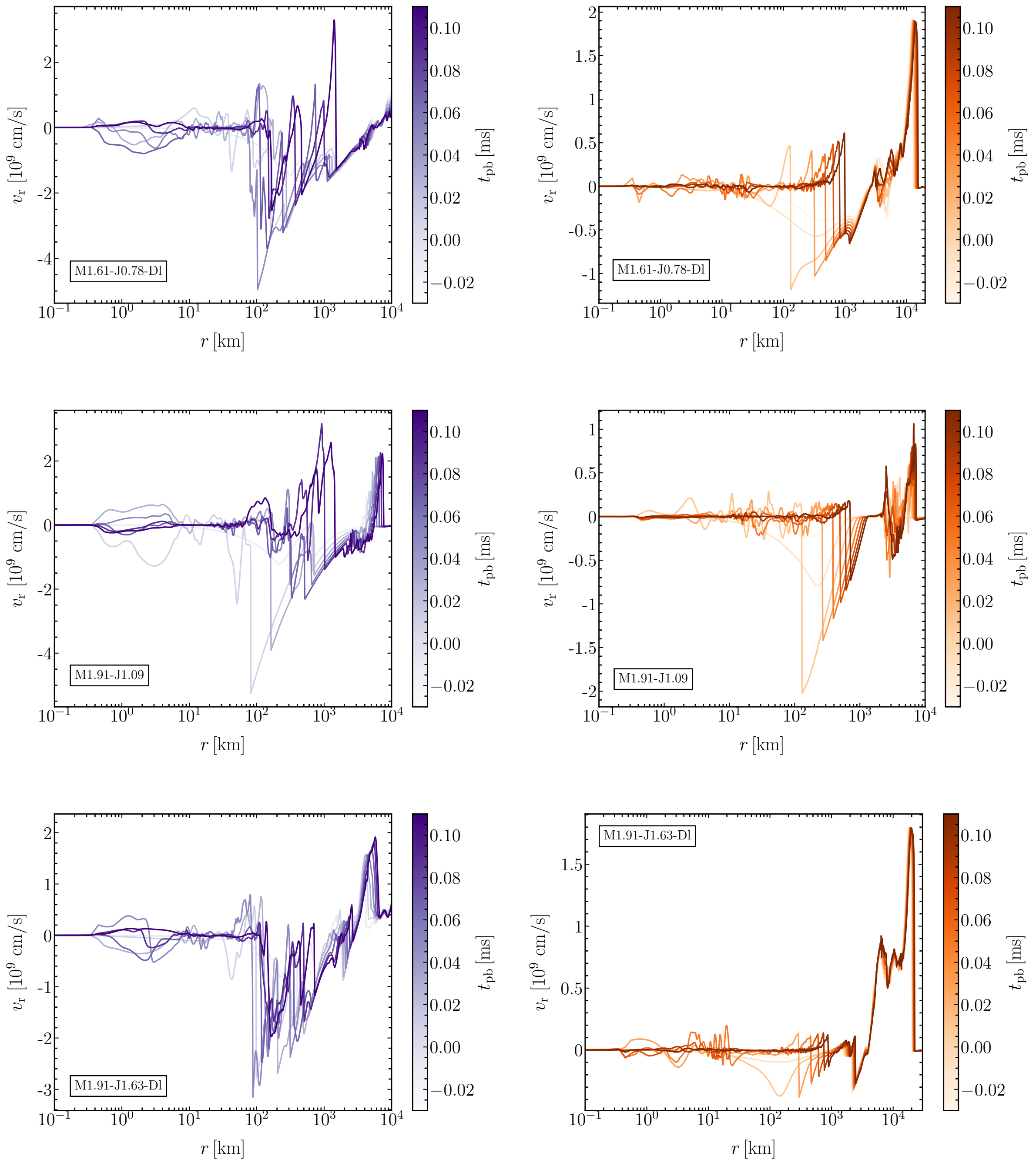

Figure 4.3: Same as figure 4.2. he first row corresponds to the model M1.61L-J0.78-Dl, the middle row to the model M1.91-J1.09, and the bottom row to the model M1.91-J1.63-Dl.

rotating models are less compact and undergo a smaller spin-up compared to their high-central-density counterparts. The aforementioned models undergo pressure bounce, similar to CCSN due to the stiffening of the EoS. Even though the rotational dynamics can alter the exact way of collapse (for example, asphericity), the bounce timescale and split into a homologous inner core and supersonic outer core is similar to all models. This means that the thermodynamics of the core set the conditions for the core bounce. In fact, the models with high density in their cores, need about $\sim 40\,\mathrm{ms}$ to collapse, while the timescale of the collapse for the models with low-central density varies from $\sim 300\,\mathrm{ms}$ to $\sim 800\,\mathrm{ms}$ with the difference being attributed to the initial rotational profile.

The models M1.42-J0.23-Dl, M1.61-J0.47, and M1.91-J1.09, undergo a pressure bounce similar to the CCSN. The inner core, which is defined as the amount of mass that is in sonic contact at the time of the bounce, ranges from 0.54 to $0.58\,\mathrm{M}_{\odot}$ apart from the fast rotating model M1.91-J1.09, which has an inner core mass of $0.72\,\mathrm{M}_{\odot}$. The large difference in the mass of the inner core for the last model is attributed to the high rotational rates in its core which provide centrifugal stability to a larger mass. Even though the model M1.91-J1.09 has the highest initial rotation at the core, its high central density leads to a fast collapse and pressure bounce.

4.1.3 Collapse and centrifugal bounce of the rotating models

All of our rotating models apart from the M1.42-J0.23-Dl, are rotating differentially which means that they are not limited by the mass-shedding on their surface. This implies that the central angular velocity can increase so much that the inner core can get rotationally supported and not undergo pressure bounce but centrifugal bounce instead. In fact, two of our models that have high initial total angular momentum and low-central density, i.e. the model M1.61-J0.78-Dl and the model M1.91-J1.63-Dl, both with low-central density, take significantly longer to collapse ($t_{\mathrm{bounce}} = 426\,\mathrm{ms}$ and $825\,\mathrm{ms}$, respectively) and their central density never reaches nuclear saturation density. These models have enough rotational support in their inner core and therefore undergo a centrifugal bounce in sub-nuclear densities, i.e. $\rho_{\mathrm{max}} = 0.499 \cdot 10^{14}$ g/cm^3 for M1.61-J0.78-Dl and $\rho_{\mathrm{max}} = 0.300 \cdot 10^{14}$ g/cm^3 for M1.91-J1.09-Dl. The collapse of the models follows a free-fall collapse timescale which scales with the central density. During the collapse, the angular momentum is conserved. Therefore, for a mass element that is centrifugally supported by $F_c \sim mj^2/r^3$, there is a point that the gravitational pull is not as strong as the centrifugal one (since the gravitational force scales with $F_g \sim GMm/r^2$). As we discuss later, this occurs for specific models with a high-value ratio of the rotational to the gravitational energy (i.e., high β value, where β is the ratio of the gravitational to the rotational energy). This effect is known in the context of iron-core collapse and has already been studied in the context of CCSN (Moenchmeyer et al., 1991; Tohline, 1984; Zwerger & Mueller, 1997).

Table 4.1 shows a summary of the parameters that characterize the core collapse for each model. For comparison, the non-rotating model M1.42-J0 has an inner core mass of $0.58\,\mathrm{M}_{\odot}$, while for the rotating models that undergo a pressure bounce, the inner core

Table 4.1: AIC properties during the infall and collapse phase. The columns list different physical parameters, where M is the mass of the white dwarf, Ω_c the central angular velocity, J the total angular momentum, and β_{init} the ratio of the total gravitational to rotational energy. The subscript "0" denotes the physical quantity at the initial state of the progenitor while the "ic,b" denotes the physical quantity of the inner core at core bounce.

Model	t_{bounce} [s]	ρ [10^{14} g/cm^3]	M_0 [M$_\odot$]	$M_{\text{ic,b}}$	Ω_0 [rad/s]	$\Omega_{\text{ic,b}}$	β_0	$\beta_{\text{ic,b}}$
M1.42-J0	0.0377	4.071	1.422	0.584	0	0	0.00	0.000
M1.42-J0.23-Dl	0.3460	3.842	1.422	0.541	0	2343.1	0.23	0.027
M1.61-J0.47	0.0396	3.188	1.609	0.569	12.000	2377.9	0.47	0.092
M1.61-J0.78-Dl	0.4263	0.498	1.611	1.478	5.554	34.8	0.78	0.137
M1.91-J1.09	0.0408	2.533	1.919	0.721	18.012	908.1	1.08	0.105
M1.91-J1.63-Dl	0.8248	0.300	1.906	1.901	5.337	15.8	1.63	0.174

increases with rotation, in accordance to the AIC models of Abdikamalov et al. (2010). The models that reach $\beta_{\text{ic,b}} \geq 13\%$, experience centrifugal bounce with very large inner cores. From now on, we will refer to them as *high-β rotating models.* In fact, the model M1.61-J0.78-Dl has an inner-core mass of 1.48 M$_\odot$ at bounce, and the model M1.91-J1.63-Dl has an inner-core mass of 1.901 M$_\odot$ out of 1.906 M$_\odot$ which is the total progenitor mass. Those models experience a slow and gradual spin-up of their central angular velocity as shown in figure 4.4. The slow collapse due to the low central densities of those models, in combination with the initial angular momentum profile, are the main contributing factors to the centrifugal bounce and the following evolution of these models.

An important parameter to distinguish between the pressure core bounce and the centrifugal bounce is the ratio of the rotational to the gravitational energy of the white dwarf, i.e., the β parameter. The fastest-rotating model that undergoes pressure bounce, i.e., the model M1.91-J1.09, is the upper limit of the models that undergo pressure bounce, with a β parameter of $\beta_{\text{ic,b}} = 10\%$ at core bounce. The rotating models with $\beta_{\text{ic,b}} \leq 13\%$ experience a pressure bounce and experience a linear effect of rotation on their collapse dynamics. To be more specific, for these models, the higher the initial rotation, the higher the β parameter at bounce, and the heavier the inner core. In contrast, models with $\beta_{\text{ic,b}} \geq 13\%$ undergo centrifugal bounce. Abdikamalov et al. (2010) report the limit between pressure and centrifugal bounce at $\beta_{\text{ic,b}} \sim 18\%$, which is higher than our value.

4.2 Development of the Neutrino-Driven Outflow from AICs

In the previous section, we identified how the rotational and thermodynamical properties of the progenitor models affect the core collapse after the onset of the gravitational instability. We continue the discussion with an overview of the onset of the "explosion". Since the AIC is sub-energetic with very little ejecta mass compared to typical CCSN of massive stars (e.g., Bollig et al., 2021; Burrows et al., 2019), we adopt the term *neutrino-driven outflow*

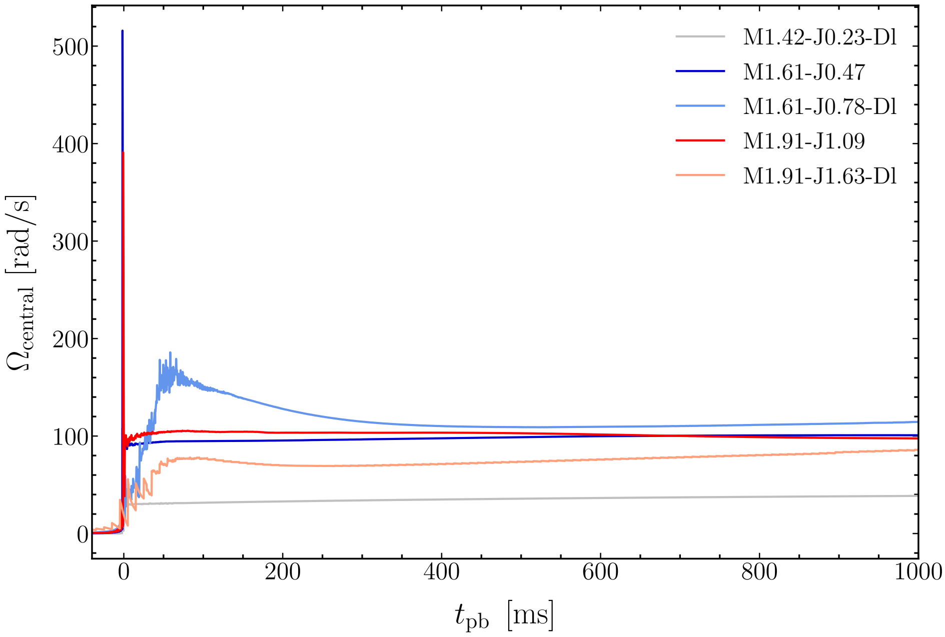

Figure 4.4: Central angular velocity as a function of post-bounce time for the rotating models. The angular velocity is calculated as a volume average of the inner 5 km. The steep rise at 0 ms is due to the core-bounce resulting from angular momentum conservation and the further increase is because of the further contraction of the PNS. The high-β models that undergo centrifugal bounce show a less steep increase of the angular velocity. Note that this is the volume-averaged angular velocity of the inner 5 km and is not identical to the angular velocity of the inner core at bounce which is listed in table 4.1.

to discribe the ejected mass. The primary mass ejection is driven by the shock wave assisted by neutrino heating, in a similar manner as in CCSN. Note that we differentiate this from the *neutrino-driven wind* which is again mass outflow due to neutrino heating but the material has high entropy and originates from the surface of the newly formed PNS. As neutrino-driven outflow from AICs we consider both ejection mechanisms

4.2.1 Overview of explosion dynamics

After the infall of the inner core and the core bounce, a rarefaction wave is formed that triggers the infall of the outer layers of the white dwarf. In the rotating models, the radial velocity depends on the polar angle; therefore, the infall is not spherically symmetric. As discussed earlier, this can be seen in the radial velocity profiles for the poles and the equator in figure 4.2 and figure 4.3. Due to the steeper density profile at the poles, the shock propagates faster in the polar direction compared to the mid-latitudes and the equator in all rotating models. This is due to the low accretion rate towards the shock compared to the large amount of mass that is accreted from the outer layers of a massive star in CCSN. The collapse and explosion dynamics are in alignment with Dessart et al. (2006)

who investigated the AIC of two rotating models with 1.46 and 1.92 $M_\odot$ in axisymmetric neutrino hydrodynamics simulations.

In all the rotating models, the shock wave breaks out of the progenitor in the polar direction due to the lack of rotational support and to the reduced accretion rate which is established by the oblique shape of the progenitor with steeper density gradient along the poles. Material at low latitude show little to no collapse but rather stay in rotational equilibrium and form a disk like structure around the PNS. The uncollapsed disk around the PNS constrains the opening angle of the ejecta. On the contrary, the model M1.42-J0, which has no rotation, the shock wave breaks out of the progenitor at around 90 ms in all latitudes and expands in a spherically symmetric way.

Figures 4.6 to 4.11 show the visual evolution of each model from a few milliseconds after bounce until the end of each simulation. In the top figures, the left panel is color-coded by the radial velocity; with blue, we show the parts with negative radial velocity, i.e., the matter that is infalling, and with red we show the matter that has positive radial velocity. The right panels show the density of the matter on a logarithmic scale. In the bottom figures, the electron fraction Y_e is shown in the left half of each plot and we always normalized the color bar to show in white the material with $Y_e = 0.5$. Neutron-rich low-Y_e material is shown in orange and proton-rich high-Y_e material is shown in dark purple. The right half of the panels are color-coded by the entropy, with lighter colors showing low-entropy regions. We show the evolution for each model close to the shock breakout from the progenitor, at 1 s after shock bounce[2], and at the end of each simulation. A more detailed visual representation of the evolution of each model can be found in additional figures in the Appendix in figure A.2 to figure A.13.

4.2.2 Non-rotating spherical symmetric model

After the stiffening of the equation of state, the core starts to develop positive radial velocities which means that matter is moving outwards. The shock wave is formed and is moving outwards in radius. Similar to CCSNe, after a few milliseconds, the radial velocities become negative behind the shock. We identify this behavior as shock stalling. However, due to the small accretion rate from the outer layers of the progenitor (since the progenitor has a low mass compared to a CCSN progenitor) and the development of the neutrino heating in the post-shock region, the shock accelerates and breaks out of the progenitor very fast at ~ 90 ms after the core bounce. At this moment, the white dwarf has contracted to a radius of 290 km.

Due to the neutrino heating in the post-shock layer, a negative entropy gradient develops which drives a convection flow (see left plots at ~ 80 ms in figure 4.6). The shock continues to move outwards, expelling the outer layers of the white dwarf. After 300 ms the neutrino-driven wind is established which drives additional mass away from the surface of the PNS. This is shown in the figure 4.5 as the additional mass shells (black lines) that are growing in

---

[2] Exception is the model M1.42-J0.23-Dl for which we show the evolution after 500 ms for better visualization purposes.

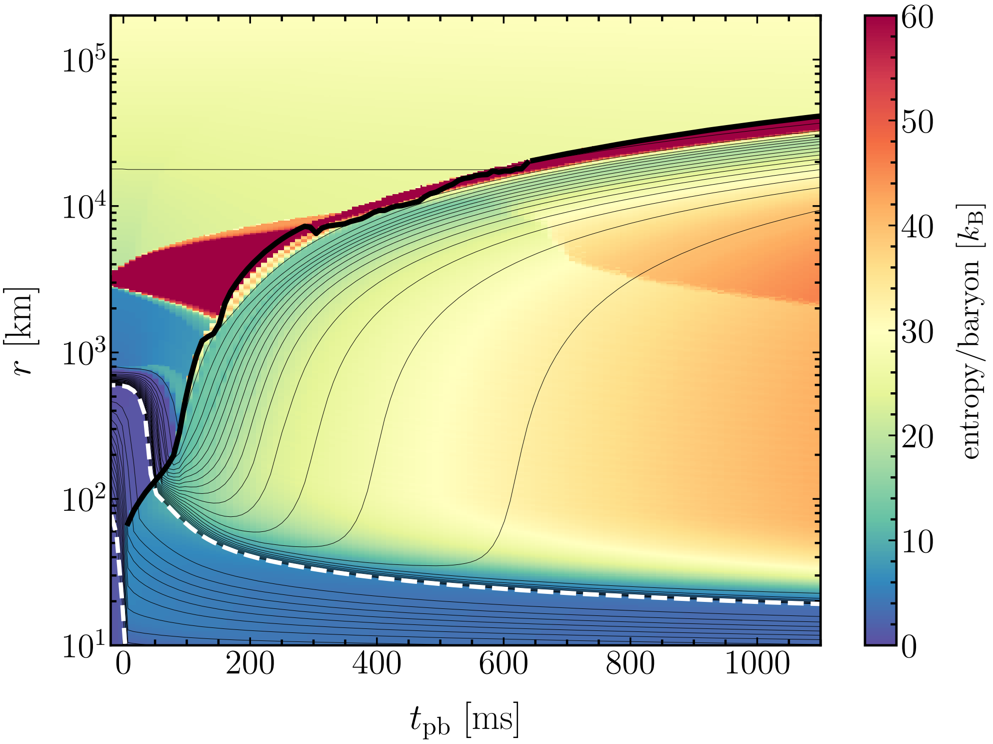

Figure 4.5: Mass-shell diagram for the simulation of M1.42-J0 color-coded by the entropy saturating at $60\,k_{\rm B}$/baryon. The Mass-shell diagram follows the radial evolution of defined mass-shells of specific mass as a function of post-bounce time. The dashed white lines correspond to the enclosed mass of $0.1\,{\rm M}_\odot$ and $1.4\,{\rm M}_\odot$. The thin black lines between the $0.1\,{\rm M}_\odot$ and the $1.4\,{\rm M}_\odot$ lines have a mass separation of $0.1\,{\rm M}_\odot$, and $0.001\,{\rm M}_\odot$ between the $1.4\,{\rm M}_\odot$ and the $1.422\,{\rm M}_\odot$ lines. The quantities shown are angle averaged.

radius and have high entropy. This material is heated by the continuous energy deposition by the neutrino radiation which declines in timescales of more than 1 second. At the end of our simulation, i.e., at 6.74 s post bounce, a total mass of $7.90{\cdot}10^{-3}\,{\rm M}_\odot$ is ejected from the model M1.42-J0 and a neutron star is created with a mass of $1.41\,{\rm M}_\odot$. An elaborate discussion on the outflow properties is to be found in chapter 6.

figure 4.5 shows the mass-shell diagram for the non-rotating model M1.420J0. This displays the evolution of radius that enclose a specific amount of mass as a function of post-bounce time. The colors show the entropy-per-baryon with blue being the low entropy material and yellow/red the high entropy material, saturated in $60\,{\rm k_B}$. The thick solid line shows the evolution of the shock wave as a function of time.

4.2.3 Rotating models

Rotating models: M1.42-J0.23, M1.61-J0.47, M1.91-J1.09

In the rotating models, the outflow develops so fast that there is insufficient time for any convective motions to set in before the shock breaks out. The main effect of the rotation in the shock formation and propagation is the strong dependence on the polar θ angle. The asphericity of the shock in rotating models has been studied in CCSNe simulations as well (Dimmelmeier et al., 2002; Ott et al., 2006). The steep density gradient and absence of centrifugal force in the polar regions allow the shock to break out in that direction in a few tenths of milliseconds. On the contrary, in the equatorial plane, the centrifugal support stabilizes most of the material which forms a quasi-Keplerian disk around the PNS. The shock propagates outwards and wraps around the progenitor which expels only little material from the outer parts of progenitor at the equator. In all the rotating models, apart from the effect in the poles, we notice another pattern emerging regarding the development of the outflow. The outflow expansion rate is higher at mid-latitudes, i.e., 30-50° away from the poles, producing a "butterfly shape" of the outflow at $\sim 100\,\mathrm{ms}$. This is noticed in the left panels (showing the radial velocity) of the sequence figures 4.7 to 4.11 which shows the time when the shock wave breaks out of the surface of the white dwarf. This part of the ejecta has more rotational energy to convert into kinetic energy compared to the ejecta mass along the poles which lack rotational support, but lower than the equatorial material which mostly stays rotationally bound. Therefore, these three components of steep density gradient at the poles, enough rotational energy at mid-latitudes to drive the outflow, and the rotationally supported disk in the equator, give form to the geometry of the outflow.

Another crucial part, that is a result of the initial angular momentum distribution and core bounce, is the angular dependence of the neutrino luminosities and mean energies. The neutrino luminosities are higher in the poles than in the equator, thus allowing more efficient heating in the poles (Dessart et al., 2006). These effects alter the electron fraction Y_e of the overflow, making it strongly angle dependent. Additionally, the increased neutrino heating along the poles increases the entropy in that direction. We thoroughly discuss the neutrino properties and how they set the temporal and angular distribution of the Y_e in the ejecta in chapter 6.

The total ejecta mass for the rotating models is larger than the non-rotating model M1.42-J0 and range in $\sim 2-5\cdot 10^{-2}\,\mathrm{M}_\odot$. The model M1.42-J0.23-Dl has the highest ejecta mass, with a total of $5.25\cdot 10^{-2}\,\mathrm{M}_\odot$ after $7.83\,\mathrm{s}$ of evolution. The reasoning behind this trend is the slow rotation of this progenitor and subsequently the low mass of the disk around the PNS. Therefore, there is more available material - which is not centrifugally supported - to be ejected.

Table 4.2: Summary of global properties for the simulations of the AIC models. The model name is listed in the first row, t_{end} is the final time of the corresponding simulation, M_{NS} is the baryonic mass of the NS, R_{NS} is the min/max radius of the NS, M_{disk} is the mass of the circum-neutron star disk, M_{ej} is the total ejected mass calculated at the end of each simulation, and E_{expl} is the explosion energy (see section 4.4).

Model	t_{end} [s]	M_{NS}[$\mathrm{M}_\odot$]	R_{NS} [km]	M_{disk} [$\mathrm{M}_\odot$]	M_{ej} [$10^{-3}\mathrm{M}_\odot$]	E_{expl}[10^{50} erg]
M1.42-J0	6.74	1.409	13.2	0.00013	7.90	1.431
M1.42-J0.23-Dl	7.83	1.295	11.55/58.12	0.05898	52.45	2.939
M1.61-J0.47	6.80	1.370	9.95/95.08	0.11581	25.91	1.662
M1.61-J0.78-Dl	4.67	1.137	8.45/101.90	0.29427	21.22	0.450
M1.91-J1.09	6.15	1.296	9.05/98.80	0.42859	18.69	1.002
M1.91-J1.63-Dl	6.09	0.965	7.75/99.56	0.75393	5.78	0.115

High-β rotating models: M1.61-J0.78-Dl, M1.91-1.63-Dl

Just before the centrifugal bounce, during the slower - compared to other models - collapse, part of the surface of the white dwarf at the poles is flying outwards due to the lack of centrifugal support. Thus, at the poles, there is a steep density gradient which makes the formed shock wave accelerate outwards with velocities that reach $\sim 10^9$ cm/s. Due to the large angular momentum budget in these models, most of the mass is staying in rotational equilibrium around the newly formed PNS. In particular, the model M1.61-J1.63-Dl ejects only $5.78\,10^{-3}\,\mathrm{M}_\odot$ after 6 s of evolution. The total ejecta mass for the model M1.61-J0.78-Dl is $18.69\,10^{-3}\,\mathrm{M}_\odot$ after 4.67 s post bounce. A large fraction of the mass from the progenitor stays around the PNS in the form of a disk, similar to the rest of the rotating models. The mass of this disk is $0.75\,\mathrm{M}_\odot$ and after 6.1 s the neutron star has mass of only $0.97\,\mathrm{M}_\odot$ for the model M1.91-J1.63-Dl. The other high-β rotating model, i.e., M1.61-J0.78-Dl, forms a larger neutron star of $1.137\,\mathrm{M}_\odot$ and the disk around it has smaller mass of $0.12\,\mathrm{M}_\odot$. This also explains the higher ejecta mass for the model M1.61-J0.78-Dl. Due to the lower initial angular momentum, there is less mass in the disk around the PNS and thus allowing more material to be ejected.

4.3 Angular Momentum Evolution and Disk Formation

Due to angular momentum conservation, the central angular velocity rises as the white dwarf collapses, as seen in figure 4.4. With the development of the neutrino-driven outflow, part of the angular momentum is carried away in the shock and outflow as the shock wraps around the collapsed progenitor but most of the angular momentum resides in the material around the PNS that forms a disk-like structure that is rotationally supported. Given the initial differential rotation of our (rotating) models, much of the rotationally supported material resides in low-latitudes close to the white dwarf surface. This part of each rotating progenitor, experiences little to no collapse and forms a quasi-Keplerian disk (Abdikamalov et al., 2010; Dessart et al., 2006). The mass of the disk that is formed around the PNS ranges from 0.06 to $0.43\,\mathrm{M}_\odot$ for the discussed rotating models (see table 4.2 for details). The

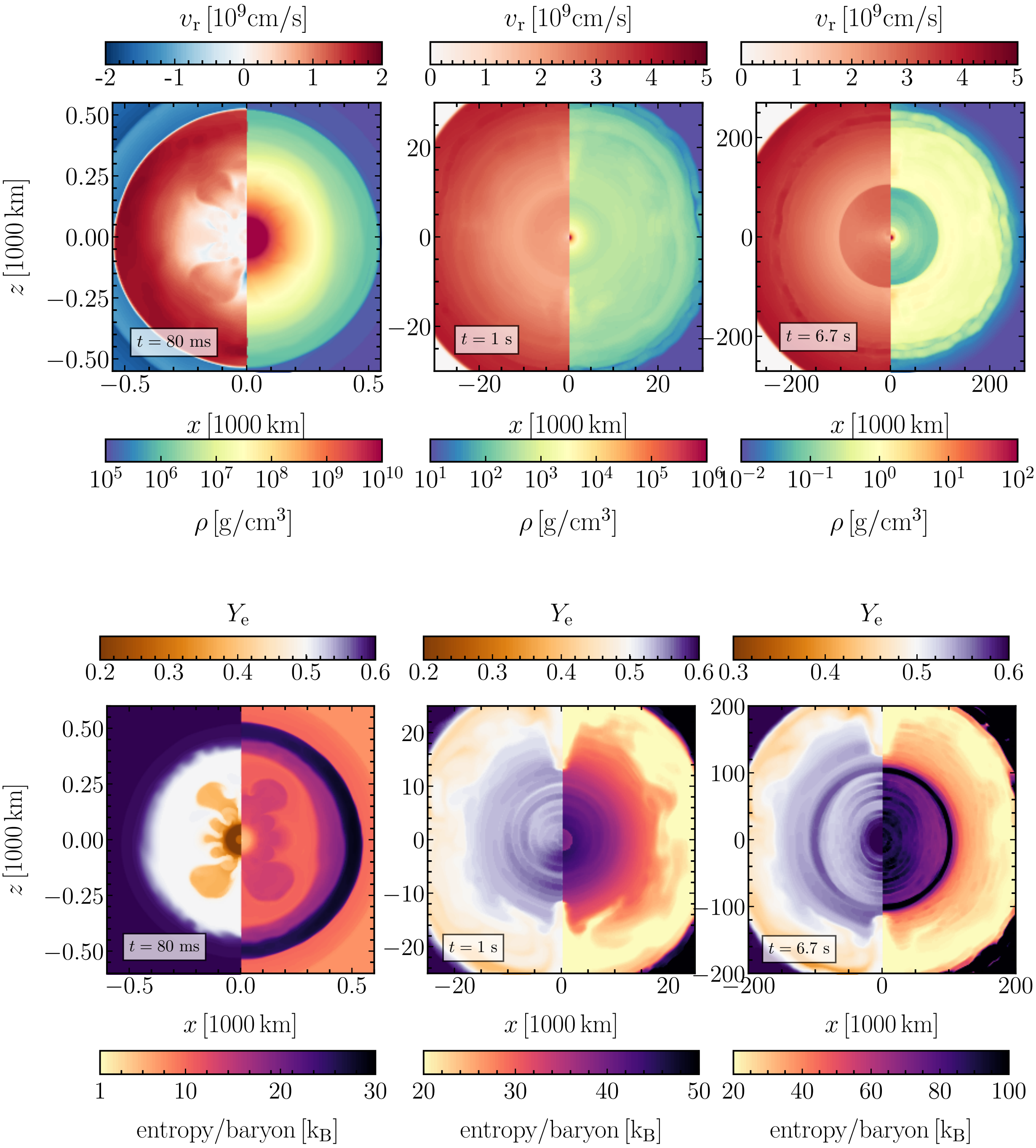

Figure 4.6: Series of color-coded cross-sections for different quantities at three different times of evolution for the model M1.42-J0. The top row shows the radial velocity (left half panels) and the density in logarithmic scale (right half panels). The radial velocity is normalized to show the parts with zero radial velocity in white. The bottom row displays the electron fraction Y_e (left half panels) and entropy (right half panels). The Y_e is normalized to show regions with $Y_e = 0.5$ in white. The different plots show the evolution of the model at 80 ms, 1 s, and at the end of the simulation at 6.7 s post bounce.

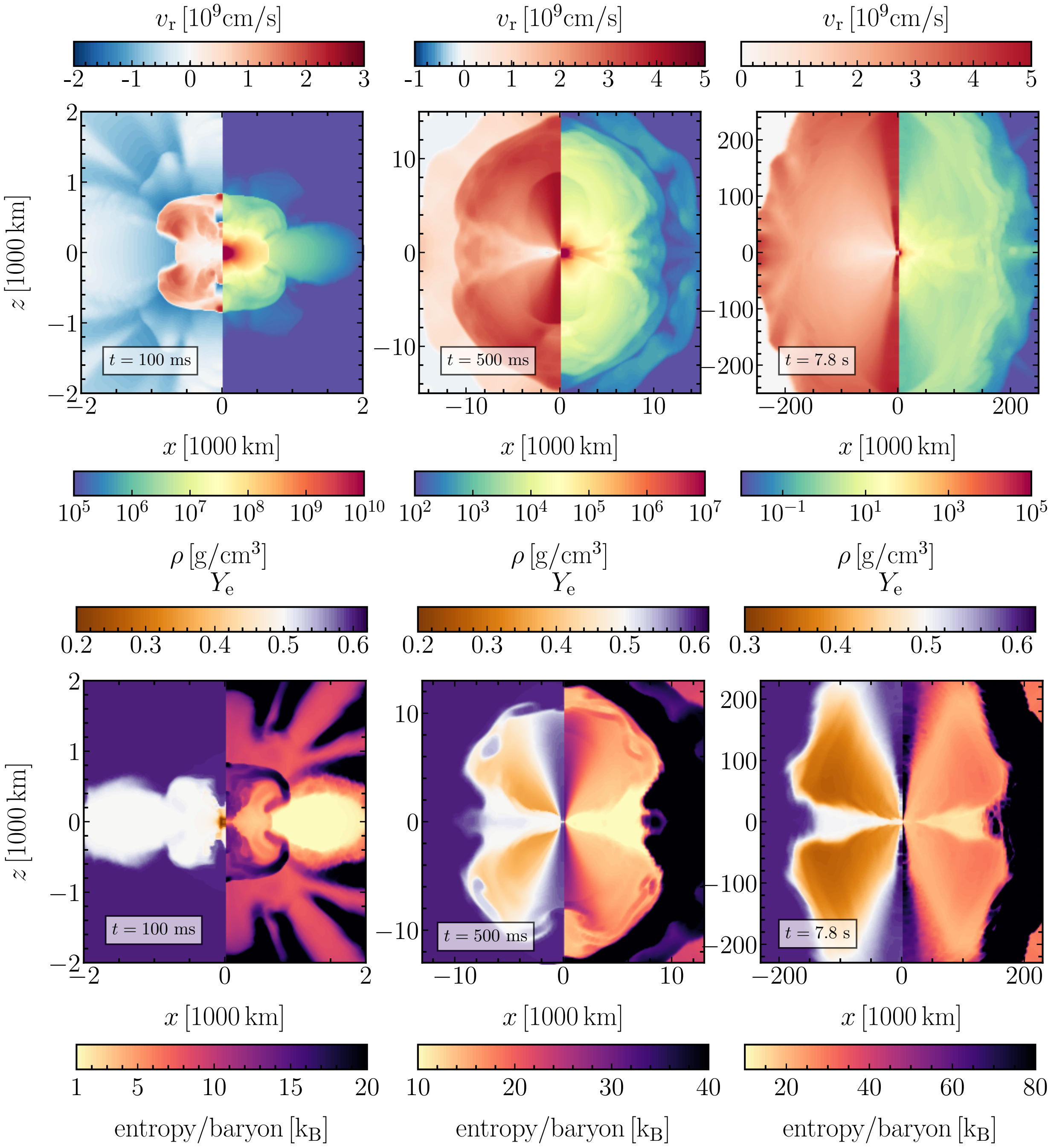

Figure 4.7: Same as in figure 4.6 for the model M1.42-J0.23-Dl. The different plots show the evolution of the model at 100 ms, 500 ms, and at the end of the simulation at 7.8 s post bounce.

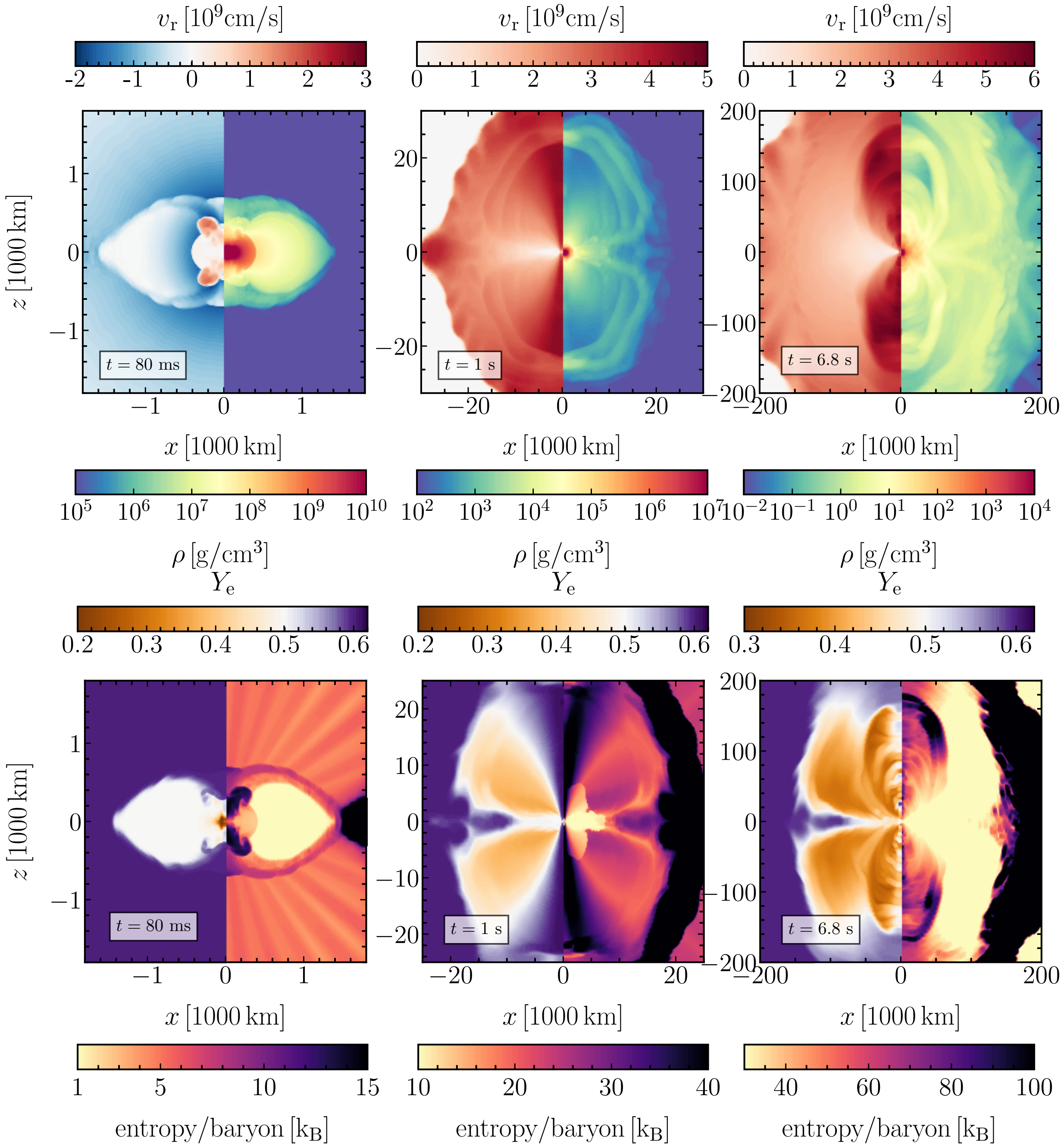

Figure 4.8: Same as in figure 4.6 for the model M1.61-J0.47. The different plots show the evolution of the model at 80 ms, 1 s, and at the end of the simulation at 6.8 s post bounce.

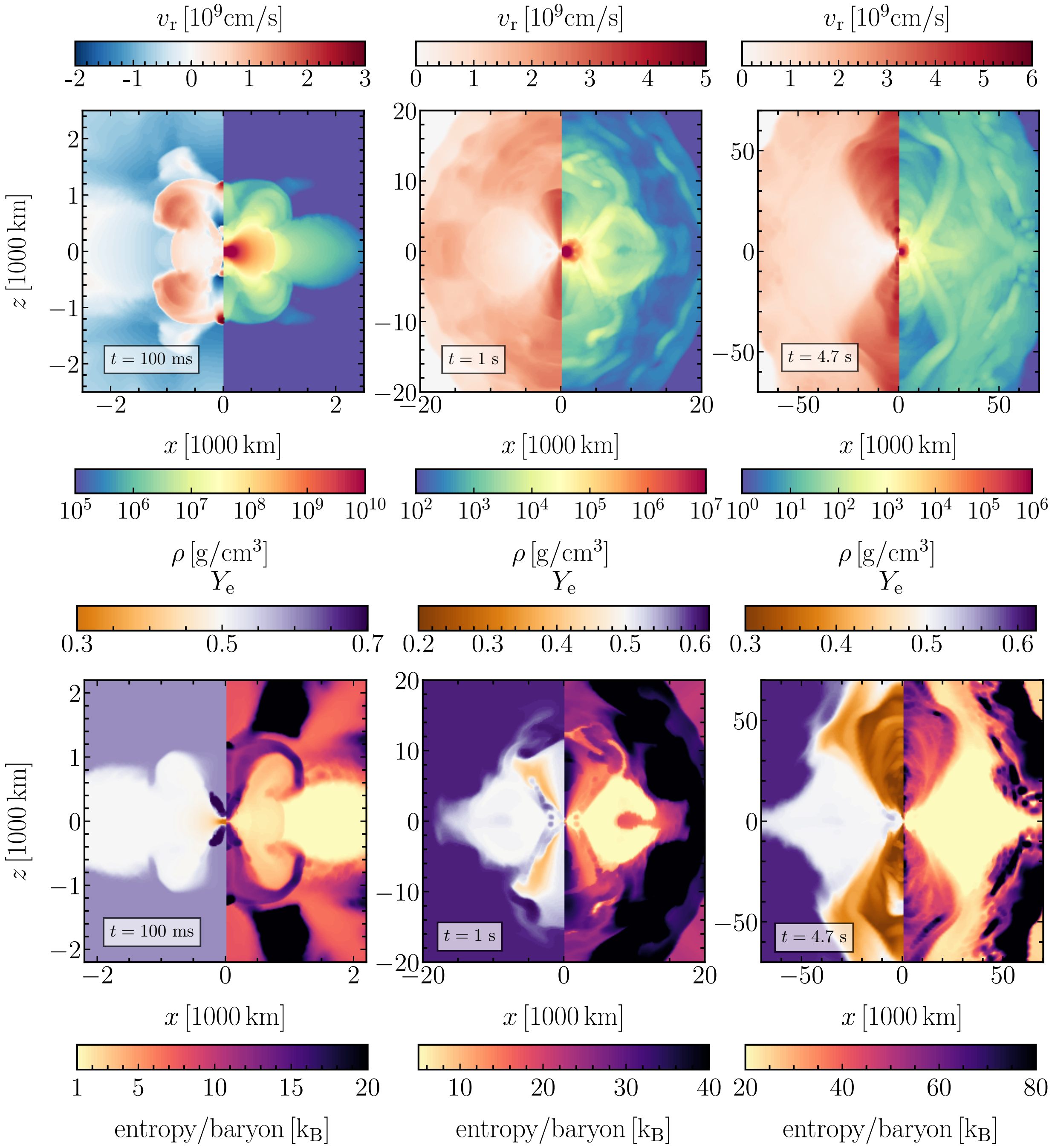

Figure 4.9: Same as in figure 4.6 for the model M1.61-J0.78-Dl. The different plots show the evolution of the model at 100 ms, 1 s, and at the end of the simulation at 4.7 s post bounce.

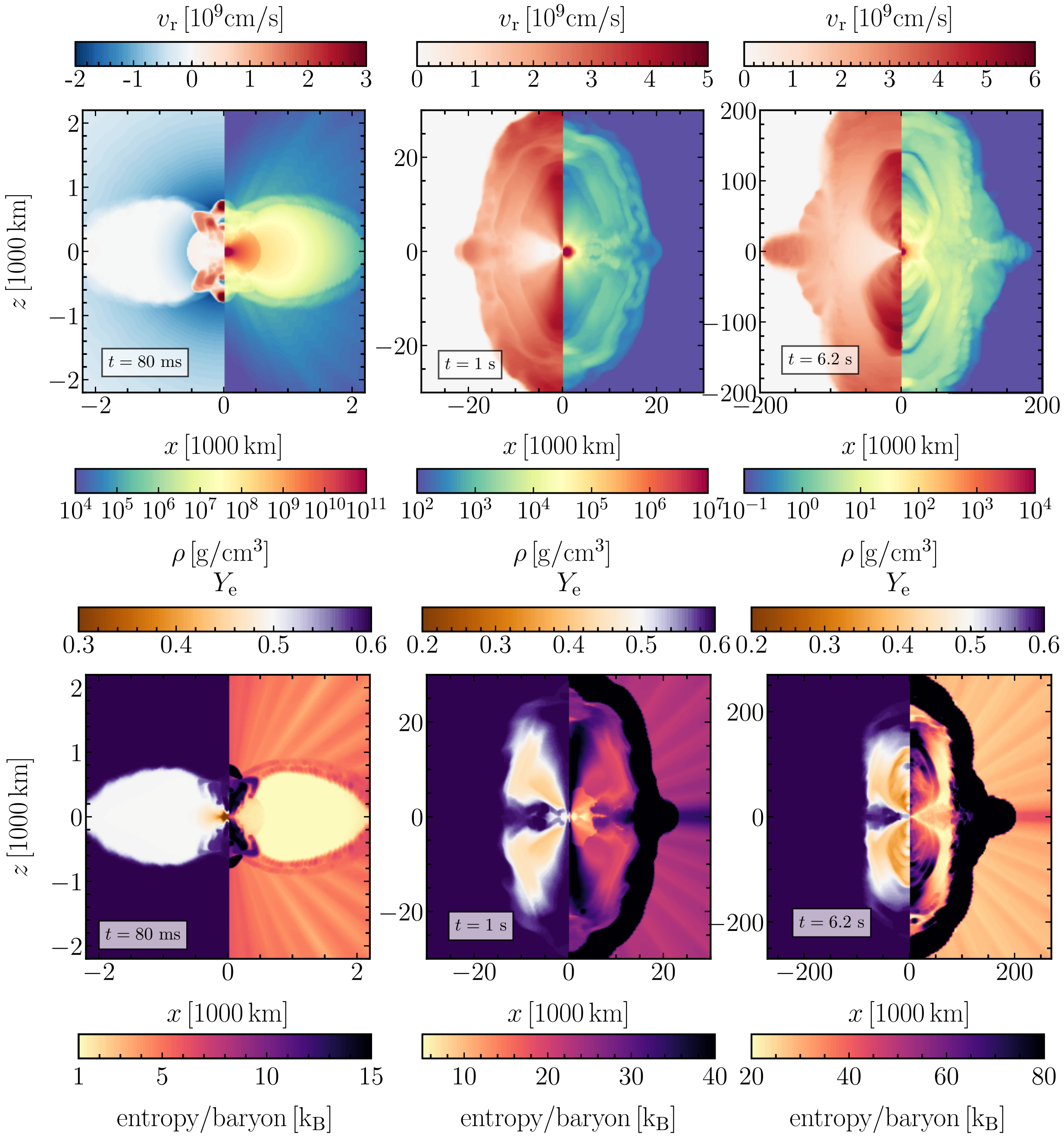

Figure 4.10: Same as in figure 4.6 for the model M1.91-J1.09. The different plots show the evolution of the model at 80 ms, 1 s, and at the end of the simulation at 6.2 s post bounce.

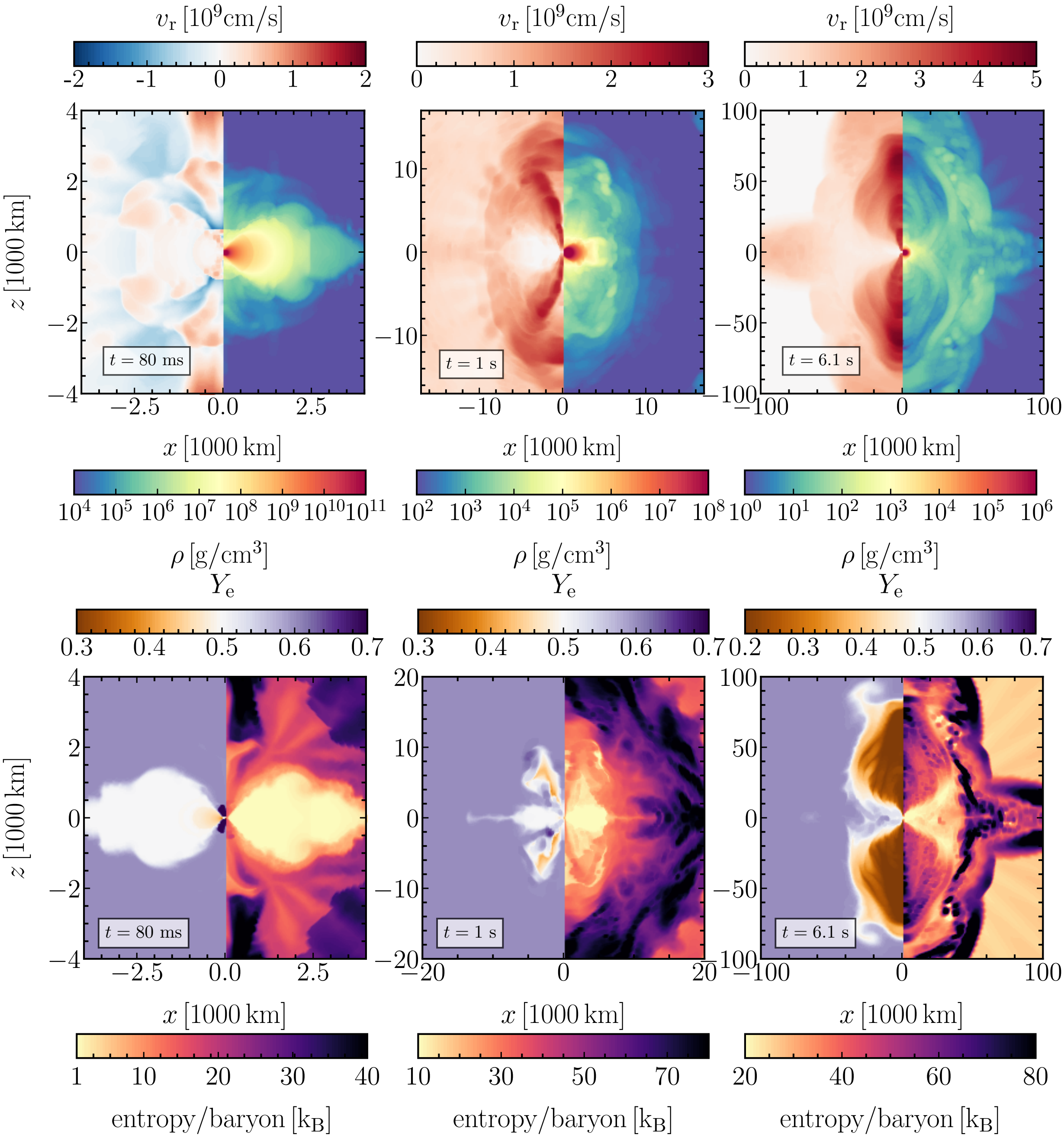

Figure 4.11: Same as in figure 4.6 for the model M1.91-J1.63-Dl. The different plots show the evolution of the model at 80 ms, 1 s, and at the end of the simulation at 6.1 s post bounce.

higher the angular momentum of the initial model, the higher the centrifugal support at the equator which manifests to a larger mass of the disk. We calculate the mass of the disk as the material that its radial velocity is smaller than the escape velocity $v_{\mathrm{esc}} = \sqrt{2Gm_{\mathrm{enc}}/r}$ and it has density $\rho \leq 10^{10}\,\mathrm{g/cm^3}$.

The mass of the disk for the rotating models is proportional to the initial angular momentum of the progenitor. The model M1.42-J0.23-Dl, which is the model with the modest rotational rates and the lower total initial angular momentum, develops a disk with a mass of $0.059\,\mathrm{M_\odot}$ while the model M1.91-J1.63-Dl, which is the model with the highest amount of initial angular momentum but not the one with the fastest central rotation, has a disk with a mass of $0.75\,\mathrm{M_\odot}$. This trend is reflected to the total ejecta masses as well. The models with the lower mass disks eject more mass despite their lower progenitor mass. With a lower mass in the disk structure, there is more mass available to be ejected by the neutrino-driven outflow.

Each plot in figure 4.12 shows the post-bounce time evolution of the z-component of the specific angular momentum as a function of radius for each of the rotating AIC models. The colored lines present the time evolution with blue being the initial specific angular momentum and red showing the specific angular momentum at the end of the specific simulation. In the inner 10-20 km, the specific angular momentum increases linearly with radius. Since the specific angular momentum is directly proportional to the angular velocity, we conclude that the neutron star rotates as a solid body to a good approximation. Our findings and conclusions are in alignment with Dessart et al. (2006) who explored the evolution of two rotating AIC models until $\sim 600\,\mathrm{ms}$ post bounce.

Since our code does not include any viscosity treatment, there is no mechanism to properly model the material in the disk. Therefore the realistic timescale for the disk accretion cannot be determined from our simulations. We expect that the continuous flux of radiated neutrinos from the PNS will cool the disk and alter the electron-to-baryon ratio $Y_e$while a part of the mass will accrete onto the neutron star further increasing its mass and spin. Metzger et al. (2009a) investigated the evolution of such disks using as the initial conditions the AIC simulations by Dessart et al. (2006). Metzger et al. report that the disk experiences neutrino cooling and become neutron-rich soon after its formation. However, due to the viscous evolution of the disk which spreads the disk to larger radii, the density drops and the neutrino radiation “reaches” more material. Thus, electron neutrinos are absorbed by neutrons, raising again the electron-to-baryon ratio of the disk close to $Y_e = 0.5$. At the point when the disk spreads enough that the weak interactions are negligible, the electron fraction Y_e is not altered anymore. After the Y_e freeze-out, the disk becomes advective and geometrically thick (Metzger et al., 2008a, 2009b). α-particles begin to form which release energy and unbind most of the disk material. These results could potentially add on the nucleosynthetic output of AICs and consequently affect the optical signal from AICs. Our simulations cannot confirm these results due to the lack of viscosity in our calculations. Apart from that, in these conditions, magnetic fields might play an important role in the redistribution of angular momentum and disk evolution. However, the study of the disk evolution using the appropriate numerical tools (e.g. Just

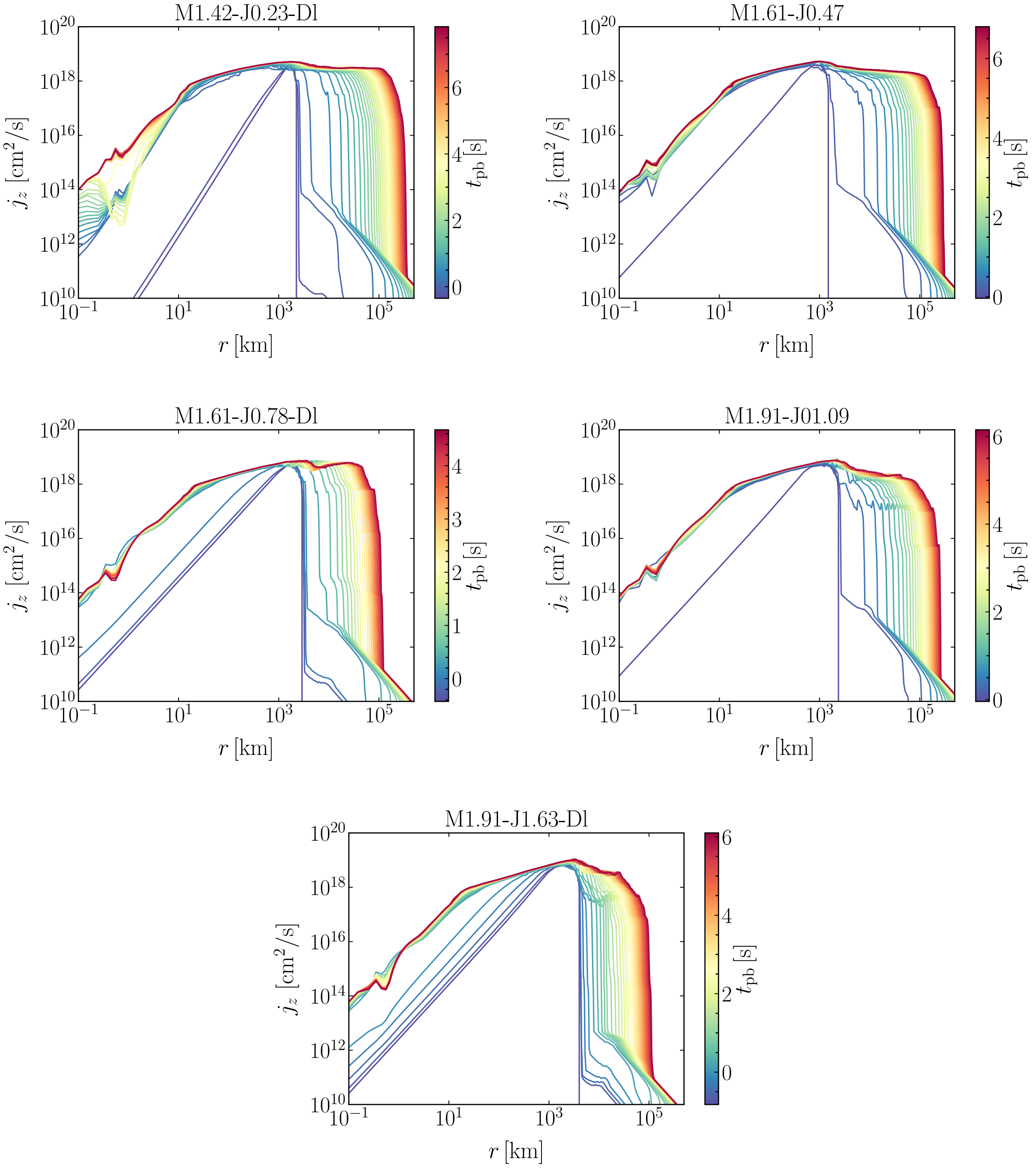

Figure 4.12: Time evolution of the z-component of the specific angular momentum as a function of radius. The colored lines present the time evolution according to the color bar with blue corresponding to the early times $j_z - r$ profile and red lines to the final stages of the simulation. Each panel presents the time evolution of the radial dependence of the specific angular momentum for each model indicated in the plot title. The same plot that shows the specific angular momentum as a function of enclosed mass, can be found in the Appendix in figure A.14.

et al., 2023) and further diagnosis of the nuclear composition of the disk is out of the scope of this Thesis.

4.4 Explosion Energy

The ejected material from our models is in the order of $10^{-2}\,\mathrm{M}_\odot$ (see table 4.2), similar to previous findings (Dessart et al., 2007, 2006). This is orders of magnitude less than the ejecta mass of a typical CCSN and therefore the explosion energy from AIC is expected to be less than the canonical SN energy of 10^{51} erg (e.g., SN1987A, Arnett, 1987). In figure 4.13 we plot the diagnostic explosion energy of the neutrino-driven outflow of each model. The diagnostic explosion energy is calculated as

$$E_{\mathrm{diag}} = \int_V e_{\mathrm{tot},>0}\, \rho\, dV \tag{4.1}$$

where e_{tot} the sum of the gravitational, internal and kinetic energy of the unbound material in the post shock region, i.e., the ejecta. At ~ 3 s, the explosion energy has reach saturation levels and is of the order of 10^{50} erg, indeed an order of magnitude lower than the typical explosion energy from a CCSN. The AICs are considered to be underenergetic because there is little mass to absorb neutrinos due to the low mass ejecta and also because a large part of the material stays rotationally bound in a disk configuration as discussed earlier.

From figure 4.13 we notice the large spread in explosion energies of our simulated models. The model with the highest explosion energy is the slowly rotating model M1.42-J0.23-Dl. This particular model has also the highest ejecta mass, i.e., $5.245{\cdot}10^{-2}\,\mathrm{M}_\odot$ after 7.83 s of evolution. The slow rotation of this model allows for most of the mass to be ejected and not form a heavy disk around the PNS.

For the rest of the rotating models (i.e., M1.42-J0.23-Dl, M1.61-J0.47, and M1.91-J1.63-Dl, the explosion energy drops with the increasing initial angular momentum. The non-rotating model M1.42-J0 exhibits a steep rise of the explosion energy in the first 100-200 ms after the onset of the neutrino-driven outflow but does not reach as high energies as the model M1.42-J0.23-Dl for example. This is due to the lower ejecta mass of the non-rotating model which is $7.90 \cdot 10^{-3}\,\mathrm{M}_\odot$. The steep rise of the explosion energy is attributed to the fact that most of the mass is ejected during the first 200 ms post bounce (see section 6.1 for the discussion on the ejecta properties). On the low end of the explosion energies lays the high-β rotating model M1.91-J1.63-Dl with a diagnostic explosion energy of $1.15 \cdot 10^{49}$ erg. This is an order of magnitude lower than the rest of the models and it is directly correlated to the very small amount of ejecta mass for this model which is only $5.78\,10^{-3}\,\mathrm{M}_\odot$. Despite the fact that the non-rotating model M1.42-J0 has ejecta mass equal to $7.9 \cdot 10^{-3}\,\mathrm{M}_\odot$ that is close to the total ejecta mass of the high-β rotating model M1.91J1.63-Dl with $M_{\mathrm{ej}} = 5.78 \cdot 10^{-3}\,\mathrm{M}_\odot$, the respective explosion energies are more than an order of magnitude apart. The underlying cause of this is the lower neutrino luminosities and mean energies for the model M1.91-J1.63-Dl, which results from the centrifugal bounce

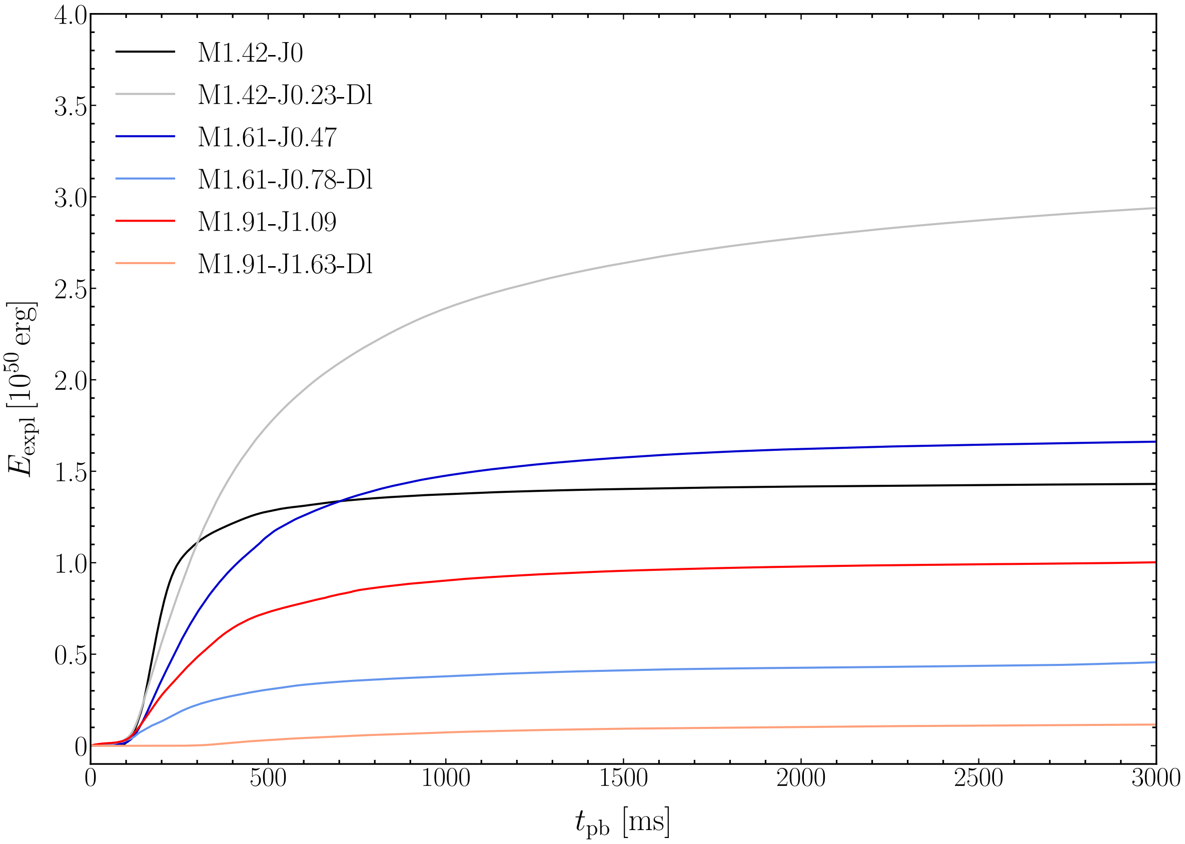

Figure 4.13: Explosion energy as a function of post-bounce time for the AIC models. The explosion energy is calculated as the sum of the gravitational, kinetic, and internal energy for the unbound material in the post-shock region.

and the high initial angular momentum of the progenitor. A comprehensive discussion of the rotational effects on the neutrino signal is given in chapter 5.

Dessart et al. (2006) find lower explosion energies, specifically $2.7 \cdot 10^{49}$ erg for their slow-rotating $1.46\,\mathrm{M}_\odot$ model and $2 \cdot 10^{49}$ erg for their fast rotating $1.92\,\mathrm{M}_\odot$ model. Even though their values are lower than ours, they report that at the end of their simulation the energies are still rising and they expect that the total energies to be higher than the reported. Similar to AIC, underenergetic explosions are expected from low-mass SN progenitors that explode as electron-capture SN (Buras et al., 2006a; Janka et al., 2008; Kitaura et al., 2006; Nomoto, 1984, 1987; Woosley et al., 2002). The resemblance with the AIC models can be ascribed to the low post-bounce accretion rate caused by the low envelope mass. Under these conditions, the neutrino-driven explosions are successful but yield underenergetic explosions, which can impact their detectability.

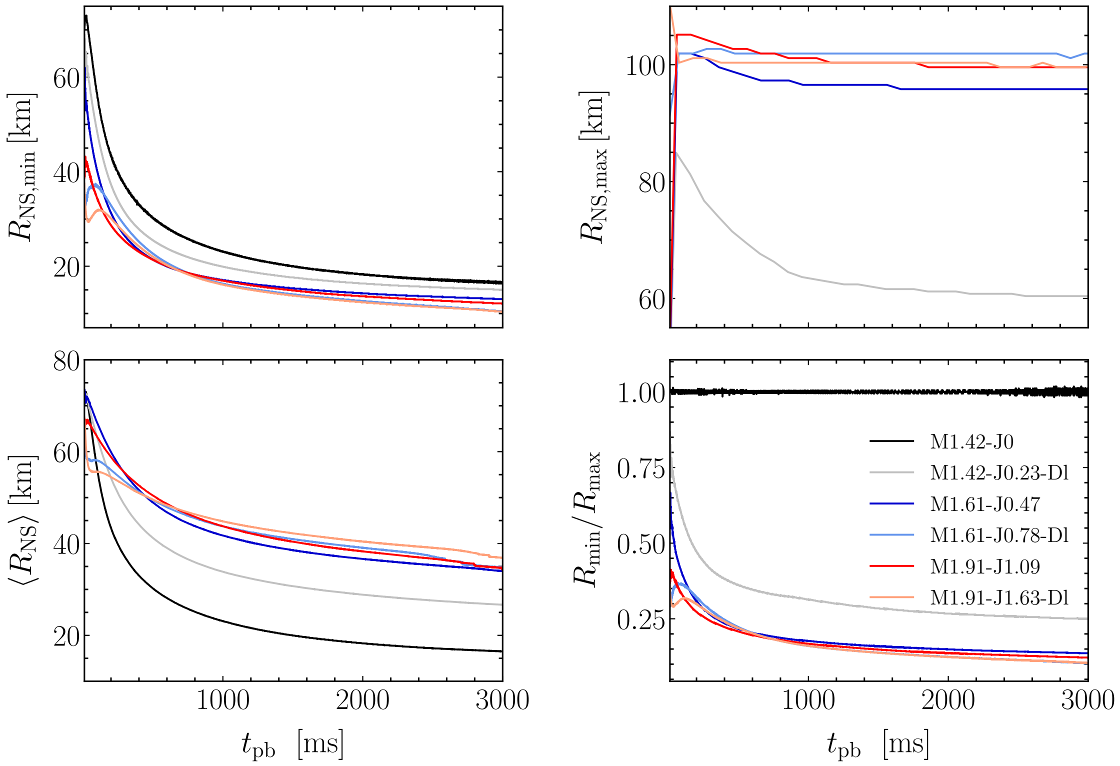

Figure 4.14: Radius of the neutron star as a function of post-bounce time. The upper left panel shows the minimum neutron star radius, the upper right panel shows the maximum neutron star radius for the aspherical rotating models, the bottom left plot shows the mean neutron star radius, and the bottom right plot shows the ratio of the minimum to the maximum radius of the neutron star as a function of post-bounce time.

4.5 Neutron Star Properties

The AIC progenitors discussed in this Thesis, evolve to form neutron stars after the core-bounce and the onset of the mass ejection by the neutrino-driven outflow. All of our models form neutron stars (Nomoto & Kondo, 1991; Woosley & Baron, 1992) with a large spread in masses and spin periods. Table 4.3 shows a summary of the masses, radii, angular velocities, rotational periods and total angular momentum for the formed neutron stars of our models.

Figure 4.14 shows the evolution of the neutron star radius as a function of post-bounce time; the upper left panel shows the minimum neutron star radius, the upper right panel shows the maximum radius for the aspherical rotating models, the bottom left plot shows the mean radius, and the bottom right plot shows the ratio of the minimum to the maximum radius of the neutron star as a function of post-bounce time. As neutron star we consider the material that has densities $\rho \geq 10^{11}$ g/cm^3. Figure 4.15 shows the baryonic neutron star mass as a function of post-bounce time (left plot) and the total angular momentum of the

Table 4.3: Summary of the neutron star properties. The first column lists the AIC models, $M_{\rm NS}$ is the neutron star mass, $R_{\rm NS}$ is the min/max radius of the neutron star, $\Omega_{\rm NS}$ the angular velocity, $P_{\rm NS}$ the neutron star spin, $J_{\rm NS}$ the total angular momentum, $I_{\rm NS}$ is the moment of inertia, and $\beta_{\rm NS}$ the ratio of the rotational to the gravitational energy of the neutron star. The quantities are evaluated at the end of each simulation.

Model	$M_{\rm NS}$ [$\mathrm{M}_\odot$]	$R_{\rm NS}$ [km]	$\Omega_{\rm NS}$ [rad/s]	$P_{\rm NS}$ [ms]	$J_{\rm NS}$ [10^{49} erg · s]	$I_{\rm NS}$ [10^{46} cm^2 · g]	$\beta_{\rm NS}$
M1.42-J0	1.409	13.2	0	0	0	0	0
M1.42-J0.23-Dl	1.295	11.55/58.12	4370.577	1.438	1.136	0.260	0.1388
M1.61-J0.47	1.370	9.95/95.08	1970.466	3.189	2.321	1.177	0.2529
M1.61-J0.78-Dl	1.137	8.45/101.90	1287.426	4.880	2.397	1.862	0.3344
M1.91-J1.09	1.296	9.05/98.80	1636.608	3.839	2.554	1.561	0.3002
M1.91-J1.63-Dl	0.965	7.75/99.56	1106.785	5.677	1.874	1.694	0.3272

rotating neutron star as a function of post bounce time. The neutron star with the highest mass is formed from the non-rotating model M1.42-J0 which is a result of the low ejecta mass. The radius of this neutron star is 13.2 km and it is spherical symmetric. This is larger than the mass that is expected from ECSN (e.g., Kitaura et al., 2006). The neutron star from the rotating models are highly aspherical, as expected from previous simulations of AIC and rotating CCSN (see e.g., Dessart et al., 2006; Janka & Moenchmeyer, 1989a,b; Liu & Lindblom, 2001; Walder et al., 2005). The ratio of the minimum to the maximum radius is in the order of ∼ 10% for all the rotating models with the exception of the model M1.42-J0.23, for which the ratio is ∼ 20% at the end of the simulation. The high-β rotating models (i.e., M1.61-J0.78-Dl and M1.91-J1.63-Dl) give birth to neutron stars with extensive equatorial radius of ∼100 km and low mass neutron star masses with 1.14 $\mathrm{M}_\odot$ for the M1.61-J0.78-Dl model and 0.97 $\mathrm{M}_\odot$ for the M1.91-J1.63-Dl. The low masses are a result of the high initial angular momentum of those models which results in a large disk material around the NS. The neutron stars for these models are among those with the longer spin periods as well. The neutron star spins every 4.88 ms and 5.67 ms for the model M1.61-J0.78-Dl and M1.91-J1.63-Dl respectively. For the rotating models, the masses range in $1.29 - 1.39\,\mathrm{M}_\odot$ and the spin rates in 1.44-3.84 ms. The models with the lowest initial rotational rates, for example the model M1.42-J.023, is the one with the shortest spin period of 1.44 ms. On the contrary, the model with the highest initial rotational rates, i.e., the model M1.91-J1.09, gives birth to a neutron star with a period of 3.84 ms. The grounds for this trend lays in the circum-neutron star disk that is formed. For the models with high initial angular momentum, there is a heavy disk formed and most of the angular momentum budget belongs to the disk. That's why the model M1.42-J0.23-Dl, that has a disk of low mass, results in a high-spinning neutron star.

Figure 4.15 (right panel) demonstrates the total z-component of the angular momentum of the neutron star as a function of time. The total angular momentum of the PNS continues to increase as the neutron star mass grows in time and receives high-j_z material from the collapse. The total angular momentum of the neutron star is the same order of magnitude

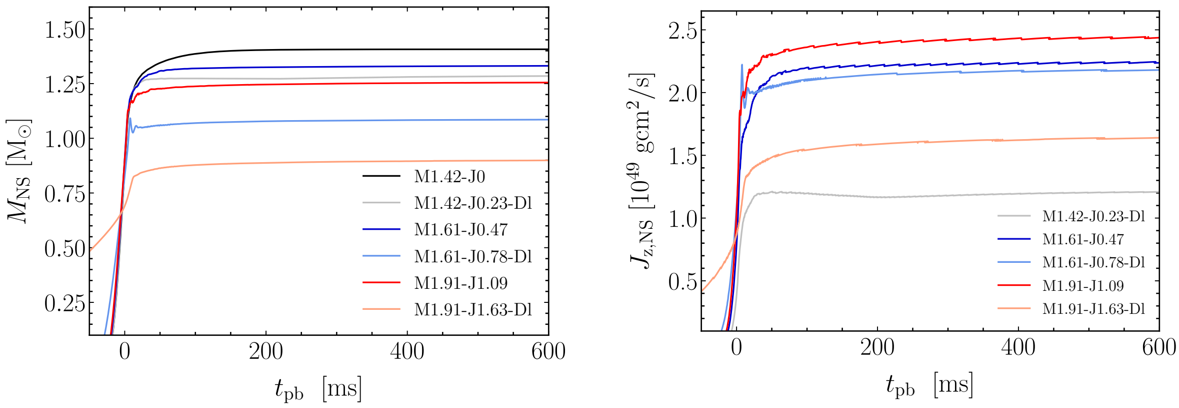

Figure 4.15: The left plot shows the baryonic mass of the formed neutron star for each AIC model as a function of post-bounce time. As neutron star we consider the material that has densities $\rho \geq 10^{11}$ g/cm^3. The right plot displays the time evolution of total angular momentum of the neutron star for each of the rotating models.

for all the models, with a higher angular momentum for the fastest rotating models as expected. The model M1.91-J1.63-Dl - the one with the highest initial angular momentum - is an exception because of the small neutron star mass and high mass of the disk around it. A similar figure of the figure 4.12 that shows the time evolution of the z-component of the specific angular momentum as a function of radius for the inner regions that correspond to the neutron star can be found in the Appendix (figure A.15).

Our model M1.91-J1.09 can be compared to the 1.92 M$_\odot$ of Dessart et al. (2006) since they have similar masses, and comparable initial rotational rates. We both find almost identical neutron star masses of 1.296 M$_\odot$ for our model and 1.30 M$_\odot$ for Dessart et al.. The rest of our models have a wide range of different initial conditions to make a direct and meaningful comparison of the neutron star properties with the ones obtained by Dessart et al.. Both Dessart et al.'s and our findings differ from the results of Fryer et al. (1999) who obtained a neutron star of $\sim$ 1.2 M$_\odot$ with a period of $\sim$1 s. The discrepancy can be attributed to the solid-body rotation of the progenitor models by Fryer et al. which does not allow for angular momentum accretion onto the neutron star. In a solid-body rotating model, most of the rotation is accumulated in the outer parts of the white dwarf and thus is carried away with the neutrino-driven outflow.

The last column of table 4.3 shows the ratio of the rotational to the gravitational energy of the neutron star. High-β values allow for the growth of secular and dynamical instabilities (Tassoul, 2000). Takiwaki et al. (2021) observed the growth of the low-T/|W| instability[3] at T/|W| $\sim$ 0.02 at bounce but they do not make a clear statement about the instability at the PNS. Earlier studies by Ott et al. (2004) found that the low-T/|W| instability can develop in the PNS even if the $\beta = T/|W|$ parameter is as low as $\sim$0.08.

---

[3] T/|W| is the definition of the β parameter and it is referred at the literature either way

The non-axisymmetric nature of the instability makes it impossible to be studied within the framework of our models. However, future 3D simulations of interesting AIC models could give an insight in the discussed instability.

Chapter 5

Neutrino Signal

The first multi-messenger signal we can expect from an AIC is neutrino emission after the core bounce. The gravitational collapse and subsequent development of a shock wave are similar to the CCSNe from massive stars, and therefore, we would expect a similar neutrino signal from the AICs. In this chapter, we focus on the neutrino signal from AICs. Neutrinos play an essential role in the launch of the outflow from AICs, shaping the composition of the ejected material. We present how the neutrino signals differ from model to model depending on their initial properties and, in particular, how the initial angular momentum profiles and central density influence the neutrino signatures.

5.1 Neutrino Signatures

In the following, we will discuss the neutrino emission properties for all AIC models from core bounce to the end of each simulation. Figure 5.1 shows the neutrino luminosities and mean energies for the electron neutrinos ν_e (left column), the electron antineutrinos $\bar{\nu}_e$ (middle panels), and the heavy-lepton neutrinos ν_x[1] (right column) as a function of time. The first row shows the luminosity, and the bottom shows the angle-averaged mean energy of the neutrinos for each one of the six simulated models. All quantities are transformed to the lab frame and evaluated at 3500 km. The mean energy for each of the evolved neutrino species ν is calculated as

$$\langle \epsilon_\nu(r) \rangle = \frac{\int F^r_\nu(r) d\epsilon d\Omega}{\int F^r_\nu(r) \epsilon^{-1} d\epsilon d\Omega}, \tag{5.1}$$

where F^r_ν is the radial neutrino flux for $\nu_e, \bar{\nu}_e, \nu_x$, and $r = 3500\,\mathrm{km}$ as mentioned above.

Electron captures on free protons and other nuclei produce a large number of neutrinos in the core of the collapsed white dwarf. In the core, the densities are high enough, so that the neutrinos are trapped and only move outwards in slow diffusive processes. Once the electron neutrinos reach densities where the matter is optically thin, they stream outwards

---

[1] As a reminder, ν_x corresponds to heavy-lepton neutrinos, i.e., $\nu_\mu, \bar{\nu}_\mu, \nu_\tau, \bar{\nu}_\tau$.

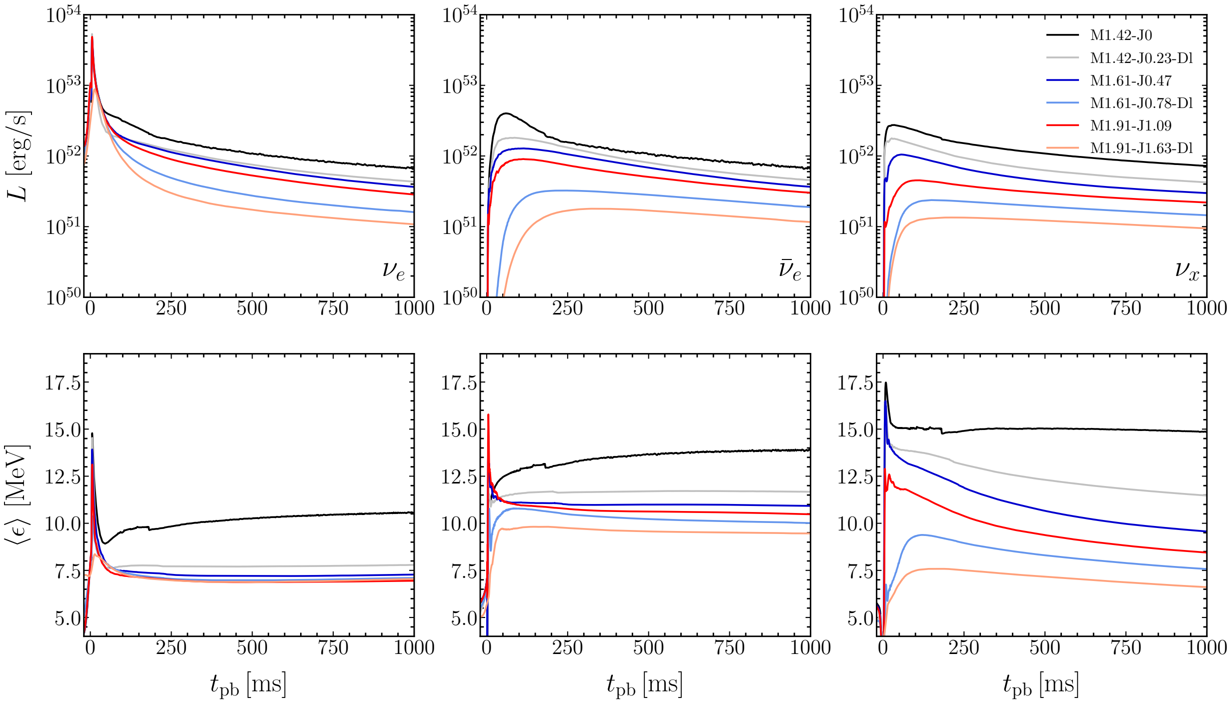

Figure 5.1: Luminosity (top row) and angle-averaged mean energy (bottom row) for the three evolved neutrino species: electron neutrinos ν_e (left column), electron antineutrinos $\bar{\nu}_e$ (middle column), and heavy-lepton neutrinos ν_x (right column) for the six AIC models as a function of time. Each colored line corresponds to one model as denoted in the legend. The quantities are transformed into the lab frame and evaluated at a radius of 3500 km. The time shown in the x-axis corresponds to the post-bounce time. Here we show the evolution of the neutrino luminosities and mean energies from the time of bounce until one second of evolution. The long-time evolution is shown in the Appendix in figure A.16.

(see, e.g., Janka, 2017b, for a review on neutrino emission in CCSNe). This corresponds to the characteristic peak in the electron neutrino luminosities (left upper panel of figure 5.1). By defining the neutrinosphere, we can estimate the radial position at which neutrinos are no longer trapped and enter the optically thin matter. Although, in nature, there is not a sharp transition to neutrino optically thin matter, we use the concept of the neutrinosphere to facilitate our understanding and discussion. To determine the position where the neutrino decoupling occurs, i.e., the radius of the neutrinosphere, we consider the effective opacity, which is a function of the absorption and scattering opacity of ν_e and $\bar{\nu}_e$. Since the opacities are energy dependent, we consider an energy-averaged neutrinosphere and use the energy-averaging effective opacities introduced in Buras et al. (2006b). Due to the high density of electron neutrinos and antineutrinos at the collapsed cores, charged current β-processes dominate the total ν_e and $\bar{\nu}_e$ opacity (see section 2.2).

We define the neutrinosphere at the point at which the flavor-dependent effective optical depth τ_{eff} equals to 2/3, where the τ_{eff} is defined as

$$\tau_{\text{eff}}(R_\nu) = \int_{R_\nu(\theta)}^{\infty} \tilde{\kappa}_{\text{eff}}(r,\theta,\nu)\rho(r,\theta)dr. \tag{5.2}$$

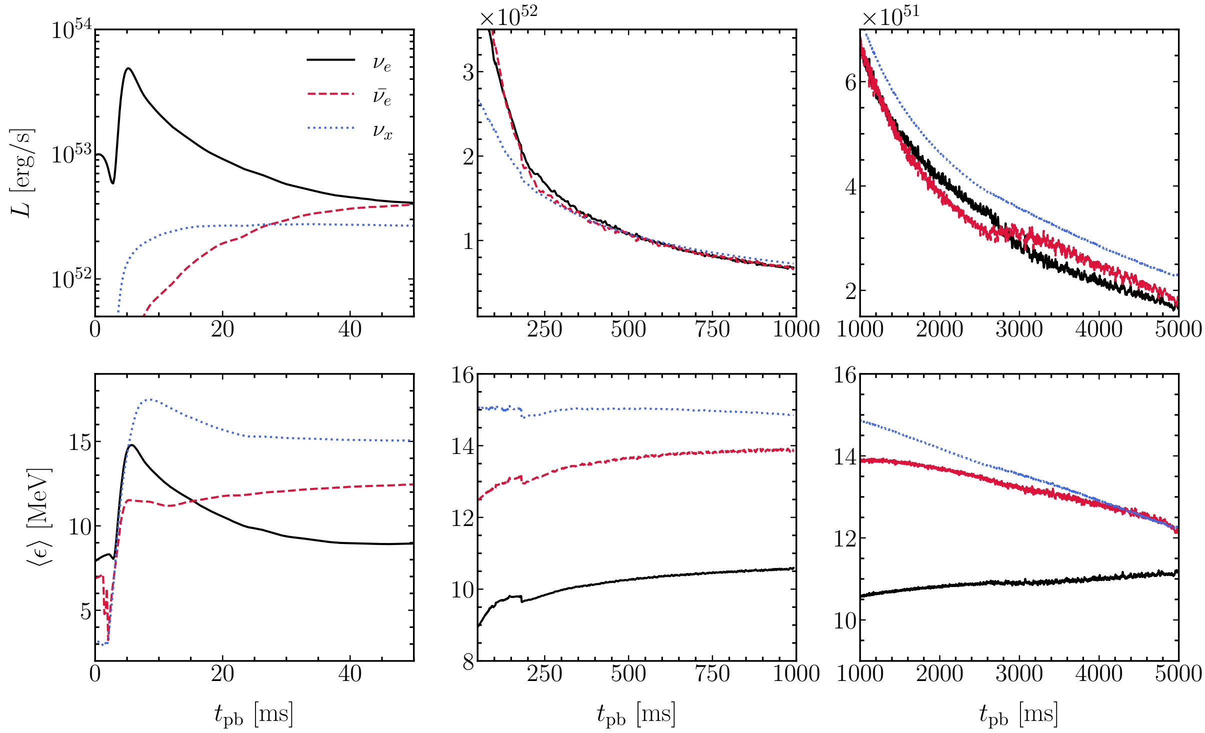

Figure 5.2: Luminosity and angle-averaged mean energy as a function of post-bounce time for the non-rotating model M1.42-J0. The luminosity (top row) is energy integrated, calculated in the lab frame at a distance of 3500 km. Each panel in the top row shows different time intervals of the luminosity evolution for the electron neutrinos ν_e in solid black lines, the electron antineutrinos $\bar{\nu}_e$ in dashed red lines, and the heavy-lepton neutrinos ν_x in dotted blue lines. The bottom row shows the angle-averaged mean energy of the electron neutrinos ν_e (solid black lines), the electron antineutrinos $\bar{\nu}_e$ (dashed red lines), and the heavy-lepton neutrinos (dotted blue lines) as a function of post-bounce time. Notice the different y-axis scales in each panel.

Here, $\tilde{\kappa}_{\mathrm{eff}}$ is the energy-averaged effective opacity of the matter in units of [g/cm^2] (Raffelt, 2001; Shapiro & Teukolsky, 1983). The effective opacity is given by

$$\kappa_{\mathrm{eff}} = \sqrt{\kappa_{\mathrm{abs}}(\kappa_{\mathrm{abs}} + \kappa_{\mathrm{sca}})}, \tag{5.3}$$

where κ_{abs} is the absorption opacity and κ_{sca} is the scattering opacity. A list of the considered reactions that are included in the opacities calculation is listed in section 2.2. The energy-average effective opacity is calculated from the effective opacity following Buras et al. (2006b) as

$$\tilde{\kappa}_{\mathrm{eff}} = \frac{\int_{\epsilon\,\mathrm{grid}} \kappa_{\mathrm{eff}}(r', \epsilon) F^r_\nu(r', \epsilon) d\epsilon}{\int_{\epsilon\,\mathrm{grid}} F^r_\nu(r', \epsilon) d\epsilon}, \tag{5.4}$$

where F^r_ν is the radial component of the neutrino flux and the energy grid (ϵ grid) is $0 - 400$ MeV in the ALCAR code (see section 3.4).

Continuing the discussion on the neutrino signal, we can use the concept of the neutrinospheres to elaborate on the neutrino properties. When the ν_e diffuse and "cross" the

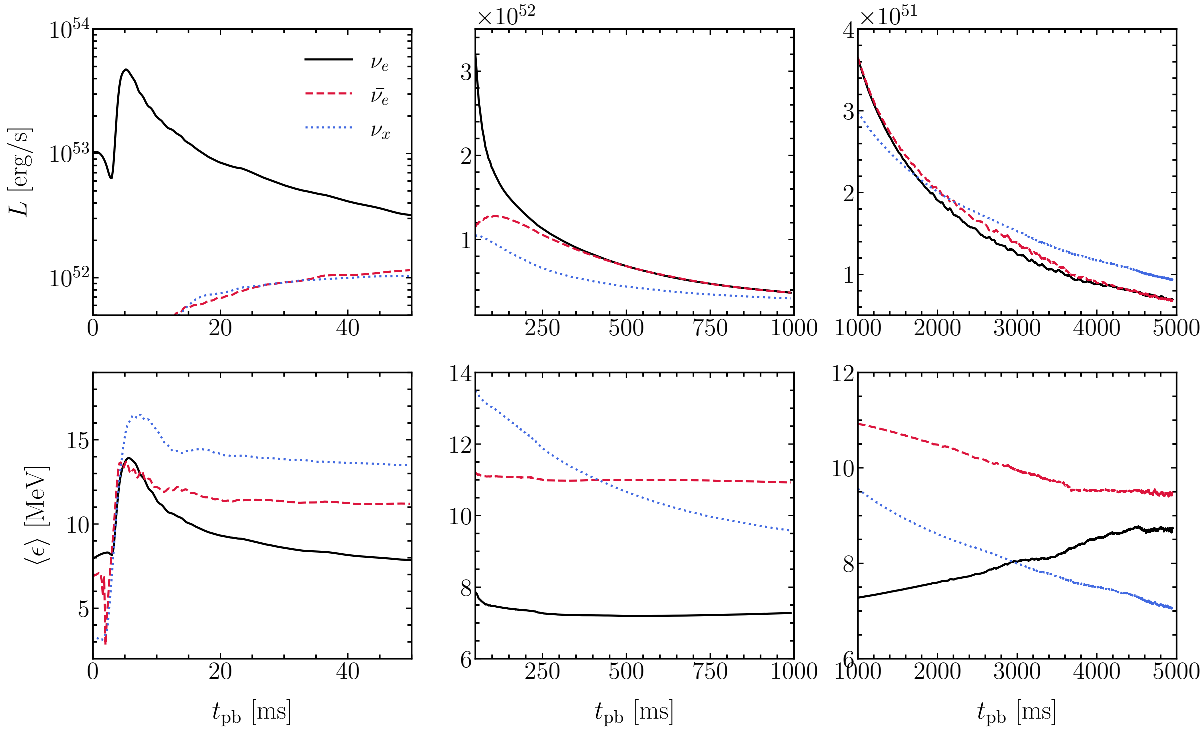

Figure 5.3: Luminosity and angle-averaged mean energy as a function of post-bounce time for the rotating model M1.61-J0.47. Same as in figure 5.2. The same figures for the rest of the models are presented in the Appendix in figure A.17 - figure A.20.

neutrinosphere, they stream outwards which is manifested in the ν_e luminosity peak seen in figure 5.1. We point out again that in reality, there is not a sharp point at which the neutrinos stream out, but rather a region that depends on the neutrino energy at which the neutrinos are not coupled to the stellar matter.

After this so-called neutrino-shock break out, which corresponds in the peak for ν_e luminosities, the $\bar{\nu}_e$ and ν_x luminosities start to rise due to their production via pair processes in the post-shock region in the first ~ 50 ms. The ν_e luminosity burst peaks at $\sim 5 \cdot 10^{53}$ erg/s and the $\bar{\nu}_e$ peaks at $4 \cdot 10^{52}$ erg/s for the spherical symmetric model M1.42-J0. The respective luminosity for the heavy lepton neutrinos ν_x peaks at $2.8 \cdot 10^{52}$ erg/s. For the rest of the models, the electron neutrino luminosity L_{ν_e} peaks between 5.3-0.9$\cdot 10^{53}$ erg/s with lower peak for the high-β model M1.91-J1.63-Dl. As the neutrino luminosities decrease in time, the relative ordering of the luminosities for each models stays the same. The decreasing trend in the luminosities for the rotating models is proportional to the central density at bounce, i.e., the lower -compared to other models- central density at bounce, the lower electron neutrino luminosity. This occurs because the lower central density at bounce implies lower temperatures and thus lower neutrino mean energies. We explain the correlation between central density at core bounce and neutrino signals due to the influence of the corresponding initial rotational profiles, which will be discussed in greater detail in section 5.2.

For the non-rotating model M1.42-J0, the mean energy for electron neutrinos ν_e peaks at 14.8 MeV simultaneously as the maximum luminosity. The mean energy for the electron antineutrinos $\bar{\nu}_e$ peaks at 12.8 MeV, and for the heavy-lepton neutrinos at 17.5 MeV. Note that the maximum values for the ν_e are calculated at the time of the ν_e-burst, while for the rest of the flavors, we chose the maximum value in the first 100 ms. The $\bar{\nu}_e$ mean energy peaks range from 15.8 to 9.7 MeV for the rest of the models. A summary of the maximum values of the luminosity and mean energy of the three neutrino species and for all models can be found in table 5.1.

Figures 5.2 and 5.3 display the total neutrino luminosity (top panels) and the angle-averaged mean energy for electron neutrinos ν_e (solid black line), electron antineutrinos $\bar{\nu}_e$ (dashed red line), and heavy-lepton neutrinos ν_x (dotted blue line) as a function of post-bounce time. Figure 5.2 shows the aforementioned quantities for the non-rotating model M1.42-J0 and the figure 5.3 shows the same for the model M1.61-J0.47. The corresponding figures for the rest of the models can be found in the Appendix in figure A.17 to figure A.20.

If we notice the evolution of the mean energies of each flavor in time (see figure 5.2) for the non-rotating model M1.42-J0, the canonical hierarchy of the mean energies $\langle\epsilon_{\nu_e}\rangle < \langle\epsilon_{\bar{\nu}_e}\rangle < \langle\epsilon_{\nu_x}\rangle$ holds after ∼20 ms. The ordering of the mean energies originates from the fact that neutrinos streamed from regions with higher temperatures, have higher mean energies. The heavy-lepton neutrinos produced in thermal reactions, such as nucleon bremsstrahlung (see section 2.2), originate from a deeper part of the PNS, which is hotter and denser (e.g., Janka, 2017b; Keil et al., 2003; Marek & Janka, 2009). Therefore, since the heavy-lepton neutrinos ν_x come from hotter regions, they have higher mean energies.

For the electron neutrinos, the neutrinosphere, i.e., the region where the neutrinos reach optically thin matter and stream outwards, is located at larger radii than the neutrinosphere of the electron antineutrinos. Once the protoneutron star is formed, it contains neutron-rich material, which results in increased ν_e opacity compared to $\bar{\nu}_e$. Therefore, the neutrinosphere for the ν_e is located further out compared to the neutrino sphere for $\bar{\nu}_e$. Hence, the $\bar{\nu}_e$ flux comes from a deeper and hotter region of the PNS. This explains the fact that electron antineutrino mean energies are higher than the electron neutrino mean energies.

The neutrino properties at core bounce are summarized in table 5.1. Note that the numbers shown there are calculated at core bounce for the electron neutrinos ν_e and in the first 100 ms for the electron antineutrinos $\bar{\nu}_e$, and the heavy-lepton neutrinos ν_x.

The luminosities and mean energies for all neutrino species continue to drop as a function of time as the PNS cools and deleptonizes. However, at late times, i.e., $t > 3$ s, we notice an unexpected rise of the ν_e mean energies (see black line in figure 5.3). This feature occurs in the rotating models at late times, between 3-5 s, and we believe it originates from the low resolution on the neutron star surface. Even though the region that includes the neutron star has a high spatial resolution, at late times, the steep density gradient, particularly at the poles, pushes the numerical modeling to its limits. Thus, we remain cautious

Table 5.1: Summary of the maximum value of the neutrino luminosity and angle-averaged mean energy for ν_e, $\bar{\nu}_e$, and ν_x. The first row shows the maximum central density at bounce (see table 4.1). The neutrino quantities are measured at the peak of the L_{ν_e} for electron neutrinos and in the first 100 ms for the rest of the neutrino species.

Model	$\rho_{\mathrm{max,b}}$ $[10^{14}\,\mathrm{g/cm^3}]$	$L_{\nu_e,\mathrm{max}}$ $[10^{53}\,\mathrm{erg/s}]$	$L_{\bar{\nu}_e,\mathrm{max}}$ $[10^{52}\,\mathrm{erg/s}]$	$L_{\nu_x,\mathrm{max}}$ $[10^{52}\,\mathrm{erg/s}]$	$\langle\epsilon_{\nu_e,\mathrm{max}}\rangle$ [MeV]	$\langle\epsilon_{\bar{\nu}_e,\mathrm{max}}\rangle$ [MeV]	$\langle\epsilon_{\nu_x,\mathrm{max}}\rangle$ [MeV]
M1.42-J0	4.071	4.886	4.019	2.749	14.784	12.771	17.476
M1.42-J0.23-Dl	3.842	5.339	1.812	1.780	14.533	11.890	16.478
M1.61-J0.47	3.188	4.737	1.272	1.049	13.921	13.701	16.488
M1.61-J0.78-Dl	0.498	2.404	0.195	0.208	10.381	10.792	9.244
M1.91-J1.09	2.533	4.860	0.887	0.447	13.123	15.780	12.894
M1.91-J1.63-Dl	0.300	0.881	0.046	0.116	8.363	9.734	7.429

in interpreting the rise of the ν_e mean energies and consider it for further analysis.

5.2 Effect of Rotation on the Neutrino Signal

The main consequence of the rotation in the progenitor models is the formation of an oblate-shaped PNS, reduced luminosities and mean energies for rotating models, and angular-dependent neutrinoshperes. This effect is seen in previous AIC simulations of Dessart et al. (2006), who also found qualitatively same results with our work.

In figure 5.4 the radius of the neutrinosphere for electron neutrinos and electron antineutrinos as a function of the polar angle θ is shown at different points in time for all of the six models. The ν_e and $\bar{\nu}_e$ neutrinospheres are spherical symmetric in the not-rotating model M1.42-J0 and consequently there is no angular variation. On the contrary, the rotating models show a highly angular dependent neutrinosphere for electron neutrinos and electron antineutrinos for all times. Around the poles, the ν_e and $\bar{\nu}_e$ neutrinospheres extend to similar radii (even though always $R_{\nu_e} > R_{\bar{\nu}_e}$) and their respective difference is reduced as time evolves due to the further contraction of the PNS. At the equator, the ν_e neutrinosphere extends at longer radii up to ~ 80 km for some models. This strong angular variation directly impacts the neutrino signals as we discuss later on.

In the rotating models we identify the peak of the neutrinosphere's radius in the mid-latitudes (i.e., around $\sim 50°$). This occurs because the neutrinospheres follow the electron-to-baryon ratio Y_e and influences the angular variation of the ejecta composition. The latitudinal variation of the neutrinospheres affect the latitudinal variation of the ν_e and $\bar{\nu}_e$ number densities and therefore the electron-to-baryon ratio Y_e via their absorption to neutrons and protons, respectively. We elaborate on this effect in the discussion on the ejecta composition in chapter 6.

The rotational effects on the neutrinospheres directly influence the neutrino signals for all neutrino species. From figure 5.1, we can extract two different trends. First and foremost, the less or absence of rotation, the higher the luminosities are across all species.

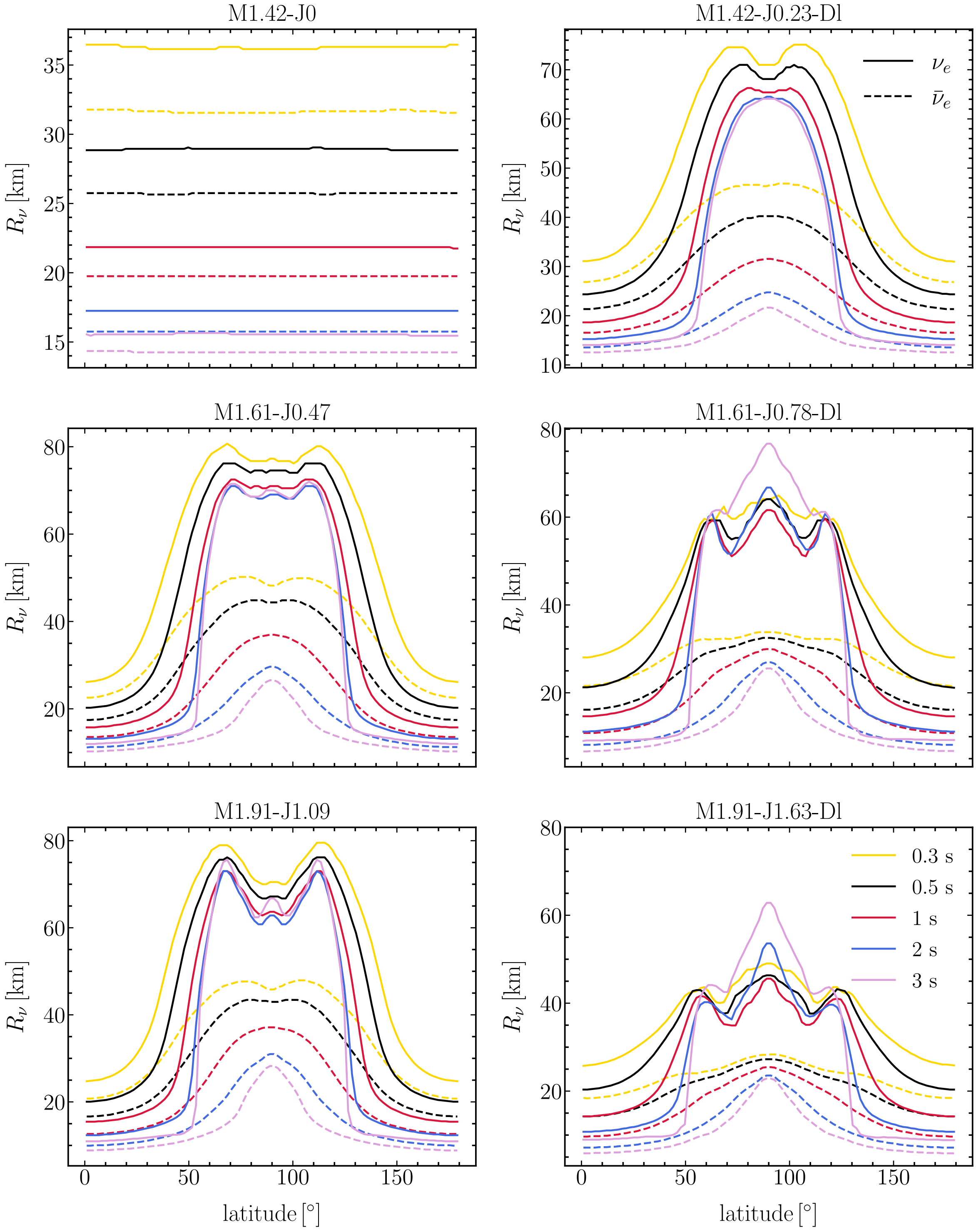

Figure 5.4: Electron neutrino and electron antineutrino neutrinospheres for all of the six models plotted at different times as a function of the polar angle θ. Each colored line corresponds to a specific time from 0.3 s to 3 s post bounce. The solid lines show the neutrinosphere radius for the electron neutrinos ν_e and the dashes lines show the radius for the electron antineutrinos $\bar{\nu}_e$. The neutrinospheres are calculated by the energy-averaged opacities as shown in equation (5.2)-equation (5.4).

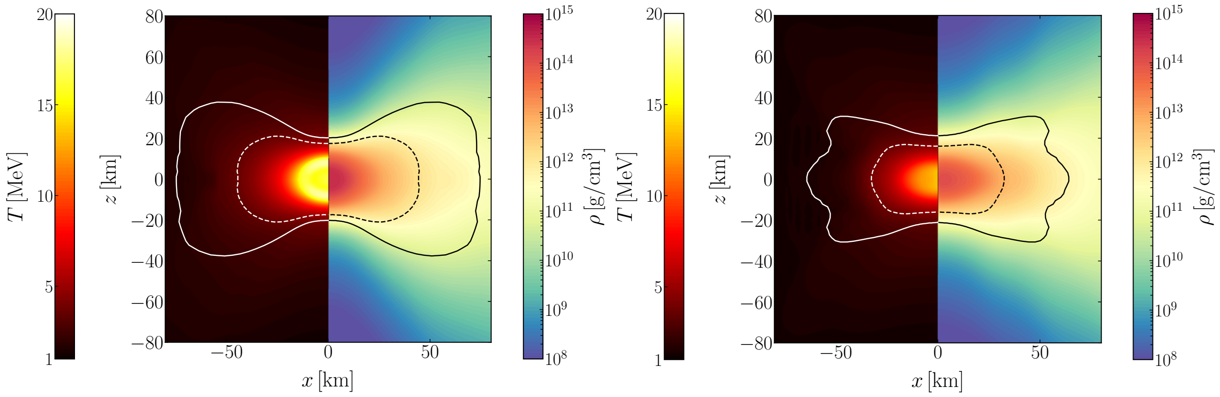

Figure 5.5: The left figure shows a cross-section of the central area of the M1.61-J0.47 AIC model at 500 ms after the bounce. The left panel is color-coded by the temperature and the right panel is color-coded by the density. The solid black/white line determines the neutrinosphere for the electron neutrinos while the dashed line shows the neutrinosphere for the electron antineutrinos. The right figure shows the same quantities for the AIC model M1.61-J0.78-Dl at 500 ms after the bounce. The color bars are chosen in the same range to enhance the different thermodynamical conditions in the core of each model.

From figure 5.1, it is apparent that the non-rotating model shows the highest neutrino luminosities and mean energies across all species. Additionally, the models that undergo a centrifugal bounce (i.e., high-β models) show even lower luminosities in all species, with the lowest showing in model M1.91-J1.63-Dl. Both these trends can be explained with the same argument. The smaller core densities at bounce that are achieved in faster-rotating models lead to lower temperatures in the core, i.e., weaker bounce and, therefore, modest neutrino emission. As we discussed in section 4.1, same-mass models with slower central rotation reach higher central densities at bounce (see table 4.1). In addition, this effect is even more prominent for the models that undergo centrifugal bounce, i.e., models M1.61-J0.78-Dl and M1.91-J1.63-Dl, because of their sub-nuclear core densities at bounce. For example, even if the model M1.61-J0.78-Dl has slower central rotation initially, with an initial central angular velocity of $\Omega_0 = 5.55\,\mathrm{rad/s}$, compared to the rotating model M1.91-J1.09, with an initial central angular velocity of $18\,\mathrm{rad/s}$, the latter model exhibits higher neutrino luminosities across all species. This is explained by the fact that the model M1.91-J1.09 has higher central density at core bounce compared to the model M.161-J0.78-Dl. As a conclusion, we notice that not only the initial rotational profile of the white dwarf has a crucial effect on the neutrino signals, but also the lower central density alters the dynamics of the explosion and therefore impacts as well the neutrino signals.

The reduction of the neutrino luminosities due to rotation is a phenomenon known from CCSN simulations (e.g., Fryer & Heger, 2000). The lower central densities and temperatures of the rotating models can also explain the latitudinal variation of the neutrinospheres (see figure 5.5,figure 5.6). Figure 5.5 shows a cross-sectional cut of the model M1.61-J0.47 (left figure) color-coded by the temperature (left panel) and the density (right panel) as well as for the same-mass model M1.61-J0.78-Dl (right figure). The black/white lines in both figures show the location of the neutrinospheres for the electron neutrinos (solid line)

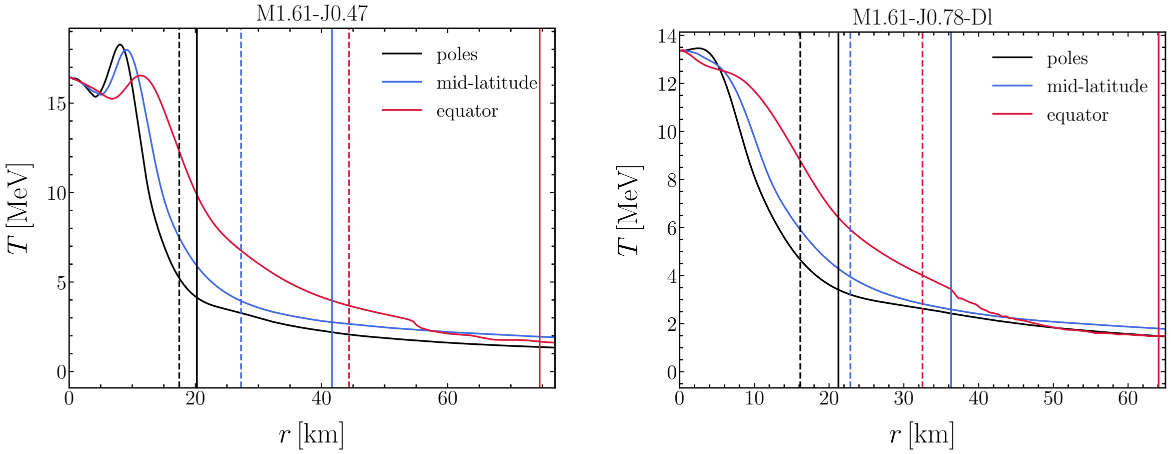

Figure 5.6: Radial profiles of temperature at the poles (black), mid-latitudes (blue), and equator (red) for the rotating model M1.61-J0.74 (left panel), and the high-β model M1.61-J0.78-Dl. Despite the same mass of these models, the different central density and rotational profiles change the temperature profiles across all latitudes. The vertical lines show the radial location of the neutrinosphere for the electron neutrinos (solid lines) and the electron antineutrinos (dashed lines) at the poles (black), mid-latitudes (blue) and equator (red), in both plots.

and the electron antineutrinos (dashed line). The ν_e-spheres are located at 20 km at the poles and extend up to 75 km at the equator for the rotating model M1.61-J0.47. The same-mass model M1.61-J0.78-Dl, which has slower initial central rotation and lower central density, shows neutrinospheres at different radii with the ν_e-sphere to extend to 21 km at the poles and 63 km at the equator. This is seen in figure 5.6, where we present the radial variation of the temperature at the poles (black lines), the mid-latitudes (blue lines), and the equator (red lines). The vertical lines identify the location of the neutrinospheres for the electron neutrinos (solid lines) and the electron antineutrinos (dashed lines), with the colors corresponding to different directions following the temperature-colored lines. The left plot of this figure presents the rotating model M1.61-J0.47 and the right plot the same-mass high-β model M1.61-J0.78-Dl. We find higher temperatures in the ν_e-neutrinosphere at the poles compared to the equator for both models. Additionally, the temperatures at the neutrinospheres for the model M1.61-J0.47, which displays a higher central density at bounce, are larger than the corresponding values for the model M1.61-0.78-Dl.

The discussed effect of the weaker bounce on the luminosity in connection to the rotational profiles of the progenitors introduces the angular variation of the luminosities and mean energies for the rotating models. In figure 5.7, we demonstrate the latitudinal dependence of the neutrino luminosities for the electron neutrinos (solid lines), electron antineutrinos (dashed lines), and heavy-lepton neutrinos (dotted lines). The luminosity for each direction is scaled to the whole surface and corresponds to the total luminosity we would observe if the selected direction were emitted in all directions. The black lines correspond to the polar direction, the blue lines to the mid-latitudes, and the red lines to the equator. Each panel corresponds to one of the six simulated models. Similar to

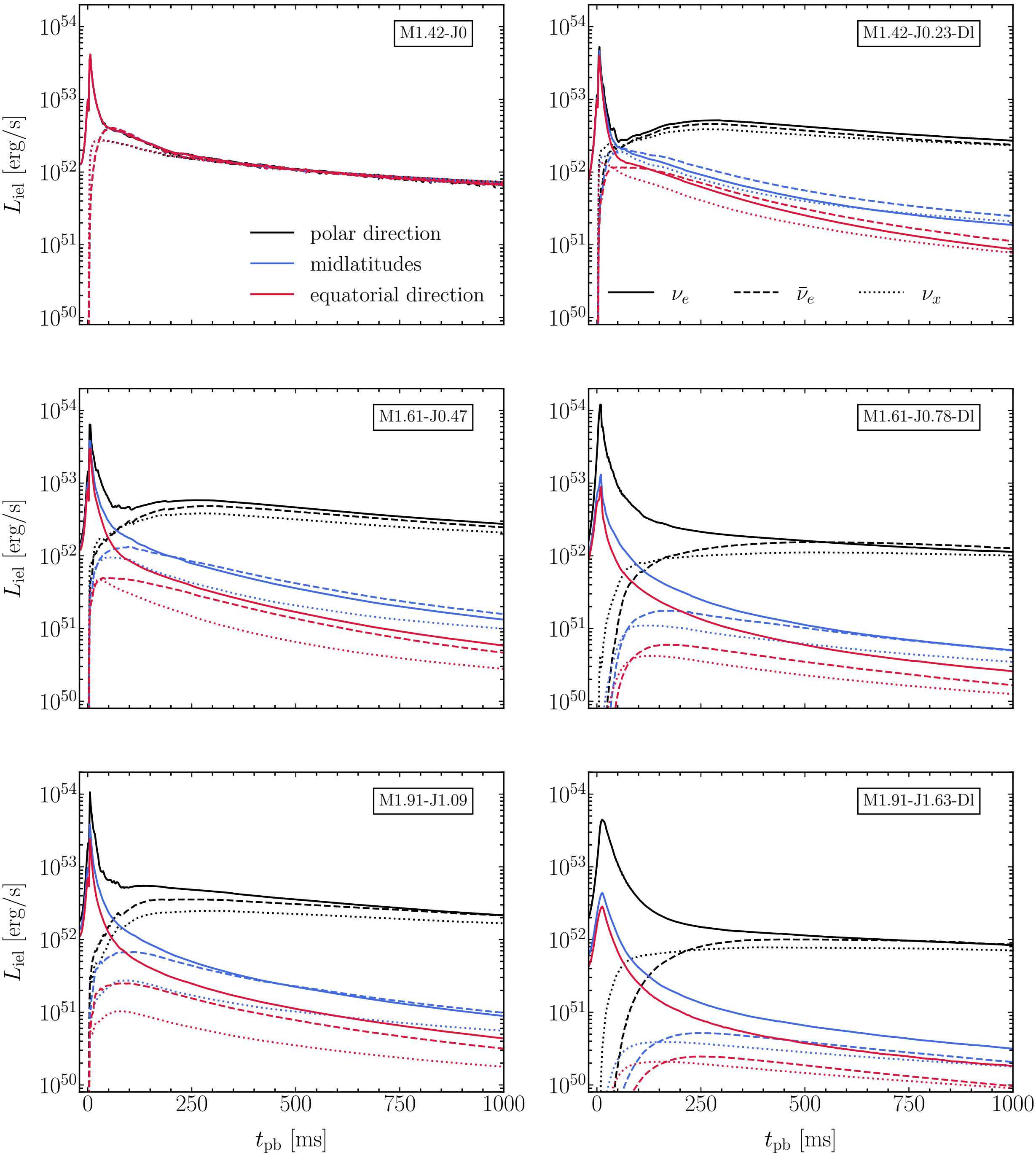

Figure 5.7: Each panel shows the luminosity as a function of post-bounce time along different directions for electron neutrinos (solid lines), electron antineutrinos (dashed lines), and heavy-lepton neutrinos (dotted lines). The black lines show the luminosity along the poles (0°), the blue lines correspond to mid-latitudes around 50°, and the red lines show the luminosity in the equatorial direction (90°). The luminosities are evaluated at a distance of 3500 km, transformed at the lab frame, and they are scaled up to the whole sphere, i.e., the directional luminosity corresponds to the total luminosity we would observe if the selected direction were emitted in all directions (see equation (5.5)). Each panel shows the luminosities for each model that is indicated in the upper left box in each figure. The same figure for longer times is shown in the Appendix in figure A.21.

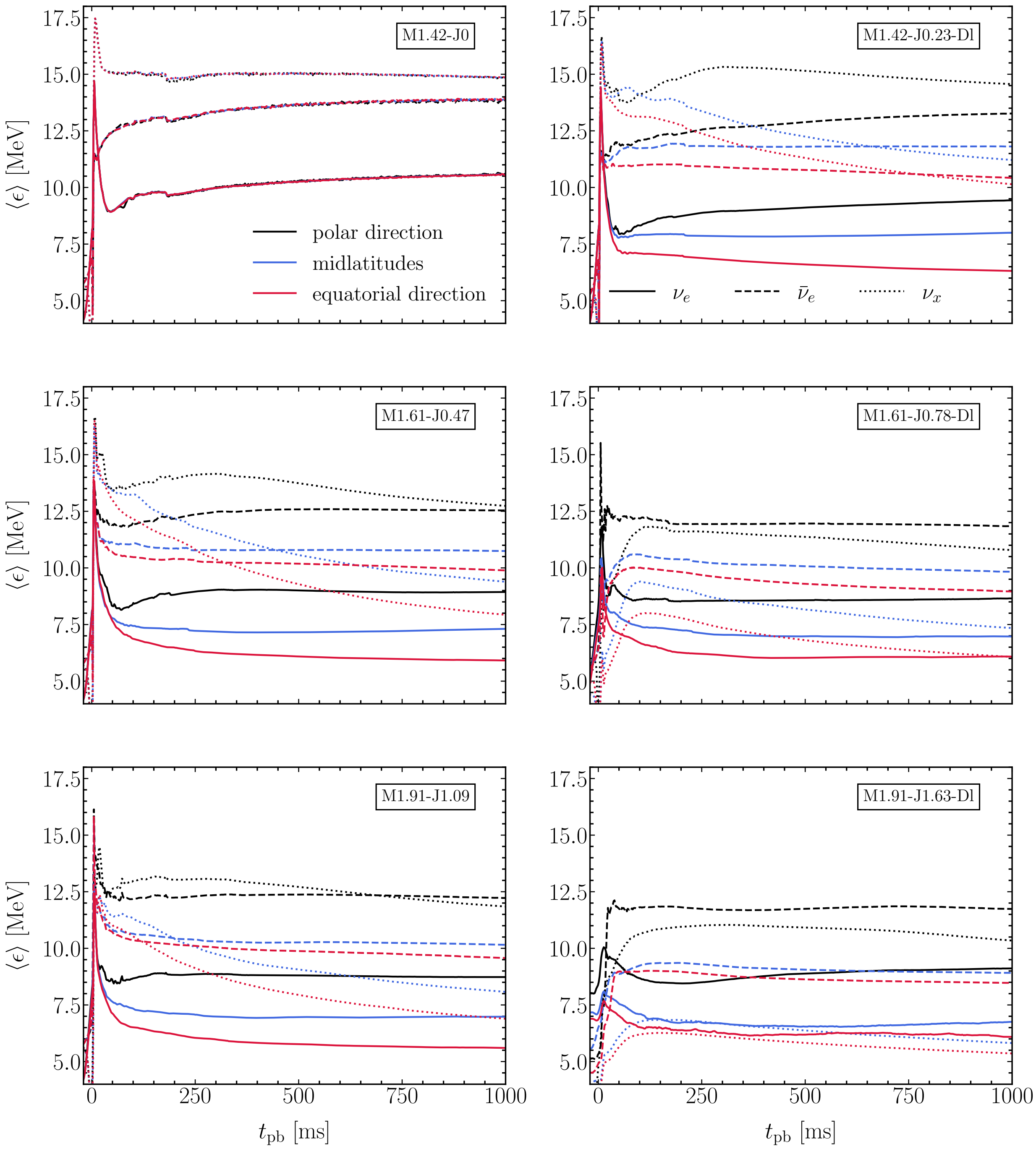

Figure 5.8: Mean energy as a function of post-bounce time angle-averaged in the polar direction (black lines), the mid-latitudes (blue lines) and the equator (red lines). The angle averaged energy is the integrated energy along 10° around 0° for the poles, 50° for the mid-latitudes and 90° for the equator, and scaled up to the whole sphere, in a similar manner as the luminosity. Each panel displays one of the six model as denoted in the corresponding label. The solid lines of each color show the electron neutrinos ν_e, the dashes lines show the electron antineutrinos ν_e, and the dotted lines show the heavy-lepton neutrinos ν_x. The same figure for longer times is shown in the Appendix in figure A.22.

figure 5.1, the luminosities are evaluated in a distance of 3500 km and transformed to the lab frame. To calculate the luminosity an observer would receive in each direction, we define the isotropic-equivalent-luminosity $L_{\rm iel}$ as follows

$$L_{\rm iel} = 4\pi r^2 \frac{\int F^r_\nu dA}{dA}, \tag{5.5}$$

where dA is the surface element in spherical coordinates, i.e., $dA = r^2 sin\theta d\theta d\phi$, and F^r_ν is the radial neutrino flux. The deformation of the central region of the PNS and the neutrinospheres shape manifests in a latitudinal dependence of the neutrino luminosities.

The non-rotating model M1.42-J0 (upper left panel in figure 5.7) does not exhibit any latitudinal variation, which is expected because of the spherical symmetric neutrinospheres that imply the same thermodynamical conditions along all angles. For the rotating models, we notice a variation of the luminosities at the poles compared to the equatorial ones, which exceed one or two orders of magnitude.

In all rotating models, the luminosities at the poles are higher compared to the ones at the equator. The material at the poles is exposed to a broader area of neutrino fluxes due to the very asymmetric shape of the neutrinospheres, extending in shorter radii along the poles and larger radii along the equator (as seen in figure 5.4 and figure 5.5). When neutrinos stream from regions with higher temperatures, they have higher mean energies and a harder spectrum (Dessart et al., 2006). As a result, the neutrino luminosities are higher in the poles due to the higher fluxes, the larger surface of the neutrinospheres and the harder spectrum.

In figure 5.8, we present the latitudinal dependence of the neutrino mean energies for the electron neutrinos (solid lines), electron antineutrinos (dashed lines), and heavy-lepton neutrinos (dotted lines). The deformed neutrinosphere surface explains the angular-dependence of the mean energies. The mean energies follow the same trend as the luminosities because the neutrinos emitted along the poles emerge from regions with higher temperatures. Therefore, we conclude that the mean energies along the poles are higher due to the shorter radii of the neutrinospheres and in the same manner, the mean energies are lower along the equator for all species.

The canonical ordering of the neutrino energies, i.e., $\langle\epsilon_{\nu_e}\rangle < \langle\epsilon_{\bar{\nu}_e}\rangle < \langle\epsilon_{\nu_x}\rangle$ holds for the non-rotating model. However, as observed in the angle-averaged mean energies evolution in figure 5.3, the electron antineutrino mean energy rises above the heavy-lepton neutrino mean energy for the rotating model M1.61-J0.47. The hierarchy of the neutrino energies can be changed to $\langle\epsilon_{\nu_e}\rangle < \langle\epsilon_{\nu_x}\rangle < \langle\epsilon_{\bar{\nu}_e}\rangle$. This is due to the strong angle dependence of the neutrino energies, which is shown in figure 5.8. For a chosen neutrino species, the mean energy is higher at the poles compared to the equator. The angle-averaged mean energies show different trends in different directions. For example, for the model M1.61-J0.47, the angle-averaged $\bar{\nu}_e$ mean energy is larger than the angle-averaged mean energy for the ν_x after $\sim$ 400 ms. However, from figure 5.8 we notice that: $\epsilon_{\bar{\nu}_e} > \epsilon_{\nu_x}$ at the equator after $\sim$ 400 ms and at $\sim$ 300 ms at mid-latitudes, while $\epsilon_{\bar{\nu}_e} < \epsilon_{\nu_x}$ at all times. Similar effects are seen in the rest of the rotating models[2]. Therefore, the angle-averaged mean energies can hide the latitudinal dependence of the mean energies of each neutrino species.

For the high-β models, the trend does not hold. Indeed, the electron antineutrinos have higher mean energies than the heavy-lepton neutrinos. Again, this is explained by the reduced central temperatures of these models that do not allow for efficient $\nu_x\bar{\nu}_{\mathrm{x}}$ production.

The evolution of core density at bounce (see figure 5.5) undoubtedly shows that the density distribution is altered due to rotation, and the temperatures significantly differ in the core from model to model. This is a striking example of how the angular momentum profile and the initial central density dramatically change the thermodynamical conditions in the core and, therefore, the neutrino emission properties. Considering the above, we conclude and confirm that the lower neutrino luminosities and the lower neutrino mean energies are due to the rotational effects on the core structure.

---

[2] rotating models apart from the high-β rotating models

Chapter 6

Ejecta Properties

In this chapter, we discuss the properties of the ejecta from all AIC models. The ejecta is defined as the mass that is expelled from the shock wave, and the neutrino heating after the core bounce is traveling outwards and is unbound (i.e., it has positive total energy[1]). Apart from the white dwarf material that is expelled due to the shock formation, there is additional matter that is driven out by the neutrino heating as the PNS cools; this is what is widely called the neutrino-driven wind; we as consider ejecta, the material that is expelled in both mechanisms. The properties of the ejected material, i.e., neutron excess, entropy, and velocity, are relevant for the nucleosynthesis that occurs in AICs. Even though precise nucleosynthesis calculations of the ejecta are out of the scope of this thesis, the ejecta properties can constrain the tendency of what elements could be formed in AICs, which is essential as a step to future studies.

6.1 Ejecta Mass

Most of the mass ejecta occurs in the first 500 ms as the shock wave drives out material, and the neutrino heating adds on top with the neutrino-driven wind driving additional material from the surface of the PNS. However, there is still mass ejection after 2 seconds which probably comes from material blown away from the semi-Keplerian disk surrounding the newly formed neutron star. For the non-rotating model, there is only $0.04 \cdot 10^{-3}\,\mathrm{M}_\odot$ ejected after 2 seconds out of the total $M_{\mathrm{ej}} = 7.9 \cdot 10^{-3}\,\mathrm{M}_\odot$ that is ejected from this model. The non-rotating model M1.42-J0 ejects less material than the rotating models. However, the non-rotating model forms a neutron star of $M_{\mathrm{NS}} = 1.4\,\mathrm{M}_\odot$, i.e., most of the initial white dwarf mass goes to the neutron star formation and thus leaving a small fraction of the white dwarf mass to be ejected. The same-mass model M1.42-J0.23-Dl, has a much larger ejecta mass with a total of $54.5 \cdot 10^{-3}\,\mathrm{M}_\odot$. This is a slowly rotating model

---

[1] The explosion energy is defined as the sum of the thermal, kinetic, and gravitational energy of one mass element.

Table 6.1: Ejecta mass in units of $10^{-3}\,\mathrm{M}_\odot$ as a function of the ejection time, which is denoted in the second row. The first column lists all the models, and each row shows the amount of mass ejected in the corresponding time interval. We start the calculation when the ejecta breaks out of the progenitor, i.e., at $\sim 0.07-0.1\,\mathrm{s}$ post-bounce time, and we follow the ejection until the end of the corresponding simulation (see table 4.2 second column and legends in figure 6.2) The last column gives the total ejected mass for each model at the end of each simulation. Note that the numbers are rounded in the third decimal.

	$M_{\mathrm{ej}}(t)$ $[10^{-3}\,\mathrm{M}_\odot]$						
t_{pb} [s]	start-0.2 s	0.2-0.3 s	0.3-0.5 s	0.5-1 s	1-2 s	2 s-end	total
M1.42-J0	2.775	2.826	1.167	0.644	0.278	0.037	7.901
M1.42-J0.23-Dl	6.942	9.717	10.346	9.564	6.338	8.781	52.454
M1.61-J0.47	3.324	4.810	5.470	4.823	2.605	4.882	25.914
M1.61-J0.78-Dl	7.194	6.049	3.173	1.732	0.799	2.274	21.221
M1.91-J1.09	3.633	3.042	3.861	2.739	1.406	4.019	18.699
M1.91-J1.63-Dl	0.130	0.149	0.880	1.502	0.984	2.122	5.767

and most of the angular momentum is located in the outer layers of the progenitor (see chapter 3, figure 3.3). Therefore, this model allows for a significantly higher amount of ejecta mass since the material that stays in a quasi-Keplerian disk form is only $0.06\,\mathrm{M}_\odot$. The rest of the rotating models, i.e., the models M1.61-J0.47 and M1.91-J1.09, have total ejecta mass of $25.91 \cdot 10^{-3}\,\mathrm{M}_\odot$ and $18.69 \cdot 10^{-3}\,\mathrm{M}_\odot$, respectively. Models with higher initial angular momentum tend to create larger disks around the PNS and thus present lower ejecta masses, as discussed in chapter 4. The same reasoning explains the ejecta mass of the high-β rotating model M1.61-J0.78-Dl that has a total ejecta mass of $21.22 \cdot 10^{-3}\,\mathrm{M}_\odot$. All models, apart from the high-β rotating model M1.91-J1.63-Dl, eject up to 80% of their respective mass ejecta in the first second of evolution. The high-β model M1.91-J1.63-Dl ejects only $\sim$ 5% of the total ejecta mass in the first 300 ms and $\sim$ 45% of the ejecta in the first second. This is due to the fact that this model forms a heavy ($0.75\,\mathrm{M}_\odot$, see table 4.2) disk around the PNS, and the outflow is driven mostly by the neutrino-driven wind and not the shock wave formed from the centrifugal core bounce which expels only little white dwarf material. This explains why this high-mass model ($1.91\,\mathrm{M}_\odot$) ejects only $5.78 \cdot 10^{-3}\,\mathrm{M}_\odot$. A summary of the ejecta mass as a function of ejected time is shown in table 6.1.

6.2 Composition of the Ejecta

A significant property of the ejecta for each model is the electron-to-baryon ratio (or electron fraction) Y_e, which describes the neutron-richness of the matter and indicates whether heavy nuclei can be synthesized in the AIC events. It is crucial to determine the Y_e range of the ejected material, the mass of the ejecta, and well as how these differ from model to model.

Figure 6.1 shows the ejected mass distribution as a function of the electron fraction Y_e. Each colored line corresponds to one model (see legend for details). We start the calculation

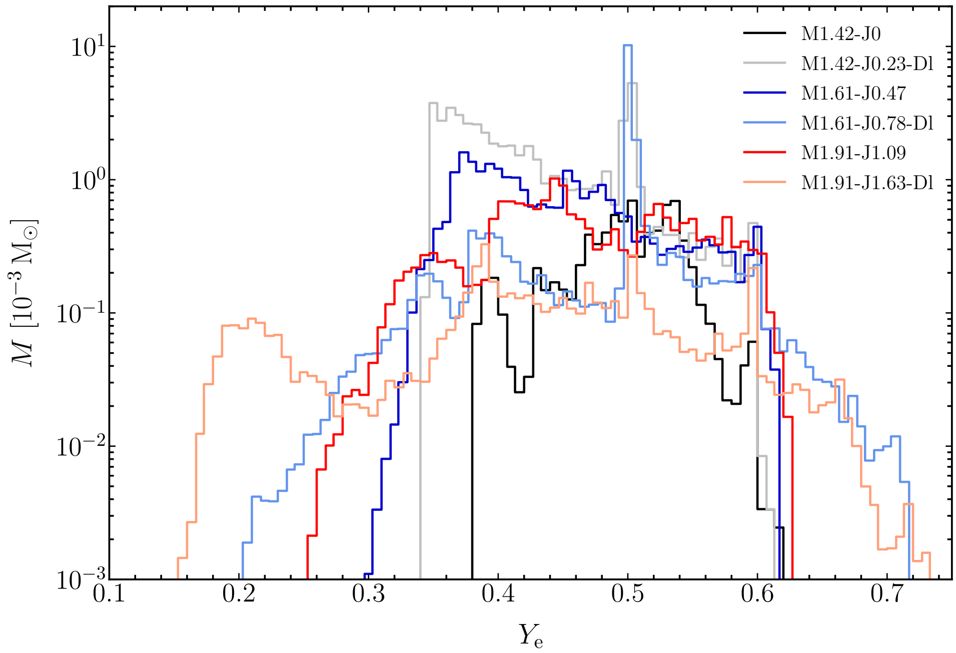

Figure 6.1: Electron-to-baryon ratio Y_e mass distribution of the ejected material. Each colored line shows the distribution of each model as denoted in the legend. The distribution is calculated as the amount of mass that crosses a designated ellipsoidal surface located around each model and has positive explosion energy from $\sim$ 100 ms after bounce until the end of each simulation. Integrating each histogram yield the total ejecta mass for each model. The bin size is the same for all distributions and set to $\delta Y_e = 0.006$.

between 70-100 ms after the core bounce, which is the time that the shock breaks out of the progenitor and carries material to the CSM, and we follow the mass outflow until the end of each simulation which is reached between 5 and 8 seconds. Thus, the histograms display the total mass ejected from each model as a function of Y_e. The Y_e distribution for the ejected mass is evaluated by considering an ellipsoidal surface above each progenitor and calculating the amount of mass that crosses this surface with a positive radial velocity given its positive explosion energy. The ellipsoidal surface is located a few kilometers above the progenitor surface and differs from model to model due to their different radii. Table 6.2 summarises the mass of the ejected material in different Y_e ranges for each individual model. From figure 6.1, we notice that each Y_e distribution and the total mass of the ejecta is unique in shape and on the lower and higher end of Y_e values. The different progenitor mass, initial rotational rates, and subsequent differentiation of the neutrino signal are the main contributing factors in the shape of the Y_e distribution. Figure 6.2 shows the time evolution of the distribution for each model as the ejecta accumulates over time. Each panel demonstrates the neutron richness of the ejected mass for each model, which is denoted in the title of each panel. The different colors are chosen to exhibit the time dependence of the Y_e distribution. As discussed above, the ejecta is calculated as the mass that crosses the chosen ellipsoidal surface with positive radial velocity (i.e., moving outwards) and positive explosion energy. Each histogram is calculated from the point in

Table 6.2: Ejecta mass in units of $10^{-3}\,\mathrm{M}_\odot$ at different Y_e range which is denoted in the second row. The first column lists all the models and each row shows the amount of mass ejected in the corresponding Y_e interval. All quantities are measured at the end of each simulation.

				$M_{\mathrm{ej}}(Y_e)\ [10^{-3}\,\mathrm{M}_\odot]$				
Y_e range	≤ 0.35	0.35-0.4	0.4-0.45	0.45-0.5	0.5-0.55	0.55-0.6	≥ 0.6	total
M1.42-J0	-	0.443	0.799	2.581	3.573	0.496	0.010	7.901
M1.42-J0.23-Dl	1.767	20.772	10.736	8.607	8.309	2.248	0.013	52.454
M1.61-J0.47	0.623	8.007	6.116	6.012	2.599	2.329	0.229	25.914
M1.61-J0.78-Dl	1.043	1.838	1.508	2.130	12.691	1.393	0.617	21.221
M1.91-J1.09	1.333	1.873	5.483	3.251	3.505	2.808	0.446	18.699
M1.91-J1.63-Dl	1.114	0.971	1.037	0.855	0.870	0.394	0.524	5.767

time when the shock breaks out of the surface of the progenitor until the end of each simulation. Each colored histogram shows the Y_e distribution of the mass ejection at a given time interval. Note that each colored histogram is cumulative of the time shown in the legend plus the previous one, which means the excess of the following colored histogram corresponds to the mass ejection at the given time. Thus the last histogram, i.e., the dark blue that shows the mass during the time 2 s-end, shows the additional mass ejected at that time interval.

The early ejecta material that has $Y_e = 0.5$ comes from the white dwarf part that did not receive enough neutrino radiation, and thus its Y_e is not altered. The asymptotic value of the Y_e depends on the competing ν_e and $\bar{\nu}_e$ absorption on neutrons and protons, respectively (e.g., Dessart et al., 2006; Qian & Woosley, 1996). The Y_e of the ejecta is determined by the initial Y_e value of the matter and the different strength of ν_e and $\bar{\nu}_e$ absorption during mass ejection. Specifically, high ν_e mean energy and flux enhances the ν_e absorption via $\nu_e + n \rightarrow p + e^-$ which increases the Y_e making the material proton-rich and high $\bar{\nu}_e$ mean energy and flux enhances the $\bar{\nu}_e$ absorption via $\bar{\nu}_e + p \rightarrow n + e^+$ which lowers the Y_e and therefore producing neutron-rich ejecta. Low-Y_e material with $Y_e < 0.5$ is neutron-rich material while $Y_e > 0.5$ is proton-rich material.

Most of the mass is found in the neutron-rich regime of the Y_e distribution, i.e., $Y_e < 0.5$. Additionally, most of the ejected mass has $Y_e > 0.35$ for all models. This is in contrast to the results found in Dessart et al. (2006), which found most of the ejecta material to have $Y_e < 0.35$. The neutron-rich material we find in some of our models comes from late time ejection after 1 s while the models of Dessart et al. stop after 600 ms after the core bounce. There are two underlying reasons for these differences. First and foremost, in the simulations of Dessart et al. (2006), there is an enforced upper limit in the $Y_e = 0.5$; thus, they cannot get material above 0.5. Apart from that, the difference in the neutrino treatment, in combination with the updated set of neutrino-matter interactions (see section 2.2) in our simulations, lead to more accurate results concerning the neutrino properties and, therefore the Y_e distributions.

As was shown in chapter 4, the Y_e distribution shows a dramatic variability with the polar angular θ (see figure 4.7 to figure 4.10). To understand the Y_e variability, we have

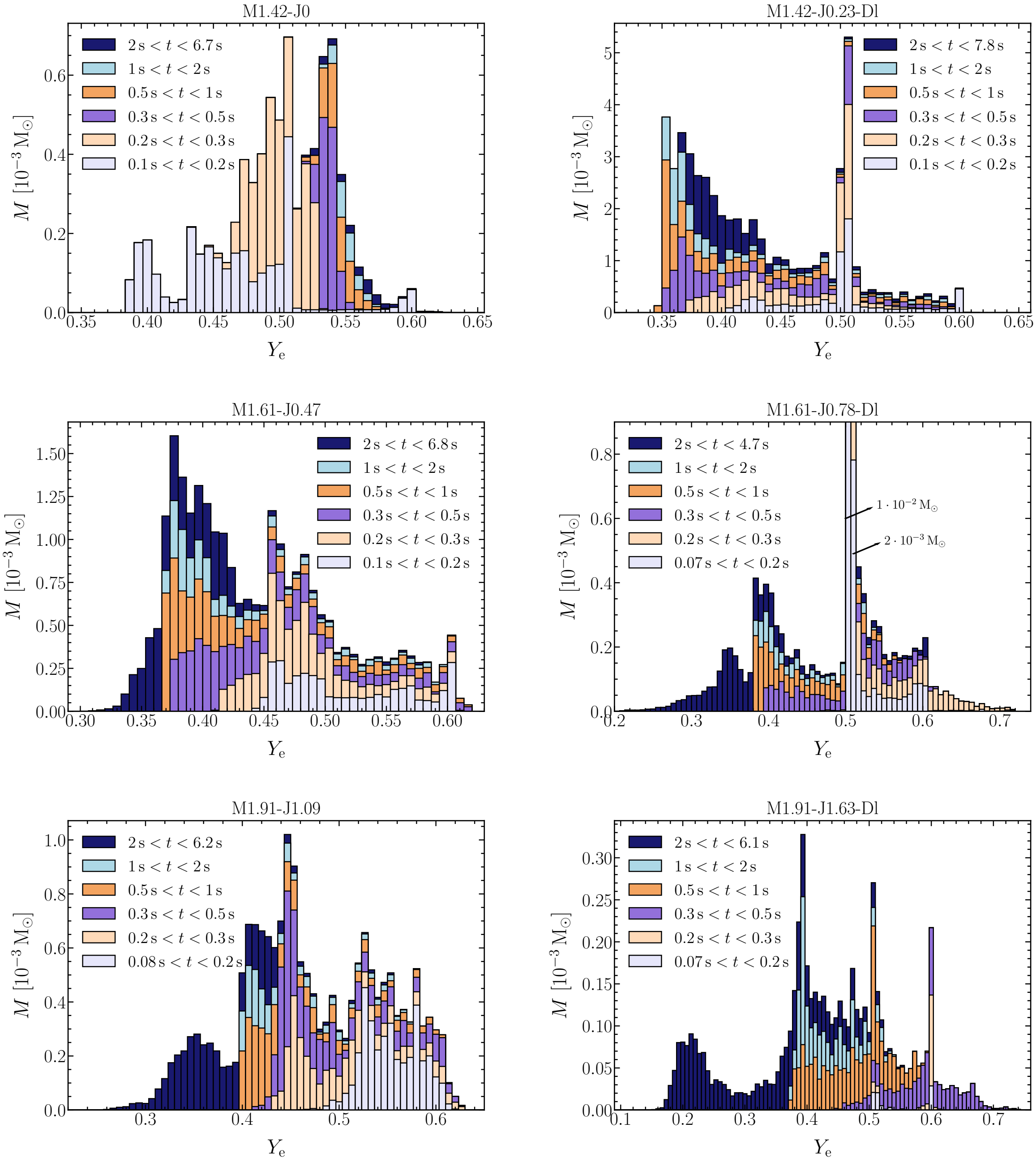

Figure 6.2: This figure is a collection of the Y_e distributions of the ejecta mass. Each panel shows the distribution of the corresponding model which is indicated by the title of each panel. As in figure 6.2, the bin-size is set to $\delta Y_e = 0.006$. The different colors represent different intervals in time at which the mass is ejected with a given Y_e. To be more specific, the distributions built on top of one another show the additional mass that is ejected in each time interval. Thus, the last time interval corresponds to the total ejected mass.

to investigate the mechanism of mass ejection for each model. Material with different Y_e comes from different parts of the progenitor. We should consider not only the different parts of the ejecta origin but also the different times that the ejecta is expelled. Table 6.2 summarizes the ejecta mass M_{ej} at the end of each simulation in the outflow at a given time interval following the rough time-dependence of the ejection is shown in the corresponding colored histograms in figure 6.2.

6.3 Effect of Rotation on the Ejecta Composition

From our discussion so far, it is clear that the specific rotational profile of each progenitor model has significant consequences on the explosion dynamics, neutrino signals, and outflow. In order to comprehend the mass contribution in different Y_e ranges, we look into the inner region of each model and the angle dependence of the mass, radial outflow velocity, and Y_e of each model at different times.

Figure 6.3 and figure 6.4 show the ejecta mass, velocity, and Y_e as a function of the polar angle θ for different times during the evolution of the ejecta. Each row corresponds to each model, with the left panels showing the ejecta mass M_{ej} per 10°, the middle panels displaying the mass-averaged radial velocity of the ejecta, and the right panels the mass-averaged Y_e, as a function of the polar angle. We calculate each quantity at an ellipsoidal surface in the same way we calculate the Y_e distribution of the mass ejecta in the histograms shown in figure 6.1 and figure 6.2. The radial velocity and the Y_e are mass-averaged for each time interval and each angular bin. Note that $Y_e = 0$ means there is no outflow in that angular bin.

Non-rotating model

The first row of figure 6.3 shows the ejecta properties for the non-rotating model M1.42-J0. The outflow develops spherically symmetric since the shock wave is spherically symmetric due to the absence of rotation. At the beginning of the shock propagation, the slight variance of the angular velocity along the polar angle θ (black and orange lines in figure 6.3; 1st row) imprints the convection activity in this model (see figure 4.6). The pattern is lost as the outflow propagates in the CSM.

At early times, neutron-rich material from the collapsed white dwarf is ejected. A negative entropy gradient is developed by neutrino heating around the PNS, leading to a short convection period (see, figure 4.6). Thus, accretion downflows are neutrino heated near the newly formed PNS and then quickly accelerated outwards. Neutron-rich material from the conversion of protons to neutrons dominates the early ejecta with Y_e as low as ~ 0.37. At later times the ν_e absorption raises the Y_e of the ejecta above 0.5. The Y_e distribution of the non-rotating model is similar to the Y_e distribution expected from ECSNe (Wanajo et al., 2011, 2018). Specifically, Wanajo et al. (2011) found Y_e distribution in the range $Y_e \sim 0.404 - 0.55$, marginally narrower than the one found in our non-rotating model.

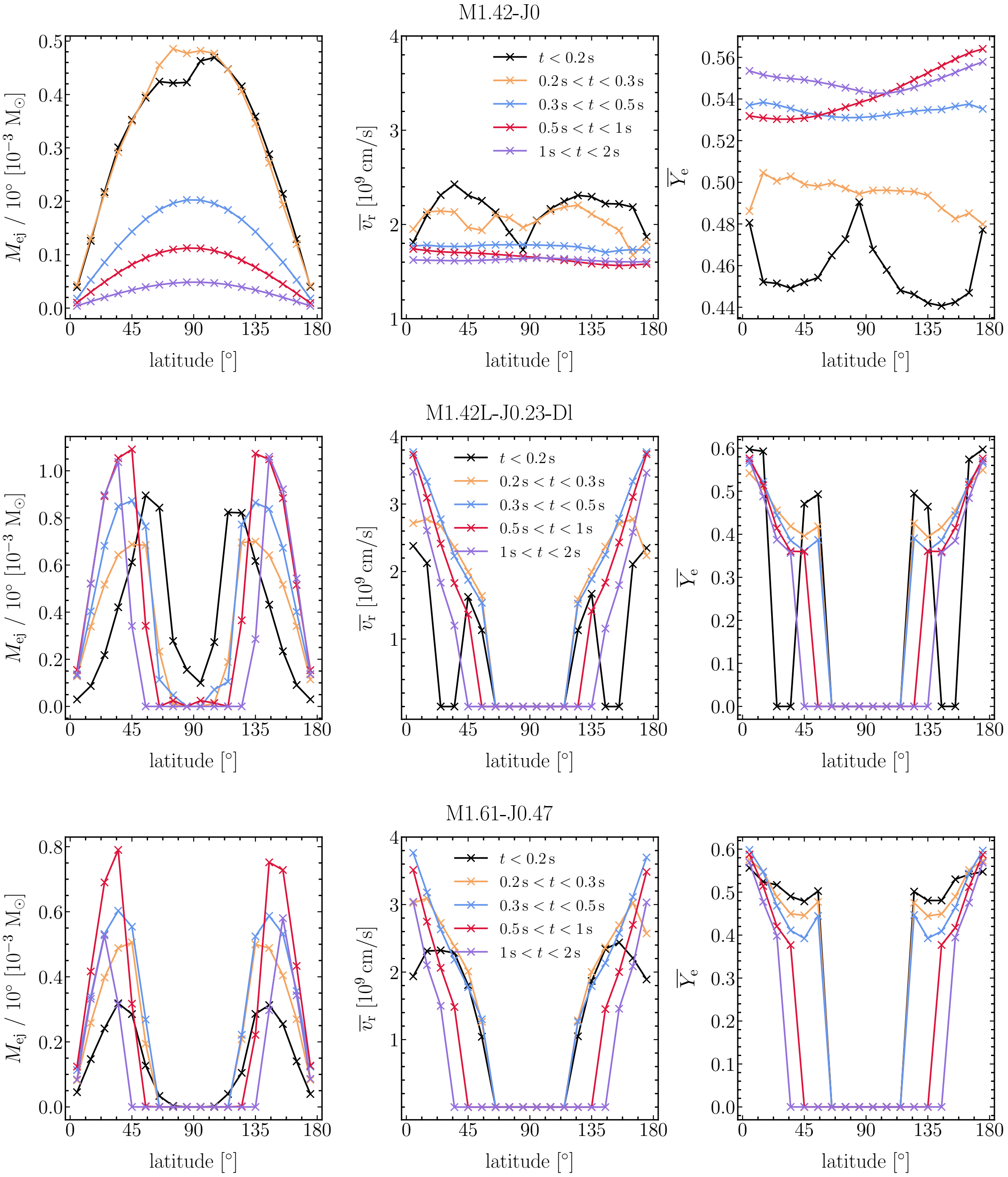

Figure 6.3: Mass-averaged ejecta properties as a function of the polar angle θ. Each row shows the properties for each model; the first row shows the spherical-symmetric model M1.42-J0, the middle row shows the rotating model M1.42-J0.23-Dl, and the bottom row the model M1.61-J0.47. For each row the left panel shows the angle-averaged (in 10° bins) mass ejecta as a function of latitude, the middle panels show the mass-averaged radial velocity of the ejecta, and the right panels show the mass-averaged Y_e. The different lines present the different time intervals; black lines show the ejecta before 200 ms after bounce, the orange lines between 200 and 300 ms, the blue lines between 300 and 500 ms, the red lines between 500 ms and 1 s, and the purple lines between 1 and 2 s post bounce. The mass ejecta properties are measured as the matter that crosses an ellipsoidal surface that is located around the progenitor in the same way as in the Y_e histograms in figure 6.1 and figure 6.2.

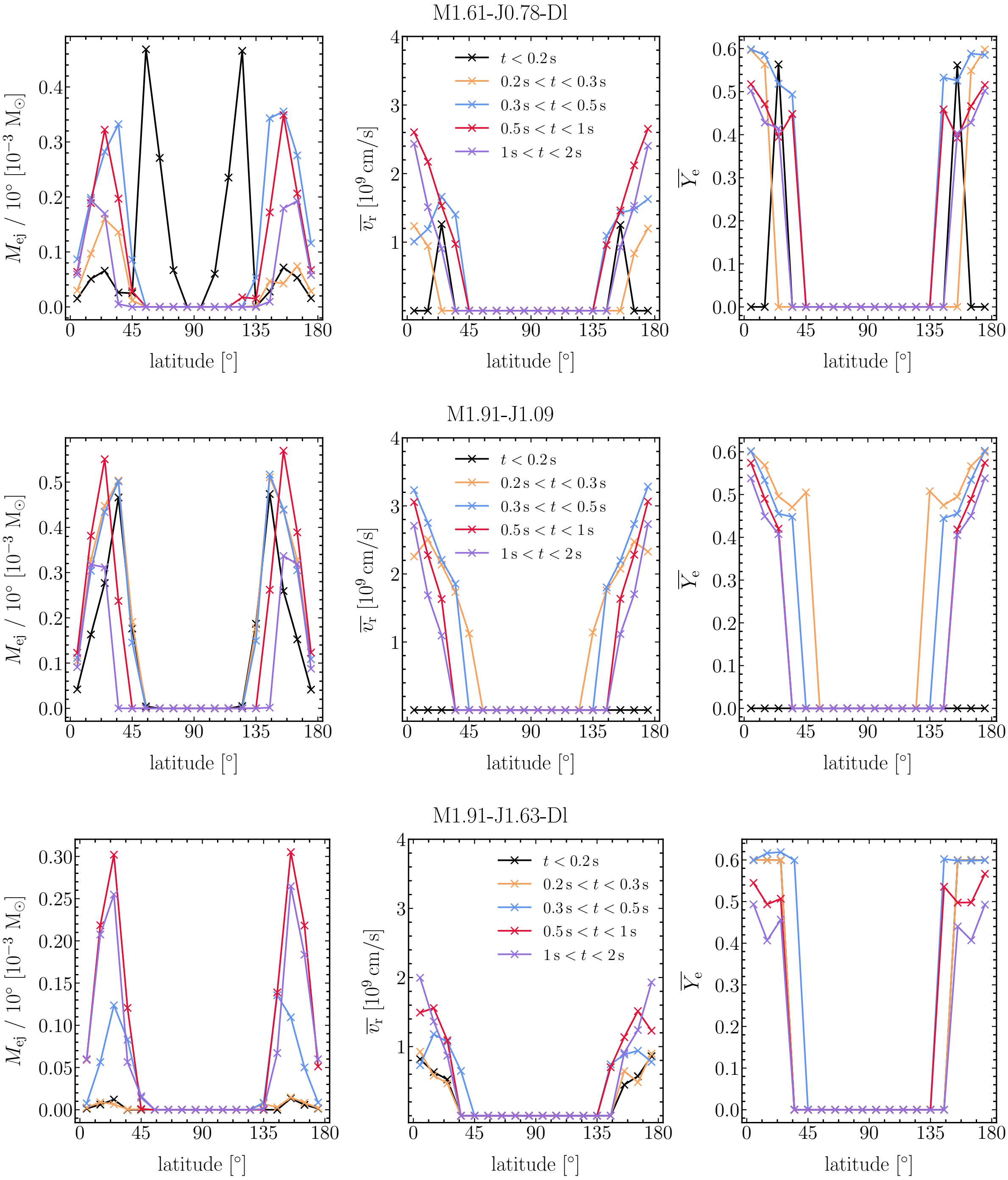

Figure 6.4: Mass-averaged ejecta properties as a function of the polar angle θ, same as in figure 6.3. Here the models M1.61-J0.78-Dl, M1.91-J1.09, and M1.91-J1.63-Dl are displayed.

Rotating models

In the rotating models, the Y_e range seen in the histograms (figure 6.2) strongly depends on how the outflow develops. As we discussed in section 4.2, in the rotating models, a rotationally supported disk is formed around the PNS, which constrains the outflow in the polar direction with an angle opening of $\theta \sim 45^{\circ}$[2]. The distinguished shape of the neutrinospheres and the angular dependence of the neutrino luminosities and mean energies are the fundamental reasons that give rise to the latitudinal Y_e variation. As shown in section 5.2, the luminosities of electron neutrinos and electron antineutrinos are higher at the poles than their equator values. Furthermore, the electron antineutrinos are produced deeper in the PNS core, and their corresponding neutrinosphere has smaller radii (see figure 5.4) and thus higher mean energies since they are streamed out of a hotter region of the PNS, compared to the electron neutrinos. The higher neutrino luminosities along the poles raise the Y_e material above 0.5. This is an outcome of the ν_e neutrinosphere shape, which has small radii along the poles and extends up to 80 km at the equator. Therefore, the ejected material mainly comes from the polar region in the rotating models and is exposed to a larger neutrino flux in the polar direction. The same reason contributes to reduced electron neutrino luminosities in the equatorial region. The high Y_e of the polar regions in the rotating models is reflected in figure 6.3 and figure 6.4.

At later times, i.e., $t \geq 1\,\mathrm{s}$, the number density of ν_e is reduced, and the ratio of the electron neutrino and electron antineutrino number densities $n(\bar{\nu}_e)/n(\nu_e)$ is close to unity. For (almost) similar number densities of ν_e and $\bar{\nu}_e$, the strength of their respective absorption to neutrons and protons depends on the individual mean energies. At the poles, the ν_e and $\bar{\nu}_e$ neutrinospheres have the same radii, which implies that the ν_e and $\bar{\nu}_e$ are streaming from a same-temperature region and that they have the same mean energies. This leads to a favored ν_e absorption via $\nu_e + n \rightarrow p + e^-$, which leads to the increase of the Y_e in the poles. The last process is easier than the $\bar{\nu}_e$ absorption on protons because the neutron has a higher mass than the proton.

The evolution as mentioned above can be seen in figure 6.5 where we show the density (upper left panels), electron fraction Y_e (upper right), the $n(\bar{\nu}_e)/n(\nu_e)$ ratio (bottom right), and the ν_e number density (bottom right), for four points in time. In figure 6.5, the rotating model M1.91-J1.09 is displayed as a representative case for the rotating models. The same plots for the rest of the models can be found in the Appendix in figure A.23 - figure A.27.

The ν_e neurtinosphere, seen in solid lines in figure 6.5, follows the neutron-rich and low-Y_e shape, which extends to larger radii in mid-latitudes. From the exact figure, we can infer that the low-Y_e material seen in the Y_e distribution of the ejecta comes from the mid-latitudes. Away from the poles, the electron neutrino number density is reduced, and the $n(\bar{\nu}_e)/n(\nu_e)$ increases. Therefore, at mid-latitudes, the reduced ν_e absorption (i.e., relative higher $\bar{\nu}_e$ absorption) gives rise to the neutron-rich tail of the Y_e distribution seen in the rotating models (figure 6.2).

---

[2] The polar angle θ is measured from the rotational axis which is perpendicular to the equatorial plane of each model.

One exception is the high-β rotating model that shows mass ejecta with Y_e down to 0.2. The same effect of the low-Y_e ejecta from the mid-latitudes still holds for this model. However, at late times there is additional neutron rich outflow from the polar regions. However, we caution that insufficient resolution may have affected this model. In particular, the amount of mass around $Y_e = 0.2$ could be affected by the increase of the ν_e and $\bar{\nu}_e$ mean energies at late times due to the insufficient resolution at the polar regions. In fact, the very steep density gradient at the poles would require finer zoning to capture the relevant physics with acceptable accuracy. This does not affect the rest of the models that develop a neutron-rich outflow at mid-latitudes.

6.4 Nucleosynthesis Implications from the AIC Ejecta

Even though detailed nucleosynthesis post-processing that would give the exact yields from AICs is out of the scope of this thesis, the Y_e distributions can indicate the nucleosynthesis expectations. There has been a debate on the extent of the contribution of AICs to heavy-element production and, in particular, if AICs are r-process sites (Dessart et al., 2006; Ehring et al., 2023; Fryer et al., 1999; Qian & Wasserburg, 2007).

Rapid neutron capture, i.e., r-process, nucleosynthesis, can explain most of the stable neutron-rich elements heavier than iron (Fe) (Burbidge et al., 1957; Cameron, 1957). Since the last decade, there has been a significant shift and increased understanding of the astrophysical sites that might be important for r-process nucleosynthesis. With advanced numerical modeling in CCSNe, the idea that neutrino-driven winds from CCSNe are a candidate for r-process nucleosynthesis is now abandoned (Fischer et al., 2010; Hüdepohl et al., 2010; Roberts et al., 2010; Wanajo et al., 2018). Numerical simulations of neutron star mergers show that the ejecta from such events fulfills the conditions to produce r-process elements (e.g., Bauswein et al., 2013b; Freiburghaus et al., 1999; Just et al., 2015a; Kasen et al., 2017; Rosswog et al., 2014; Wanajo et al., 2014). With the recent observation of the double neutron star merger that was detected in gravitational waves as GW170817 (Abbott et al., 2017) and in the electromagnetic spectrum as AT2017gfo (Tanvir et al., 2017), it is now confirmed that neutron star - neutron star mergers are sites of r-process nucleosynthesis.

Neutron-rich ejecta with $Y_e \leq 0.25$ can synthesize lanthanites and heavier elements (Lippuner & Roberts, 2015). In our work, for all models, most of the mass is ejected with $Y_e > 0.35$, which sets severe constraints in the r-process nucleosynthesis from AICs. Late-time ejecta from the disk surface show low Y_e around 0.2 could form r-process material. However, this is only relevant for $\sim 0.45 \cdot 10^{-3}\,\mathrm{M}_\odot$ of the ejecta and is found only in one model that develops a large disk around the PNS.

Our results do not indicate strong r-process nucleosynthesis. Instead, middle-range elements with atomic numbers $A \simeq 60 - 110$, are more likely to be synthesized. Therefore, with our AIC modeling, we predict that the synthesized material can populate the first r-process peak and bearly reach the second r-process peak. Additionally, AICs are not

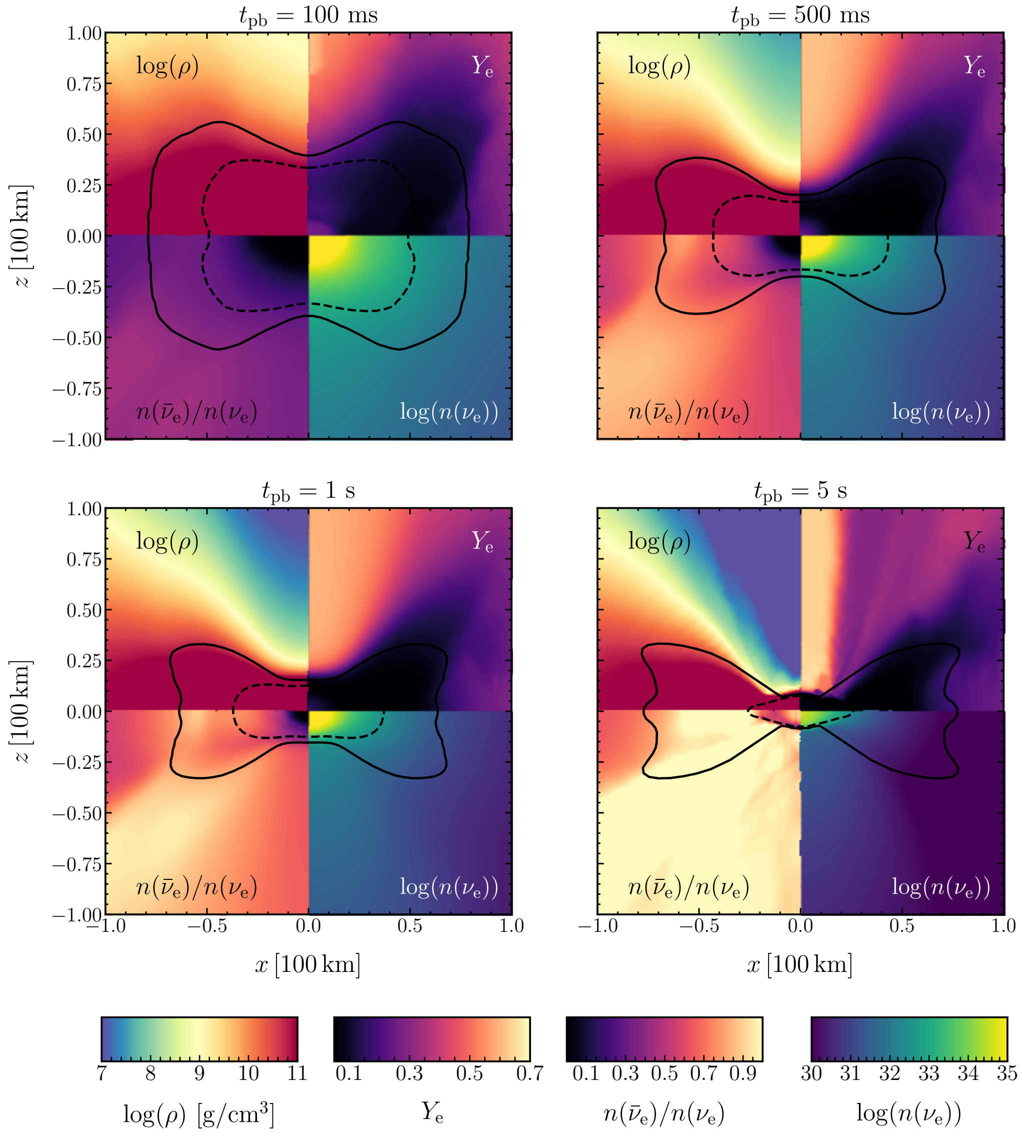

Figure 6.5: A collection of cross sectional cuts at different points in time, color-coded by four different quantities. In each plot, that represents one point in time shown in the title of each plot, the left upper panel shows the logarithm of the density, the right upper panel shows the electron fraction Y_e, the bottom left shows the ratio of the electron antineutrino number density to the electron neutrino number density, i.e., $n(\bar{\nu}_e)/n(\nu_e)$, and the right bottom panel shows the logarithm of the ν_e number density. The same figure for the rest of the models can be found in the Appendix in figure A.23 - figure A.27.

expected to produce heavy elements above the second r-process peak, such as lanthanides.

This could raise implications in the conclusions drawn by Gillanders et al. (2020), who excluded the AIC as a potential scenario to explain the transient AT2018kzr. Gillanders et al. and McBrien et al. disregard the AICs because their analysis does not fit the bulk composition predicted by previous studies that suggest r-process element production from AICs (Dessart et al., 2006; Fryer et al., 1999). However, our models, contradicting strong r-process, could match the bulk composition found in Gillanders et al. (2020) and McBrien et al. (2019). For conclusions and a strong argument in favor of an AIC explaining the transient AT2018kzr, detailed post-processing of the nucleosynthesis is required.

Chapter 7

Summary and Conclusions

The accretion-induced collapse (AIC) of white dwarfs to neutron stars is an alternative evolutionary scenario for accreting white dwarfs, apart from SN Type Ia. Accretion of mass from a companion star, associated with considerable amounts of angular momentum, can push the white dwarf to its Chandrasekhar mass limit, or the white dwarf can collide and merge with a white dwarf companion. Both scenarios can lead to nuclear burning and a subsequent runaway in a thermonuclear explosion, i.e., a type Ia SN. Alternatively, electron captures on free nuclei and nucleons at sufficiently high densities in the interior of the white dwarf can trigger gravitational instability and the collapse of the white dwarf to a neutron star in a so-called accretion-induced collapse event (Nomoto & Kondo, 1991; Schwab et al., 2015).

At sufficient high densities and temperatures, electron captures are initiated, and the white dwarf loses pressure support from the degenerate electrons, and implosion is stopped when the density of nuclear matter is reached. The sudden halt of the infall at the moment of "core bounce" leads to the generation of a quickly expanding shock wave, in the wake of which a small fraction of the white dwarf's matter is blown out as a "wind" powered by the energy transfer from the vast flux of neutrinos radiated by the hot PNS which is formed in the center. Thus, the outcome of AICs is a neutrino-driven and fast outflow, a newly formed neutron star, and in the case of rotating white dwarfs, a semi-Keplerian disk around the neutron star (Dessart et al., 2006; Fryer et al., 1999; Woosley & Baron, 1992).

The AICs are an alternative scenario for neutron star formation, are thought to explain transients that do not fit the standard scenarios of stellar explosion (Gillanders et al., 2020; McBrien et al., 2019), and also be a source of heavy element nucleosynthesis (e.g., Fryer et al., 1999; Metzger et al., 2009a). It is crucial to study AICs with numerical simulations involving all the relevant physics (i.e., matter-neutrino interaction, EoS, etc.) and follow the evolution of the object until the homologous expansion of the ejecta. This is a required step in order to be able to make any observational predictions and connect the theoretical modeling with the observations.

In this thesis, we investigate the accretion-induced collapse of white dwarfs using axisymmetric neutrino-hydrodynamics simulations for six non-rotating and rotating AIC models from the onset of the white dwarf collapse through core bounce and the expansion of the ejecta for several seconds. Our pre-collapse configurations were computed in rotating equilibrium (Abdikamalov et al., 2010; Ehring, 2019). Even though our initial models do not result from stellar evolution calculations, they represent physically motivated pre-collapse conditions for AICs. We employ the fully multi-dimensional, multi-energy-group neutrino transport code ALCAR with a state-of-the-art description of the neutrino interactions and a modern nuclear equation of state (Just et al., 2018, 2015b; Steiner et al., 2013).

Results

All models collapse on a dynamic timescale depending on the initial central density. The unique rotational and density profile of each model alters the collapse. In two models, we find structures that reach $\beta \leq 13\%$ at bounce, where β is the ratio of the rotational to the gravitational energy $T/|W|$. The high-β models do not reach nuclear saturation densities in their cores at collapse because the core becomes rotationally supported, and these models undergo centrifugal bounce. The non-rotating model and the rest of the rotating models undergo pressure bounce due to the stiffening of the EoS and rise of the adiabatic index similar to CCSNe.

We find neutrino-driven outflows with modest explosion energies of the order of $\sim 10^{50}$ erg, which is one order of magnitude lower than the typical energy for CCSNe. The explosion energy reflects the amount of mass ejected by each model. Rotating models have higher explosion energy with higher ejecta mass which scales inversely with the total angular momentum of each model. Specifically, models with high initial angular momentum develop a rotationally supported disk around the neutron star, leaving little mass to be ejected. Therefore, models with high initial angular momentum that create heavy disks and have lower ejecta mass show lower explosion energies. The lower explosion energy of the order of $\sim 10^{49}$ erg is found in the high-β models M1.61-J0.78-Dl and M1.91-J1.63-Dl. The highest explosion energy is found in the model M1.42-J0.23-Dl with an explosion energy of $3 \cdot 10^{50}$ erg. In AICs, no canonical explosion energy is inferred from our models due to the large spread from model to model. The under-energetic explosions from AICs and the variety of explosion energies based on the exact dynamics could increase the difficulty of their detection.

The neutron stars formed in our AIC models range from $1.1\,\mathrm{M}_\odot$ to $1.4\,\mathrm{M}_\odot$. The exception is the high-β model M1.91-J1.63-Dl with a neutron mass as low as $0.96\,\mathrm{M}_\odot$. However, the model mentioned above forms a heavy disk of $0.75\,\mathrm{M}_\odot$, which is expected to be partially accreted and thus increase the neutron star's mass. The neutron stars formed in rotating AICs are oblate-shaped, with the minimum radius reaching 10% of the maximum radius of the neutron star.

The shock wave, formed after the collapse of the white dwarf, ejects material from the outer layers of the white dwarf. In addition, the neutrino-driven wind ejects additional material from the surface of the PNS. These two mechanisms create the neutrino-driven outflow of AICs. In the rotating models, the outflow is constrained around the polar region because of the formed disk stays centrifugally stabilized around the neutron star. Our models yield ejecta masses up to $10^{-2}\,\mathrm{M}_{\odot}$ for the rotating models. The non-rotating model has a low ejecta mass of $8 \cdot 10^{-3}\,\mathrm{M}_{\odot}$ since most of the white dwarf mass goes into the creation of a neutron star with a mass of $1.4\,\mathrm{M}_{\odot}$. The other extreme comes from the high-β model M1.91-J1.63-Dl that ejects only $6 \cdot 10^{-3}\,\mathrm{M}_{\odot}$. Despite the low ejecta mass, the neutron star of this model also has a very low mass, in contrast to the non-rotating model. In this case, the low ejecta mass is a consequence of the heavy disk formed in this model.

The initial rotation of each model results in a highly deformed density profile in the center, which gives rise to oblate-shaped neutron stars. Moreover, the ν_e and $\bar{\nu}_e$ neutrinospheres, which are the approximate regions that ν_e and $\bar{\nu}_e$ decouple from the stellar matter and stream outwards, show a strong latitudinal dependence. In fact, in all rotating models, the polar radius of the neutrinosphere is much shorter than the equatorial. This results in angular-dependent neutrino luminosities and mean energies for all neutrino species.

The highly asymmetric neutrino emission subsequently develops angle-dependent outflow properties, such as density, electron-to-baryon ratio, and entropy. The latitudinal variation of the outflow properties impacts the observed signal from AICs. Specifically, we find proton-rich outflow in the polar direction and neutron-rich ejecta at mid-latitudes for the rotating models. This is a direct consequence of the unique neutrinosphere shape due to rotational effects and angular-dependent neutrino properties. The latitudinal dependence of the electron-to-baryon ratio Y_e will affect the nucleosynthesis in different directions causing angle-dependent spectra. This leads to the conclusion that the electromagnetic signal observed by AICs is strongly subject to the observer's line of sight toward the object.

We find that the ejecta composition for the non-rotating model is similar to what is expected by ECSNe. In contrast, the rotating models show a wider Y_e distribution of the ejecta mass with proton-rich material up to $Y_e \sim 0.7$ and neutron-rich material as low as $Y_e \sim 0.2$. However, most rotating models expel little to no material with $Y_e < 0.3$. This constrains the indications of strong r-process nucleosynthesis. We only find $\sim 20\%$ of the total ejecta with $Y_e \sim 0.2$ in one of the simulated models under particular circumstances, including late time outflow from the disk's surface. This concerns the model M1.91-J1.63-Dl which forms a very low mass neutron star (i.e., $0.96\,\mathrm{M}_{\odot}$) and a heavy disk around it. A summary of the most significant quantities for our simulations are summarized in table A.1 in the Appendix.

Summary

In this thesis, we investigated the accretion-induced collapse of white dwarfs to neutron stars. We performed neutrino-hydrodynamics simulations of six non-rotating and rotating

AIC models in axisymmetry with varying masses, rotational rates, and angular momentum profiles of the progenitor models. Our models cover, for the first time, the evolution from the onset of the white dwarf collapse until the late stages of the PNS cooling and ejecta evolution for up to $\sim 5-8\,\mathrm{s}$. The individual initial rotational profile of the progenitor is a crucial factor that influences the explosion dynamics and the ejecta and neutron star properties. In particular, our calculations show how rotation creates an angle variation on the electron-to-proton fraction Y_e, which is significant for nucleosynthesis. We demonstrated that AICs produce neutrino-driven outflows and are under-energetic events with low explosion energies in the range $0.1-3\cdot 10^{50}\,\mathrm{erg}$. Our models yield outflows with total ejecta mass $\sim 10^{-2}\,\mathrm{M}_\odot$ with a large spread in the Y_e distribution and disfavor strong r-process nucleosynthesis.

Outlook

Our numerical simulations provide long-evolution AIC models for various progenitor initial conditions that can be further used to bridge the gap between theoretical modeling and observational predictions.

Our models can be used for post-processing in terms of nucleosynthesis. Heavy element production in the Universe is significant in comprehending the abundance of the elements in our solar system and beyond. Furthermore, identifying the astrophysical nucleosynthetic sites, such as AICs, is essential for our Galaxy's chemo-galactic evolution. Therefore, a natural next step of our study is to perform nucleosynthesis calculations for the AICs ejecta and determine which elements can be synthesized in these systems.

The element production from AICs could also be used to identify the rates of AICs and therefore limit the neutron star birth from this channel. Additionally, our models can be employed in calculating the electromagnetic signal we could expect from AICs. With the increasing number of transient observations and observatories, such as the Zwicky Transient Facility (ZTF), we expect to identify more low-luminosity transients soon. The modeling of the expected signal from AICs will assist in the search and confirmation of such events for the first time.

Last but not least, AICs are sources of gravitational waves. The prediction of the gravitational wave signal from AICs, mainly using our rotating models, is crucial as future detectors, such as the Laser Interferometer Space Antenna (LISA), could detect the AICs independently of their electromagnetic signal.

Appendix **A**

Appendix

In this appendix we provide additional figures as supplementary material to the main thesis. The content of the figures have already been discussed in the main text. The following material is used for completeness and concerns the chapter 4, on the AIC dynamical evolution, chapter 5, and on the ejecta composition discussed on chapter 6.

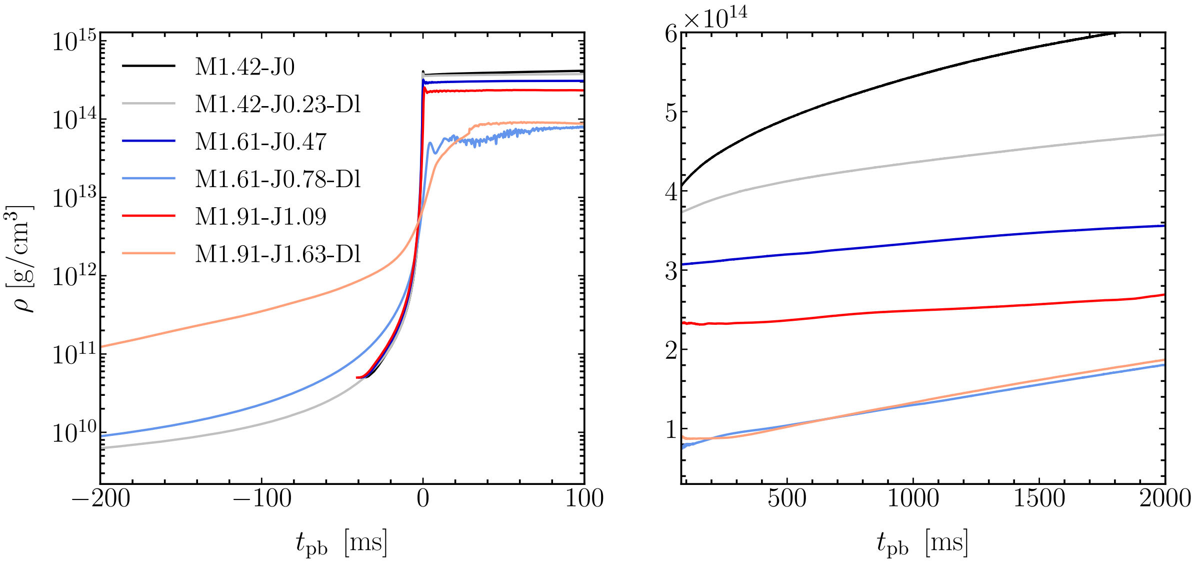

Figure A.1: Maximum central density as a function of post-bounce time. The time $t = 0$ is the moment of the core bounce. The time of the bounce is calculated as the time that the inner $\sim 100\,$km have entropy $\leq 3\,k_{\rm B}$. The models M1.61-J0.78-Dl and M1.91-J1.63-Dl, undergo centrifugal bounce and they do not reach nuclear saturation densities. However, the steep density increase at the same time as the models that undergo pressure bounce seems as a good approximation for these models as well. The spread of the central densities comes from the influence of the rotation on the core bounce. We discuss the collapse of the white dwarfs in section 4.1.

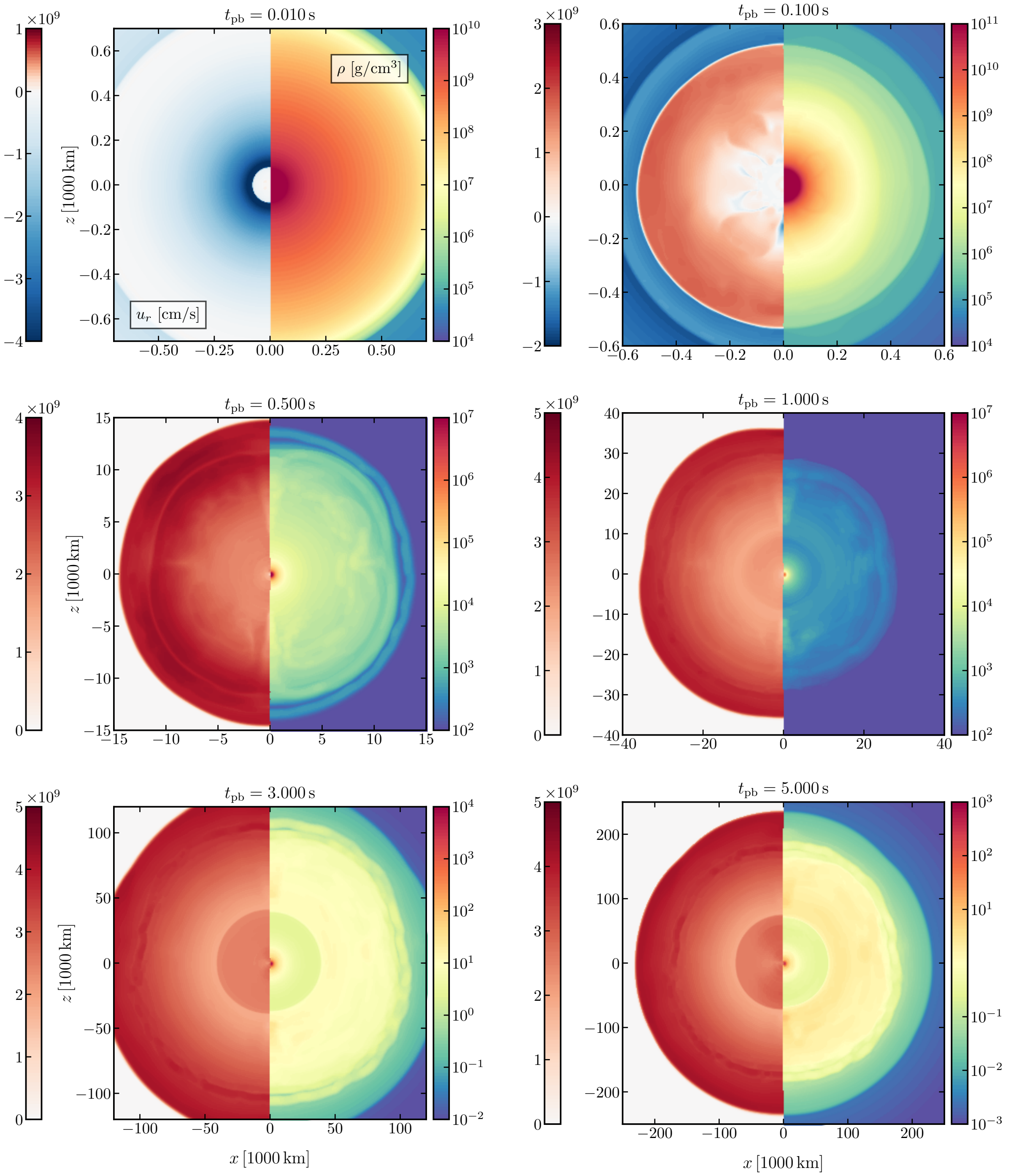

Figure A.2: A sequence of cross-sectional cuts of the model *M1.42-J0*. Each plot shows the density (right-half panels) and the radial velocity (left half panels) in the xz plane at different points in time. The blue-red color bar for the radial velocity is normalized, so the parts with zero radial velocity are shown in white. The core collapses homologously, and at the core bounce, the shock wave develops spherically symmetric. A neutron star of 1.4 $M_\odot$ is born in this AIC model, and the ejecta propagates spherically symmetric. At late times, the ejecta detaches from the central region and propagates in a shell-like configuration.

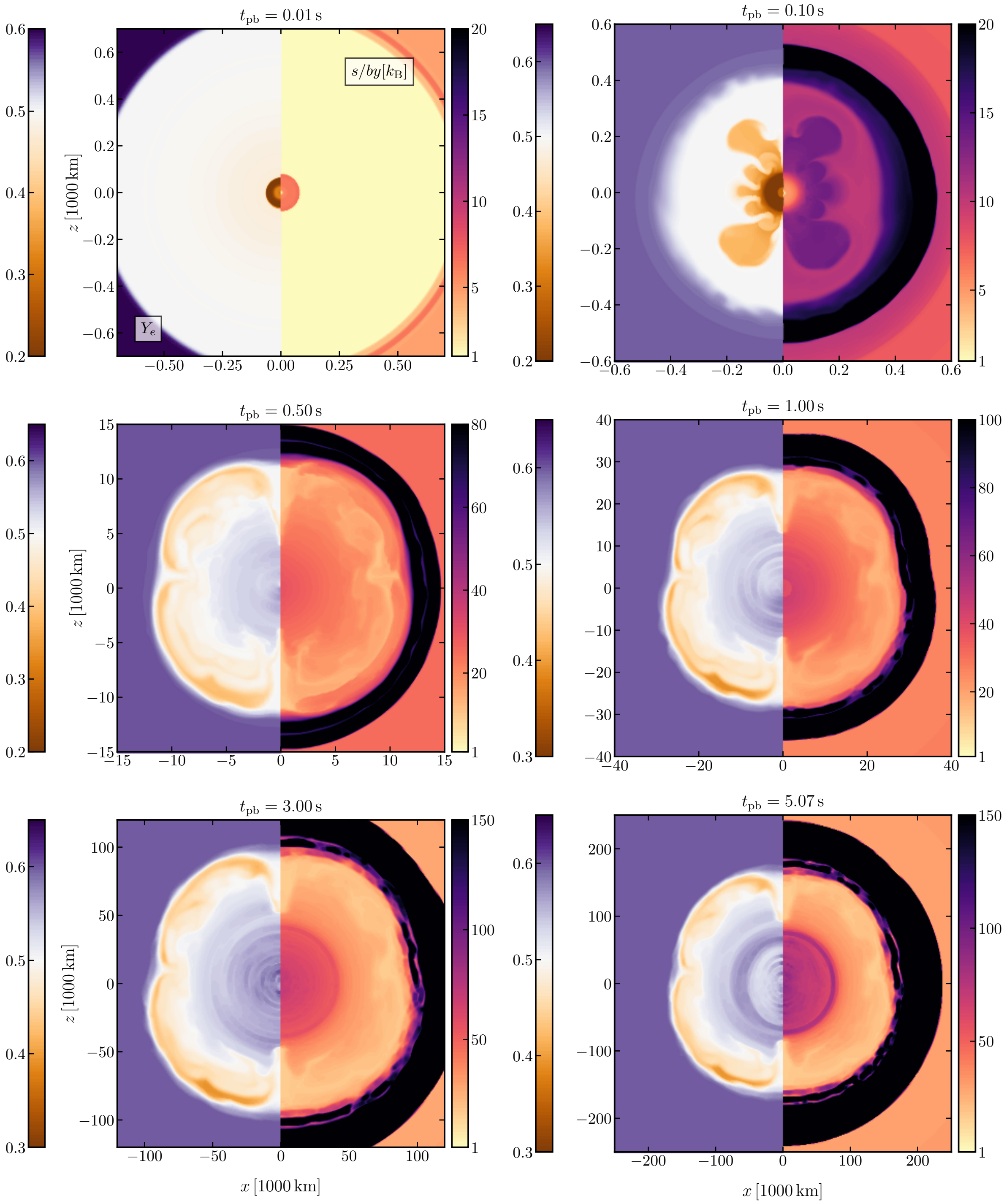

Figure A.3: A sequence of cross-sectional cuts of the model *M1.42-J0* color-coded by the electron fraction Y_e (left-half panels) and entropy-per-baryon (right-half panels) from the start of the collapse until 5 s of post-bounce evolution. After the core bounce, a short period of convection is developed, which drives neutron-rich material in the ejecta, which is expelled by the shock wave. At later times, ν_e absorption raises the Y_e, creating proton-rich material in the ejecta.

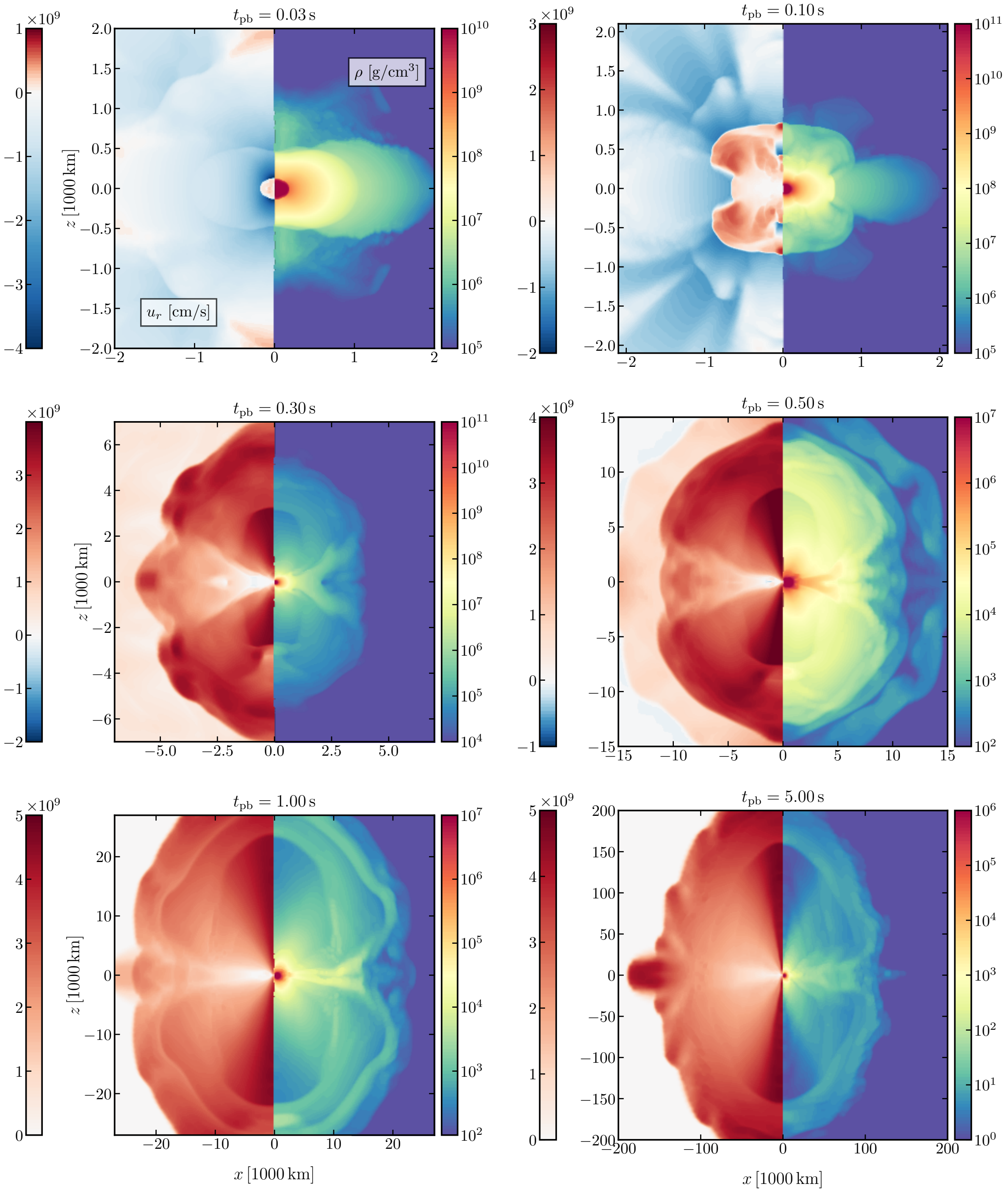

Figure A.4: Time sequence of cross-sectional cuts color-coded by the density (right-half panels) and the radial velocity (left-half panels) for the rotating model *M1.42-J0.23-Dl*. This model is slowly rotating and creates a low-mass disk of $0.06\,{\rm M}_\odot$, which leaves enough material to be ejected. The total ejecta mass is $52.5 \cdot 10^{-3}$, and the neutron star has a mass of $1.3\,{\rm M}_\odot$.

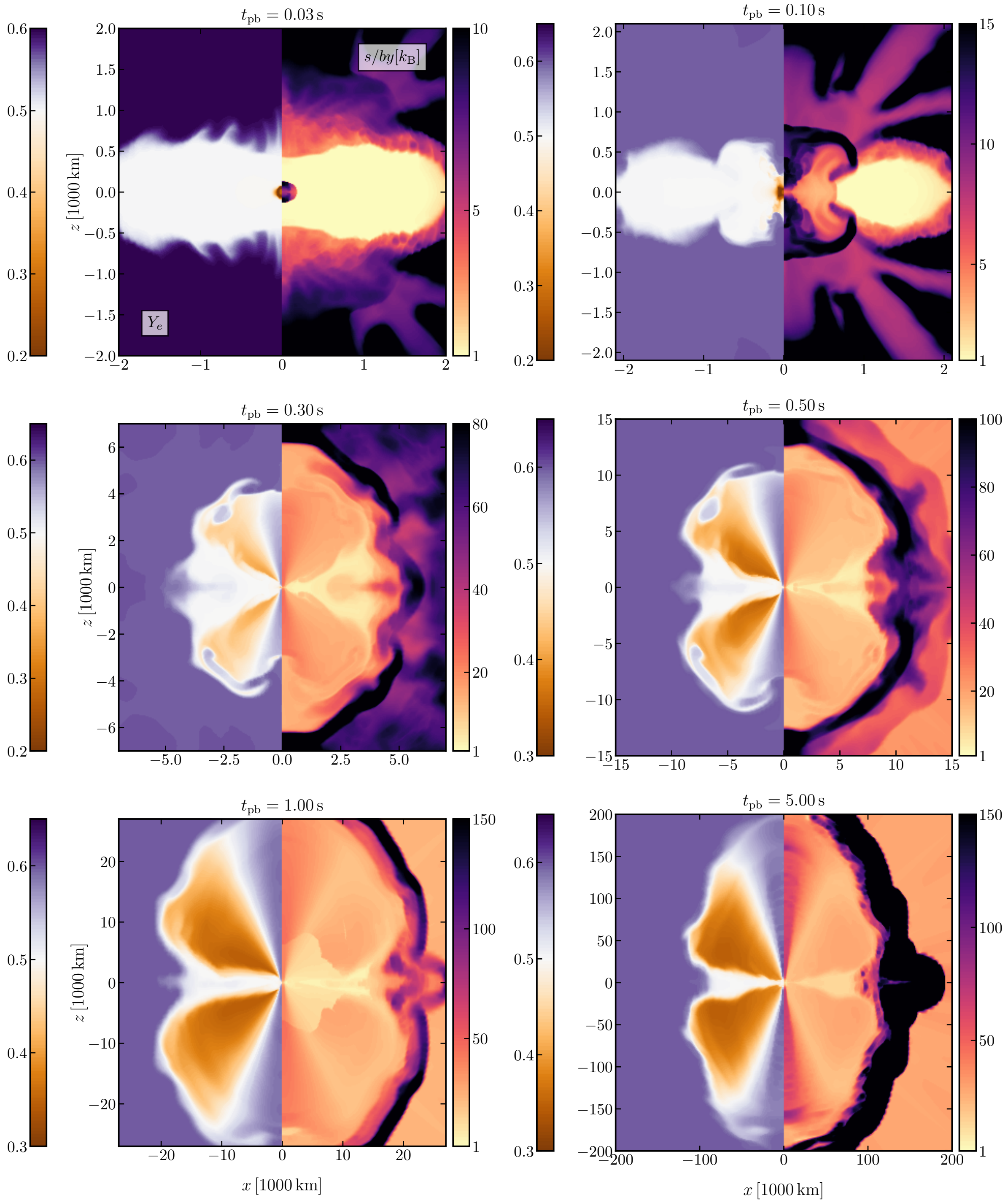

Figure A.5: Time sequence of cross-sectional cuts color-coded by the electron fraction Y_e (left-half panels) and the entropy-per-baryon (right-half panels) for the rotating model *M1.42-J0.23-Dl*. The angular variation of the neutrino luminosities creates the characteristic butterfly-shaped ejecta in the Y_e space. In the poles, we find high-entropy proton-rich material in the ejecta, while at the mid-latitudes, we find lower entropy neutron-rich ejecta. At the equatorial plane, the Y_e stays at 0.5, which is the initial value of the progenitor. Because of the disk that stays centrifugally supported in the equator, the ejecta there do not receive neutrino luminosity; thus, no ν_e or $\bar{\nu}_e$ absorption can alter the electron fraction.

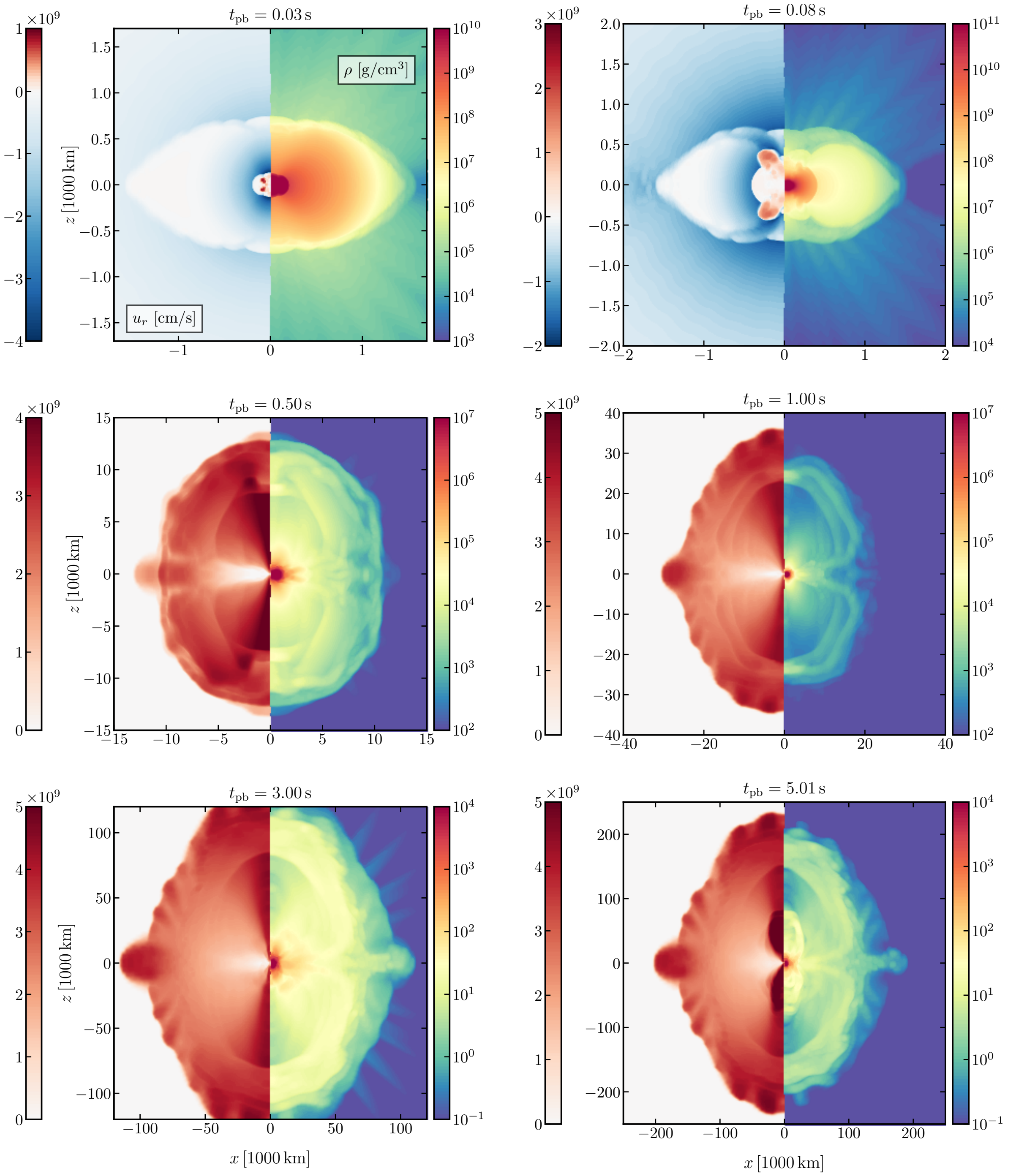

Figure A.6: Time sequence of cross-sectional cuts color-coded by the density (right-half panels) and the radial velocity (left-half panels) for the rotating model *M1.61-J0.47*. This model has a high central density at initialization and collapses fast. The outflow is constrained in the polar direction due to the disk forming around the neutron star. This model yields a total of $25.9 \cdot 10^{-3}\,\mathrm{M}_\odot$ and a forms a neutron star of $1.37\,\mathrm{M}_\odot$.

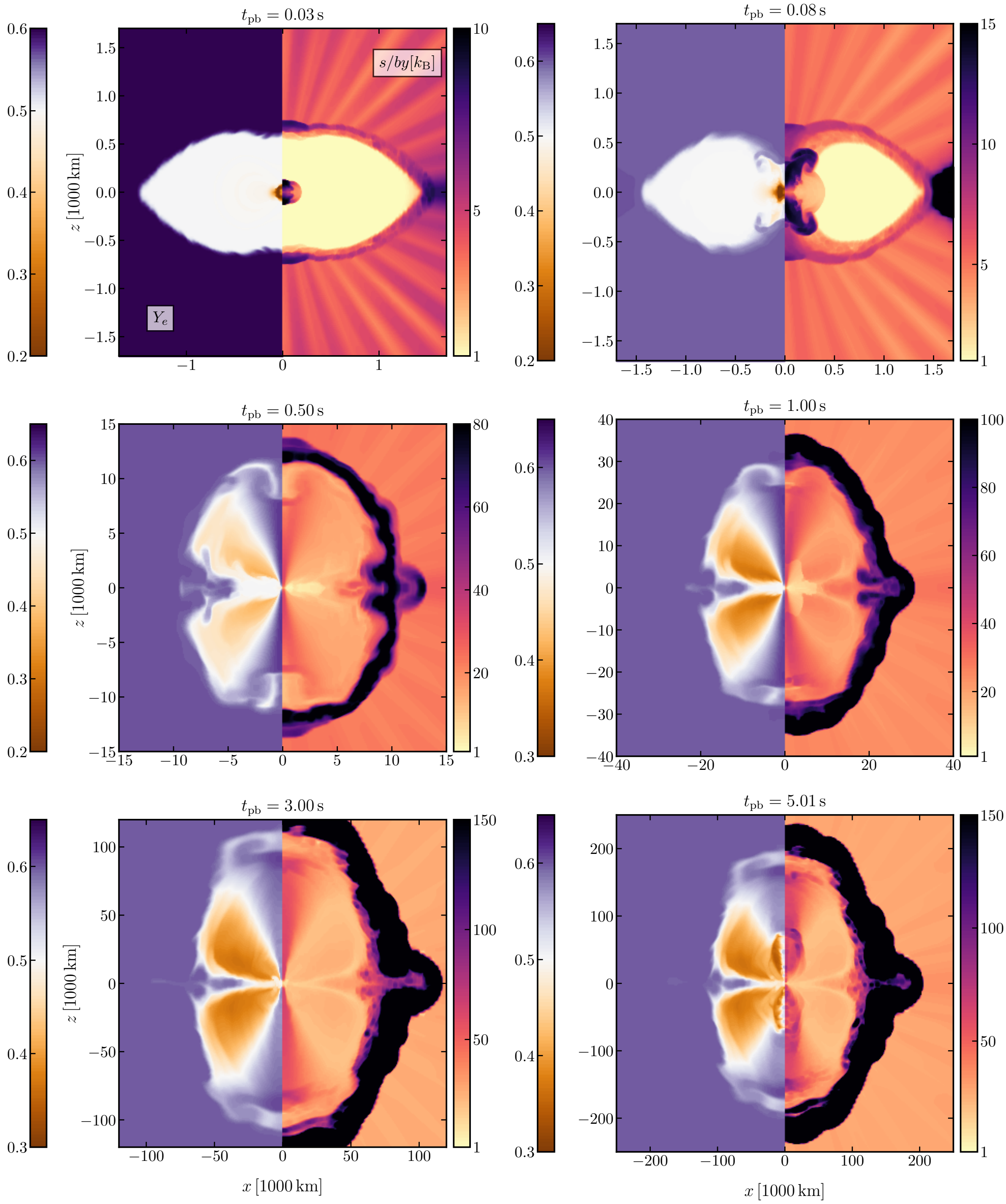

Figure A.7: Time sequence of cross-sectional cuts color-coded by the electron fraction Y_e (left-half panels) and the entropy-per-baryon (right-half panels) for the rotating model *M1.61-J0.47*. This rotating model shows the latitudinal variation of the Y_e as in the case of M1.42-J0.23-Dl.

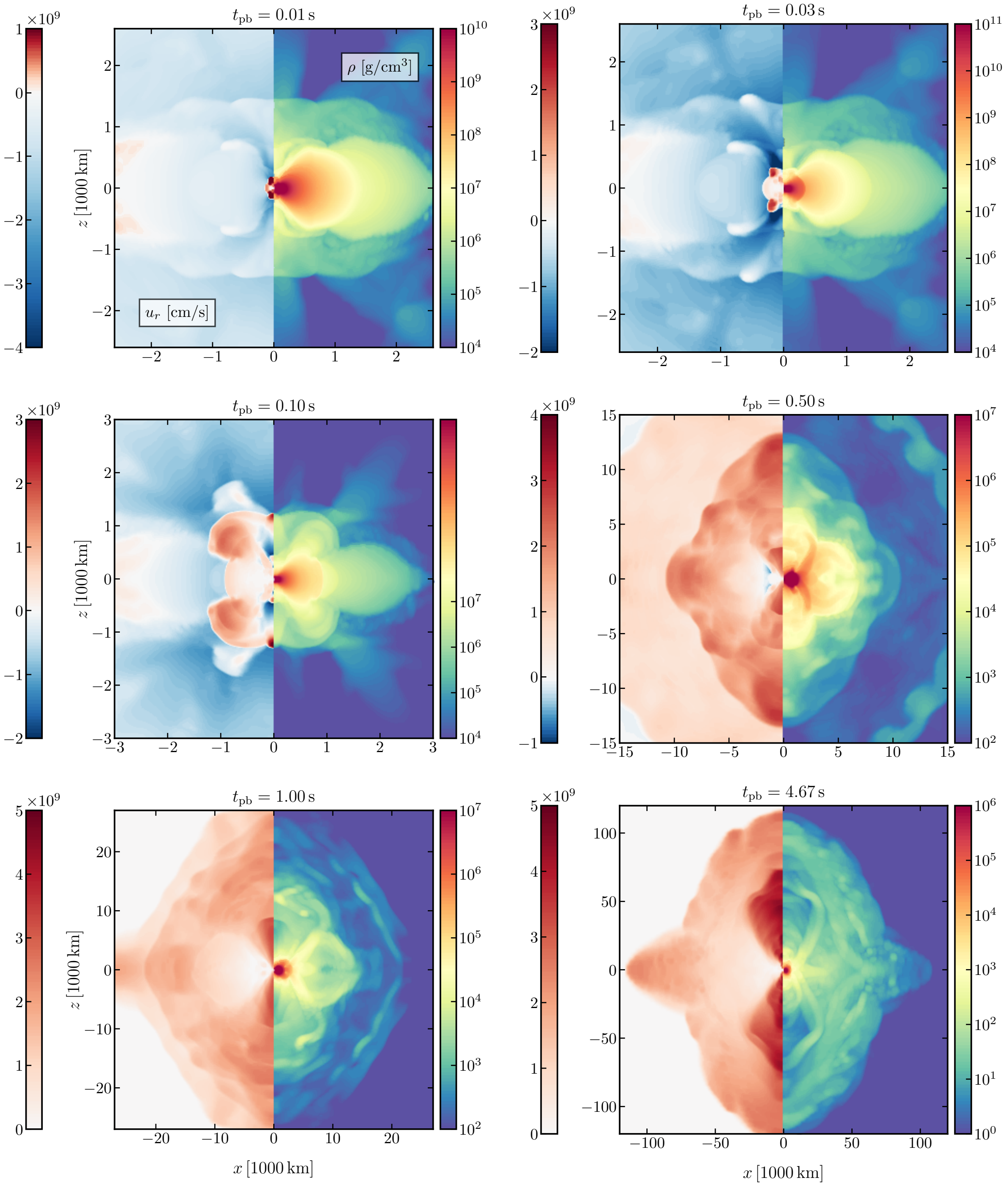

Figure A.8: Time sequence of cross-sectional cuts color-coded by the density (right-half panels) and the radial velocity (left-half panels) for the high-β rotating model *M1.61-J0.78-Dl*. This model undergoes centrifugal collapse because during collapse the core becomes rotationally supported. In this model the newly born neutron star has a mass of $1.14\,\mathrm{M}_\odot$, the disk that surrounds the neutron star has a mass of $0.29\,\mathrm{M}_\odot$ and a total of $21.22 \cdot 10^{-3\,\mathrm{M}_\odot}$ are ejected.

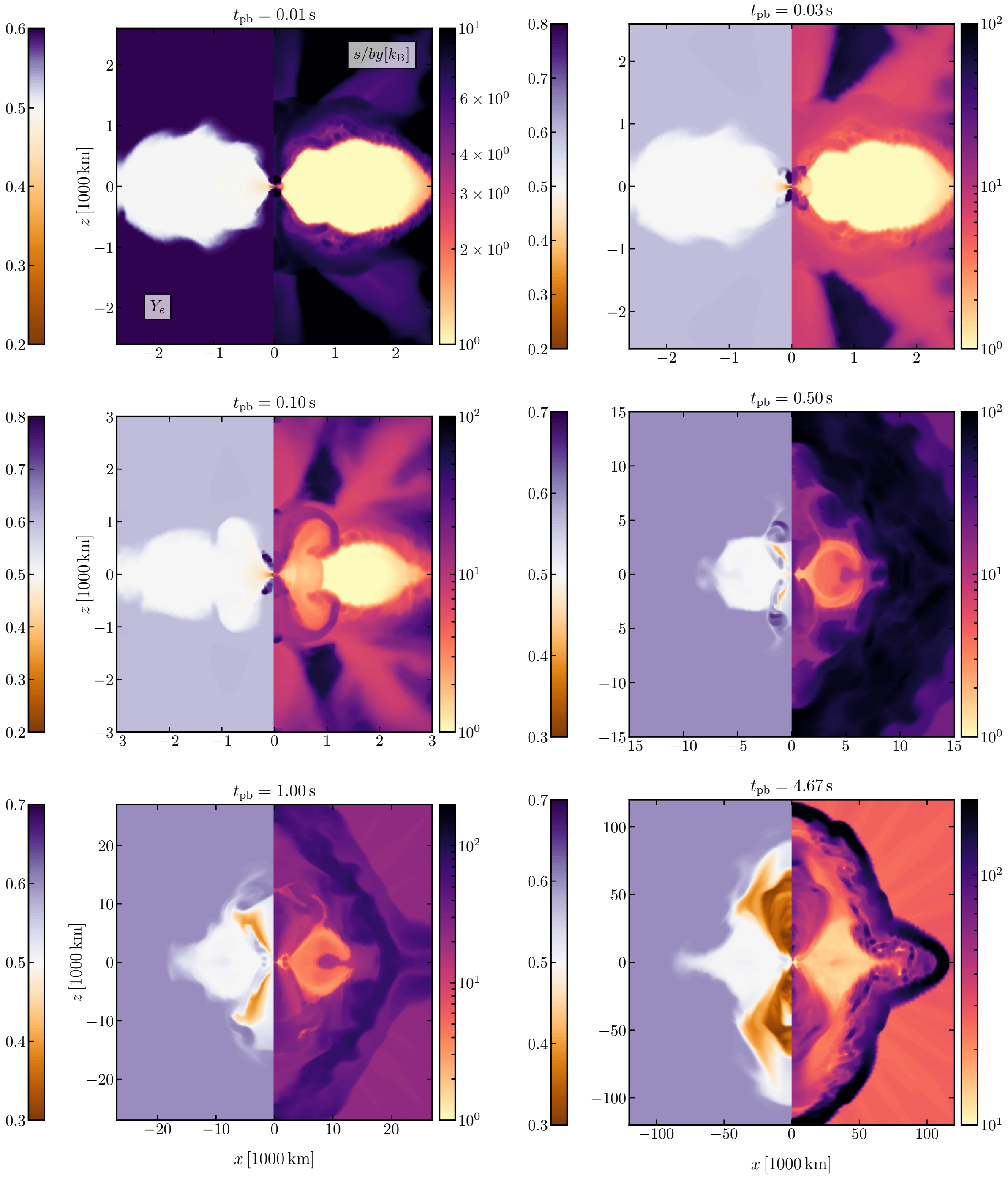

Figure A.9: Time sequence of cross-sectional cuts color-coded by the electron fraction Y_e (left-half panels) and the entropy-per-baryon (right-half panels) for the high-β-rotating model *M1.61-J0.78-Dl*. In this model, much of the equatorial material is swiped away as the shock wraps around the progenitor. This is seen as the white parts of the Y_e, which is white dwarf material that has not received neutrino luminosity to alter its Y_e. The neutron-rich part of the ejecta comes at later times but again from the mid-latitudes.

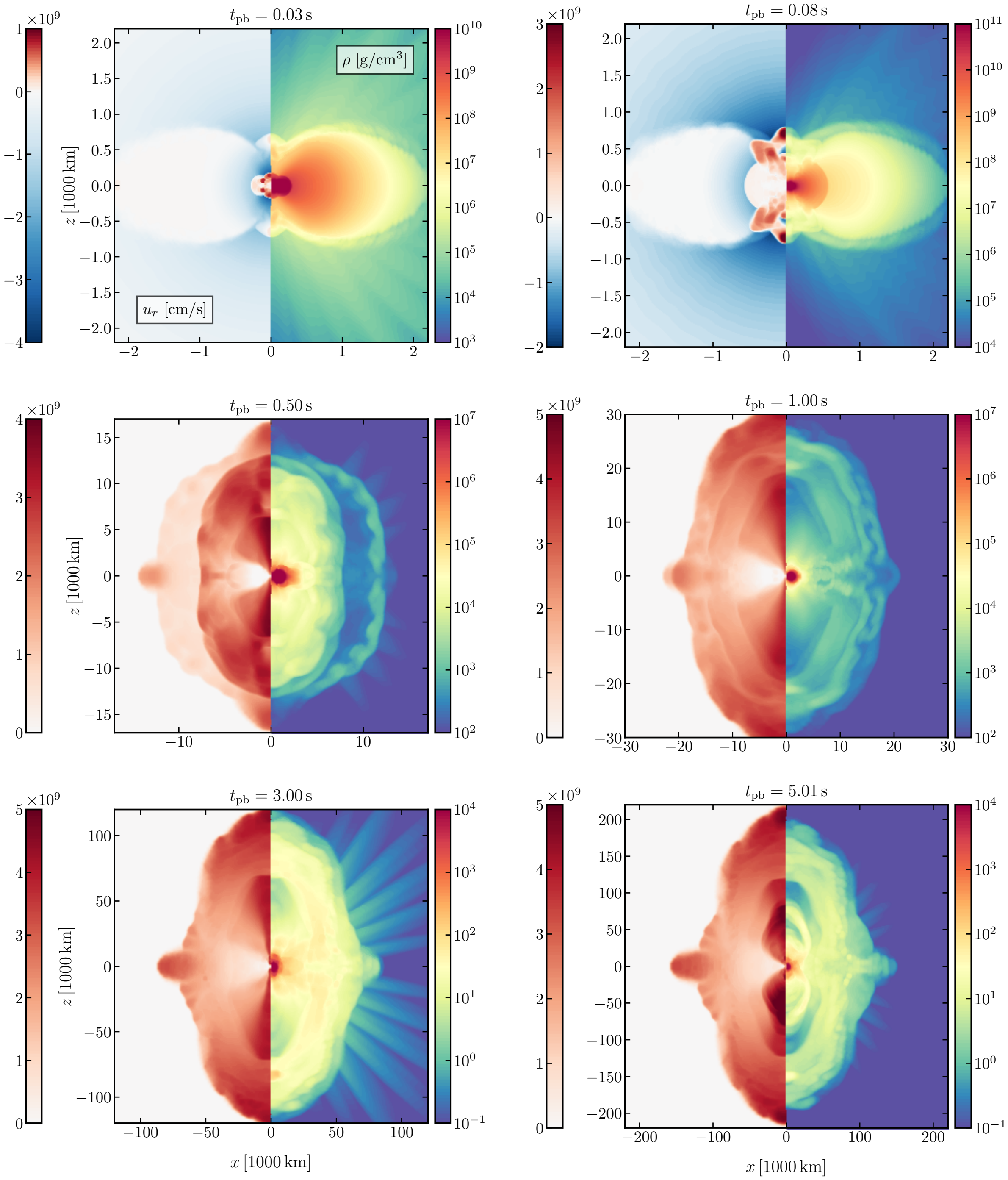
$t_{\mathrm{pb}} = 0.03\,\mathrm{s}$

$t_{\mathrm{pb}} = 0.08\,\mathrm{s}$

$t_{\mathrm{pb}} = 0.50\,\mathrm{s}$

$t_{\mathrm{pb}} = 1.00\,\mathrm{s}$

$t_{\mathrm{pb}} = 3.00\,\mathrm{s}$

$t_{\mathrm{pb}} = 5.01\,\mathrm{s}$

Figure A.10: Time sequence of cross-sectional cuts color-coded by the density (right-half panels) and the radial velocity (left-half panels) for the rotating model *M1.91-J1.09*. This model shows similar collapse and explosion dynamics as the rotating model M1.61-J0.47. Due to the higher degree of rotation and higher mass, this model creates a larger disk, compared of the model M1.61-J0.47, with a mass of $0.43\,\mathrm{M}_\odot$. The total ejecta mass is $18.69 \cdot 10^{-3}\,\mathrm{M}_\odot$ and the neutron star has a mass of $1.29\,\mathrm{M}_\odot$.

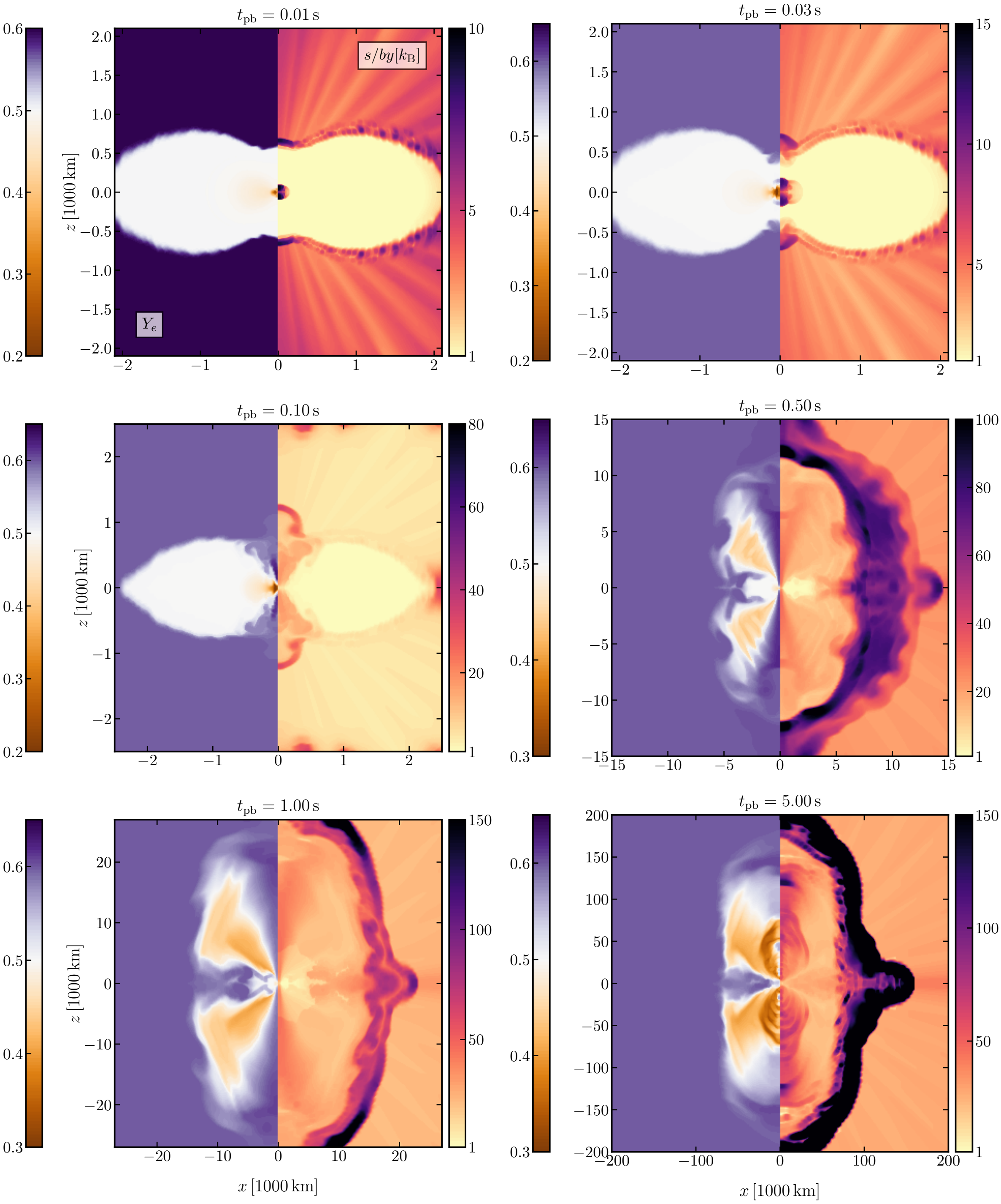

Figure A.11: Time sequence of cross-sectional cuts color-coded by the electron fraction Y_e (left-half panels) and the entropy-per-baryon (right-half panels) for the rotating model *M1.91-J1.09*. The evolution of the ejecta properties is similar to the rotating model M1.61-J0.47.

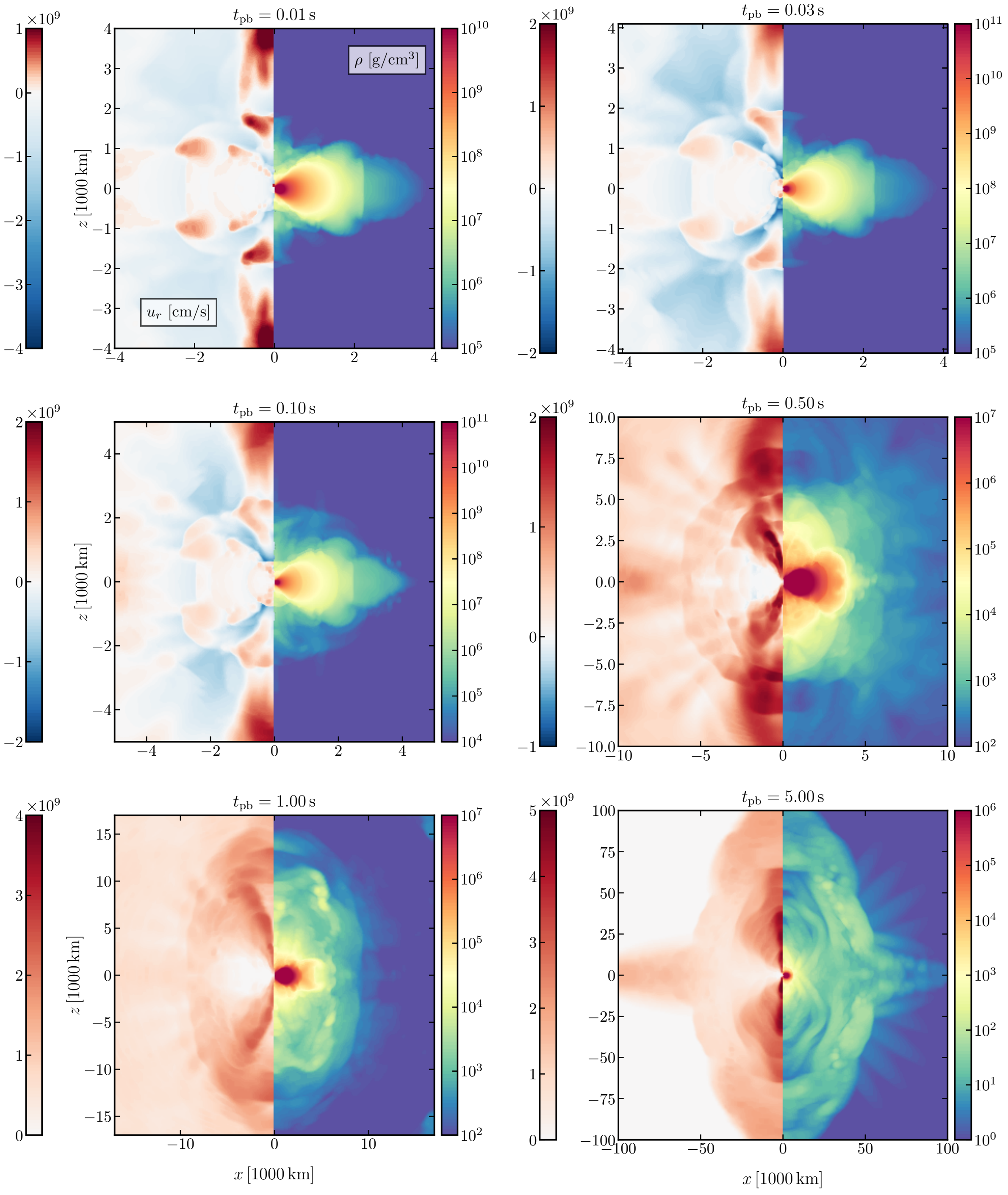

Figure A.12: Time sequence of cross-sectional cuts color-coded by the density (right-half panels) and the radial velocity (left-half panels) for the high-β rotating model *M1.91-J1.63-Dl*. This model has the highest angular momentum of all models and low central density. It collapses very slowly, and while that is, the outer layer of the progenitor gets unbound. This model undergoes a centrifugal bounce. The remnant consists of a neutron star with a mass of $0.96\,\mathrm{M}_\odot$, a centrifugally supported disk of $0.75\,\mathrm{M}_\odot$. The total ejecta mass of this model is $5.7 \cdot 10^{-3}\,\mathrm{M}_\odot$.

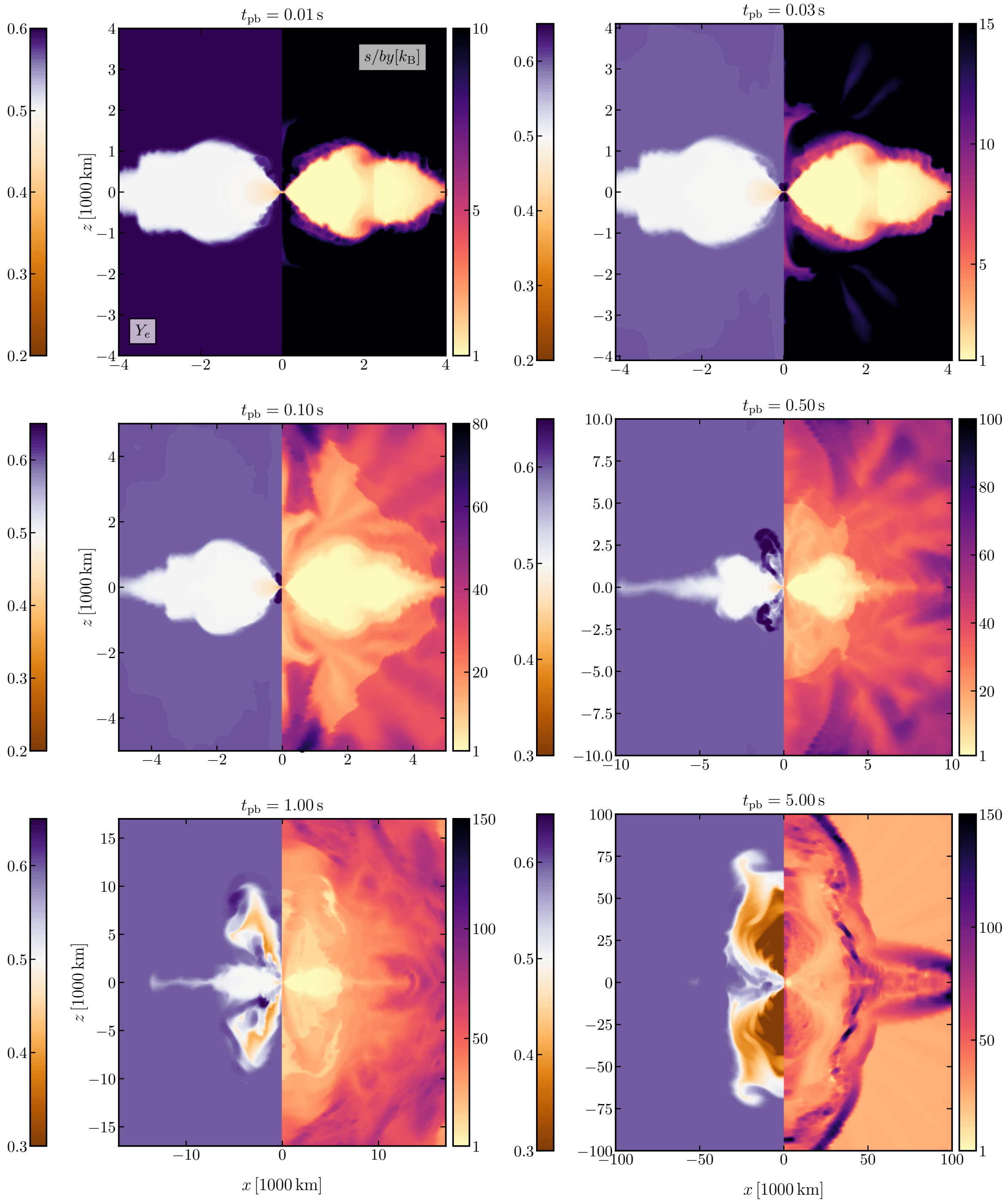

Figure A.13: Time sequence of cross-sectional cuts color-coded by the electron fraction Y_e (left-half panels) and the entropy-per-baryon (right-half panels) for the high-β rotating model *M1.91-J1.63-Dl*. This model's particular collapse and explosion dynamics allow very little material to be ejected. In contrast, most of the ejecta comes later as the neutrino-driven wind ejects material from the surface of the PNS and the surface of the disk. At late times, we find neutron-rich outflow mainly from the polar regions.

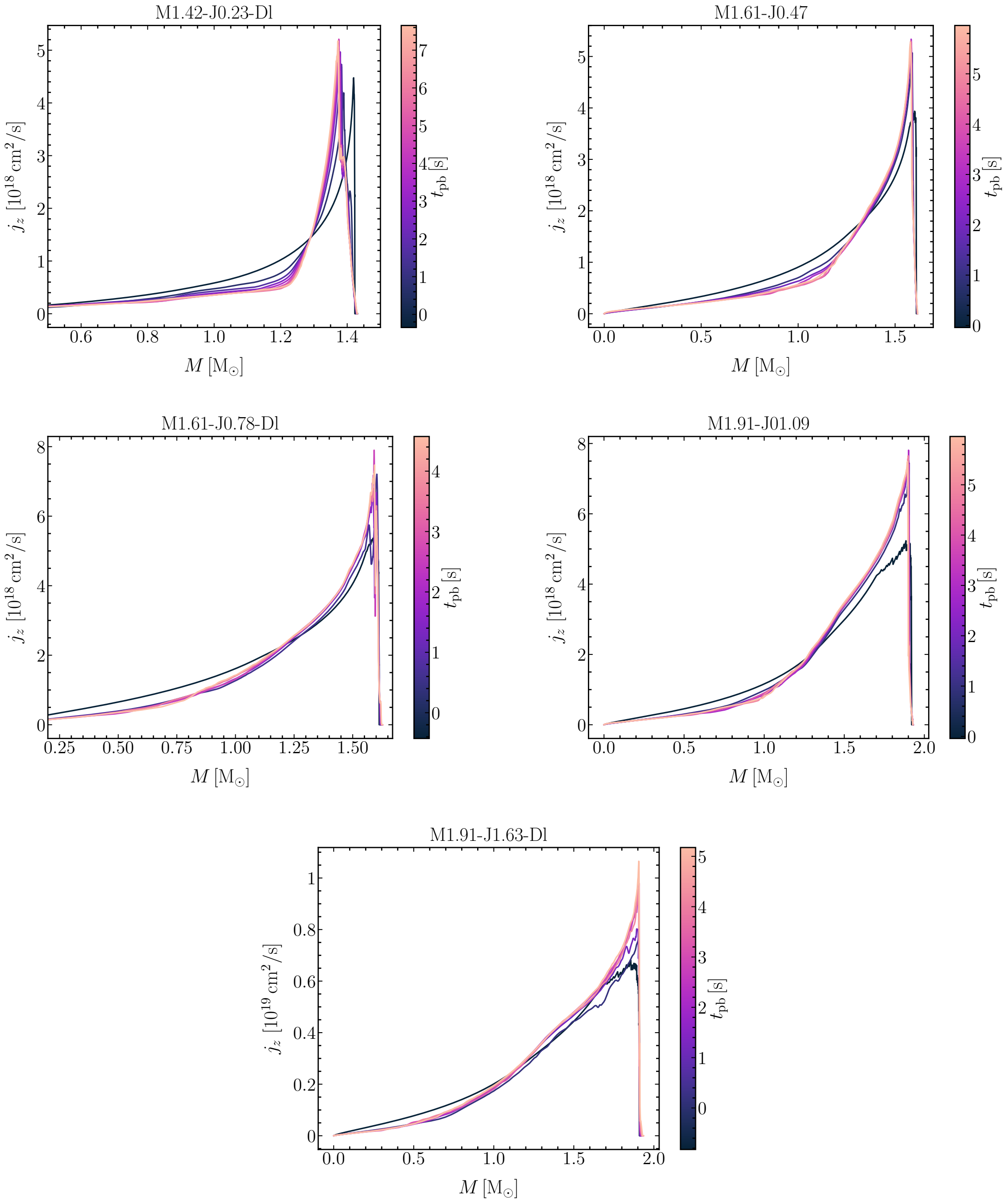

Figure A.14: Time evolution of the z-component of the specific angular momentum as a function of the enclosed mass. The colored lines present the time evolution according to the color bar, with black and dark blue corresponding to the initial j_z and purple to pink lines to the final stages of the simulation. Each panel presents the evolution of the specific angular momentum for each model indicated in the plot title. This is supplementary to the specific angular momentum evolution as a function of radius shown in figure 4.12.

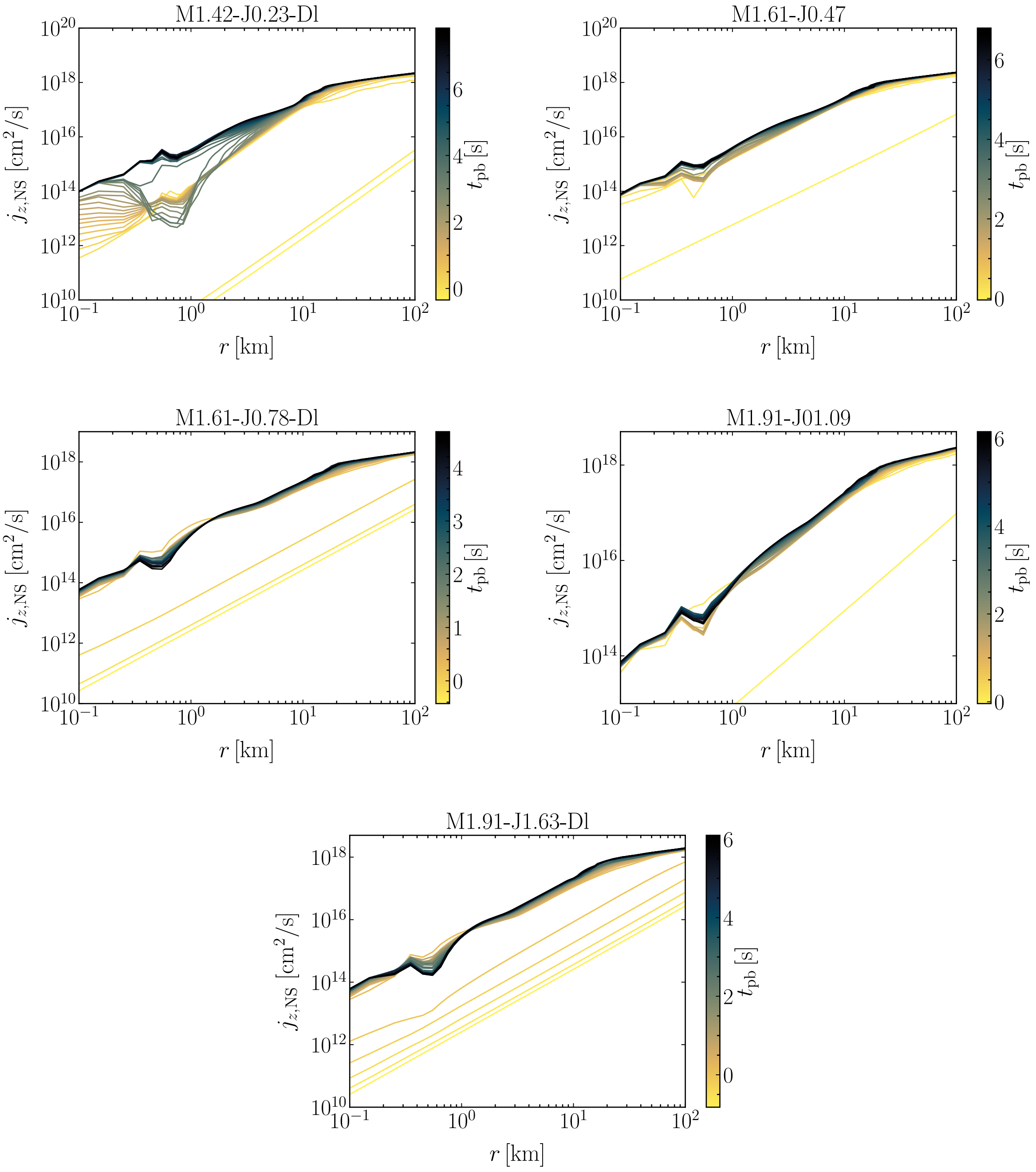

Figure A.15: Each panel displays the z-component of the specific angular momentum as a function of radius. The color-coding of the lines show the time evolution with yellow being the early times, i.e., before the collapse and at core bounce, and the darker shades show the late time evolution until the end of each simulation. Here we display the inner regions until 100 km which is approximately the maximum radius of the neutron stars formed (apart from the model M1.42-J0.23-Dl that the equatorial radius of the neutron star is 58 km). This is an addition to the figure 4.12.

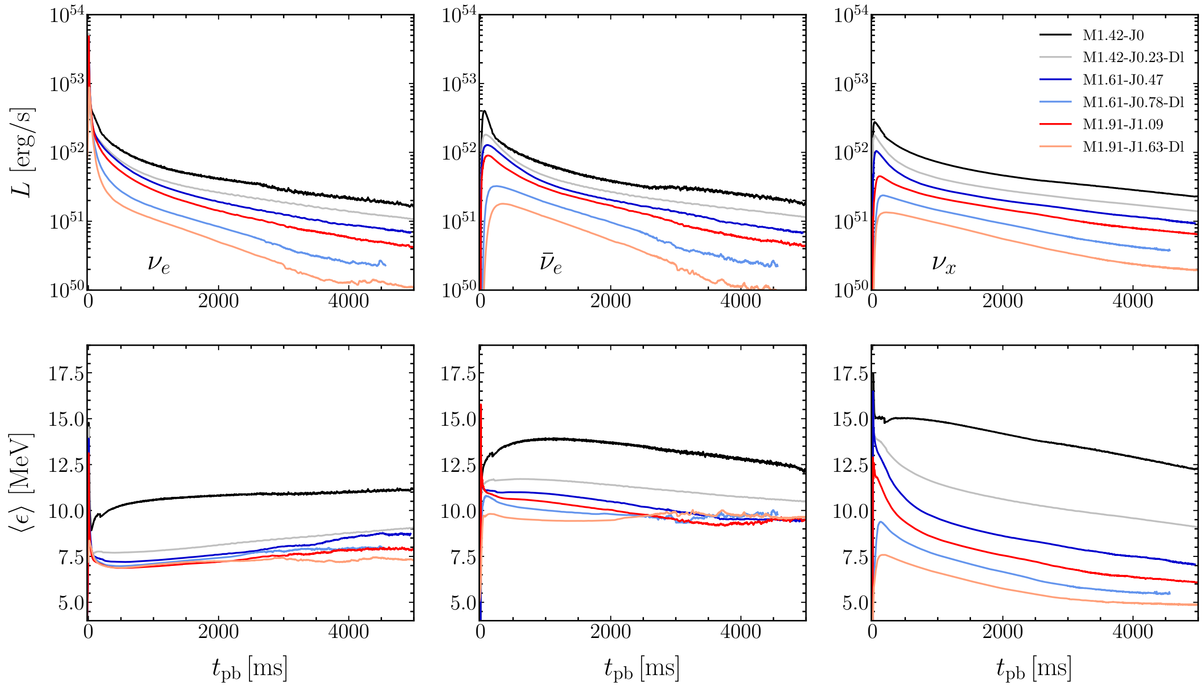

Figure A.16: Luminosity (top row) and angle-averaged mean energy (bottom row) for the three evolved neutrino species: electron neutrinos ν_e (left column), electron antineutrinos $\bar{\nu}_e$ (middle column), and heavy-lepton neutrinos ν_x (right column) for the six AIC models as a function of post-bounce time until 5 s. Each colored line corresponds to one model, as denoted in the legend. The quantities are transformed into the lab frame and evaluated at a radius of 3500 km. The time shown in the x-axis corresponds to the post-bounce time. This shows the long-time evolution of the luminosities and the mean energies, in addition to figure 5.1. The large spread of the different values in the luminosities directly affects rotation, which alters the shape of the neutrinospheres in the PNS and the thermodynamical conditions at the neutrinospheres. The higher the spin rates, the lower the central density and temperature in the core at bounce, which leads to a modest neutrino emission. This is true for the rotating models. The high-β rotating models have lower central spin rates, but due to the large reservoir of angular momentum, they undergo centrifugal bounce, which translates to lower central densities. Therefore, the high-β models, i.e., M1.61-J0.78-Dl and M1.91-1.63-Dl, have even lower luminosities than the rest.

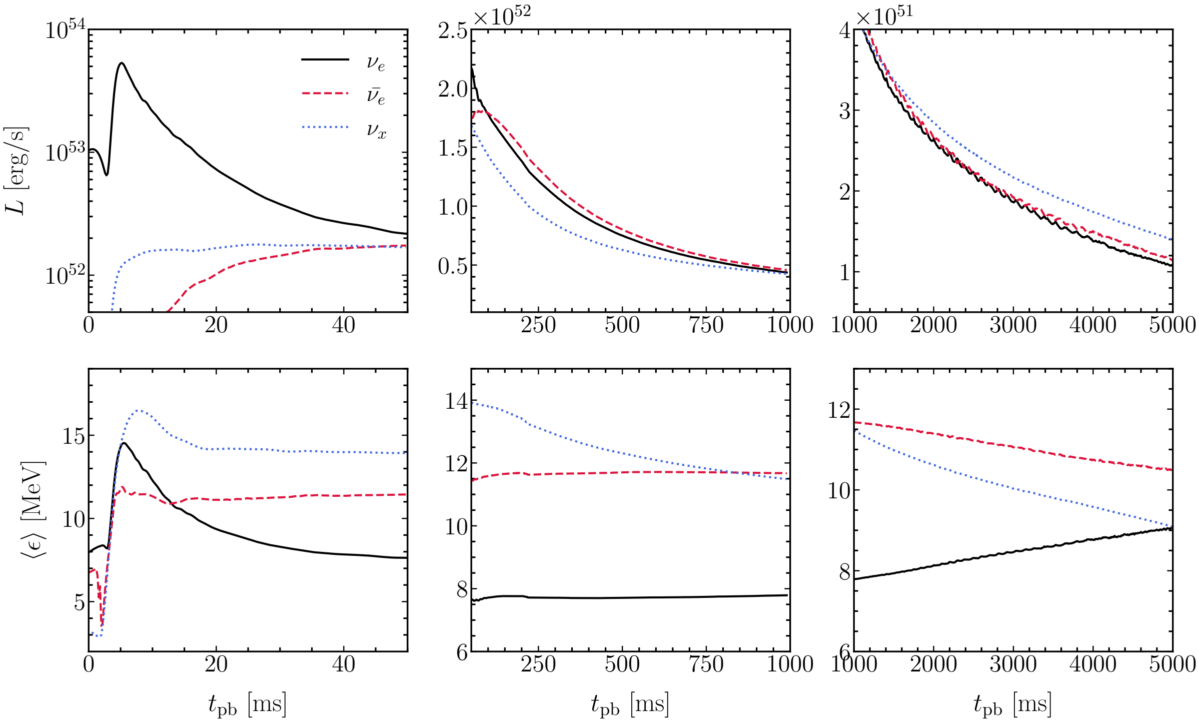

Figure A.17: Luminosity and angle-averaged mean energy as a function of post-bounce time for the model *M1.42-J0.23-Dl*. The luminosity (top row) is energy integrated, calculated in the lab frame at a distance of 3500 km. Each panel in the top row shows different time intervals of the luminosity as a function of time and the bottom rows the angle-averaged mean energy as a function of time. In each panel the three evolved neutrino species are shown; the electron neutrinos ν_e in solid black lines, the electron antineutrinos $\bar{\nu}_e$ in dashed red lines, and the heavy-lepton neutrinos ν_x in dotted blue lines. The bottom row shows the angle-averaged mean energy of the electron neutrinos ν_e (solid black lines), the electron antineutrinos $\bar{\nu}_e$ (dashed red lines), and the heavy-lepton neutrinos (dotted blue lines) as a function of post-bounce time. Notice the different y-axis scales in each panel. This appends on the figure 5.2, and figure 5.3.

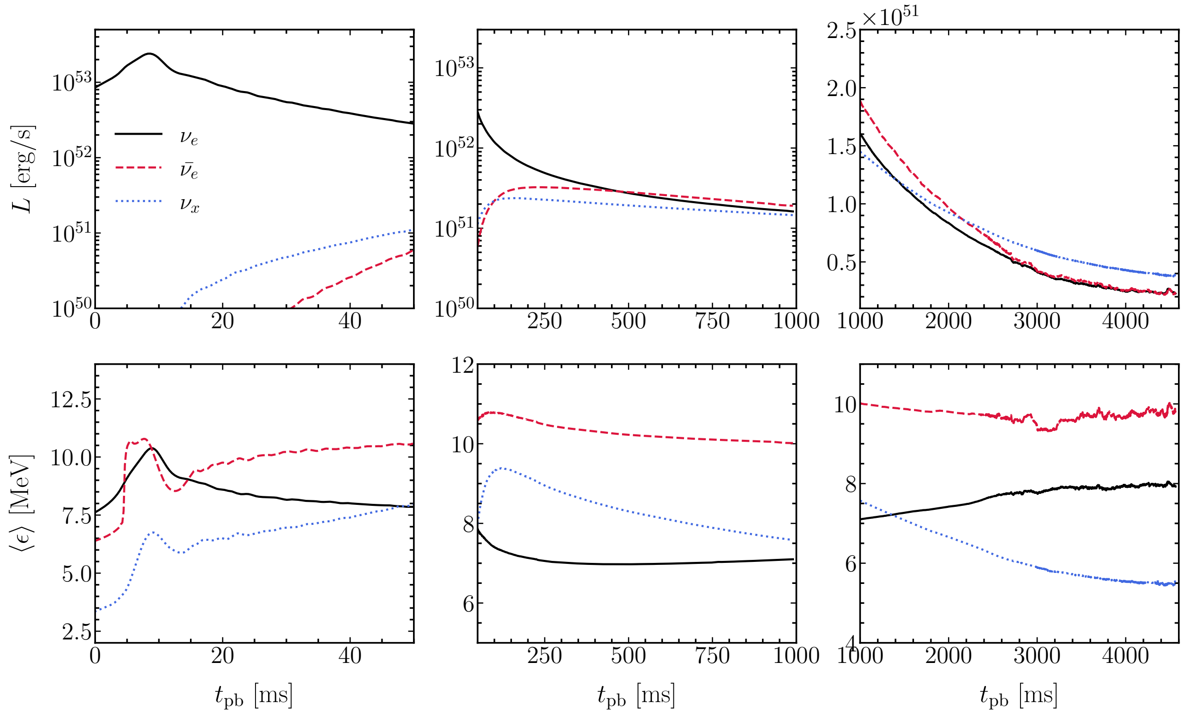

Figure A.18: Same as figure A.17 for the model *M1.61-J0.78-Dl*.

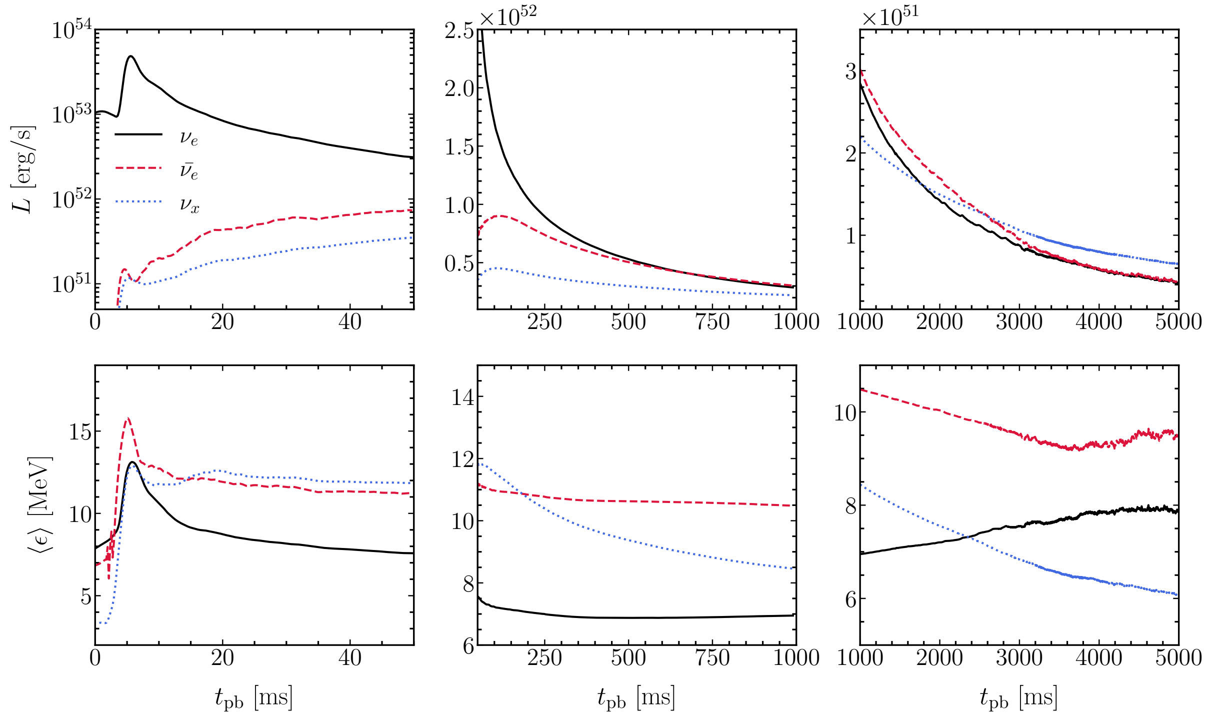

Figure A.19: Same as figure A.17 for the model *M1.91-J1.09*.

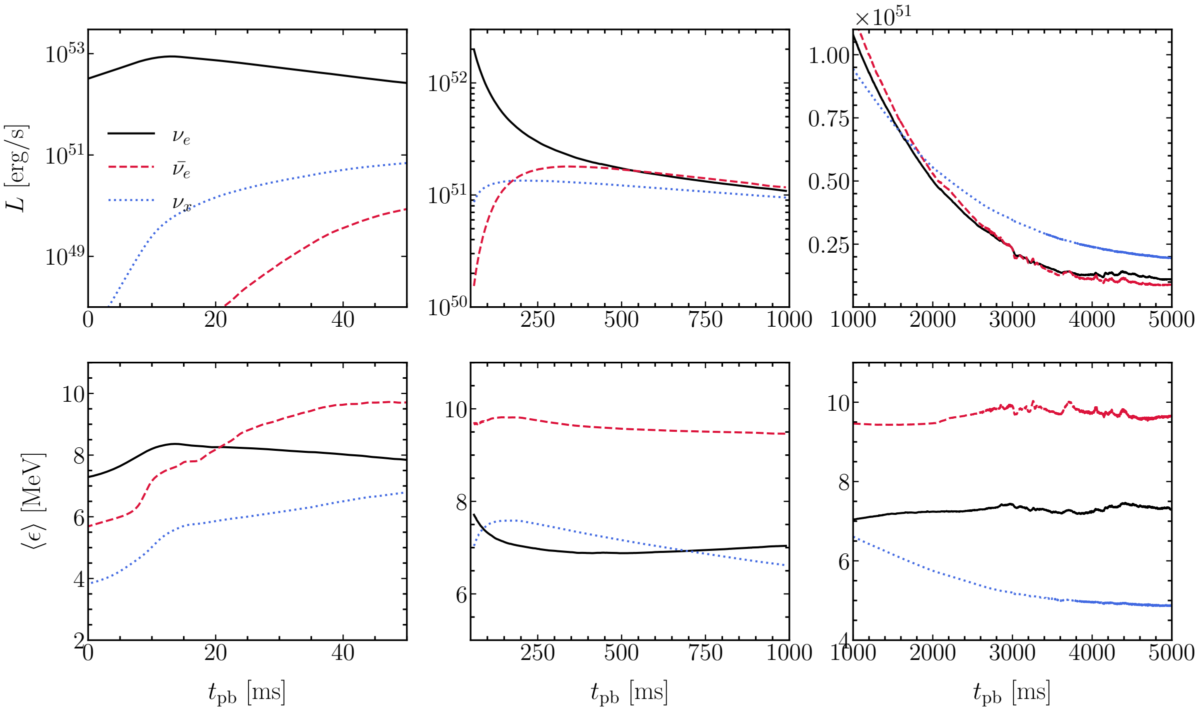

Figure A.20: Same as figure A.17 for the model *M1.91-J1.63-Dl*.

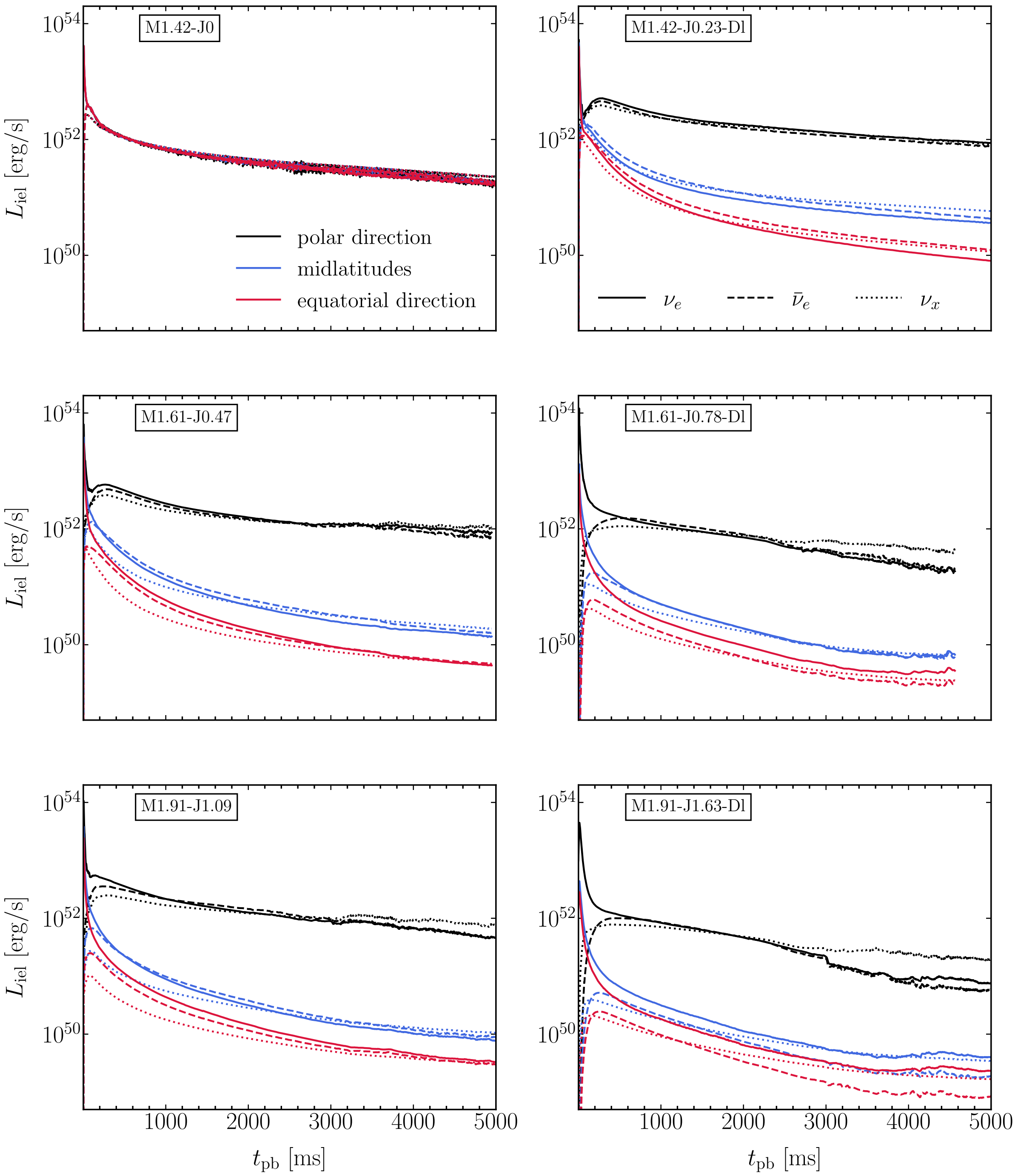

Figure A.21: Each panel shows the luminosity as a function of post-bounce time along different directions for electron neutrinos (solid lines), electron antineutrinos (dashed lines), and heavy-lepton neutrinos (dotted lines). The black lines show the luminosity along the poles, the blue lines correspond to mid-latitudes around 50°, and the red lines show the luminosity in the equatorial direction. The luminosities are evaluated at a distance of 3500 km, transformed at the lab frame, and they are scaled up to the whole sphere, i.e., the directional luminosity corresponds to the total luminosity we would observe if the selected direction were emitted in all directions. Each panel shows the luminosities for each model that is indicated in the upper left box in each figure. We define this luminosity as the isotropic-equivalent-luminosity and is calculated by equation (5.5).

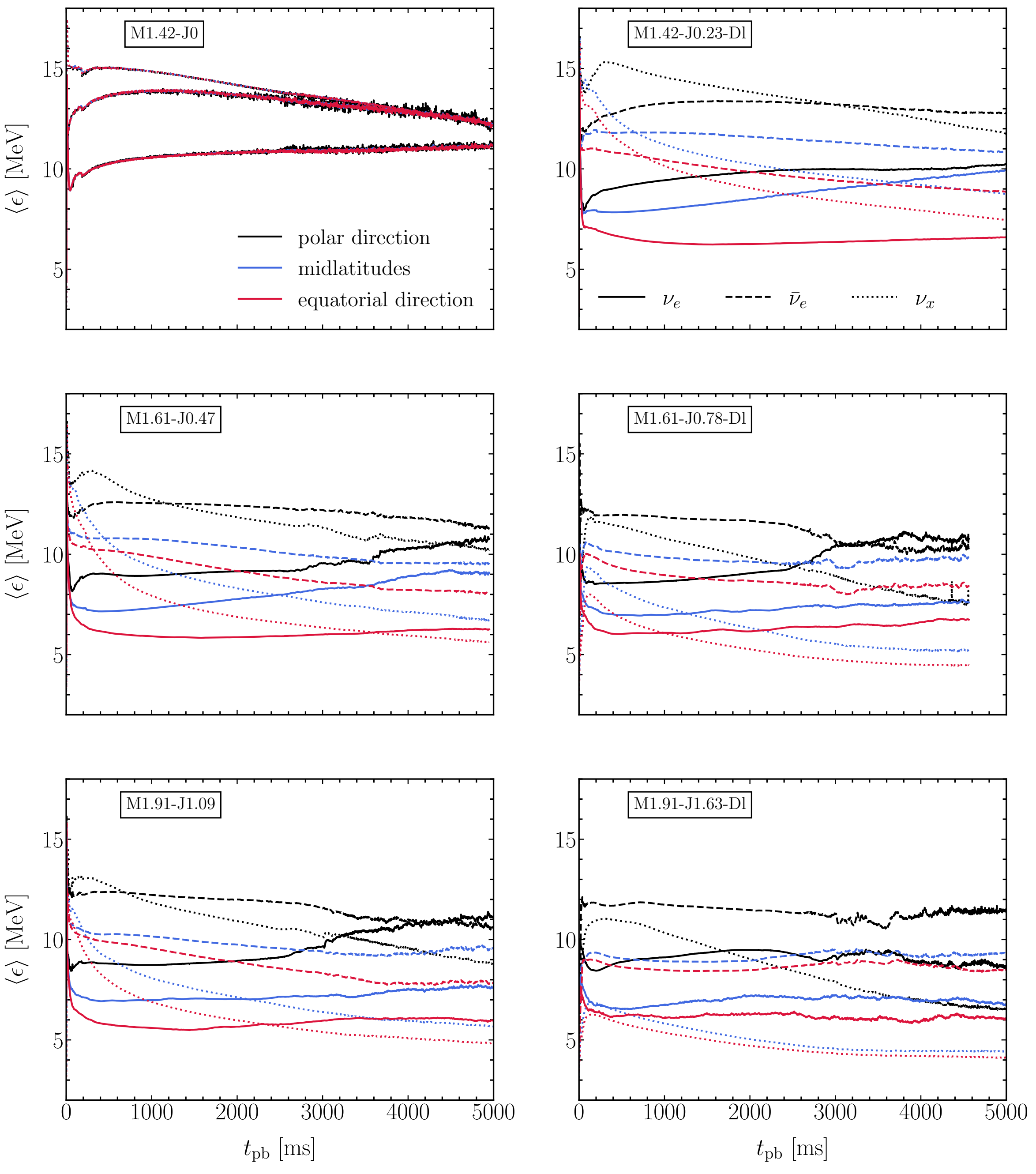

Figure A.22: Mean energy as a function of post-bounce time angle-averaged in the polar direction (black lines), the mid-latitudes (blue lines) and the equator (red lines). The angle averaged energy is the integrated energy along 10° around 0° for the poles, 50° for the mid-latitudes and 90° for the equator, and scaled up to the whole sphere, similarly as the luminosity. Each panel displays one of the six model as denoted in the corresponding label. The solid lines of each color show the electron neutrinos ν_e, the dashes lines show the electron antineutrinos ν_e, and the dotted lines show the heavy-lepton neutrinos ν_x.

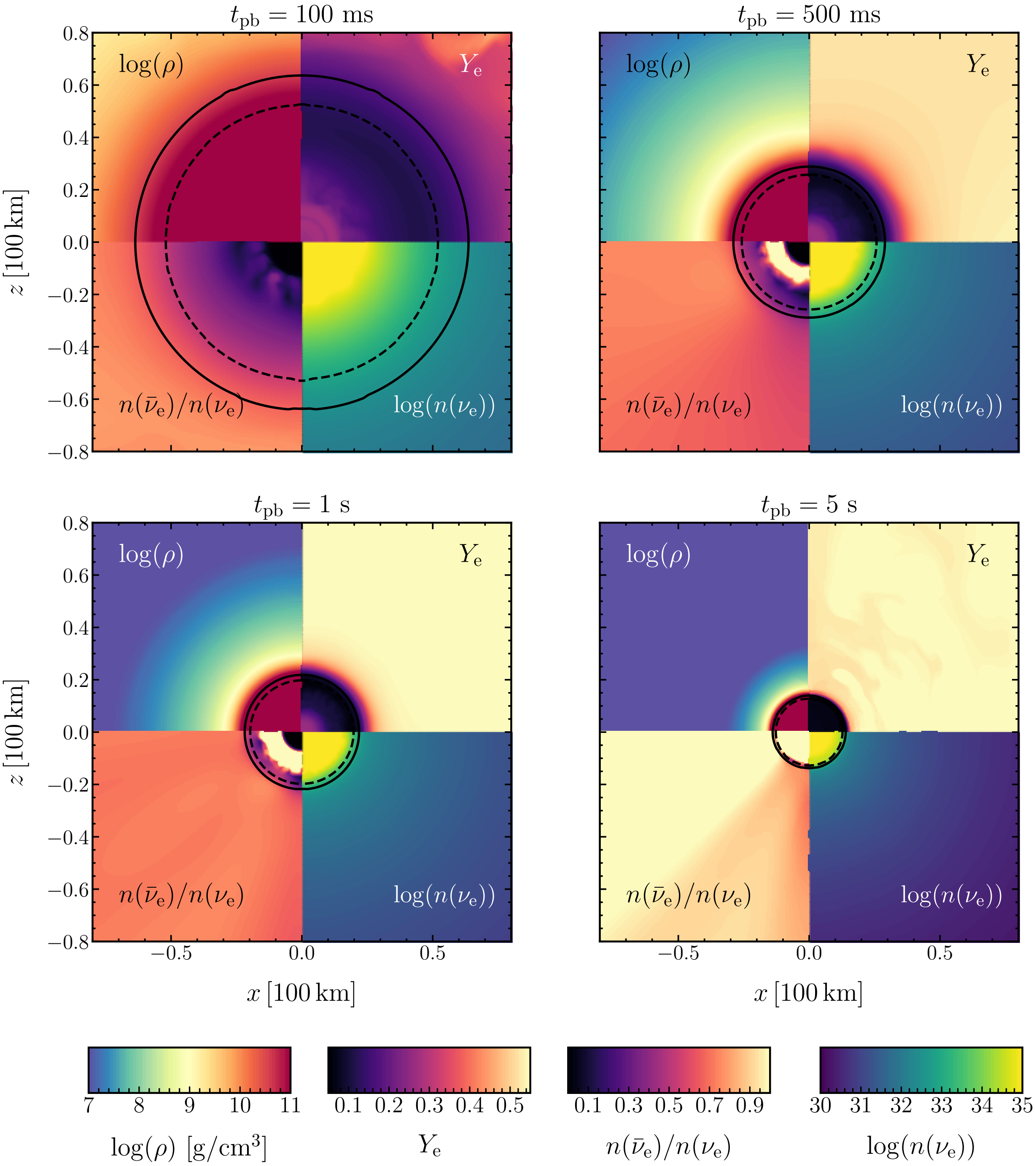

Figure A.23: Non-rotating model *M1.42-J0*. A collection of cross sectional cuts at different points in time, color-coded by four different quantities. In each plot, that represents one point in time shown in the title of each plot, the left upper panel shows the logarithm of the density, the right upper panel shows the electron fraction Y_e, the bottom left shows the ratio of the electron antineutrino number density to the electron neutrino number density, i.e., $c(\bar{\nu}_e)/n(\nu_e)$, and the right bottom panel shows the logarithm of the ν_e number density.

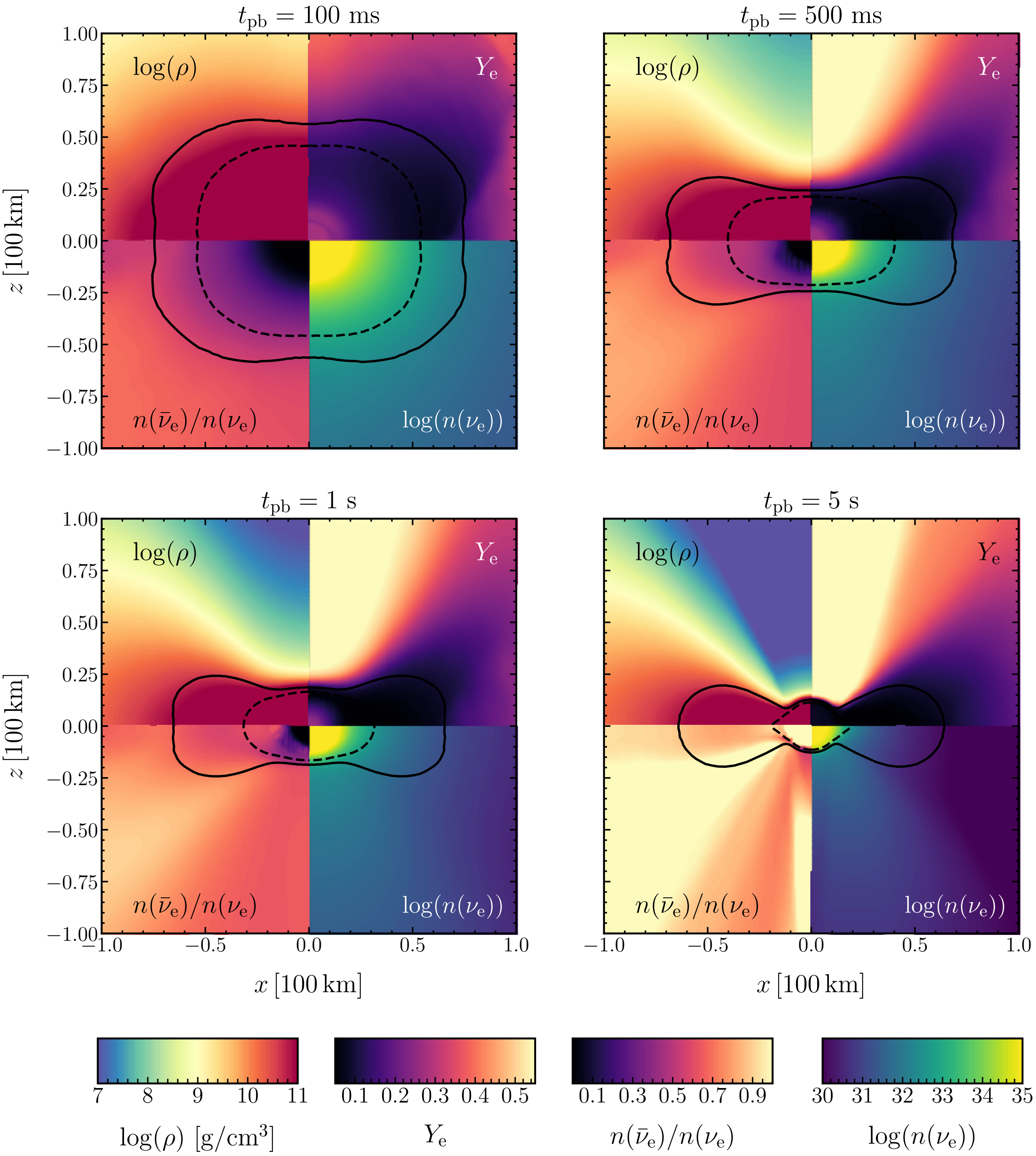

Figure A.24: Rotating model *M1.42-J0.23-Dl*. Same figure as figure A.23.

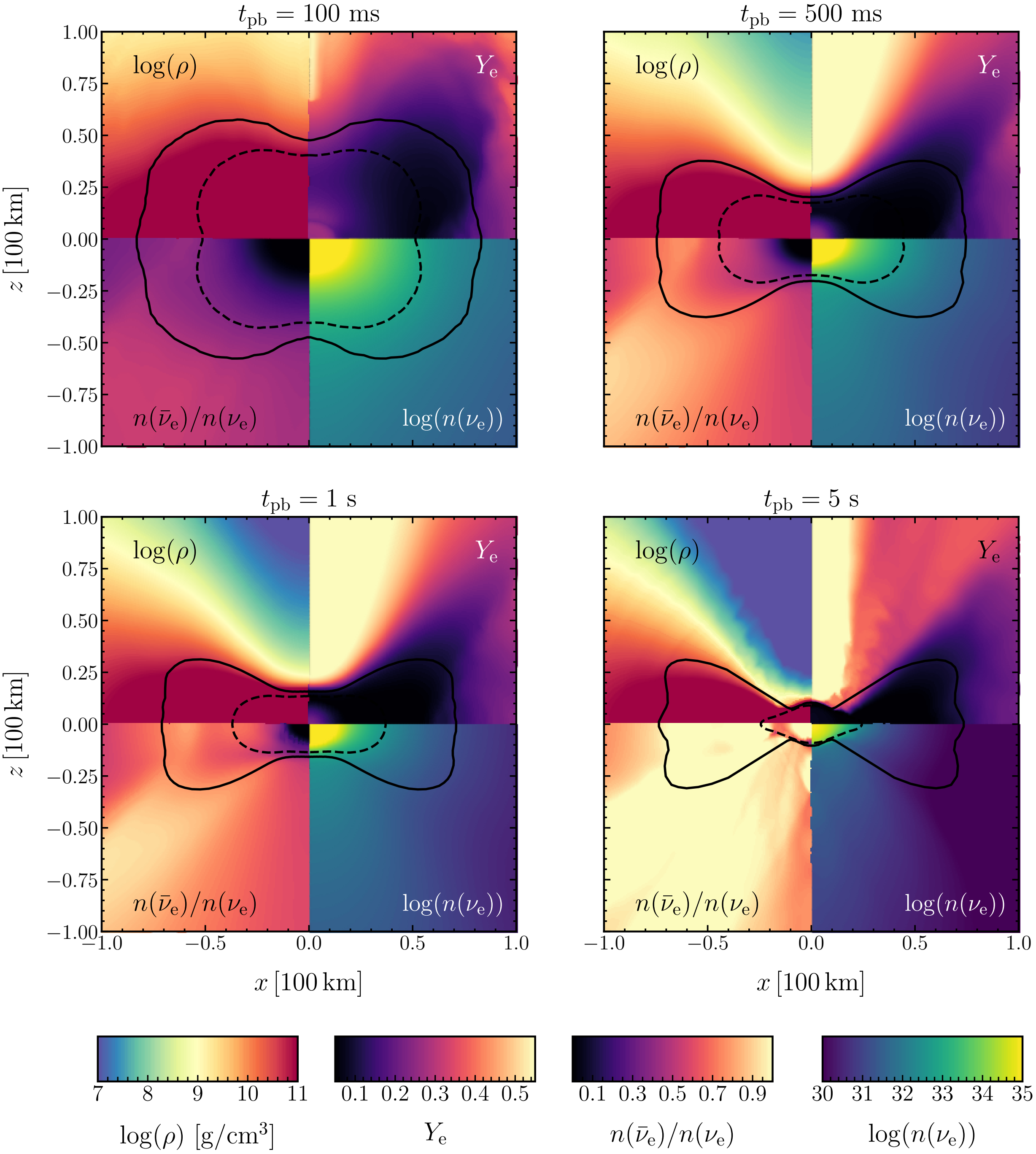

Figure A.25: Rotating model *M1.61-J0.47*. Same figure as figure A.23.

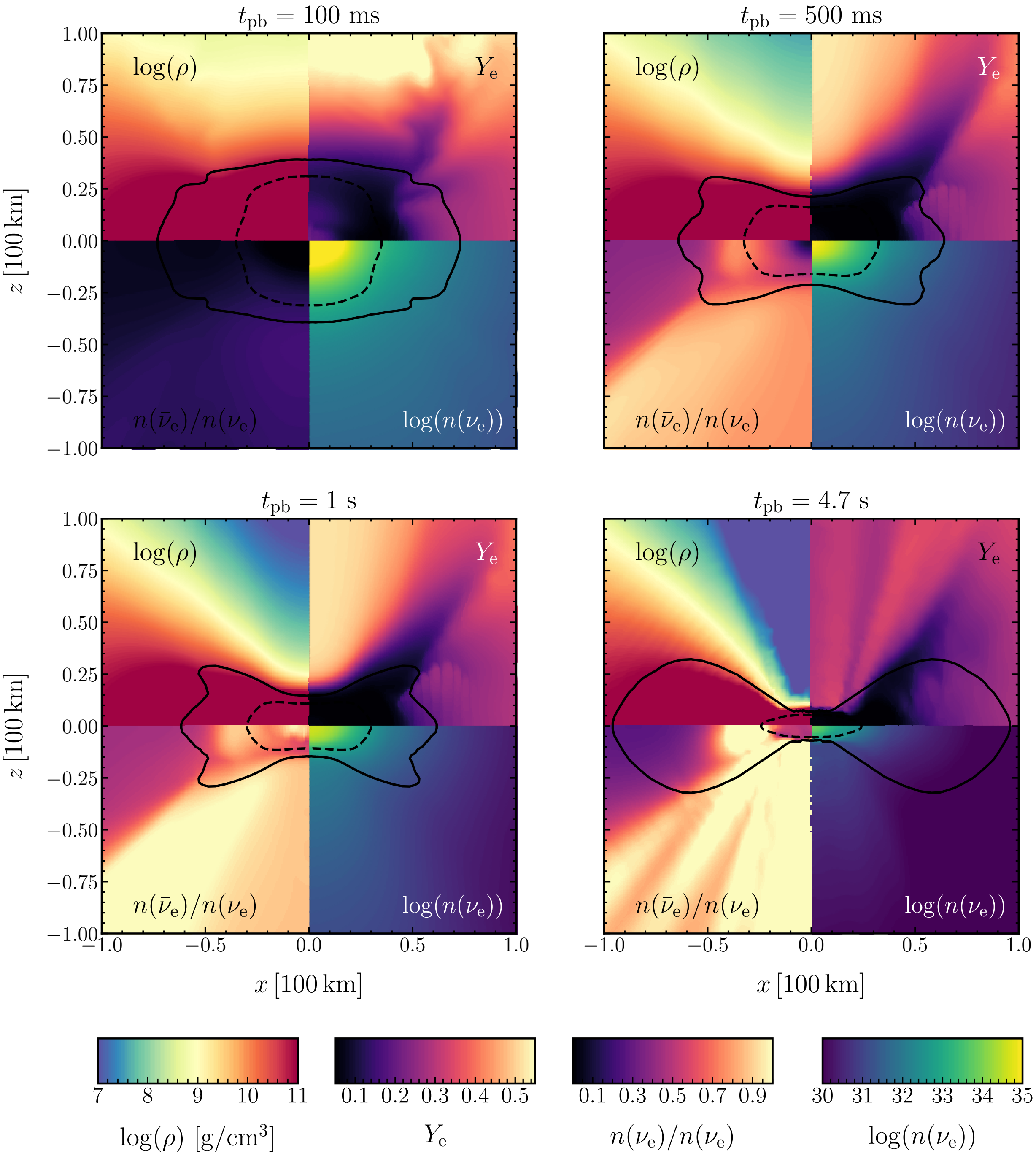

Figure A.26: High-β rotating model *M1.61-J0.78-Dl*. Same figure as figure A.23.

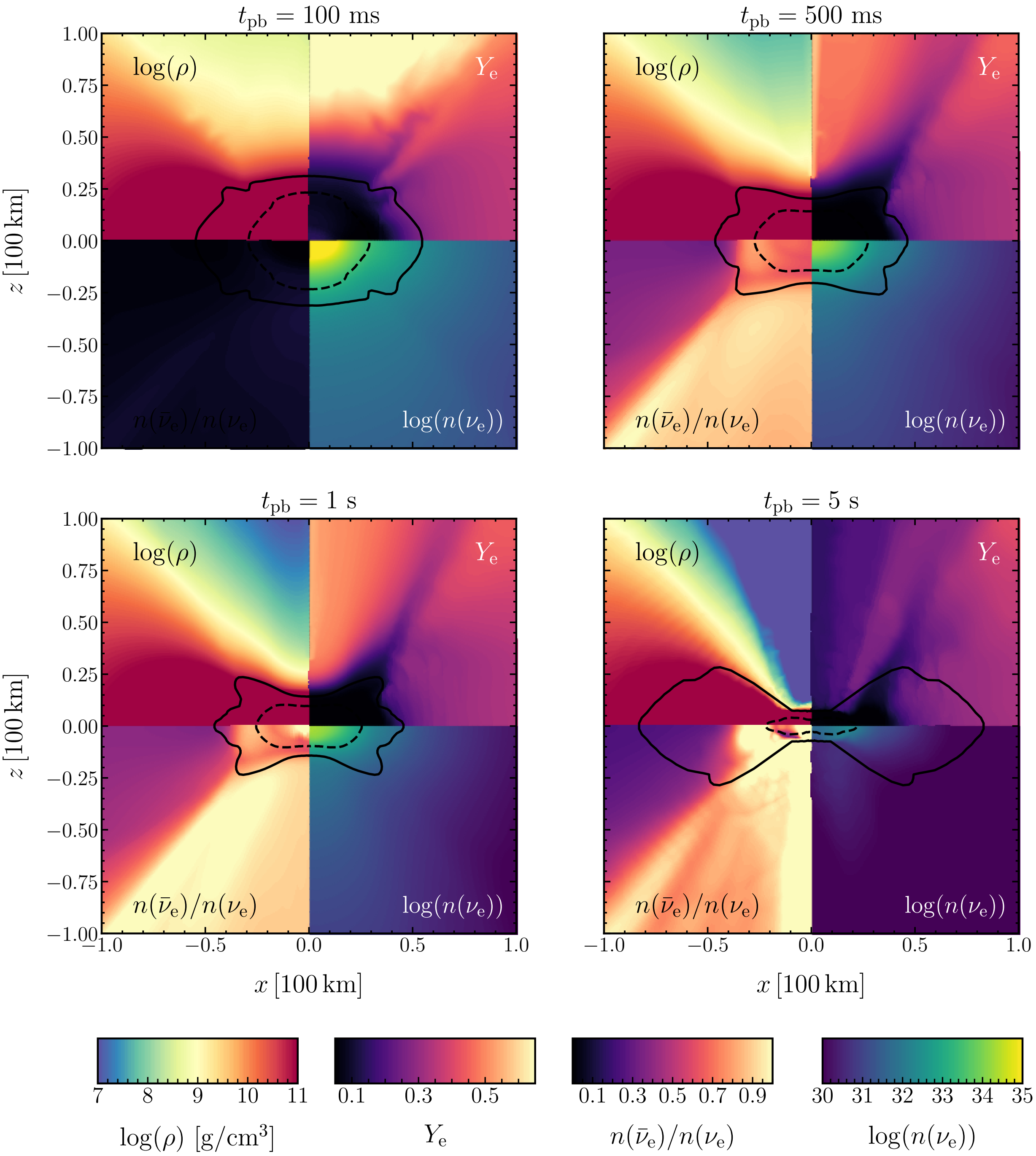

Figure A.27: High-β rotating model *M1.91-J1.63-Dl*. Same figure as figure A.23.

Table A.1: Summary of the basic parameters of the AIC models initially, at core bounce, and the end of the simulation. M is the mass, Ω the angular velocity, R is the radius, ρ the density, T is the temperature, J the angular momentum, $E_{\rm rot}$ the total rotational energy, β is the ratio to the total rotational to gravitational energy, t is the time, P is the spin period, I is the moment of inertia, and $E_{\rm expl}$ is the explosion energy. The first nine rows show the designated quantities of the progenitors, quantities with subscript "b" are measured at core bounce, "ic" stands for the inner core, and "NS" for neutron star. The quantities of the neutron star and ejecta mass are calculated at the end of each simulation.

Model	M1.42-J0	M1.42-J0.23-Dl	M1.61-J0.47	M1.61-J0.78-Dl	M1.91-J1.09	M1.91-J1.63-Dl
M [M$_\odot$]	1.422	1.422	1.609	1.611	1.919	1.906
$\Omega_{\rm c}$ [rad/s]	0	0	12.0	5.55	18.0	5.33
$\Omega_{\rm max}$ [rad/s]	0	3.80	19.64	6.13	25.66	8.22
$R_{\rm eq}$ [km]	816	2250	1498	2897	2377	3982
$\rho_{\rm c}$ [10^{10} g/cm^3]	5.00	0.40	5.00	0.40	5.00	0.40
T_c [10^{10}K]	1.00	0.413	1.00	0.413	1.00	0.413
J [10^{50} erg $\cdot$ s]	0	0.231	0.471	0.782	1.085	1.630
$E_{\rm rot}$ [10^{50}erg]	0	0.299	3.941	2.094	10.471	5.033
$\beta_{\rm init}$	0	0.007	0.038	0.046	0.082	0.091
$t_{\rm b}$ [s]	0.0377	0.346	0.0396	0.426	0.041	0.825
$\rho_{\rm b,max}$ [10^{14} g/cm^3]	4.071	3.842	3.188	0.498	2.533	0.300
$M_{\rm ic,b}$ [M$_\odot$]	0.584	0.541	0.569	1.478	0.721	1.901
$\Omega_{\rm ic,b}$ [rad/s]	0	2343.1	2377.9	34.8	908.1	15.8
$\beta_{\rm ic,b}$	0	0.027	0.092	0.137	0.105	0.174
$t_{\rm end}$ [s]	6.74	7.83	6.80	4.67	6.15	6.09
$M_{\rm NS}$ [M$_\odot$]	1.4093	1.2952	1.3704	1.1371	1.2960	0.9648
$\Omega_{\rm NS}$ [rad/s]	0	4370.578	1970.466	1287.4262	1636.608	1106.785
$P_{\rm NS}$ [ms]	0	1.438	3.1887	4.880	3.839	5.677
$R_{\rm NS}$ [km]	13.2	11.55/58.12	9.95/95.08	8.45/101.90	9.05/98.80	7.75/99.56
$J_{\rm NS}$ [10^{49} erg $\cdot$ s]	0	1.136	2.321	2.397	2.554	1.875
$I_{\rm NS}$ [10^{46} cm^2 $\cdot$ g]	0	2.599	1.178	1.862	1.560	1.694
$\beta_{\rm NS}$	0	0.1388	0.2529	0.3344	0.3002	0.3272
$M_{\rm disk}$ [M$_\odot$]	0.00013	0.05898	0.11581	0.29427	0.42859	0.75393
$M_{\rm ej}$ [10^{-3} M$_\odot$]	7.901	52.454	25.914	21.221	18.699	5.767
$E_{\rm expl}$ [10^{50} erg]	1.431	2.939	1.662	0.450	1.002	0.115

Additional Information

Resources This research project is funded by the Max Planck Institute for Astrophysics, part of the Max Planck Society. The simulations carried out in this Thesis have made use of the granted computed time from the Leibniz Supercomputing Centre (LRZ) of a total of 18.3 Million core hours under the project number pn49sa. Additionally, parts of the calculations and testing have been carried out on the HPC systems Cobra and Raven of the Max Planck Computing and Data Facility (MPCDF).

Software The simulations are carried out with the code ALCAR (Just et al., 2018, 2015b; Obergaulinger, 2008). The post-processing of the simulations uses IPYTHON, and in particular, the following modules are used; Matplotlib (Hunter, 2007), NumPy (Harris et al., 2020), Scipy (Virtanen et al., 2020), and CMasher[1] (van der Velden, 2020).
This research has made use of NASA's Astrophysics Data System Bibliographic Services.

---

[1] https://pypi.org/project/cmasher/

List of Figures

1.1 Schematic representation of neutron star (NS) formation channels. Neutron stars are mainly formed in the core collapse of massive stars with masses $\geq 8\,\mathrm{M}_\odot$ that have evolved through the advanced nuclear-burning stages to create an onion-shell structure. Apart from the massive stellar collapse, they are also formed in the accretion-induced collapse of ONeMg white dwarfs. However, existing ones in a binary neutron star system can merge and also give birth to a new neutron star. Sizes are not shown in scale. 3

1.2 Mass accretion rate as a function of the mass of an ONeMg white dwarf (left panel) and a CO white dwarf (right panel). Nomoto & Kondo (1991) present the regions where white dwarf collapse is possible by electron captures. In the case of a massive and cold CO white dwarf, C deflagration could still lead to the collapse because of the high central densities. Figure taken from Nomoto & Kondo (1991). 8

3.1 Color-coded density of each progenitor in the xz plane. From left to right, the upper left model has a mass of $1.42\,\mathrm{M}_\odot$, high central density, and no rotation, i.e. the model M1.42-J0, the bottom left one is the M1.42-J0.23-Dl with the same mass and slow rotation on the surface. The middle panels show the rotating progenitors with $1.61\,\mathrm{M}_\odot$, i.e., M1.61-J0.47 (middle top) and M1.61-J0.78-Dl (middle bottom). The right panels show the rotating progenitors with $1.91\,\mathrm{M}_\odot$, i.e., M1.91-J1.09 (right top) and M1.91-J1.63-Dl (right bottom). Mass and rotation increase towards the right panels. The models are embedded in a CSM with radially decreasing density and temperature profiles. 27

3.2 Color-coded angular velocity of each progenitor in the xz plane. From left to right, the bottom left is the model M1.42-J0.23-Dl, with a mass of 1.42 $M_\odot$. The middle panels show the rotating progenitors with 1.61 $M_\odot$, i.e., M1.61-J0.47 (middle top) and M1.61-J0.78-Dl (middle bottom). The right panels show the rotating progenitors with 1.91 $M_\odot$, i.e., M1.91-J1.09 (right top) and M1.91-J1.63-Dl (right bottom). The angular velocity in our progenitors depends on the distance x to the rotational axis. The circum-stellar medium is non-rotating. 28

3.3 Color-coded z-component of the specific angular momentum of each progenitor in the xz plane. From left to right, the bottom left one is the model M1.42-J0.23-Dl. The middle panels show the rotating progenitors with M1.61-J0.47 in the middle top and M1.61-J0.78-Dl in the middle bottom panel. The right panels show the rotating progenitors M1.91-J1.09 in the right top and M1.91-J1.63-Dl in the right bottom panel. The z-component of the specific angular momentum depends on the distance x to the rotational axis, as does the angular velocity. 30

3.4 Rotational profiles of the angular velocity at the equator as a function of radius for all models. All models reach an angular velocity maximum at a certain radius except the non-rotating one (M.142-J0) and its low-density counterpart M1.42-J0.23, which shows increasing rotation on its surface. . 31

4.1 Maximum central density as a function of post-bounce time. We follow the evolution of the maximum density of the central region of the progenitor. The black line shows the central density of the non-rotating model M1.42-J0, the grey line shows its low-density counterpart M1.42-J0.23-Dl, the blue line corresponds to the rotating model M1.61-J0.47, the light blue line to the low-density model M1.61-J0.78-Dl, the red line displays the central density of the model M1.91-J1.09, and the light orange of the model M1.91-J1.63-Dl. We follow this color-scheme throughout this Thesis. For later times, we refer the reader to the corresponding figure A.1 in the Appendix. 35

4.2 Radial profiles of the radial velocity at the poles (left panels, purple lines) and at the equator (right panels, orange lines) for each model. The different color lines show the time evolution from approximately 20 ms before the bounce until ∼100 ms after the bounce, with lighter purple/orange lines to represent early times and darker lines to correspond to later times. The first row corresponds to the model M1.42-J0, the middle row to the model M1.42-J0.23-Dl, and the bottom row to the model M1.61-J0.47. 37

4.3 Same as figure 4.2. he first row corresponds to the model M1.61L-J0.78-Dl, the middle row to the model M1.91-J1.09, and the bottom row to the model M1.91-J1.63-Dl. 38

4.4 Central angular velocity as a function of post-bounce time for the rotating models. The angular velocity is calculated as a volume average of the inner 5 km. The steep rise at 0 ms is due to the core-bounce resulting from angular momentum conservation and the further increase is because of the further contraction of the PNS. The high-β models that undergo centrifugal bounce show a less steep increase of the angular velocity. Note that this is the volume-averaged angular velocity of the inner 5 km and is not identical to the angular velocity of the inner core at bounce which is listed in table 4.1. 41

4.5 Mass-shell diagram for the simulation of M1.42-J0 color-coded by the entropy saturating at $60\,k_\mathrm{B}$/baryon. The Mass-shell diagram follows the radial evolution of defined mass-shells of specific mass as a function of post-bounce time. The dashed white lines correspond to the enclosed mass of $0.1\,\mathrm{M}_\odot$ and $1.4\,\mathrm{M}_\odot$. The thin black lines between the $0.1\,\mathrm{M}_\odot$ and the $1.4\,\mathrm{M}_\odot$ lines have a mass separation of $0.1\,\mathrm{M}_\odot$, and $0.001\,\mathrm{M}_\odot$ between the $1.4\,\mathrm{M}_\odot$ and the $1.422\,\mathrm{M}_\odot$ lines. The quantities shown are angle averaged. 43

4.6 Series of color-coded cross-sections for different quantities at three different times of evolution for the model M1.42-J0. The top row shows the radial velocity (left half panels) and the density in logarithmic scale (right half panels). The radial velocity is normalized to show the parts with zero radial velocity in white. The bottom row displays the electron fraction Y_e (left half panels) and entropy (right half panels). The Y_e is normalized to show regions with $Y_e = 0.5$ in white. The different plots show the evolution of the model at 80 ms, 1 s, and at the end of the simulation at 6.7 s post bounce. . 46

4.7 Same as in figure 4.6 for the model M1.42-J0.23-Dl. The different plots show the evolution of the model at 100 ms, 500 ms, and at the end of the simulation at 7.8 s post bounce. 47

4.8 Same as in figure 4.6 for the model M1.61-J0.47. The different plots show the evolution of the model at 80 ms, 1 s, and at the end of the simulation at 6.8 s post bounce. 48

4.9 Same as in figure 4.6 for the model M1.61-J0.78-Dl. The different plots show the evolution of the model at 100 ms, 1 s, and at the end of the simulation at 4.7 s post bounce. 49

4.10 Same as in figure 4.6 for the model M1.91-J1.09. The different plots show the evolution of the model at 80 ms, 1 s, and at the end of the simulation at 6.2 s post bounce. 50

4.11 Same as in figure 4.6 for the model M1.91-J1.63-Dl. The different plots show the evolution of the model at 80 ms, 1 s, and at the end of the simulation at 6.1 s post bounce. 51

4.12 Time evolution of the z-component of the specific angular momentum as a function of radius. The colored lines present the time evolution according to the color bar with blue corresponding to the early times $j_z - r$ profile and red lines to the final stages of the simulation. Each panel presents the time evolution of the radial dependence of the specific angular momentum for each model indicated in the plot title. The same plot that shows the specific angular momentum as a function of enclosed mass, can be found in the Appendix in figure A.14. 53
4.13 Explosion energy as a function of post-bounce time for the AIC models. The explosion energy is calculated as the sum of the gravitational, kinetic, and internal energy for the unbound material in the post-shock region. 55
4.14 Radius of the neutron star as a function of post-bounce time. The upper left panel shows the minimum neutron star radius, the upper right panel shows the maximum neutron star radius for the aspherical rotating models, the bottom left plot shows the mean neutron star radius, and the bottom right plot shows the ratio of the minimum to the maximum radius of the neutron star as a function of post-bounce time. 56
4.15 The left plot shows the baryonic mass of the formed neutron star for each AIC model as a function of post-bounce time. As neutron star we consider the material that has densities $\rho \geq 10^{11}$ g/cm^3. The right plot displays the time evolution of total angular momentum of the neutron star for each of the rotating models. 58

5.1 Luminosity (top row) and angle-averaged mean energy (bottom row) for the three evolved neutrino species: electron neutrinos ν_e (left column), electron antineutrinos $\bar{\nu}_e$ (middle column), and heavy-lepton neutrinos ν_x (right column) for the six AIC models as a function of time. Each colored line corresponds to one model as denoted in the legend. The quantities are transformed into the lab frame and evaluated at a radius of 3500 km. The time shown in the x-axis corresponds to the post-bounce time. Here we show the evolution of the neutrino luminosities and mean energies from the time of bounce until one second of evolution. The long-time evolution is shown in the Appendix in figure A.16. 62
5.2 Luminosity and angle-averaged mean energy as a function of post-bounce time for the non-rotating model M1.42-J0. The luminosity (top row) is energy integrated, calculated in the lab frame at a distance of 3500 km. Each panel in the top row shows different time intervals of the luminosity evolution for the electron neutrinos ν_e in solid black lines, the electron antineutrinos $\bar{\nu}_e$ in dashed red lines, and the heavy-lepton neutrinos ν_x in dotted blue lines. The bottom row shows the angle-averaged mean energy of the electron neutrinos ν_e (solid black lines), the electron antineutrinos $\bar{\nu}_e$ (dashed red lines), and the heavy-lepton neutrinos (dotted blue lines) as a function of post-bounce time. Notice the different y-axis scales in each panel. 63

5.3 Luminosity and angle-averaged mean energy as a function of post-bounce time for the rotating model M1.61-J0.47. Same as in figure 5.2. The same figures for the rest of the models are presented in the Appendix in figure A.17 - figure A.20. 64

5.4 Electron neutrino and electron antineutrino neutrinospheres for all of the six models plotted at different times as a function of the polar angle θ. Each colored line corresponds to a specific time from 0.3 s to 3 s post bounce. The solid lines show the neutrinosphere radius for the electron neutrinos ν_e and the dashes lines show the radius for the electron antineutrinos $\bar{\nu}_e$. The neutrinospheres are calculated by the energy-averaged opacities as shown in equation (5.2)-equation (5.4). 67

5.5 The left figure shows a cross-section of the central area of the M1.61-J0.47 AIC model at 500 ms after the bounce. The left panel is color-coded by the temperature and the right panel is color-coded by the density. The solid black/white line determines the neutrinosphere for the electron neutrinos while the dashed line shows the neutrinosphere for the electron antineutrinos. The right figure shows the same quantities for the AIC model M1.61-J0.78-Dl at 500 ms after the bounce. The color bars are chosen in the same range to enhance the different thermodynamical conditions in the core of each model. 68

5.6 Radial profiles of temperature at the poles (black), mid-latitudes (blue), and equator (red) for the rotating model M1.61-J0.74 (left panel), and the high-β model M1.61-J0.78-Dl. Despite the same mass of these models, the different central density and rotational profiles change the temperature profiles across all latitudes. The vertical lines show the radial location of the neutrinosphere for the electron neutrinos (solid lines) and the electron antineutrinos (dashed lines) at the poles (black), mid-latitudes (blue) and equator (red), in both plots. 69

5.7 Each panel shows the luminosity as a function of post-bounce time along different directions for electron neutrinos (solid lines), electron antineutrinos (dashed lines), and heavy-lepton neutrinos (dotted lines). The black lines show the luminosity along the poles (0°), the blue lines correspond to mid-latitudes around 50°, and the red lines show the luminosity in the equatorial direction (90°). The luminosities are evaluated at a distance of 3500 km, transformed at the lab frame, and they are scaled up to the whole sphere, i.e., the directional luminosity corresponds to the total luminosity we would observe if the selected direction were emitted in all directions (see equation (5.5)). Each panel shows the luminosities for each model that is indicated in the upper left box in each figure. The same figure for longer times is shown in the Appendix in figure A.21. 70

5.8 Mean energy as a function of post-bounce time angle-averaged in the polar direction (black lines), the mid-latitudes (blue lines) and the equator (red lines). The angle averaged energy is the integrated energy along 10° around 0° for the poles, 50° for the mid-latitudes and 90° for the equator, and scaled up to the whole sphere, in a similar manner as the luminosity. Each panel displays one of the six model as denoted in the corresponding label. The solid lines of each color show the electron neutrinos ν_e, the dashes lines show the electron antineutrinos ν_e, and the dotted lines show the heavy-lepton neutrinos ν_x. The same figure for longer times is shown in the Appendix in figure A.22. 71

6.1 Electron-to-baryon ratio Y_e mass distribution of the ejected material. Each colored line shows the distribution of each model as denoted in the legend. The distribution is calculated as the amount of mass that crosses a designated ellipsoidal surface located around each model and has positive explosion energy from $\sim$ 100 ms after bounce until the end of each simulation. Integrating each histogram yield the total ejecta mass for each model. The bin size is the same for all distributions and set to δY_e= 0.006. 77

6.2 This figure is a collection of the Y_e distributions of the ejecta mass. Each panel shows the distribution of the corresponding model which is indicated by the title of each panel. As in figure 6.2, the bin-size is set to δY_e= 0.006. The different colors represent different intervals in time at which the mass is ejected with a given Y_e. To be more specific, the distributions built on top of one another show the additional mass that is ejected in each time interval. Thus, the last time interval corresponds to the total ejected mass. 79

6.3 Mass-averaged ejecta properties as a function of the polar angle θ. Each row shows the properties for each model; the first row shows the spherical-symmetric model M1.42-J0, the middle row shows the rotating model M1.42-J0.23-Dl, and the bottom row the model M1.61-J0.47. For each row the left panel shows the angle-averaged (in 10° bins) mass ejecta as a function of latitude, the middle panels show the mass-averaged radial velocity of the ejecta, and the right panels show the mass-averaged Y_e. The different lines present the different time intervals; black lines show the ejecta before 200 ms after bounce, the orange lines between 200 and 300 ms, the blue lines between 300 and 500 ms, the red lines between 500 ms and 1 s, and the purple lines between 1 and 2 s post bounce. The mass ejecta properties are measured as the matter that crosses an ellipsoidal surface that is located around the progenitor in the same way as in the Y_e histograms in figure 6.1 and figure 6.2. 81

6.4 Mass-averaged ejecta properties as a function of the polar angle θ, same as in figure 6.3. Here the models M1.61-J0.78-Dl, M1.91-J1.09, and M1.91-J1.63-Dl are displayed. 82

6.5 A collection of cross sectional cuts at different points in time, color-coded by four different quantities. In each plot, that represents one point in time shown in the title of each plot, the left upper panel shows the logarithm of the density, the right upper panel shows the electron fraction Y_e, the bottom left shows the ratio of the electron antineutrino number density to the electron neutrino number density, i.e., $n(\bar{\nu}_e)/n(\nu_e)$, and the right bottom panel shows the logarithm of the ν_e number density. The same figure for the rest of the models can be found in the Appendix in figure A.23 - figure A.27. 85

A.1 Maximum central density as a function of post-bounce time. The time $t = 0$ is the moment of the core bounce. The time of the bounce is calculated as the time that the inner $\sim 100\,\mathrm{km}$ have entropy $\leq 3\,k_\mathrm{B}$. The models M1.61-J0.78-Dl and M1.91-J1.63-Dl, undergo centrifugal bounce and they do not reach nuclear saturation densities. However, the steep density increase at the same time as the models that undergo pressure bounce seems as a good approximation for these models as well. The spread of the central densities comes from the influence of the rotation on the core bounce. We discuss the collapse of the white dwarfs in section 4.1. 91

A.2 A sequence of cross-sectional cuts of the model *M1.42-J0*. Each plot shows the density (right-half panels) and the radial velocity (left half panels) in the xz plane at different points in time. The blue-red color bar for the radial velocity is normalized, so the parts with zero radial velocity are shown in white. The core collapses homologously, and at the core bounce, the shock wave develops spherically symmetric. A neutron star of $1.4\,\mathrm{M}_\odot$ is born in this AIC model, and the ejecta propagates spherically symmetric. At late times, the ejecta detaches from the central region and propagates in a shell-like configuration. 92

A.3 A sequence of cross-sectional cuts of the model *M1.42-J0* color-coded by the electron fraction Y_e (left-half panels) and entropy-per-baryon (right-half panels) from the start of the collapse until 5 s of post-bounce evolution. After the core bounce, a short period of convection is developed, which drives neutron-rich material in the ejecta, which is expelled by the shock wave. At later times, ν_e absorption raises the Y_e, creating proton-rich material in the ejecta. 93

A.4 Time sequence of cross-sectional cuts color-coded by the density (right-half panels) and the radial velocity (left-half panels) for the rotating model *M1.42-J0.23-Dl*. This model is slowly rotating and creates a low-mass disk of $0.06\,\mathrm{M}_\odot$, which leaves enough material to be ejected. The total ejecta mass is $52.5 \cdot 10^{-3}$, and the neutron star has a mass of $1.3\,\mathrm{M}_\odot$. 94

A.5 Time sequence of cross-sectional cuts color-coded by the electron fraction Y_e (left-half panels) and the entropy-per-baryon (right-half panels) for the rotating model *M1.42-J0.23-Dl*. The angular variation of the neutrino luminosities creates the characteristic butterfly-shaped ejecta in the Y_e space. In the poles, we find high-entropy proton-rich material in the ejecta, while at the mid-latitudes, we find lower entropy neutron-rich ejecta. At the equatorial plane, the Y_e stays at 0.5, which is the initial value of the progenitor. Because of the disk that stays centrifugally supported in the equator, the ejecta there do not receive neutrino luminosity; thus, no ν_e or $\bar{\nu}_e$ absorption can alter the electron fraction. 95

A.6 Time sequence of cross-sectional cuts color-coded by the density (right-half panels) and the radial velocity (left-half panels) for the rotating model *M1.61-J0.47*. This model has a high central density at initialization and collapses fast. The outflow is constrained in the polar direction due to the disk forming around the neutron star. This model yields a total of $25.9 \cdot 10^{-3}\,\mathrm{M}_{\odot}$ and a forms a neutron star of $1.37\,\mathrm{M}_{\odot}$. 96

A.7 Time sequence of cross-sectional cuts color-coded by the electron fraction Y_e (left-half panels) and the entropy-per-baryon (right-half panels) for the rotating model *M1.61-J0.47*. This rotating model shows the latitudinal variation of the Y_e as in the case of M1.42-J0.23-Dl. 97

A.8 Time sequence of cross-sectional cuts color-coded by the density (right-half panels) and the radial velocity (left-half panels) for the high-β rotating model *M1.61-J0.78-Dl*. This model undergoes centrifugal collapse because during collapse the core becomes rotationally supported. In this model the newly born neutron star has a mass of $1.14\,\mathrm{M}_{\odot}$, the disk that surrounds the neutron star has a mass of $0.29\,\mathrm{M}_{\odot}$ and a total of $21.22 \cdot 10^{-3\mathrm{M}_{\odot}}$ are ejected. 98

A.9 Time sequence of cross-sectional cuts color-coded by the electron fraction Y_e (left-half panels) and the entropy-per-baryon (right-half panels) for the high-β-rotating model *M1.61-J0.78-Dl*. In this model, much of the equatorial material is swiped away as the shock wraps around the progenitor. This is seen as the white parts of the Y_e, which is white dwarf material that has not received neutrino luminosity to alter its Y_e. The neutron-rich part of the ejecta comes at later times but again from the mid-latitudes. 99

A.10 Time sequence of cross-sectional cuts color-coded by the density (right-half panels) and the radial velocity (left-half panels) for the rotating model *M1.91-J1.09*. This model shows similar collapse and explosion dynamics as the rotating model M1.61-J0.47. Due to the higher degree of rotation and higher mass, this model creates a larger disk, compared of the model M1.61-J0.47, with a mass of $0.43\,\mathrm{M}_{\odot}$. The total ejecta mass is $18.69 \cdot 10^{-3}\,\mathrm{M}_{\odot}$ and the neutron star has a mass of $1.29\,\mathrm{M}_{\odot}$. 100

A.11 Time sequence of cross-sectional cuts color-coded by the electron fraction Y_e (left-half panels) and the entropy-per-baryon (right-half panels) for the rotating model *M1.91-J1.09.* The evolution of the ejecta properties is similar to the rotating model M1.61-J0.47. 101

A.12 Time sequence of cross-sectional cuts color-coded by the density (right-half panels) and the radial velocity (left-half panels) for the high-β rotating model *M1.91-J1.63-Dl.* This model has the highest angular momentum of all models and low central density. It collapses very slowly, and while that is, the outer layer of the progenitor gets unbound. This model undergoes a centrifugal bounce. The remnant consists of a neutron star with a mass of $0.96\,\mathrm{M}_{\odot}$, a centrifugally supported disk of $0.75\,\mathrm{M}_{\odot}$. The total ejecta mass of this model is $5.7 \cdot 10^{-3}\,\mathrm{M}_{\odot}$. 102

A.13 Time sequence of cross-sectional cuts color-coded by the electron fraction Y_e (left-half panels) and the entropy-per-baryon (right-half panels) for the high-β rotating model *M1.91-J1.63-Dl.* This model's particular collapse and explosion dynamics allow very little material to be ejected. In contrast, most of the ejecta comes later as the neutrino-driven wind ejects material from the surface of the PNS and the surface of the disk. At late times, we find neutron-rich outflow mainly from the polar regions. 103

A.14 Time evolution of the z-component of the specific angular momentum as a function of the enclosed mass. The colored lines present the time evolution according to the color bar, with black and dark blue corresponding to the initial j_{z} and purple to pink lines to the final stages of the simulation. Each panel presents the evolution of the specific angular momentum for each model indicated in the plot title. This is supplementary to the specific angular momentum evolution as a function of radius shown in figure 4.12. . 104

A.15 Each panel displays the z-component of the specific angular momentum as a function of radius. The color-coding of the lines show the time evolution with yellow being the early times, i.e., before the collapse and at core bounce, and the darker shades show the late time evolution until the end of each simulation. Here we display the inner regions until 100 km which is approximately the maximum radius of the neutron stars formed (apart from the model M1.42-J0.23-Dl that the equatorial radius of the neutron star is 58 km). This is an addition to the figure 4.12. 105

A.16 Luminosity (top row) and angle-averaged mean energy (bottom row) for the three evolved neutrino species: electron neutrinos ν_e (left column), electron antineutrinos $\bar{\nu}_e$ (middle column), and heavy-lepton neutrinos ν_x (right column) for the six AIC models as a function of post-bounce time until 5 s. Each colored line corresponds to one model, as denoted in the legend. The quantities are transformed into the lab frame and evaluated at a radius of 3500 km. The time shown in the x-axis corresponds to the post-bounce time. This shows the long-time evolution of the luminosities and the mean energies, in addition to figure 5.1. The large spread of the different values in the luminosities directly affects rotation, which alters the shape of the neutrinospheres in the PNS and the thermodynamical conditions at the neutrinospheres. The higher the spin rates, the lower the central density and temperature in the core at bounce, which leads to a modest neutrino emission. This is true for the rotating models. The high-β rotating models have lower central spin rates, but due to the large reservoir of angular momentum, they undergo centrifugal bounce, which translates to lower central densities. Therefore, the high-β models, i.e., M1.61-J0.78-Dl and M1.91-1.63-Dl, have even lower luminosities than the rest. 106

A.17 Luminosity and angle-averaged mean energy as a function of post-bounce time for the model *M1.42-J0.23-Dl*. The luminosity (top row) is energy integrated, calculated in the lab frame at a distance of 3500 km. Each panel in the top row shows different time intervals of the luminosity as a function of time and the bottom rows the angle-averaged mean energy as a function of time. In each panel the three evolved neutrino species are shown; the electron neutrinos ν_e in solid black lines, the electron antineutrinos $\bar{\nu}_e$ in dashed red lines, and the heavy-lepton neutrinos ν_x in dotted blue lines. The bottom row shows the angle-averaged mean energy of the electron neutrinos ν_e (solid black lines), the electron antineutrinos $\bar{\nu}_e$ (dashed red lines), and the heavy-lepton neutrinos (dotted blue lines) as a function of post-bounce time. Notice the different y-axis scales in each panel. This appends on the figure 5.2, and figure 5.3. 107

A.18 Same as figure A.17 for the model *M1.61-J0.78-Dl*. 108

A.19 Same as figure A.17 for the model *M1.91-J1.09*. 108

A.20 Same as figure A.17 for the model *M1.91-J1.63-Dl*. 109

A.21 Each panel shows the luminosity as a function of post-bounce time along different directions for electron neutrinos (solid lines), electron antineutrinos (dashed lines), and heavy-lepton neutrinos (dotted lines). The black lines show the luminosity along the poles, the blue lines correspond to mid-latitudes around 50°, and the red lines show the luminosity in the equatorial direction. The luminosities are evaluated at a distance of 3500 km, transformed at the lab frame, and they are scaled up to the whole sphere, i.e., the directional luminosity corresponds to the total luminosity we would observe if the selected direction were emitted in all directions. Each panel shows the luminosities for each model that is indicated in the upper left box in each figure. We define this luminosity as the isotropic-equivalent-luminosity and is calculated by equation (5.5). 110

A.22 Mean energy as a function of post-bounce time angle-averaged in the polar direction (black lines), the mid-latitudes (blue lines) and the equator (red lines). The angle averaged energy is the integrated energy along 10° around 0° for the poles, 50° for the mid-latitudes and 90° for the equator, and scaled up to the whole sphere, similarly as the luminosity. Each panel displays one of the six model as denoted in the corresponding label. The solid lines of each color show the electron neutrinos ν_e, the dashes lines show the electron antineutrinos ν_e, and the dotted lines show the heavy-lepton neutrinos ν_x. . 111

A.23 Non-rotating model *M1.42-J0.* A collection of cross sectional cuts at different points in time, color-coded by four different quantities. In each plot, that represents one point in time shown in the title of each plot, the left upper panel shows the logarithm of the density, the right upper panel shows the electron fraction Y_e, the bottom left shows the ratio of the electron antineutrino number density to the electron neutrino number density, i.e., $c(\bar{\nu}_e)/n(\nu_e)$, and the right bottom panel shows the logarithm of the ν_e number density. 112

A.24 Rotating model *M1.42-J0.23-Dl.* Same figure as figure A.23. 113

A.25 Rotating model *M1.61-J0.47.* Same figure as figure A.23. 114

A.26 High-β rotating model *M1.61-J0.78-Dl.* Same figure as figure A.23. 115

A.27 High-β rotating model *M1.91-J1.63-Dl.* Same figure as figure A.23. 116

List of Tables

3.1 AIC progenitor properties. The columns list different physical parameters, where M is the mass of the white dwarf, $\Omega_{\rm c}$ the central angular velocity, $\Omega_{\rm max}$ the maximum value of the angular velocity at the equator, $R_{\rm eq}$ the equatorial radius, T_c the central temperature, J the initial total angular momentum, $E_{\rm rot}$ the total rotational energy, and $\beta_{\rm init}$ the ratio of the rotational to the gravitational energy in the initial white dwarf model. 26

4.1 AIC properties during the infall and collapse phase. The columns list different physical parameters, where M is the mass of the white dwarf, $\Omega_{\rm c}$ the central angular velocity, J the total angular momentum, and $\beta_{\rm init}$ the ratio of the total gravitational to rotational energy. The subscript "0" denotes the physical quantity at the initial state of the progenitor while the "ic,b" denotes the physical quantity of the inner core at core bounce. 40

4.2 Summary of global properties for the simulations of the AIC models. The model name is listed in the first row, $t_{\rm end}$ is the final time of the corresponding simulation, $M_{\rm NS}$ is the baryonic mass of the NS, $R_{\rm NS}$ is the min/max radius of the NS, $M_{\rm disk}$ is the mass of the circum-neutron star disk, $M_{\rm ej}$ is the total ejected mass calculated at the end of each simulation, and $E_{\rm expl}$ is the explosion energy (see section 4.4). 45

4.3 Summary of the neutron star properties. The first column lists the AIC models, $M_{\rm NS}$ is the neutron star mass, $R_{\rm NS}$ is the min/max radius of the neutron star, $\Omega_{\rm NS}$ the angular velocity, $P_{\rm NS}$ the neutron star spin, $J_{\rm NS}$ the total angular momentum, $I_{\rm NS}$ is the moment of inertia, and $\beta_{\rm NS}$ the ratio of the rotational to the gravitational energy of the neutron star. The quantities are evaluated at the end of each simulation. 57

5.1 Summary of the maximum value of the neutrino luminosity and angle-averaged mean energy for ν_e, $\bar{\nu}_e$, and ν_x. The first row shows the maximum central density at bounce (see table 4.1). The neutrino quantities are measured at the peak of the L_{ν_e} for electron neutrinos and in the first 100 ms for the rest of the neutrino species. 66

6.1 Ejecta mass in units of $10^{-3}\,\mathrm{M}_\odot$ as a function of the ejection time, which is denoted in the second row. The first column lists all the models, and each row shows the amount of mass ejected in the corresponding time interval. We start the calculation when the ejecta breaks out of the progenitor, i.e., at $\sim 0.07 - 0.1\,\mathrm{s}$ post-bounce time, and we follow the ejection until the end of the corresponding simulation (see table 4.2 second column and legends in figure 6.2) The last column gives the total ejected mass for each model at the end of each simulation. Note that the numbers are rounded in the third decimal. 76

6.2 Ejecta mass in units of $10^{-3}\,\mathrm{M}_\odot$ at different Y_e range which is denoted in the second row. The first column lists all the models and each row shows the amount of mass ejected in the corresponding Y_e interval. All quantities are measured at the end of each simulation. 78

A.1 Summary of the basic parameters of the AIC models initially, at core bounce, and the end of the simulation. M is the mass, Ω the angular velocity, R is the radius, ρ the density, T is the temperature, J the angular momentum, E_{rot} the total rotational energy, β is the ratio to the total rotational to gravitational energy, t is the time, P is the spin period, I is the moment of inertia, and E_{expl} is the explosion energy. The first nine rows show the designated quantities of the progenitors, quantities with subscript "b" are measured at core bounce, "ic" stands for the inner core, and "NS" for neutron star. The quantities of the neutron star and ejecta mass are calculated at the end of each simulation. 117

Bibliography

Bibliography

Abbott, B. P., Abbott, R., Abbott, T. D., et al. 2017, Physical Review Letters, 119, 161101, doi: 10.1103/PhysRevLett.119.161101

Abdikamalov, E. B., Ott, C. D., Rezzolla, L., et al. 2010, Physical Review D, 81, 044012, doi: 10.1103/PhysRevD.81.044012

Anderson, G. E., Miller-Jones, J. C. A., Middleton, M. J., et al. 2019, Monthly Notices of the Royal Astronomical Society, 489, 1181, doi: 10.1093/mnras/stz1303

Arnett, W. D. 1987, The Astrophysical Journal, 319, 136, doi: 10.1086/165439

Baade, W., & Zwicky, F. 1934, Physical Review, 46, 76, doi: 10.1103/PhysRev.46.76.2

Bailyn, C. D., & Grindlay, J. E. 1990, The Astrophysical Journal, 353, 159, doi: 10.1086/168602

Bauswein, A., Baumgarte, T. W., & Janka, H. T. 2013a, Physical Review Letters, 111, 131101, doi: 10.1103/PhysRevLett.111.131101

Bauswein, A., Goriely, S., & Janka, H. T. 2013b, The Astrophysical Journal, 773, 78, doi: 10.1088/0004-637X/773/1/78

Belczynski, K., Askar, A., Arca-Sedda, M., et al. 2018, Astronomy & Astrophysics, 615, A91, doi: 10.1051/0004-6361/201732428

Bethe, H. A. 1990, Reviews of Modern Physics, 62, 801, doi: 10.1103/RevModPhys.62.801

Bhattacharya, D., & van den Heuvel, E. P. J. 1991, Physics Reports, 203, 1, doi: 10.1016/0370-1573(91)90064-S

Bollig, R., Yadav, N., Kresse, D., et al. 2021, The Astrophysical Journal, 915, 28, doi: 10.3847/1538-4357/abf82e

Boyles, J., Lorimer, D. R., Turk, P. J., et al. 2011, The Astrophysical Journal, 742, 51, doi: 10.1088/0004-637X/742/1/51

Brooks, J., Bildsten, L., Schwab, J., & Paxton, B. 2016, The Astrophysical Journal, 821, 28, doi: 10.3847/0004-637X/821/1/28

Brooks, J., Schwab, J., Bildsten, L., et al. 2017, The Astrophysical Journal, 850, 127, doi: 10.3847/1538-4357/aa9568

Bruenn, S. W. 1985, Astrophysical Journal Supplement Series, 58, 771, doi: 10.1086/191056

Bugli, M., Guilet, J., Foglizzo, T., & Obergaulinger, M. 2023, Monthly Notices of the Royal Astronomical Society, 520, 5622, doi: 10.1093/mnras/stad496

Bugli, M., Guilet, J., & Obergaulinger, M. 2021, Monthly Notices of the Royal Astronomical Society, 507, 443, doi: 10.1093/mnras/stab2161

Buras, R., Janka, H. T., Rampp, M., & Kifonidis, K. 2006a, Astronomy & Astrophysics, 457, 281, doi: 10.1051/0004-6361:20054654

Buras, R., Rampp, M., Janka, H. T., & Kifonidis, K. 2006b, Astronomy & Astrophysics, 447, 1049, doi: 10.1051/0004-6361:20053783

Burbidge, E. M., Burbidge, G. R., Fowler, W. A., & Hoyle, F. 1957, Reviews of Modern Physics, 29, 547, doi: 10.1103/RevModPhys.29.547

Burgio, G. F., Schulze, H. J., Vidaña, I., & Wei, J. B. 2021, Progress in Particle and Nuclear Physics, 120, 103879, doi: 10.1016/j.ppnp.2021.103879

Burrows, A. 2013, Reviews of Modern Physics, 85, 245, doi: 10.1103/RevModPhys.85.245

Burrows, A., Radice, D., & Vartanyan, D. 2019, Monthly Notices of the Royal Astronomical Society, 485, 3153, doi: 10.1093/mnras/stz543

Caiazzo, I., Burdge, K. B., Fuller, J., et al. 2021, Nature, 595, 39, doi: 10.1038/s41586-021-03615-y

Cameron, A. G. W. 1957, The Publications of the Astronomical Society of the Pacific, 69, 201, doi: 10.1086/127051

Canal, R., Isern, J., & Labay, J. 1990, Annual Review of Astronomy and Astrophysics, 28, 183, doi: 10.1146/annurev.astro.28.1.183

Cao, X.-F., Yu, Y.-W., & Zhou, X. 2018, The Astrophysical Journal, 858, 89, doi: 10.3847/1538-4357/aabadd

Chan, H.-S., Chu, M.-c., & Leung, S.-C. 2022, The Astrophysical Journal, 941, 115, doi: 10.3847/1538-4357/aca09b

—. 2023, The Astrophysical Journal, 945, 133, doi: 10.3847/1538-4357/acbc1d

Chandrasekhar, S. 1931, Monthly Notices of the Royal Astronomical Society, 91, 456, doi: 10.1093/mnras/91.5.456

—. 1935, Monthly Notices of the Royal Astronomical Society, 95, 207, doi: 10.1093/mnras/95.3.207

Clark, D. H., & Stephenson, F. R. 1977, The historical supernovae

Clark, G. W. 1975, The Astrophysical Journal Letters, 199, L143, doi: 10.1086/181869

Colella, P., & Woodward, P. R. 1984, Journal of Computational Physics, 54, 174, doi: 10.1016/0021-9991(84)90143-8

Colgate, S. A., & Johnson, M. H. 1960, Phys. Rev. Lett., 5, 235, doi: 10.1103/PhysRevLett.5.235

Colgate, S. A., & White, R. H. 1966, The Astrophysical Journal, 143, 626, doi: 10.1086/148549

Comella, J. M., Craft, H. D., Lovelace, R. V. E., & Sutton, J. M. 1969, Nature, 221, 453, doi: 10.1038/221453a0

Cooray, A., Farmer, A. J., & Seto, N. 2004, The Astrophysical Journal Letters, 601, L47, doi: 10.1086/381780

Courant, R., Friedrichs, K., & Lewy, H. 1928, Mathematische Annalen, 100, 32, doi: 10.1007/BF01448839

Darbha, S., Metzger, B. D., Quataert, E., et al. 2010, Monthly Notices of the Royal Astronomical Society, 409, 846, doi: 10.1111/j.1365-2966.2010.17353.x

Dessart, L., Burrows, A., Livne, E., & Ott, C. D. 2007, The Astrophysical Journal, 669, 585, doi: 10.1086/521701

Dessart, L., Burrows, A., Ott, C. D., et al. 2006, The Astrophysical Journal, 644, 1063, doi: 10.1086/503626

Dimmelmeier, H., Font, J. A., & Müller, E. 2002, Astronomy & Astrophysics, 388, 917, doi: 10.1051/0004-6361:20020563

Dimmelmeier, H., Ott, C. D., Marek, A., & Janka, H. T. 2008, Physical Review D, 78, 064056, doi: 10.1103/PhysRevD.78.064056

Duez, M. D., Liu, Y. T., Shapiro, S. L., Shibata, M., & Stephens, B. C. 2006, Physical Review Letters, 96, 031101, doi: 10.1103/PhysRevLett.96.031101

Ehring, J. 2019, Accretion Induced Collapse of White Dwarfs (MSc Thesis, Ludwig-Maximilians Universität München)

Ehring, J., Batziou, E., Janka, H.-T., Just, O., & Abdikamalov, E. 2023, in prep.

Einfeldt, B. 1988, SIAM Journal on numerical analysis, 25, 294

Einfeldt, B., Munz, C.-D., Roe, P. L., & Sjögreen, B. 1991, Journal of computational physics, 92, 273

Evans, C. R., Iben, Icko, J., & Smarr, L. 1987, The Astrophysical Journal, 323, 129, doi: 10.1086/165812

Fischer, T., Whitehouse, S. C., Mezzacappa, A., Thielemann, F. K., & Liebendörfer, M. 2010, Astronomy & Astrophysics, 517, A80, doi: 10.1051/0004-6361/200913106

Foglizzo, T., Kazeroni, R., Guilet, J., et al. 2015, Publications of the Astronomical Society of Australia, 32, e009, doi: 10.1017/pasa.2015.9

Fontaine, G., Brassard, P., & Bergeron, P. 2001, The Publications of the Astronomical Society of the Pacific, 113, 409, doi: 10.1086/319535

Freiburghaus, C., Rosswog, S., & Thielemann, F. K. 1999, The Astrophysical Journal Letters, 525, L121, doi: 10.1086/312343

Fryer, C., Benz, W., Herant, M., & Colgate, S. A. 1999, The Astrophysical Journal, 516, 892, doi: 10.1086/307119

Fryer, C. L., & Heger, A. 2000, The Astrophysical Journal, 541, 1033, doi: 10.1086/309446

Giacomazzo, B., & Perna, R. 2013, The Astrophysical Journal Letters, 771, L26, doi: 10.1088/2041-8205/771/2/L26

Gillanders, J. H., Sim, S. A., & Smartt, S. J. 2020, Monthly Notices of the Royal Astronomical Society, 497, 246, doi: 10.1093/mnras/staa1822

Glas, R. 2019, PhD thesis, Technische Universität München

Glas, R., Janka, H. T., Capozzi, F., et al. 2020, Physical Review D, 101, 063001, doi: 10.1103/PhysRevD.101.063001

Glas, R., Janka, H. T., Melson, T., Stockinger, G., & Just, O. 2019a, The Astrophysical Journal, 881, 36, doi: 10.3847/1538-4357/ab275c

Glas, R., Just, O., Janka, H. T., & Obergaulinger, M. 2019b, The Astrophysical Journal, 873, 45, doi: 10.3847/1538-4357/ab0423

Godunov, S. K. 1959, Math. Sb, 47, 217

Goldreich, P., & Weber, S. V. 1980, The Astrophysical Journal, 238, 991, doi: 10.1086/158065

Gvaramadze, V. V., Gräfener, G., Langer, N., et al. 2019, Nature, 569, 684, doi: 10.1038/s41586-019-1216-1

Hachisu, I., Kato, M., & Nomoto, K. 1996, The Astrophysical Journal Letters, 470, L97, doi: 10.1086/310303

Han, Z., & Podsiadlowski, P. 2004, Monthly Notices of the Royal Astronomical Society, 350, 1301, doi: 10.1111/j.1365-2966.2004.07713.x

Han, Z., & Webbink, R. F. 1999, Astronomy & Astrophysics, 349, L17

Hannestad, S., & Raffelt, G. 1998, The Astrophysical Journal, 507, 339, doi: 10.1086/306303

Harris, C. R., Millman, K. J., van der Walt, S. J., et al. 2020, Nature, 585, 357, doi: 10.1038/s41586-020-2649-2

Hartle, J. B. 1978, Physics Reports, 46, 201, doi: 10.1016/0370-1573(78)90140-0

Hewish, A., Bell, S. J., Pilkington, J. D. H., Scott, P. F., & Collins, R. A. 1968, Nature, 217, 709, doi: 10.1038/217709a0

Hillebrandt, W., & Niemeyer, J. C. 2000, Annual Review of Astronomy and Astrophysics, 38, 191, doi: 10.1146/annurev.astro.38.1.191

Horowitz, C. 1997, Physical Review D, 55, 4577

Horowitz, C. J. 2002, Physical Review D, 65, 043001, doi: 10.1103/PhysRevD.65.043001

Hüdepohl, L., Müller, B., Janka, H. T., Marek, A., & Raffelt, G. G. 2010, Physical Review Letters, 104, 251101, doi: 10.1103/PhysRevLett.104.251101

Hunter, J. D. 2007, Computing in Science & Engineering, 9, 90, doi: 10.1109/MCSE.2007.55

Hurley, J. R., Tout, C. A., Wickramasinghe, D. T., Ferrario, L., & Kiel, P. D. 2010, Monthly Notices of the Royal Astronomical Society, 402, 1437, doi: `10.1111/j.1365-2966.2009.15988.x`

Iben, I., J., & Tutukov, A. V. 1984, The Astrophysical Journal, 282, 615, doi: `10.1086/162241`

Isern, J., Canal, R., & Labay, J. 1991, The Astrophysical Journal Letters, 372, L83, doi: `10.1086/186029`

Ivanova, N., Heinke, C. O., Rasio, F. A., Belczynski, K., & Fregeau, J. M. 2008, Monthly Notices of the Royal Astronomical Society, 386, 553, doi: `10.1111/j.1365-2966.2008.13064.x`

Janka, H.-T. 2012, Annual Review of Nuclear and Particle Science, 62, 407, doi: `10.1146/annurev-nucl-102711-094901`

—. 2017a, Neutrino-Driven Explosions, Handbook of supernovae (Springer International Publishing), 1095, doi: `10.1007/978-3-319-21846-5_109`

—. 2017b, in Handbook of Supernovae, ed. A. W. Alsabti & P. Murdin, 1575, doi: `10.1007/978-3-319-21846-5_4`

Janka, H. T., Langanke, K., Marek, A., Martínez-Pinedo, G., & Müller, B. 2007, Physics Reports, 442, 38, doi: `10.1016/j.physrep.2007.02.002`

Janka, H. T., & Moenchmeyer, R. 1989a, Astronomy & Astrophysics, 209, L5

—. 1989b, Astronomy & Astrophysics, 226, 69

Janka, H. T., Müller, B., Kitaura, F. S., & Buras, R. 2008, Astronomy & Astrophysics, 485, 199, doi: `10.1051/0004-6361:20079334`

Joglekar, H., Gangal, K., Vahia, M., & Sule, A. 2011, Puratattva-Bulletin of the Indian Archaeological Society, 41, 207

Jones, S., Hirschi, R., & Nomoto, K. 2014, The Astrophysical Journal, 797, 83, doi: `10.1088/0004-637X/797/2/83`

Just, O. 2012, PhD thesis, Technische Universität München

Just, O., Aloy, M. A., Obergaulinger, M., & Nagataki, S. 2022, The Astrophysical Journal Letters, 934, L30, doi: `10.3847/2041-8213/ac83a1`

Just, O., Bauswein, A., Ardevol Pulpillo, R., Goriely, S., & Janka, H. T. 2015a, Monthly Notices of the Royal Astronomical Society, 448, 541, doi: `10.1093/mnras/stv009`

Just, O., Bollig, R., Janka, H. T., et al. 2018, Monthly Notices of the Royal Astronomical Society, 481, 4786, doi: `10.1093/mnras/sty2578`

Just, O., Obergaulinger, M., & Janka, H. T. 2015b, Monthly Notices of the Royal Astronomical Society, 453, 3386, doi: `10.1093/mnras/stv1892`

Just, O., Vijayan, V., Xiong, Z., et al. 2023, arXiv e-prints, arXiv:2302.10928, doi: `10.48550/arXiv.2302.10928`

Kasen, D., Metzger, B., Barnes, J., Quataert, E., & Ramirez-Ruiz, E. 2017, Nature, 551, 80, doi: 10.1038/nature24453

Keil, M. T., Raffelt, G. G., & Janka, H.-T. 2003, The Astrophysical Journal, 590, 971, doi: 10.1086/375130

Kitaura, F. S., Janka, H. T., & Hillebrandt, W. 2006, Astronomy & Astrophysics, 450, 345, doi: 10.1051/0004-6361:20054703

Kotake, K., Sato, K., & Takahashi, K. 2006, Reports on Progress in Physics, 69, 971, doi: 10.1088/0034-4885/69/4/R03

Kromer, M., Pakmor, R., Taubenberger, S., et al. 2013, The Astrophysical Journal Letters, 778, L18, doi: 10.1088/2041-8205/778/1/L18

Langanke, K., & Schatz, H. 2013, Physica Scripta Volume T, 152, 014011, doi: 10.1088/0031-8949/2013/T152/014011

Langer, N., Deutschmann, A., Wellstein, S., & Höflich, P. 2000, Astronomy & Astrophysics, 362, 1046, doi: 10.48550/arXiv.astro-ph/0008444

Lattimer, J. M. 2012, Annual Review of Nuclear and Particle Science, 62, 485, doi: 10.1146/annurev-nucl-102711-095018

Lattimer, J. M., & Swesty, D. F. 1991, Nuclear Physics A, 535, 331, doi: 10.1016/0375-9474(91)90452-C

Leung, S.-C., Zha, S., Chu, M.-C., Lin, L.-M., & Nomoto, K. 2019, The Astrophysical Journal, 884, 9, doi: 10.3847/1538-4357/ab3b5e

Li, X. D., & van den Heuvel, E. P. J. 1997, Astronomy & Astrophysics, 322, L9

Li, X. D., & Wang, Z. R. 1998, The Astrophysical Journal, 500, 935, doi: 10.1086/305771

Liebendörfer, M., Rampp, M., Janka, H. T., & Mezzacappa, A. 2005, The Astrophysical Journal, 620, 840, doi: 10.1086/427203

Lippuner, J., & Roberts, L. F. 2015, The Astrophysical Journal, 815, 82, doi: 10.1088/0004-637X/815/2/82

Liu, D., & Wang, B. 2020, Monthly Notices of the Royal Astronomical Society, 494, 3422, doi: 10.1093/mnras/staa963

Liu, Y. T., & Lindblom, L. 2001, Monthly Notices of the Royal Astronomical Society, 324, 1063, doi: 10.1046/j.1365-8711.2001.04395.x

Manchester, R. N., Hobbs, G. B., Teoh, A., & Hobbs, M. 2005, The Astrophysical Journal, 129, 1993, doi: 10.1086/428488

Marek, A., Dimmelmeier, H., Janka, H. T., Müller, E., & Buras, R. 2006, Astronomy & Astrophysics, 445, 273, doi: 10.1051/0004-6361:20052840

Marek, A., & Janka, H. T. 2009, The Astrophysical Journal, 694, 664, doi: 10.1088/0004-637X/694/1/664

Margalit, B., Berger, E., & Metzger, B. D. 2019, The Astrophysical Journal, 886, 110, doi: 10.3847/1538-4357/ab4c31

Margalit, B., & Metzger, B. D. 2019, The Astrophysical Journal Letters, 880, L15, doi: 10.

3847/2041-8213/ab2ae2

McBrien, O. R., Smartt, S. J., Chen, T.-W., et al. 2019, The Astrophysical Journal Letters, 885, L23, doi: 10.3847/2041-8213/ab4dae

Metzger, B. D. 2019, Living Reviews in Relativity, 23, 1, doi: 10.1007/s41114-019-0024-0

Metzger, B. D., Piro, A. L., & Quataert, E. 2008a, Monthly Notices of the Royal Astronomical Society, 390, 781, doi: 10.1111/j.1365-2966.2008.13789.x

—. 2009a, Monthly Notices of the Royal Astronomical Society, 396, 1659, doi: 10.1111/j.1365-2966.2009.14909.x

—. 2009b, Monthly Notices of the Royal Astronomical Society, 396, 304, doi: 10.1111/j.1365-2966.2008.14380.x

Metzger, B. D., Quataert, E., & Thompson, T. A. 2008b, Monthly Notices of the Royal Astronomical Society, 385, 1455, doi: 10.1111/j.1365-2966.2008.12923.x

Mezzacappa, A., & Bruenn, S. W. 1993, The Astrophysical Journal, 405, 637, doi: 10.1086/172394

Mignone, A. 2014, Journal of Computational Physics, 270, 784, doi: https://doi.org/10.1016/j.jcp.2014.04.001.

Minerbo, G. N. 1978, Journal of Quantitative Spectroscopy and Radiative Transfer, 20, 541, doi: 10.1016/0022-4073(78)90024-9

Miyaji, S., Nomoto, K., Yokoi, K., & Sugimoto, D. 1980, Publications of the Astronomical Society of Japan, 32, 303

Moenchmeyer, R., Schaefer, G., Mueller, E., & Kates, R. E. 1991, Astronomy & Astrophysics, 246, 417

Moriya, T. J. 2019, Monthly Notices of the Royal Astronomical Society, 490, 1166, doi: 10.1093/mnras/stz2627

Müller, E., & Steinmetz, M. 1995, Computer Physics Communications, 89, 45, doi: 10.1016/0010-4655(94)00185-5

Munier, A., & Weaver, R. 1986a, Computer Physics Reports, 3, 127, doi: 10.1016/0167-7977(86)90007-9

—. 1986b, Computer Physics Reports, 3, 165, doi: 10.1016/0167-7977(86)90008-0

Nagakura, H., Burrows, A., Vartanyan, D., & Radice, D. 2021, Monthly Notices of the Royal Astronomical Society, 500, 696, doi: 10.1093/mnras/staa2691

Nelemans, G., Yungelson, L. R., & Portegies Zwart, S. F. 2001, Astronomy & Astrophysics, 375, 890, doi: 10.1051/0004-6361:20010683

—. 2004, Monthly Notices of the Royal Astronomical Society, 349, 181, doi: 10.1111/j.1365-2966.2004.07479.x

Nomoto, K. 1984, The Astrophysical Journal, 277, 791, doi: 10.1086/161749

—. 1987, The Astrophysical Journal, 322, 206, doi: 10.1086/165716

Nomoto, K., & Iben, I., J. 1985, The Astrophysical Journal, 297, 531, doi: 10.1086/163547

Nomoto, K., & Kondo, Y. 1991, The Astrophysical Journal Letters, 367, L19, doi: 10.1086/185922

Nomoto, K., Miyaji, S., Sugimoto, D., & Yokoi, K. 1979, in IAU Colloq. 53: White Dwarfs and Variable Degenerate Stars, ed. H. M. van Horn, V. Weidemann, & M. P. Savedoff, 56

Obergaulinger, M. 2008, PhD thesis, Technische Universität München

Obergaulinger, M., & Aloy, M. Á. 2021, Monthly Notices of the Royal Astronomical Society, 503, 4942, doi: 10.1093/mnras/stab295

Obergaulinger, M., Janka, H. T., & Aloy, M. A. 2014, Monthly Notices of the Royal Astronomical Society, 445, 3169, doi: 10.1093/mnras/stu1969

Oskinova, L. M., Gvaramadze, V. V., Gräfener, G., Langer, N., & Todt, H. 2020, Astronomy & Astrophysics, 644, L8, doi: 10.1051/0004-6361/202039232

Ostriker, J. P., & Bodenheimer, P. 1968, The Astrophysical Journal, 151, 1089, doi: 10.1086/149507

Ott, C. D., Burrows, A., Livne, E., & Walder, R. 2004, The Astrophysical Journal, 600, 834, doi: 10.1086/379822

Ott, C. D., Burrows, A., Thompson, T. A., Livne, E., & Walder, R. 2006, Astrophysical Journal Supplement Series, 164, 130, doi: 10.1086/500832

O'Connor, E. 2015, The Astrophysical Journal Supplement Series, 219, 24

Pakmor, R., Kromer, M., Röpke, F. K., et al. 2010, Nature, 463, 61, doi: 10.1038/nature08642

Pakmor, R., Kromer, M., Taubenberger, S., et al. 2012, The Astrophysical Journal Letters, 747, L10, doi: 10.1088/2041-8205/747/1/L10

Pakmor, R., Callan, F. P., Collins, C. E., et al. 2022, Monthly Notices of the Royal Astronomical Society, 517, 5260, doi: 10.1093/mnras/stac3107

Pons, J., Miralles, J., & Ibáñez, J. M. 1998, Astronomy and Astrophysics Supplement Series, 129, 343, doi: 10.1051/aas:1998189

Powell, J., Müller, B., Aguilera-Dena, D. R., & Langer, N. 2023, Monthly Notices of the Royal Astronomical Society, doi: 10.1093/mnras/stad1292

Qian, Y. Z., & Wasserburg, G. J. 2007, Physics Reports, 442, 237, doi: 10.1016/j.physrep.2007.02.006

Qian, Y. Z., & Woosley, S. E. 1996, The Astrophysical Journal, 471, 331, doi: 10.1086/177973

Raffelt, G. G. 2001, The Astrophysical Journal, 561, 890, doi: 10.1086/323379

Rampp, M., & Janka, H. T. 2002, Astronomy & Astrophysics, 396, 361, doi: 10.1051/0004-6361:20021398

Raskin, C., Kasen, D., Moll, R., Schwab, J., & Woosley, S. 2014, The Astrophysical

Journal, 788, 75, doi: 10.1088/0004-637X/788/1/75

Roberts, L. F., Woosley, S. E., & Hoffman, R. D. 2010, The Astrophysical Journal, 722, 954, doi: 10.1088/0004-637X/722/1/954

Romani, R. W., Kandel, D., Filippenko, A. V., Brink, T. G., & Zheng, W. 2022, The Astrophysical Journal Letters, 934, L17, doi: 10.3847/2041-8213/ac8007

Rosswog, S., Korobkin, O., Arcones, A., Thielemann, F. K., & Piran, T. 2014, Monthly Notices of the Royal Astronomical Society, 439, 744, doi: 10.1093/mnras/stt2502

Ruiter, A. J., Belczynski, K., Benacquista, M., Larson, S. L., & Williams, G. 2010, The Astrophysical Journal, 717, 1006, doi: 10.1088/0004-637X/717/2/1006

Ruiter, A. J., Sim, S. A., Pakmor, R., et al. 2013, Monthly Notices of the Royal Astronomical Society, 429, 1425, doi: 10.1093/mnras/sts423

Saio, H., & Nomoto, K. 1985, Astronomy & Astrophysics, 150, L21

Scholz, P., Spitler, L. G., Hessels, J. W. T., et al. 2016, The Astrophysical Journal, 833, 177, doi: 10.3847/1538-4357/833/2/177

Schwab, J., Quataert, E., & Bildsten, L. 2015, Monthly Notices of the Royal Astronomical Society, 453, 1910, doi: 10.1093/mnras/stv1804

Schwab, J., Quataert, E., & Kasen, D. 2016, Monthly Notices of the Royal Astronomical Society, 463, 3461, doi: 10.1093/mnras/stw2249

Shapiro, S. L., & Teukolsky, S. A. 1983, Black holes, white dwarfs, and neutron stars: The physics of compact objects (John Wiley & Sons)

Sharon, A., & Kushnir, D. 2020, The Astrophysical Journal, 894, 146, doi: 10.3847/1538-4357/ab8a31

Shibata, M., & Sekiguchi, Y.-I. 2004, Physical Review D, 69, 084024, doi: 10.1103/PhysRevD.69.084024

Shibata, M., & Taniguchi, K. 2006, Physical Review D, 73, 064027, doi: 10.1103/PhysRevD.73.064027

Shibata, M., & Uryū, K. ō. 2000, Physical Review D, 61, 064001, doi: 10.1103/PhysRevD.61.064001

Siegel, D. M., Ciolfi, R., Harte, A. I., & Rezzolla, L. 2013, Physical Review D, 87, 121302, doi: 10.1103/PhysRevD.87.121302

Sneppen, A., Watson, D., Bauswein, A., et al. 2023, Nature, 614, 436, doi: 10.1038/s41586-022-05616-x

Steiner, A. W., Hempel, M., & Fischer, T. 2013, The Astrophysical Journal, 774, 17, doi: 10.1088/0004-637X/774/1/17

Sumiyoshi, K., Yamada, S., Suzuki, H., et al. 2005, The Astrophysical Journal, 629, 922, doi: 10.1086/431788

Summa, A., Janka, H.-T., Melson, T., & Marek, A. 2018, The Astrophysical Journal, 852, 28, doi: 10.3847/1538-4357/aa9ce8

Taam, R. E., & van den Heuvel, E. P. J. 1986, The Astrophysical Journal, 305, 235, doi: 10.1086/164243

Takiwaki, T., Kotake, K., & Foglizzo, T. 2021, Monthly Notices of the Royal Astronomical Society, 508, 966, doi: 10.1093/mnras/stab2607

Tanvir, N. R., Levan, A. J., González-Fernández, C., et al. 2017, The Astrophysical Journal Letters, 848, L27, doi: 10.3847/2041-8213/aa90b6

Tassoul, J.-L. 2000, Stellar rotation, Vol. 36 (Cambridge University Press)

Taubenberger, S., Kromer, M., Pakmor, R., et al. 2013, The Astrophysical Journal Letters, 775, L43, doi: 10.1088/2041-8205/775/2/L43

Tauris, T. M., Sanyal, D., Yoon, S. C., & Langer, N. 2013, Astronomy & Astrophysics, 558, A39, doi: 10.1051/0004-6361/201321662

Tohline, J. E. 1984, The Astrophysical Journal, 285, 721, doi: 10.1086/162550

Toro, E. F. 2013, Riemann solvers and numerical methods for fluid dynamics: a practical introduction (Springer Science & Business Media)

van der Velden, E. 2020, The Journal of Open Source Software, 5, 2004, doi: 10.21105/joss.02004

van Riper, K. A. 1979, The Astrophysical Journal, 232, 558, doi: 10.1086/157314

Vartanyan, D., Coleman, M. S. B., & Burrows, A. 2022, Monthly Notices of the Royal Astronomical Society, 510, 4689, doi: 10.1093/mnras/stab3702

Virtanen, P., Gommers, R., Oliphant, T. E., et al. 2020, Nature Methods, 17, 261, doi: 10.1038/s41592-019-0686-2

Walder, R., Burrows, A., Ott, C. D., et al. 2005, The Astrophysical Journal, 626, 317, doi: 10.1086/429816

Wanajo, S., Janka, H.-T., & Müller, B. 2011, The Astrophysical Journal Letters, 726, L15, doi: 10.1088/2041-8205/726/2/L15

Wanajo, S., Müller, B., Janka, H.-T., & Heger, A. 2018, The Astrophysical Journal, 852, 40, doi: 10.3847/1538-4357/aa9d97

Wanajo, S., Sekiguchi, Y., Nishimura, N., et al. 2014, The Astrophysical Journal Letters, 789, L39, doi: 10.1088/2041-8205/789/2/L39

Wang, B. 2018, Monthly Notices of the Royal Astronomical Society, 481, 439, doi: 10.1093/mnras/sty2278

Wang, B., Justham, S., Liu, Z. W., et al. 2014, Monthly Notices of the Royal Astronomical Society, 445, 2340, doi: 10.1093/mnras/stu1891

Wang, B., & Liu, D. 2020, Research in Astronomy and Astrophysics, 20, 135, doi: 10.1088/1674-4527/20/9/135

Wang, B., Podsiadlowski, P., & Han, Z. 2017, Monthly Notices of the Royal Astronomical Society, 472, 1593, doi: 10.1093/mnras/stx2192

Waxman, E. 2017, The Astrophysical Journal, 842, 34, doi: 10.3847/1538-4357/aa713e

Webbink, R. F. 1984, The Astrophysical Journal, 277, 355, doi: 10.1086/161701

Wheeler, J. C., Cowan, J. J., & Hillebrandt, W. 1998, The Astrophysical Journal Letters, 493, L101, doi: 10.1086/311133

Whelan, J., & Iben, Icko, J. 1973, The Astrophysical Journal, 186, 1007, doi: 10.1086/152565

Woosley, S. E., & Baron, E. 1992, The Astrophysical Journal, 391, 228, doi: 10.1086/171338

Woosley, S. E., Heger, A., & Weaver, T. A. 2002, Reviews of Modern Physics, 74, 1015, doi: 10.1103/RevModPhys.74.1015

Wu, C., Wang, B., & Liu, D. 2019, Monthly Notices of the Royal Astronomical Society, 483, 263, doi: 10.1093/mnras/sty3176

Wu, C., Xiong, H., Lin, J., et al. 2023, The Astrophysical Journal Letters, 944, L54, doi: 10.3847/2041-8213/acb6f3

Yasin, H., Schäfer, S., Arcones, A., & Schwenk, A. 2020, Physical Review Letters, 124, 092701, doi: 10.1103/PhysRevLett.124.092701

Yoon, S. C., & Langer, N. 2005, Astronomy & Astrophysics, 435, 967, doi: 10.1051/0004-6361:20042542

Yoon, S. C., Podsiadlowski, P., & Rosswog, S. 2007, Monthly Notices of the Royal Astronomical Society, 380, 933, doi: 10.1111/j.1365-2966.2007.12161.x

Yueh, W. R., & Buchler, J. R. 1977, The Astrophysical Journal, 217, 565, doi: 10.1086/155605

Zha, S., Chu, M.-C., Leung, S.-C., & Lin, L.-M. 2019, The Astrophysical Journal, 883, 13, doi: 10.3847/1538-4357/ab3640

Zwerger, T., & Mueller, E. 1997, Astronomy & Astrophysics, 320, 209

Acknowledgements

This Thesis would not have been possible without the contribution and support of several people in my life.

First of all, I would like to express my gratitude to my supervisor, Hans-Thomas Janka, for giving me the opportunity to work with his group at the Max Planck Institute for Astrophysics in Garching. I am thankful for the fruitful discussions, guidance, advice, and support that helped me to grow as a scientist in the last few years.

I want to thank Benedetta Ciardi and Achim Weiss for being members of my thesis committee and always guiding me in a supportive way while I was navigating the PhD journey.

I am very grateful to Robert Glas for being a mentor during my PhD years; for the introduction and assistance with the code ALCAR, for always being willing to answer my questions, and for the guidance and overall support during my PhD. I want to thank Jakob Ehring for introducing me to the AIC topic and for all the valuable discussions concerning the physics of AICs. I would like to thank Oliver Just for providing the code ALCAR and for always being willing to assist with the code and answer my questions. Many thanks to my colleagues; Daniel, Jakob E., Jakob H., Johannes, Liliya, Naveen, Malte, and Robert, for all these years of enjoyable coffee breaks, kicker breaks, MPA parties, and, of course, daily scientific interaction.

Constantina, Jessie, and Liliya, thank you for being amazing friends and making my everyday life at MPA more beautiful. Laura and Maja, you are the best officemates I could have wished for.

Thank you to Robert, Ulli, Tiara, Stephen, Andre, Jakob E., Jakob H., and Constantina for proofreading parts of this Thesis.

This journey would not have been possible without some significant people in my life. I would like to thank Ulli for his support, guidance, inspiration, and all the beautiful moments together. This journey was by far easier with you by my side. Alkistis, thank you for always being there for me, supporting me in every moment, being my adventure buddy, and constantly reminding me to be true to myself. I would like to deeply thank my long-distance friends Artemis and Niki for supporting me through this journey in their own unique and lovely way. I want to express my deepest gratitude to the best friends I could ever have in Munich; Dimitris, Myrto, Nancy, and Vasiliki; I could not have done this without you. Thank you for everything - you know what I mean.

I want to thank Lena, Vaggelis, and Vassilis for helping me navigate the turbulent PhD journey and beyond.

Θα ήθελα να ευχαριστήσω τους γονείς μου Μπάμπη και Ράνια, και τον αδερφό μου Σπύρο που είναι πηγή υποστήριξης όλα αυτα τα χρόνια, που πάντα πίστευαν σε εμένα και διαμόρφωσαν τον άνρθωπο που είμαι σήμερα.